

Characterisation of Contrast Agents for Photoacoustic Imaging



Thomas Stahl

Department of Medical Physics and Biomedical Engineering

University College London

Supervisors:

Prof. Paul C. Beard

Prof. Helen C. Hailes

Prof. Alethea Tabor

Thesis submitted for the degree of Doctor of Philosophy (Ph.D.)

at University College London

2016

*I have seen flowers come in stony places
And kind things done by men with ugly faces
And the gold cup won by the worst horse at the races,
So I trust, too.*

John Masefield

Abstract

Photoacoustic imaging is a promising imaging modality which combines both excellent spatial resolution with high contrast and specificity. This makes it well suited to clinical and pre-clinical studies of the physiological changes which accompany conditions such as cancer and cardiovascular disease. In order to fully realize the potential of this technique, new contrast agents with the ability to generate strong PA signals upon excitation with light in the near infrared, good stability and biocompatibility, are required. Previously, numerous absorbing materials have been proposed for this purpose. Their potential to generate PA contrast is frequently evaluated using purely optical methods (e.g. absorption spectroscopy). This practice however fails to account for relevant thermodynamic properties involved in the PA signal generation process, namely the thermalisation efficiency (E_t) and the Grüneisen coefficient (Γ). To address this, a PVDF-based PA spectroscopic set-up was designed and methods developed which allowed the determination of the absorption coefficient (μ_a), E_t , Γ , PA amplitude and μ_a spectra as well as enabling analysing the photostability.

In order to identify promising contrast agents for molecular PA imaging an array of nanoparticles was synthesised and together with various commercial available nanoparticles and organic dyes their ability to generate strong PA signals was evaluated using the PA spectroscope. π -conjugated polymeric nanoparticles demonstrated the ability to generate strong PA signals upon excitation and were therefore analysed in preliminary *in vitro* targeting experiments. In order to show the ability of the π -conjugated polymeric nanoparticles to generate strong PA signals under realistic conditions, *in vivo* animal experiments were carried out. The *in vivo* experiments demonstrate that at 800 nm the novel π -conjugated polymeric nanoparticle based on the polymer INDT-BT can be detected in the presence of the endogenous chromophores such as haemoglobin and water, allowing to unambiguously image the presence of the nanoparticles.

Declaration

I, Thomas Stahl, confirm that the work presented in this thesis is my own. Where information has been derived from other sources, I confirm that this has been indicated in the thesis.

A handwritten signature in black ink that reads "Thomas Stahl". The signature is written in a cursive style with a prominent loop at the end of the last name.

14 September 2016

Acknowledgements

First and foremost, I would like to thank my supervisor, Prof. Paul C. Beard, for his continual help and guidance throughout the whole term of the project. Especially the countless meetings and discussions, in person or during the last period of the project via video chat, gave me encouragement and determination. I am also grateful to my second and third supervisors, Prof. Helen Hailes and Prof. Alethea Tabor, for their enthusiasm for my project and their insight and support preparing the various nanoparticles.

My deepest appreciation and gratitude extends to many members of the Photoacoustic Imaging group who have contributed to making this work possible: in particular, to Dr. Edward Zhang, Dr. Jan Laufer (TU Berlin, Germany), Dr. Thomas Allen, Dr. James Guggenheim, Dr. Robert Ellwood and Dr. Daniil Nikitichev and for their time and assistance answering various experimental and theoretical queries and their help designing and validating the PA spectroscope and to Dr. Olumide Ogunlade for his unlimited support generating *in vivo* and *in vitro* PA images. Furthermore, my appreciation extends to various individuals and departments throughout UCL for offering their time and facilities, especially the members of the Department of Chemistry at UCL: Dr. Robin Bofinger for his time and his much valued support with various preparation protocols, Dr. Hugo Bronstein and Dr. Kealan Fallon for supplying the π -conjugated semiconducting polymers, Mr Ivan Lam for providing the short PEG chain maleimide lipid and his preliminary work on the preparation of polymeric π -conjugated semiconducting nanoparticles and Dr. Zoe Wright (UCL Department of Chemistry) for her help preparing copper sulphide nanoparticles and the members of the UCL Cancer institute: Prof. R. Barbara Pedley for generously providing the facilities for the *in vitro* experiments, Dr. Peter Johnson for providing the cells and animals for this research and his on-going interest and support of my work, Dr. Vineeth Rajkumar and Dr. Vessileva Vessel for their help with the antigen targeting experiments and Mr. Mathew Robson for repeatedly carrying out the intratumoral injections of the contrast agents prepared.

My most personal thanks I owe to my friends and family for their loving support and enduring encouragement, especially to my parents for their constant moral, material and financial support.

In addition I would also express my appreciation to the Engineering and Physical Science Research Council (EPSRC) who provided the funding for this project.

Contents

Abstract	1
Declaration	2
Acknowledgements	3
Contents	4
List of Figures	7
List of Tables	15
List of Abbreviations	17
List of Symbols	19
Chapter 1 Introduction	21
1.1 Motivation	21
1.2 Aims of the project	22
1.3 Thesis structure	23
Chapter 2 Background	25
2.1 Photoacoustic imaging	25
2.2 Molecular photoacoustic imaging	32
2.3 Exogenous contrast agents	36

Chapter 3 Characterisation of the photoacoustic spectroscope	56
3.1 Introduction	56
3.2 Photoacoustic spectroscope	57
3.3 Validation	72
3.4 Conclusion	90
Chapter 4 Characterisation of contrast agents	93
4.1 Introduction	93
4.2 Materials	94
4.3 TEM measurements	97
4.4 Dynamic light scattering measurements	99
4.5 ζ -potential measurements	101
4.6 Spectrophotometer measurements	104
4.7 Photoacoustic spectroscopy and extinction coefficient measurements	105
4.8 Thermalisation efficiency measurements	111
4.9 Grüneisen coefficient measurements	113
4.10 Photostability measurements	123
4.11 Conclusion	128
Chapter 5 In vitro and in vivo analysis	132
5.1 Introduction	132
5.2 <i>In vitro</i> targeting experiments	133
5.3 <i>In vivo</i> experiments	136
5.4 Conclusion	140

Chapter 6 Conclusions	142
6.1 Conclusions	142
6.2 Summary of findings	142
6.3 Suggestions for future work	147
Appendix	150
A1 Preparation of contrast agents	150
6.1 Introduction:	150
6.2 Methods	151
6.3 Conclusion	167
A2 Commercial evaluation of semiconducting polymeric nanoparicles	168
Introduction	168
Potential applications	170
Production costs	182
Intellectual property	186
Conclusion	186
Bibliography	187

List of Figures

- Figure 2-1:** Schematic describing the PA effect from excitation to ultrasound emission. The excitation with modulated light (a) induces an excited state of the light absorbing compound (b), which relaxes non-radiatively to its ground state (c). The rapid heating causes the emission of an ultrasound (d). t_{ex} = time of introducing excitation light; Φ_0 = Initial fluence; Φ_t = Fluence after excitation. 26
- Figure 2-2:** Scheme of the crystal structure of PZT, showing the displacement of the Titanium or Zirconium ions in centre of the unit, introducing polarity..... 28
- Figure 2-3:** Chemical structure of 1,1-Difluoroethylene (a) and PVDF (b). The high electronegativity of the fluoride ligand gives rise to the piezoelectric effect due to the formation of charge separation, as depicted by the two coloured blocks indicating the opposing charges. 29
- Figure 2-4:** Working principle of the Fabry-Perot element. 29
- Figure 2-5:** Chemical structure of heme B (a), part of haemoglobin, and melanin (b). 30
- Figure 2-6:** Absorption spectra of the strongest endogenous absorbers haemoglobin (contained within whole blood) and water. The values were taken from reference ²¹. 32
- Figure 2-7:** Chemical structure of PEG. n is the number of repeat units. 36
- Figure 2-8:** Chemical structure of DSPE PEG 2000 COOH 36
- Figure 2-9:** Chemical structure of methylene blue. 37
- Figure 2-10:** Chemical structure of benzene (a) and indocyanine green (b), showing the difference in the extent of the conjugated π -systems of the two molecules. Due to the size of the conjugated π -system of indocyanine green, spanning from the outer benzenes across the heptamethine system its absorption maximum lies within the near infrared whilst benzene absorbs in the ultraviolet. 38
- Figure 2-11:** General synthesis of an azo dye. The synthesis consists of two steps: the formation of a reactive diazonium ion (a) and the azo coupling (b). 39
- Figure 2-12:** Resonance structure of an example of a cyanine dye (Cy5). 40

- Figure 2-13:** Band structure of H- and J-aggregates. The energy level of S_1 increases in H-aggregates compared to the monomeric species and results in a shift of the absorption and emission band to shorter wavelength. J-aggregates result in a shift of the absorption and emission band to longer wavelength. 41
- Figure 2-14:** Sizes of different Biological nano sized materials, man-made nanoparticles and other materials. 43
- Figure 2-15:** Schematic showing the bottom-up and the top-down approach for the synthesis of nanoparticles. 44
- Figure 2-16:** Reactions involved for bottom-up synthesis of gold nanorods. Two step reduction of chloroauric acid to elementary gold, forming the nano-construct. 44
- Figure 2-17:** Profile of single-walled carbon nanotube (a) and multi-walled carbon nanotubes with a spiral profile (b) and concentric cylinders (c). 49
- Figure 2-18:** Basic arrangement of carbon atoms in carbon nanotubes and graphene-sheets (a). a_1 and a_2 are the unit vectors and C1-6 the positions of the individual carbon atoms. (b) shows three different examples for carbon nanotube folding, using various chiral indices: Zigzag configuration (chiral indices $(n,0)$; blue dotted line), armchair configuration (chiral indices $(n = m)$; green dotted line) and an example of a graphene-sheet with the chiral indices $(4,2)$. C_n is the resulting vector (red arrow) and T the resulting tube axis (red dashed arrow). 50
- Figure 2-19:** Examples of electronic transitions of metallic and semiconducting carbon nanotubes. E_{11} = First van Hove optical transition; E_{22} = Second van Hove optical transition; CB = Conduction band; VB= Valence band; DOS = Density of states. 51
- Figure 2-20:** Chemical structure of the polymeric semiconductor PCPDTBT. 52
- Figure 3-1:** Schematic of instrumentation used for PA characterisation measurements (top) and a zoom of the sample cuvette (bottom left) with a diagram showing the exponential decay of the light intensity traveling through a purely absorbing medium (bottom right). OPO = Excitation laser system; P = Integrating sphere with photodiode; B = Beam splitter; S = Sample cuvette; W = Water tank; US = Ultrasound transducer; AD = Analog-to-digital converter. Depending on the laser system used the AD is either a digital oscilloscope or a data acquisition card installed on a PC. Also depending on the laser system the beam splitter and the photodiode were replaced by a laser inbuilt power meter. z = depth; $H(z)$ = Absorbed energy density as a function of depth. 58
- Figure 3-2:** Photograph of a homemade cuvette containing an aqueous solution of IR-820. 59

- Figure 3-3:** Schematic of liquids in a container forming either a concave (a) or a convex (b) meniscus. A practical solution to avoid the formation of such a meniscus is to completely enclose the liquid with a lid (c). 60
- Figure 3-4:** Two designs of the PVDF ultrasound transducers. Initial design (left) using a drilled hole for the electrical connection between the PVDF film and the BNC connector. The final design (right) uses a silver ink track for the electrical connection..... 61
- Figure 3-5:** Modelled PA signals generated in homogeneous purely absorbing solutions with μ_a varying between 0 and 50mm^{-1} (left). Modelled frequency spectra (right) of the PA signals shown on the left. The orange line indicates 10% and the blue line 5% of the power density. The points at which the lines cross the curves were plotted in the inset (top right), which shows μ_a versus the bandwidth (frequency) at 10% (orange points) and 5% (blue squares) of the amplitude..... 64
- Figure 3-6:** Laser generated ultrasound signals recorded using a Fabry-Perot sensor (red dotted line) and a PVDF transducer (black line). 66
- Figure 3-7:** Measured normal incidence frequency response of a PVDF ultrasound transducer of $52\ \mu\text{m}$ thickness (black crosses) and comparison to the modelled frequency response (black line). The modelled data was obtained by modelling Equation 3-1. Also shown is the Fourier transformation of the signal recorded using the Fabry-Perot sensor (FP, red dashed line) and the PVDF transducer (blue dashed line). 67
- Figure 3-8:** Setup used for the measurement of the directional response of the ultrasound transducer. LU = Laser generated ultrasound source made from black painted PMMA disc mounted in a cylindrical housing for the generation of ultrasound, mounted on a motorised rotation stage. Nd:YAG = Nd:YAG Q-switched laser; W = Water tank; US = ultrasound transducer; AD = Analog-to-digital converter; Amp = Amplifier. 68
- Figure 3-9:** Signal amplitude recorded at various angles using the PVDF transducer. The inset shows a plot of the peak signal amplitude versus the angle of incidence. 69
- Figure 3-10:** Measured directivity as a function of frequency at angles ranging from -15° to 15° of a PVDF transducer with a thickness of $52\ \mu\text{m}$ and dimensions of $9 \times 9\ \text{mm}^2$ 70
- Figure 3-11:** Left: Fitted Bessel functions (dashed lines) to the angular response of the PVDF transducer (full lines). Right: Effective radius of the PVDF transducer as a function of frequency. The error bars are the average standard deviation of the Bessel function from the angular response of the PVDF transducer..... 71

- Figure 3-12:** Example of PA signal generated by water irradiated with laser light of a wavelength of 1450 nm (solid, black line) showing the corresponding exponential fit (dashed, red line) used to determine the absorption coefficient and the PA amplitude S_0 . The dashed blue line is the exponential fit to the reflection of the signal..... 75
- Figure 3-13:** Comparison of PA signals recorded using an enclosed cuvette filled with an aqueous solution of IR 820. The chromophore solution within the sample cuvette is either bordering air (red dashed line) or water (black line) on the top of it. The inset on the bottom left shows the signal generated using the impedance matching layer on top of the cuvette on a greater time-scale..... 76
- Figure 3-14:** Near-infrared spectrum of water measured using the PA spectroscopy (blue circles μ_a and red crosses PA amplitude spectrum) and a spectrophotometer (PS; green triangles). The inset shows μ_a (blue circles) and PA amplitude (red crosses) measured using the PA spectroscopy versus μ_a measured using the spectrophotometer of water with wavelength between 1400 nm and 2000 nm. The dashed black line shows theoretical line of μ_a where μ_a measured using the PA spectroscopy is equal to that measured using the spectrophotometer. The error bars are the standard deviation of ten subsequent measurements. The maximum error is 15% and the minimum 3% of the spectrophotometer values. 79
- Figure 3-15:** μ_a versus SNR measured using water irradiated by different wavelength at varying fluences. These wavelengths were chosen in order to gain different values of μ_a in the range of 1-13 mm^{-1} . The solid lines are the true μ_a values measured using the spectrophotometer. The symbols are the measured values at a specific wavelength and fluence. 81
- Figure 3-16:** μ_a (black dots) and PA amplitude (red crosses) measured using the PA spectroscopy versus μ_a based on the known ϵ of IR 820 at its absorption maxima ($\epsilon(820 \text{ nm}) = 2.3 \cdot 10^5 \text{ M}^{-1} \text{ cm}^{-1}$). The inset on the top left is a zoom into the area indicated by the grey dashed box..... 82
- Figure 3-17:** Error in % of μ_a and the PA amplitude measured compared to the calculated values over the μ_a 82
- Figure 3-18:** Comparison between Fabry-Perot sensors (200 MHz and 60 MHz) and the PVDF ultrasound transducer. The dashed horizontal lines indicate the upper detection limits for the PA amplitude measurements for the PVDF transducer and the 40 μm thick Fabry-Perot transducer. 83
- Figure 3-19:** Comparison between signals generated by rhodamine B at different concentrations, yielding E_t values between 48% and 85%, and methanol (MeOH) at 1550 nm ($E_t = 100\%$). Signals of IR 780 ($E_t \sim 100\%$) at different concentrations were included for comparison..... 86

- Figure 3-20:** Φ_F of rhodamine B (red circles) and rhodamine 6G (black stars and crosses) versus the concentration, estimated using the reference-absorber method (method 1) and the self-referencing method (method 2). Literature values are plotted for comparison (lines with squares). The error bars are the standard deviation of five measurements. 87
- Figure 3-21:** Γ versus %vol. of water in methanol and ethanol. The black lines represent the linear trend of the two alcohol/water mixtures, with variances of $R^2 = 0.993$ for methanol/water and $R^2 = 0.9865$ for ethanol/water. The dashed red lines are an extension of the linear trend lines. 89
- Figure 3-22:** Photobleaching characteristic of rhodamine B, irradiated over 20,000 laser pulses with a wavelength of 550 nm. 90
- Figure 4-1:** (a) Chemical structure of IR 820 (1), methylene blue (2), cresyl violet (3) and fluorescein (4). (b) Image of a selection of nanoparticles and organic dyes within sample containers. From left to right the sample containers are filled with gold nanorods, carbon nanotubes, IR 820, methylene blue, cresyl violet and fluorescein solutions. 95
- Figure 4-2:** Chemical structure of semiconducting polymers. Top left: INDT-T: X=S; INDT-S: X=Se; Top right: INDT-BT; Bottom: DPPTT-T: X=S; DPPTT-S: X=Se. 96
- Figure 4-3:** TEM images of DPPTT-T (right) and DPPTT-S (left) nanoparticles. 98
- Figure 4-4:** Particle size distribution INDT-X and PCPDTBT. The numbers below the labels are the z-average values - the average particle size measured in nm. 100
- Figure 4-5:** Diagram showing an example of a spherical particle, dispersed in solution, surrounded by the various layers of ions (top) and the potential differences as a function of distance from the particle surface. 102
- Figure 4-6:** Particle diameter over time of three PCPDTBT nanoparticles samples with different surface modifications. 104
- Figure 4-7:** Extinction spectra of various chromophores, measured using the PA spectroscopy (symbols) and reference measurements using the spectrophotometer (lines). FL = Fluorescein; R6G = Rhodamine 6G; RB = Rhodamine B; CV = Cresyl violet; MB = Methylene blue; PCPDTBT = PCPDTBT nanoparticles; PPy = Polypyrrole nanoparticles; Gold NRs = Gold nanorods. Note: The extinction coefficients of the nanoparticles (PCPDTBT, PPy, INDT-BT and gold nanorods) are plotted on a logarithmic scale, corresponding to the right hand axis. 106
- Figure 4-8:** Extinction spectra of various nanoparticles, measured using the PA spectroscopy (symbols) and reference measurements using the spectrophotometer (lines). 107

- Figure 4-9:** Γ versus the concentration of CuCl_2 (black crosses) and NiCl_2 (red dots) in water and Γ of pure water. 114
- Figure 4-10:** Results of the Γ measurements (red dots) compared to literature values (black line) at temperatures ranging from about 4 °C to 23 °C. The plot also shows the decreasing PA amplitude (black crosses) in the temperature range measured..... 116
- Figure 4-11:** Γ (red stars), PA amplitude (black crosses) and μ_a (black line) spectra of IR 820. 117
- Figure 4-12:** PA amplitude (red crosses), μ_a (red dashed line) and Γ (red stars) spectra of CuCl_2 (200 gL^{-1}) in water at 20 °C compared to PA amplitude (black crosses), μ_a (black line) and Γ (black squares) spectra of CuCl_2 (200 gL^{-1}) in water at 4 °C. 118
- Figure 4-13:** Γ (red stars), PA amplitude (black crosses) and μ_a (black line) spectra of the CuCl_2 solutions using various solvents and PA amplitude spectra of the pure solvents used for the experiments (blue squares). The solvents used were water (H_2O), isopropanol (IPA), methanol (MeOH), ethanol (EtOH), acetone (DMK) and dimethyl sulfoxide (DMSO). 120
- Figure 4-14:** Scheme of the hydrogen bonding pattern in the first three hydration shells (left) and an example of a metal ion trapped by water molecules (right). The red spheres in the scheme on the right represent oxygen atoms, the white spheres hydrogen atoms and the grey spheres the metal ion. Dashed lines represent hydrogen bonds. 121
- Figure 4-15:** Photobleaching profile of gold nanorods, methylene blue, fluorescein, cresyl violet, IR 780, IR 820, rhodamine B, rhodamine 6G and polypyrrole nanoparticles. 124
- Figure 4-16:** PA amplitude spectra recorded at fluences between 1.2 mJcm^{-2} and 7.8 mJcm^{-2} . The solid line is the ϵ spectrum measured using a spectrophotometer (PS). The PA amplitude spectra recorded at 4.9 mJcm^{-2} and 7.8 mJcm^{-2} do not show the characteristic absorption peak at about 800 nm, due to photo induced melting of the nanorod samples. 126
- Figure 4-17:** PA signals recorded using gold nanorods irradiated by laser light with a wavelength of 820 nm and a light fluence of 3 mJcm^{-1} (black line) and 5 mJcm^{-1} (red dashed line)..... 127
- Figure 4-18:** PA amplitude of gold nanorods at fluences between 2 mJcm^{-2} and 6 mJcm^{-2} . Signals were recorded at the wavelength of peak absorption - 810nm. 127
- Figure 4-19:** Plot of E_t versus ϵ and λ_{max} of the contrast agents characterised. 130

- Figure 5-1:** *In vivo* PA images (x-y maximum intensity projection; area 14 x 14 mm²) at excitation wavelengths of 750 nm, 800 nm and 850 nm before injection (a), 1 h (b) and 5 h post intratumoral injection (c). The red arrow shows the same blood vessel at the different time points, allowing to judge the position of the tumour on the PA scanner. The green arrow indicates the site of injection. The red dashed line shows the tumour margin..... 137
- Figure 5-2:** Multi wavelength *in vivo* photoacoustic showing spectral dependence of INDT-BT nanoparticles and vasculature: Photoacoustic images (a) before (b) after subcutaneous injection of INDT-BT nanoparticles in the flank of a mouse. x-y maximum intensity projections (top rows, area 14 x 14 mm²) and y-z maximum intensity projection (bottom rows, area 14 x 6 mm²) acquired at different excitation wavelengths are shown. 139
- Figure 5-3:** Normalised wavelength dependence of INDT-BT nanoparticles *in vivo*. The PA *in vivo* values (red circles) are the normalised image intensities of the 3D PA images (Figure 5-2) over the regions corresponding to the nanoparticles. PA S_0 (black circles) is the PA amplitude and PA ϵ (black dots) the extinction coefficient measured using PA spectroscopy. SP (dashed line) is the extinction coefficient spectrum measured using a spectrophotometer. 140
- Figure A1-1:** Absorption spectra of PS IR 780 before and after each washing step. 154
- Figure A1-2:** Absorption spectra of PS IR 820 before and after each washing step. 154
- Figure A1-3:** PA amplitude (S_0) of IR 820 (black dashed line with black crosses) and PS IR 820 nanoparticles (NPs) (blue dashed line with blue circles) and μ_a spectra of IR 820 (black line with black stars) and PS IR820 nanoparticles (blue line with blue squares), showing a red shift of about 30nm.. 155
- Figure A1-4:** Antibody conjugation reaction using PS-COOH. The grey ball represents the PS nanoparticle. Reaction of the COOH functional group with EDC forming an intermediate, which subsequently reacts with solfo-NHS. In the final step the formed PS-NHS conjugate reacts with the N-terminus or a lysine residue of an antibody to form the conjugate..... 156
- Figure A1-5:** PA amplitude and μ_a measured using the PA spectroscopy ($\mu_a(\text{PA})$) and transmission spectra ($\mu_a(\text{SP})$) of a batch of poly (allylamine) nanoparticles..... 158
- Figure A1-6:** PA amplitude and ϵ measured using the PA spectroscopy ($\epsilon(\text{PA})$) and transmission spectra ($\epsilon(\text{SP})$) of the polypyrrole gifted by Sheffield University..... 160
- Figure A1-7:** Chemical structure of polystyrene sulfonate (left) and PEDOT (right)..... 160
- Figure A1-8:** Chemical structure of four-arm PEG-amine..... 161
- Figure A1-9:** Chemical structure of the novel short PEG chain maleimide lipid. 164

- Figure A1-10:** Conjugation reaction of semiconducting nanoparticles (grey ball) with sulfhydryl on a protein (plain circle). 165
- Figure A2-1:** Potential commercial applications and properties of the PSNs desirable for each individual application. PTT = Photothermal therapy. 169
- Figure A2-2:** Schematic of semiconducting polymeric nanoparticles, showing the porous polymeric core (green lines) stabilized by surfactants (blue lines). The red shapes represent molecules such as antibodies, conjugated to the surfactants; the red spheres symbolize another material which is loaded and retained within the porous structure of the polymer. 170
- Figure A2-3:** Volume of various biomedical and medical markets (in billion dollars) with potential application for PSNs. 177
- Figure A2-4:** Market volume of nanoparticles used in theranostic applications (in billion dollars) from 2012 till 2020. The values for 2017 and 2020 are based on an annual growth rate of 10.8%. 178
- Figure A2-5:** Working principle of second generation barcoding based on fluorescence nanoparticles (top left). There different types of nanoparticles (PSN 1, 2 and 3) are used to generate a specific fluorescent spectrum (top right) which can be read by a handheld spectroscope. 181
- Figure A2-6:** Potential customers for semiconducting polymeric nanoparticles. 185

List of Tables

Table 2-1: Examples of commercially available dyes, their manufacturers and optical properties. The values for λ_{Ex} , λ_{Em} , ϵ and Φ_f are taken from Manufacturer data. λ_{Ex} = Peak absorption wavelength; λ_{Em} = Peak emission wavelength, Φ_f = quantum yield.....	39
Table 2-2: Properties of two commercial available organic dyes with absorption in the near-infrared - Atto 740 and HiLyte 750. The values for λ_{max} , ϵ_{max} , the E_t and the photobleaching have been taken from the supplier's website.....	42
Table 2-3: Properties of two commercial available gold nanoparticeles - gold nanospheres (GNS) and gold nanorods (GNR). The values for λ_{max} , ϵ_{max} , the thermalisation efficiency and the photostability have been taken from the supplier's website. The fluence threshold is the fluence required to melt the particle - causing reshaping and coalescence of the molten metal particles.	47
Table 2-4: Properties of nanoparticles made from two commercial available semiconducting polymers - PCPDTBT and polypyrrole. The values for λ_{max} , ϵ_{max} and the thermalisation efficiency have been taken from reference ¹¹⁸ and ¹¹⁹	53
Table 2-5: Overview of exogenous contrast agents for PA imaging.	55
Table 3-1: NEP of various PVDF ultrasound transducers.....	63
Table 3-2: Detection limit of the PA spectroscopie.	84
Table 4-1: List of contrast agents analysed.....	95
Table 4-2: Average particle size and PDI of various home-made polymeric nanoparticles. The numbers in brackets are the number of sample batches analysed n, followed by the standard deviation of the average particle size.....	100
Table 4-3: Particle diameter, PDI and ζ -potential of various polymeric nanoparticles. PCPDTBT-DPPC: PCPDTBT nanoparticles with DPPC as a stabiliser; PCPDTBT-Maleimide: PCPDTBT nanoparticles with DPPC as a stabiliser and 5mol% PEG-2000-Maleimide; PCPDTBT-COOH: PCPDTBT nanoparticles with DPPC as a stabiliser and 5mol% PEG-2000-COOH.	103
Table 4-4: Comparison between measured and literature ϵ of various chromophores. * ϵ from suppliers documentation.	109

Table 4-5: Comparison between ϵ of various chromophores measured using the PA spectroscope (ϵ_{PA}) and the spectrophotometer (ϵ_{trans}).	110
Table 4-6: Results of E_t measurements using various chromophores. Literature values for E_t of the polymeric nanoparticles marked with an x were due to the novelty of the nanoparticles not available.	112
Table 4-7: Measurements of various sample chromophores in solution of concentrations.	115
Table A1-1: Results from the initial attempt to form a stable colloid solution using single walled carbon nanotubes (SWCNT) or multi walled carbon nanotubes (MWCNT).	151
Table A1-2: Table of the various concentrations of PAH and Na_2HPO_4 used for the formulation of poly (allylamine hydrochloride) nanoparticles and the resulting particle size and PDI..	157
Table A1-3: Size and PDI of poly (allylamine) nanoparticles after nanoparticle formation (step 1 of the synthesis) and after complete synthesis.	158
Table A2-1: Break-down of the approximate materials cost for the preparation of a small batch (2.5 mg semiconducting polymeric nanoparticles) and a bigger batch (100 mg semiconducting polymeric nanoparticles). Prices are based on quotes from appropriate manufacturers.	183
Table A2-2: Approximate costs to establish a start-up company aiming to commercialise semiconducting polymeric nanoparticles. Prices are based on quotes from online vendors, estimations or based on quotes.	184
Table A2-3: Summary of the commercial potential for the applications evaluated.	187

List of Abbreviations

CHCl ₂	Dichloromethane
CHCl ₃	Chloroform
CuCl ₂	Copper chloride
DMK	Dimethyl ketone (Acetone)
DMSO	Dimethyl sulfoxide
EDC	n-(3-dimethylaminopropyl-n'-ethylcarbodiimide) hydrochloride
EGFR	Epidermal growth factor receptor
ELISA	Enzyme-linked immunosorbent assay
EtOH	Ethanol
FDA	US-Food and Drug Administration
ICG	Indocyanine green
IPA	Isopropanol
MeOH	Methanol
MWCO	Molecular weight cut off
Na ₂ HPO ₄	disodium phosphate
NaOH	Sodium hydroxide
NEP	Noise equivalent pressure
NHS	N-Hydroxysuccinimide
NiCl ₂	Nickel chloride
PA	Photoacoustic
PAH	Poly (allylamine hydrochloride)
PBS	Phosphate buffered saline
PEG	Polyethylene glycol
PLGA	Poly[lactic-co-glycolic acid] co-polymer
PVDF	Polyvinylidene fluoride
PPy	Polypyrrole
PS	Polystyrene
PZT	Lead zirconate titanate
RMS	Root mean square
RPM	Rounds per minute
SDS	Sodium dodecyl sulphate
SNR	signal to noise ratio
THF	Tetrahydrofuran

List of Symbols

a	Radius
c	Concentration
c_p	Heat capacity at constant pressure
c_s	Sound speed
$D(\theta)$	Directivity function as a function
d_c	Diameter of cylindrical region irradiated by light
E_t	Thermalisation efficiency
$H(z)$	Absorbed energy density as a function of depth
J_1	First order Bessel function
k	Acoustic wave number;
K	Measurement constant
K_s	Adiabatic bulk modulus
l	Thickness of the sensing film
l_g	Thickness of the adhesive layer
$M(\lambda)$	External power meter readings
$O(\lambda)$	Photodiode or internal power meter readings
$P_1(k)$	Theoretical frequency response
R_0	Pressure amplitude reflection coefficient, due to an acoustic impedance mismatch between the adhesive layer and the backing material
R_2	Pressure amplitude reflection coefficient, due to an acoustic impedance mismatch between the sensing layer and the surrounding medium
S_0	Signal amplitude at t_0
T	Pressure amplitude transmission coefficient due to an acoustic impedance mismatch between the adhesive layer and the sensing layer
T_r	Temperature
z	Depth
α_{th}	Thermal diffusivity
β	Volume thermal expansion coefficient
ϵ	Extinction coefficient
θ	Angle
λ	Wavelength
λ_{Ex}	Peak absorption wavelength
λ_{Em}	Peak emission wavelength
π_L	Laplace pressure
ρ	Density
σ	Interfacial tension of a droplet

τ_{Th}	Thermal relaxation time
Φ_0	Initial fluence
Φ_f	Quantum yield
Γ	Grüneisen coefficient
μ_a	Absorption coefficient

This page was intentionally left blank

Chapter 1

Introduction

The work carried out in order to meet the objectives of this thesis was completed in the Department of Medical Physics and Biomedical Engineering, Department of Chemistry and Cancer Institute at University College London (UCL) between September 2012 and March 2016. The project was funded by the Engineering and Physical Sciences Research Council (EPSRC) and project supervisors were Prof. Paul Beard (Department of Medical Physics and Biomedical Engineering, UCL), Prof. Helen Hailes (Department of Chemistry, UCL) and Prof. Alethea Tabor (Department of Chemistry, UCL).

This initial chapter is intended to introduce the motivation and the aims of the project, as well as to give an overview of the rest of the thesis.

1.1 Motivation

The motivation for this project was to identify useful materials for the potential application as contrast agents for molecular PA imaging from the broad array of nanoparticles and organic dyes. Choosing which of the compounds is suitable for any particular application depends critically upon the magnitude of the PA signal it generates in response to the excitation laser pulse as this defines image contrast and thus the detectability of the agent. This in turn depends on the optical and thermodynamic properties of the contrast agent as these govern the effectiveness with which incident photons are converted to acoustic pressure. This involves three physical processes: (1) the absorption of incident photons of wavelength λ , a measure of which is provided by the extinction coefficient $\epsilon(\lambda)$. (2) The conversion of absorbed optical energy to heat represented by the thermalisation efficiency E_t and (3) the conversion of heat energy to pressure characterized by the Grüneisen coefficient Γ . All three processes contribute to the signal transduction mechanism yet it is often assumed that a spectrophotometer

measurement of optical absorption alone is sufficient to characterize a PA contrast agent. Although true in some cases, there are significant exceptions where this is insufficient. Most obviously, a measure of optical absorption alone is insufficient for the purposes of characterising substances that fluoresce to any significant extent or are required to be dissolved in sufficiently high concentrations that the Grüneisen parameter is altered. Moreover in the case of nanoparticle based agents, the signal generation efficiency can depend strongly upon the differential thermodynamic properties of the absorber and surrounding medium and provide a significantly larger signal than an organic dye of the same absorption coefficient. Comparing nanoparticles with each other for their ability to generate PA signals is another case that emphasises the importance of fully characterising the PA signal generation process. A good example of this has been provided by Chen et al who compared gold nanorods (a promising class of contrast agent for PA imaging) with different coatings¹. The various samples used in their study were optically identical with the same $\epsilon(\lambda)$ and absorption spectra. However, a strong dependency of the PA signal amplitude on the interfacial properties of the gold nanorods was observed. The analysis of this important class of contrast agents (gold nanorods) shows that the PA signal amplitude can be changed without changing the optical properties of the nanoparticles. This highlights the inadequacy of measuring only the optical properties for the purpose of developing and selecting contrast agents. In these cases measurement of all three parameters involved in the PA signal generation process ($\epsilon(\lambda)$, E_t and Γ) is required in order to fully characterize the contrast agent. In addition to the thermodynamic properties, effects such as photobleaching of chromophores and photo-induced melting of plasmonic nanoparticles can significantly alter the PA signal generation and needs to be accounted for.

Therefore, in order to determine all the parameters involved in the PA signal generation process and identify suitable compounds for molecular PA imaging, a measurement apparatus and the methodology is required. The apparatus in conjunction with the methodology allows characterising organic dyes and nanoparticles and identify compounds suitable for molecular PA imaging based on their PA signal generation.

1.2 Aims of the project

The aim of this project was to identify suitable compounds for their potential application as contrast agents for molecular photoacoustic (PA) imaging. This requires designing and optimising the individual parts required for a PA spectroscopy, such as an ultrasound transducer and sample cuvettes, and assembling the parts. After assembling and optimisation, the limitations of the PA spectroscopy are identified. In order to fulfil the aims of this project, methods needed to be developed enabling the determination of the individual parameters involved in the PA signal generation as well as for the determination of the PA amplitude and μ_a spectra and the photostability of organic dyes and nanoparticles using the PA spectroscopy.

To meet the aim of this thesis the following key points needed to be fulfilled:

- i. Design and assemble a PA spectroscopy and identify its limitations.
- ii. Development of methods for the determination of $\epsilon(\lambda)$, E_t , Γ and the photostability using the PA spectroscopy.
- iii. Synthesis of compounds exhibiting promising properties for the application as contrast agents for molecular PA imaging.
- iv. Characterisation of commercially available and the synthesised nanoparticles and organic dyes using the PA spectroscopy and the methods proposed and identify compounds generating strong PA signals upon excitation.
- v. Analyse the behaviour of the chosen compounds in *in vitro* and *in vivo* experiments.

The primary emphasis of this thesis is on the work carried out to meet objectives (i), (ii) and (iv). Objectives (iii) and (v) are subordinate aims and need to be expanded on in future work.

1.3 Thesis structure

The thesis is divided into five parts.

The first part provides an introduction to the field of molecular PA imaging and sets the project in context. Initially the principle of PA imaging including the signal generation and the ultrasound detection are detailed, followed by the description of chromophores present in the human body used for PA imaging. Subsequently, targeting strategies for molecular PA imaging are explained followed by information about the routes of administration, biocompatibility and toxicity of exogenous contrast agents. The last section of the first chapter gives a detailed description of compounds previously used as contrast agents for molecular PA imaging such as organic dyes and nanoparticles.

A key part of this thesis is Part II addressing the primary objectives (i) and (ii). It contains a detailed description of the PA spectroscopy used throughout this thesis and the analysis of its limitations. A description of the individual parts of the PA spectroscopy, such as the laser system, the ultrasound transducer and the sample cuvette, are also included. This part also comprises the design of an ultrasound transducer and the thorough evaluation of its properties. The last chapter of Part II of this thesis details the methods for the determination of μ_a , E_t , Γ , PA amplitude and μ_a spectra as well as analyse the photostability of a compound using the PA spectroscopy. The individual methods used for the determination of the parameters involved in the PA signal generation were validated using solutions of absorbers with known E_t , Γ and optical properties.

The third part of this thesis addresses objective (iv) and details the characterisation of a number of potential PA contrast agents using the methods described in Part II of this thesis. The characterisation adds to the list of contrast agents for PA contrast agents and helps identifying useful contrast agents for a given application. The chapter starts with a short description of the methods used for the analysis of the physical properties of the nanoparticles, such as transmission electron microscopy (TEM) and dynamic light scattering. After this the procedure for the preparation of various semiconducting polymeric nanoparticles is described, before the results of the characterisation of the sample chromophores are presented. The characterisation included the determination of the PA amplitude and μ_a spectrum as well as ϵ , E_t , Γ and the photostability. The chapter concludes with an overview of the measurement results, which allows appointing useful materials for the applications as PA contrast agent.

After determination of the parameters involved in the PA signal generation of the various organic dyes and nanoparticles, a compound exhibiting strong PA signal generation - a novel π -conjugated semiconducting nanoparticle - was used for preliminary *in vitro* and *in vivo* analysis. These experiments are described in Part IV. Part IV includes the description of the methods used for the analysis of the ability of molecular targeting of the nanoparticles, a brief overview over the PA imaging set-up and a demonstration of the ability of the nanoparticles in preliminary *in vivo* experiments. The *in vivo* experiments show that at 800nm the polymeric nanoparticles have a significantly stronger optical absorbance than the endogenous chromophores, allowing to unambiguously imaging the presence of the nanoparticles relative to the vasculature of a mouse.

After concluding and giving an outlook and suggestions for future work, an appendix is attached. The first part of the appendix contains the procedures used for the preparation of various promising nanoparticles and the conjugation to targeting moieties and fluorescent markers. The procedures for the preparation of the nanoparticles and the conjugation reactions have been adapted from the literature and were refined to meet the requirements to generate a contrast agent for PA imaging. The chapter comprises procedures for the preparation of carbon nanotubes, copper sulphide nanoparticles, dye loaded PS nanoparticles, poly (allylamine) nanoparticles, PEDOT:PSS nanoparticles, polypyrrole nanoparticles and PCPDTBT semiconducting polymer nanoparticles.

The second part of the appendix contains the analysis of the commercial potential of novel semiconducting polymer nanoparticles. This chapter was written as a result of a scholarship awarded by UCL Advances.

Chapter 2

Background

2.1 Photoacoustic imaging

PA imaging is based on the light induced generation of ultrasound within tissue, using modulated light. It combines the advantages of ultrasound imaging, sub-millimetre spatial resolution up to an imaging depth of centimetres, with the high contrast and specificity of optical imaging². PA imaging is a useful tool with a wide variety of applications in clinical and preclinical medicine research like the detection of cancer cells³, sentinel lymph nodes⁴, angiogenesis⁵, the characterization of atherosclerotic plaques⁶, blood flow and blood oxygenation measurements^{7,8} as well as melanoma imaging⁹. Two different modes are currently used to acquire PA images, namely: (i) PA tomography and (ii) PA microscopy. PA tomography utilizes a large diameter excitation beam and an array of ultrasound transducers or a scanning system to generate data for the image reconstruction. PA microscopy on the other hand uses either a focused excitation beam or a focused ultrasound transducer. For PA microscopic imaging a single-element ultrasonic transducer is mechanically scanned across the region of interest for the detection of PA signals. In contrast to PA tomography, the acquired data with PA microscopy does not require image reconstruction. PA endoscopy is a useful application of PA tomography enabling the visualisation of internal organs such as the gastrointestinal tract. PA tomography utilizes optical fibres delivering light pulses for the excitation closer to the region of interest. The miniature probes used for PA endoscopy are composed of a glass-fibre for the excitation and an ultrasound detector. Detecting the generated ultrasound can be accomplished using piezoelectric materials or using Fabry-Perot sensors allowing for excitation and detection through the same glass fibre. Images are reconstructed from PA signals generated by compounds emitting broadband ultrasound signals up on excitation with pulsed light. The PA signal generation process is described in the next section in detail.

2.1.1 PA signal generation process

The signal generation process is based on the PA effect described by Alexander Bell in the late 19th century¹⁰. The PA effect describes the conversion of light to an acoustic pressure. This process requires converting the energy introduced by the light source various times, until the energy is emitted in form of a pressure wave. A schematic of each of the individual conversions of the light energy for PA signal generation is shown in Figure 2-1.

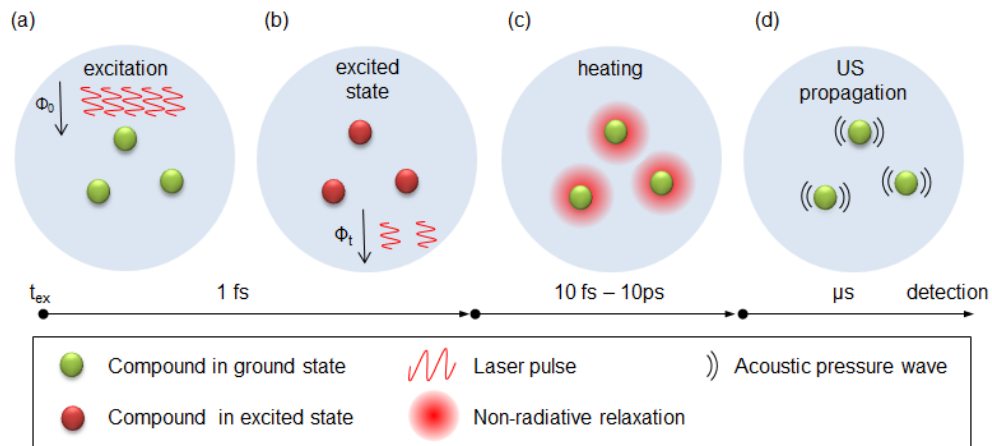


Figure 2-1: Schematic describing the PA effect from excitation to ultrasound emission. The excitation with modulated light (a) induces an excited state of the light absorbing compound (b), which relaxes non-radiatively to its ground state (c). The rapid heating causes the emission of an ultrasound (d). t_{ex} = time of introducing excitation light; Φ_0 = Initial fluence; Φ_t = Fluence after excitation.

The schematic depicted in Figure 2-1 shows the separate steps involved in the PA signal generation in detail. Initially the light absorbing compounds within the solution are in their ground state (depicted as green spheres) when a short pulse of light with the fluence Φ_0 is introduced (a). A measure for the ability of a compound to absorb light at specific wavelength is the extinction coefficient ϵ . Upon absorption of a photon the compound is promoted to an excited electronic state, a process that occurs on the time-scale of femtoseconds (b). The compound subsequently relaxes to its ground state via non-radiative transitions causing a local temperature rise (c). The relaxation process from an electronic excited to the ground state of a compound can occur via different mechanisms such as radiative emission of photon or quenching processes induced by other molecules, yet only the non-radiative relaxation pathway contributes to the PA signal generation. A measure of the efficiency of the relaxation of a substance via non-radiative relaxation is provided by the thermalisation efficiency E_t . The heat energy dissipates on a time-scale of tens of femtoseconds up to tens of picoseconds generating an acoustic pressure wave (d). The Grüneisen coefficient Γ provides a measure of the ability of a material to convert heat energy to an acoustic pressure. For the PA effect to occur thermal and stress confinement conditions need to be fulfilled.

For the efficient heating of a light absorbing medium the thermal confinement condition needs to be satisfied, which means that the excitation light pulse is required to be sufficiently shorter than the thermal relaxation time τ_{th} . This ensures that all the electromagnetic energy is deposited in the medium before it starts to diffuse out via thermal diffusion. The thermal relaxation time of an absorbing medium, such as a contrast agent in a cuvette or chromophores in tissue, describes the thermal diffusion through it and can be estimated using:

$$\tau_{th} = \frac{d_c^2}{\alpha_{th}} \quad \text{Equation 2-1}$$

where d_c is the dimension of a cylindrical region heated by light absorption and α_{th} is the thermal diffusivity of the heated region¹¹. t_{opt} is the laser pulse duration and depends on the excitation source. In the case of $t_{opt} \ll \tau_{th}$ the energy is deposited within the medium before energy starts to diffuse out. If the thermal confinement condition is not satisfied, the acoustic signal generation becomes less efficient¹².

The stress confinement condition is fulfilled when the excitation pulse is sufficiently shorter than the acoustic relaxation time of an absorbing medium t_{exp} - the time needed for an acoustic wave to propagate one optical penetration depth within the absorbing medium. If obeyed ($t_{opt} \ll t_{exp}$) the volume expansion of the absorbing medium during electromagnetic excitation can be neglected, otherwise losses in the acoustic signal generation can be expected.

The generated acoustic pressure wave propagates through the surrounding medium and is detected by an ultrasound detector. Frequently used materials for the detection of ultrasound are discussed in the next section of this introduction.

2.1.2 Signal detection

One of the key elements for PA imaging and PA spectroscopy is the ultrasound transducer, used to convert broadband (tens of megahertz), low-amplitude (kPa) acoustic waves, to a detectable electric signal. Piezoelectric materials such as polyvinylidene fluoride (PVDF) or lead zirconate titanate (PZT) are frequently used for the detection of ultrasounds and are described in the next section. Subsequently, Fabry-Perot sensors are briefly described, which have also been used successfully as ultrasound sensors for PA imaging.

2.1.2.1 Piezoelectric transducers

The piezoelectric effect was first described in 1880 and is defined as the generation of an electrical charge in response to a mechanical stress, or vice versa. Piezoelectric materials can be found in many fields of application such as medical ultrasound imaging, audio-technology, clocks, transmitters and SONAR. The effect occurs in ferroelectric solids, formed from elementary cells without centre of symmetry such as quartz, barium-titanate ($BaTiO_3$), PZT and

PVDF. The asymmetry induces a dipole, which gives rise to the piezoelectric effect. In single crystals these dipoles align naturally, whilst polycrystalline materials require polarization.

Figure 2-2 shows the crystal structure of PZT and its polarization.

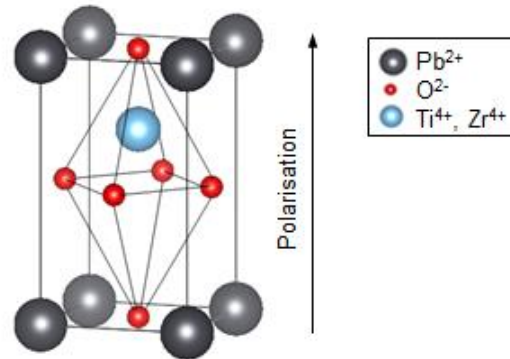


Figure 2-2: Scheme of the crystal structure of PZT, showing the displacement of the Titanium or Zirconium ions in centre of the unit, introducing polarity.

Subjecting such piezoelectric material to a mechanical force, changes the relative distance between the charges and an electrical field across the dipoles can be measured in form of a voltage. The opposite effect can also be observed; an external electrical field will attract or oppose the two electrical charges of the dipole, causing the mechanical deformation of the crystal.

Due to the ability of piezoelectric materials to convert mechanical pressures into electrical signals, these materials are frequently used for the detection of ultrasound. Ceramic materials, such as PZT, BaTiO₃ and lithium niobate (LiNbO₃), exhibit strong piezoelectric effects, however polymeric materials such as PVDF are sometimes preferred for the application as ultrasound transducers due to their broadband frequency response and matching acoustic impedance with biological tissue. PVDF is made from 1,1-Difluoroethylene and receives its piezoelectric properties formed from the alternating hydrogen and fluorine ligands along the carbon backbone of the polymer (see Figure 2-3b)

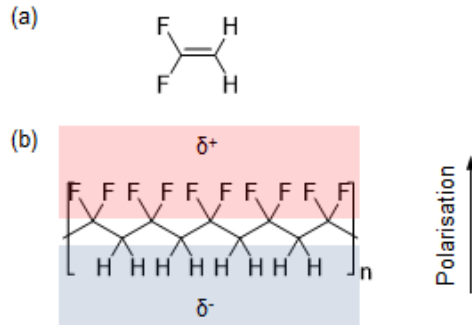


Figure 2-3: Chemical structure of 1,1-Difluoroethylene (a) and PVDF (b). The high electronegativity of the fluoride ligand gives rise to the piezoelectric effect due to the formation of charge separation, as depicted by the two coloured blocks indicating the opposing charges.

2.1.2.2 Fabry-Perot ultrasound sensors

Fabry-Perot interferometers are optical interferometers composed of two parallel reflecting surfaces separated by a spacer material (see

Figure 2-4).

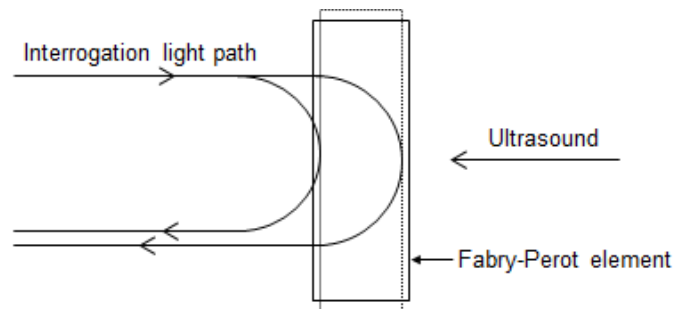


Figure 2-4: Working principle of the Fabry-Perot element.

For ultrasound transduction the spacer material can be made from a polymer film, such as polyethylene terephthalate (PET) or Parylene (poly(p-xylylene)) and the reflecting surfaces from metallic or dielectric materials, with a reflectivity $> 90\%$. To ensure an even surface without defects the materials are applied to a substrate via methods such as spin coating or vapour deposition techniques. Depending on the bandwidth requirements the spacing between the two reflectors is typically in the range of tens of micrometres. The transduction mechanism is based on the linear conversion of external acoustic pressure to a change in the optical thickness of the spacer material, resulting in an optical phase shift. Detecting the optical phase shift using the interferometer enables conversion to the intensity modulation allowing for the reconstruction of the ultrasound signal. For the detection of the optical thickness of the interferometer a continuous wave laser is used for the interrogation and a photodiode for the detection of the

reflected light. The element size of the transducer is approximately the spot size of the laser beam used for interrogation and is typically in the range of tens of micrometres.

In a PA tomography setting, the focused interrogation laser beam is scanned across the surface of a Fabry-Perot element, to acquire a three-dimensional image. Depositing of the Fabry-Perot element on the tip of a glass fibre allows using this type of ultrasound transducers to be miniaturised for application as endoscopic probes. Small element sizes and the high sensitivity of the sensors render Fabry-Perot sensors a very useful solution for PA imaging applications, providing high resolution and a close to omni-directional response to acoustic pressures.

2.1.3 Endogenous contrast

As mentioned above, for PA signal generation optical absorbers are required enabling the efficient conversion of the excitation light to a measurable acoustic pressure. The most abundant chromophores in mammals, including humans, are haemoglobin, melanin and water. In mammals 95% of the content of red blood cells consists of the protein haemoglobin, which plays a major part in the oxygen transport in the body. It carries oxygen from the respiratory organs to the rest of the body, where it is released. Haemoglobin is also capable of binding to other ligands than oxygen (e.g. carbon dioxide (CO_2)) and transports them towards the respiratory organs. The protein consists of a non-protein group (cofactor), called heme (see Figure 2-5a for chemical structure) and is made from a porphyrin ring with side chains and an iron atom in the centre.

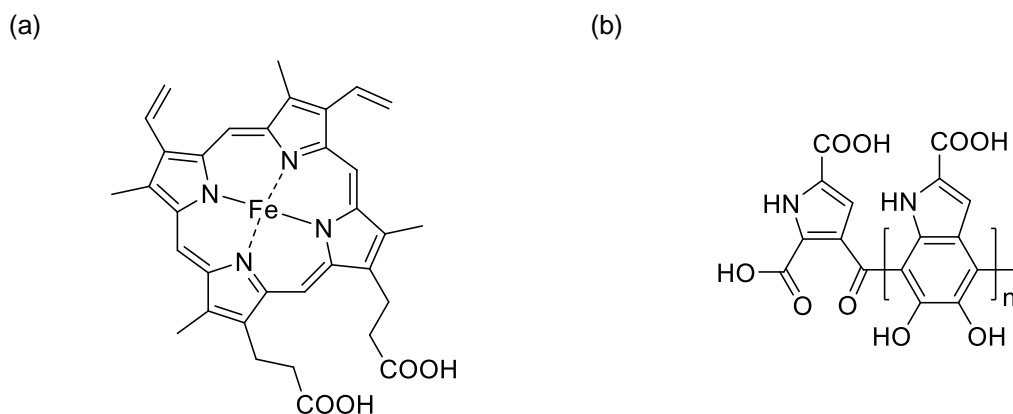


Figure 2-5: Chemical structure of heme B (a), part of haemoglobin, and melanin (b).

The iron occurs in different oxidative states (Fe^{II} and Fe^{III}), depending on the ligand bound to it. Oxygenated haemoglobin appears bright red (oxy-haemoglobin: $\epsilon(415 \text{ nm}) = 5.2 \cdot 10^5 \text{ cm}^{-1}\text{M}^{-1}$), whilst deoxygenated haemoglobin appears in a darker red tone (deoxy-haemoglobin: $\epsilon(434 \text{ nm}) = 5.5 \cdot 10^5 \text{ cm}^{-1}\text{M}^{-1}$), which is due to a photoinduced charge transfer from an iron excited state to the porphyrin π -electron structure. The energy required, for the charge transfer to occur, is dependent on the oxidative state of the iron atom, red-shifting with ligands like CO_2 ¹³. The major absorption peaks appear in the ultraviolet and the visible region of the spectrum, whilst the

absorption occurring in the infrared is relatively low. Compared to other chromophores naturally occurring in tissue, haemoglobin exhibits relatively high absorption in the visible, which allows generating strong PA signals and consequently has been utilized for various PA imaging applications, including structural and functional imaging of a rat's brain¹⁴, angiogenesis¹⁵ research and blood oxygen saturation measurements¹⁶.

Melanin on the other hand, is a pigment that can be found in most lining organisms as well as the epidermis, the top 50-100 μm of human skin, in cells called melanosomes. Melanins are polyacetylene-derivates, in humans most commonly occurring in the form of eumelanin and pheomelanin, which are polymerized and arrange in a periodic structure (see Figure 2-5b for chemical structure of eumelanin). The absorption of melanin peaks in the ultraviolet and decreases gradually with longer wavelength (eumelanin: $\epsilon(400 \text{ nm}) = 4 \cdot 10^3 \text{ cm}^{-1}\text{M}^{-1}$), dropping off in the near-infrared. The overall attenuation of the natural pigment can be considerable and therefore has found applications in the field of biomedical imaging. Images of subcutaneous melanomas in nude mice have been obtained using PA imaging at two wavelengths: for the imaging of the surrounding tissue (764 nm) and the melanoma (584 nm)¹⁷. Zhang et al also demonstrated the ability of PA imaging to image melanomas¹⁵. In this study the researchers exploited the optical properties of haemoglobin and melanin for *in vivo* acquisitions of images showing angiogenesis and the relative oxygen saturation in rodents and determined the concentration of haemoglobin in human blood vessels.

Human tissue consists to 70-90 % of water, making water an important chromophore when considering biomedical imaging contrast. Optically water can be characterized by its strong absorption in the ultraviolet and near-infrared ($\mu_a(950 \text{ nm}) = 0.5 \text{ cm}^{-1}$; $\mu_a(1450 \text{ nm}) = 31.5 \text{ cm}^{-1}$). Due to the abundance and the strong absorption of water, it needs to be considered when performing PA measurements.

Even though, endogenous chromophores have been successfully utilised for *in vivo* PA imaging of blood vessels¹⁸, melanomas¹⁹ and the brain perfusion²⁰, contrast agents have the potential to elevate PA imaging to a molecular imaging modality which could be an important tool helping understanding biological processes on a molecular level. By tuning the absorption of contrast agents to the region where the endogenous chromophores exhibit minimal absorption in the near-infrared (called "optical window of tissue") imaging depth and contrast of PA images can be increased.

2.1.3.1 Optical window of tissue

As shown in Figure 2-6, common intrinsic chromophores within biological tissue exhibit strong optical absorption in the visible (up to 600 nm) and near-infrared region (from 900 nm) of the electromagnetic spectrum, limiting the light penetration depth at a fixed fluence. However, the absorption of these endogenous chromophores displays a minimum the near-infrared (600-900 nm), allowing the excitation light to penetrate up to several centimetres deep into the tissue.

This region in the near-infrared is called the optical window of biological tissue. Exogenous contrast agents, such as organic dyes and nanoparticles, are often designed to strongly absorb light within this optical window, increasing the contrast and allowing to detect the contrast agents at depth up to several centimetres.

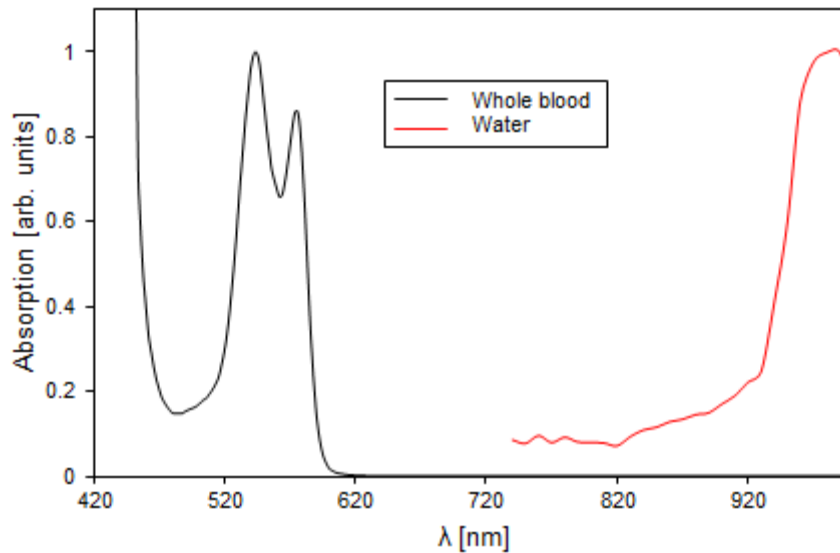


Figure 2-6: Absorption spectra of the strongest endogenous absorbers haemoglobin (contained within whole blood) and water. The values were taken from reference ²¹.

The next section of this chapter gives an introduction to the newly emerging field of molecular PA imaging using exogenous contrast agents and describes targeting strategies, routes of administration and briefly discusses toxicity concerns using such compounds.

2.2 Molecular photoacoustic imaging

The PA signal generation is based on the conversion of light to an acoustic signal mediated by a light absorbing compound. However, diseases such as cancer cells pose little, if any, different absorption characteristics compared to their healthy counterparts and thus generates PA signal indistinguishable from each other because they are of the same chemical and biological makeup. This limitation can be overcome via the introduction of exogenous contrast agents targeting for a specific disease and thus making it possible to distinguish diseased from healthy cells. This approach has the potential to promote PA imaging to a molecular imaging modality, enabling visualization of biological processes on a molecular level. The following sections are aimed to introduce to the field of molecular PA imaging. The first part describes strategies used to target exogenous contrast agents for a specific disease in order to distinguish healthy from diseased cells via PA imaging.

2.2.1 Targeting strategies

The idea of targeting a disease with a drug, and thus curing the diseased cells whilst sparing the healthy ones, dates back to the end of the 18th century. Today this approach is utilized not only for drug treatments, but also for targeted imaging and the combination of both. After administration to the organism, ideal targeted contrast agents (or drugs) are retained and accumulate at the site of interest in the organism at concentrations high enough for the desired effect - strong signal generation (or eradication of the disease). The remainder of the administered dose of the contrast agent (or drug), not bound to the target, is rapidly cleared from the blood stream and eventually the organism without posing any toxic effect. For PA imaging, targeted contrast agents are of high importance due to a lack of contrast displayed by many diseases, especially in their early stage of development, e.g. cancer. Detecting cancer at an early stage is highly desirable in order to reduce mortality of cancer patients. In cancer imaging, two approaches have been used to navigate contrast agents to the target, a passive and an active targeting approach, which are discussed below.

2.2.1.1 Passive targeting

In cancer imaging and treatment, passive targeting utilizes the physical properties of tumours - the enhanced permeation and retention (EPR) effect. This effect is due to the enhanced permeability of blood vessels recruited for nutrient supply of the tumour and an insufficient drainage of the lymphatic system surrounding it. Blood vessels recruited tend to be porous, allowing small particles to leak out. Leaky blood vessels in combination with an ineffective lymphatic system can cause a contrast agent or a drug to accumulate in the extracellular space surrounding the tumour and hence allow for site specific imaging and treatment. The EPR effect is mostly if not exclusively observed in tumour xenograft models in animals and has not been proven significant in human patients. The reason for this might be the great growth rate of the xenograft compared to the growth rate of an endogenously tumour. The efficiency of the accumulation depends on the blood circulation properties of the contrast agent or the drug used as well as the physiology of the tumour and its development stage. Blood circulation and passive targeting via EPR of a compound introduced to the blood-pool can be influenced by optimising size, shape and surface characteristics of the compound.

Several PA imaging studies utilizing the EPR effect were able to show increased contrast at the site of interest, using various contrast agents. De la Zerda *et al* were able to demonstrate PA imaging of single walled carbon nanotubes retained in a tumour by passive targeting using the EPR effect²². In the same study the researchers were able to directly compare passive and active targeting. They were able to show, that both the passively targeted and the actively targeted carbon nanotubes accumulated at the tumour. However, the actively targeted carbon nanotubes were retained at higher concentrations evident by an about two times greater PA

signal generated by the actively targeted contrast agent. The approach using actively targeted compounds is described in the next section.

2.2.1.2 Active targeting

For the active targeting approach, molecules with the ability to selectively bind to a specific target are used to retain a compound such as drugs or imaging agents at the site of interest. Actively targeted compounds enable the controlled release of compounds and improve specificity resulting in decreased systemic toxicity. Therefore, targeting moieties are conjugated to the compound before administration to the organism. After administration, the conjugates perfuse throughout the organism being retained at the site of interest, whilst the remaining conjugates are released from the organism. For an actively targeted compound to be retained in the tumour tissue, the compound is required to passively accumulate at the site. Targeting moieties for this purpose are often composed of antibodies or short peptides binding to the target with high affinity. These targeting moieties can substantially increase the size and the bioactivity of the compound which might lead to decreased passive accumulation in the tumour tissue and immune reactions. Examples of targeting moieties that have been employed for this purpose are tumour necrosis factor- α ²³, LYVE-1²⁴ and ICAM-1 antibody²⁵ and cell penetrating peptides²⁶. This targeting approach relies on tissue specific properties, like an overexpression of specific receptors on the cell surfaces of malignant tissues. Receptor tyrosine-protein kinase erbB-2 (HER2) is such a receptor. It is a member of the epidermal growth factor receptors (EGFR) and plays a role in the development of many types of breast cancers. HER2 is overexpressed by the cells of malignant tissue and has frequently been applied as target for molecular PA imaging.

Various studies demonstrated the ability to actively target for HER2 biomarker using antibody conjugated nanoparticles and organic dyes, such as gold nanorods^{27,28}, silica encapsulated gold nanorods²⁹, gold coated iron nanoparticles³⁰, silver nanoplates³¹ and Alexa750³², as a contrast agent. Trastuzumab is an example of a monoclonal antibody known to target for HER2. The antibody is conjugated to the contrast agents via the fragment crystallisable region of the molecule. Another target that has been used previously for PA molecular imaging is $\alpha_v\beta_3$ integrin, a transmembrane receptor overexpressed in the tumour vasculature, associated with tumour angiogenesis. Various studies have shown the feasibility of targeting for $\alpha_v\beta_3$ integrin receptor using cyclic peptides. Gold nanospheres⁵, carbon nanotubes^{33,34} and IRDye800³⁵ are examples of contrast agents that have been conjugated to peptides in order to target for the transmembrane receptor. For instance IRDye800-NHS was conjugated via the ester function of the contrast agent to a cyclic peptide (cyclo(Lys-Arg-Gly-Asp-Phe)) to target for the $\alpha_v\beta_3$ integrin receptor overexpressed in mice bearing brain U87 glioblastoma tumours. 24 h after administration of the targeted PA contrast agent to the tail vein strong PA signals, originating from the contrast agent within tumour margins, were recorded, demonstrating the feasibility of molecular PA imaging. Organic dyes such as IR-808³⁶, IR-780³⁷ and rhodamine 123³⁸ on the other hand don't require conjugation to a targeting moiety due to their inherent ability to target for mitochondria of various cancerous cell lines. This behaviour is due to the electrical

properties of these lipophilic cationic dyes, which preferentially accumulate in the mitochondria of various tumour cells lines, enabling molecular targeting without the need of conjugation to a targeting moiety.

2.2.2 Routes of administration

Intravenous administration is the method of choice for the administration of contrast agents for molecular PA imaging. Agents injected intravenously are required to avoid degradation within the blood-pool and evade the immune system response in order to reach the targeted site. For successful delivery, the physical and chemical properties of the contrast agent need to be accurately controlled. The most important parameters to control are size, shape and the electrical surface-charge of the compound. Once injected to the blood-stream, small molecular (>10 nm) probes rapidly perfuse into various organs but exhibit only a short blood elimination half-life and are within hours to days excreted from the body via renal and/or hepatic routes. Although tumour accumulation using small molecules is generally low, molecular targeted probes can improve this limitation. Nanoparticles on the other hand are taken up by and retained for a long time - month to years - in the reticuloendothelial system (RES) organs, such as liver, spleen etc. or are slowly - weeks to month - excreted into bile and faeces through hepatic routes. To avoid clearance by first pass renal filtration particle diameter needs to be bigger than 10 nm³⁹ and to be able to diffuse into the tumour interstitium and be retained for a significant amount of time the diameter needs to be smaller than 200 nm³⁹. Once the contrast agent has reached the diseased site via the EPR effect it often is required to pass the extracellular matrix to reach the surface of the cells targeted for.

2.2.3 Biocompatibility and toxicity of contrast agents

A compound foreign to an organism bears potential cytotoxic, tissue specific and systemic toxic effects. Their toxicity depends on various parameters, including size³⁹, shape⁴⁰, composition, biodegradability, clearance rate, delivery method and site delivered to. In addition a bioactive compound administered to the organism might provoke an immune system response and be eliminated from the organism before reaching the target. To avoid this, contrast agents are often coated or otherwise encapsulated using biocompatible molecules. These coatings are used to alter the solubility, encapsulate toxic materials, work as a stealth coating and enable conjugation to targeting moieties or drugs. Polyethylene glycol (PEG) is one of the most widely used materials for biocompatibility coatings and is essential part of some US-Food and Drug Administration (FDA) approved diagnostic and therapeutic nanoagents (see Figure 2-7 for the chemical structure).

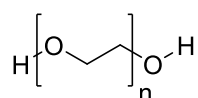


Figure 2-7: Chemical structure of PEG. n is the number of repeat units.

It's a biological inert polyether, which enables longer blood circulation of contrast agents coated with the polymer. PEG has been used to coat various contrast agents and enables binding to a broad range of targeting materials. An example of a modified PEG for the encapsulation and bioconjugation is DSPE PEG 2000 COOH (1,2-distearoyl-sn-glycero-3-phosphoethanolamine-N-[carboxy(polyethylene glycol)-2000]) – the chemical structure is shown in Figure 2-8. It consists of a polar head-group and a non-polar tail. The carboxylic head group allows stabilise water-insoluble materials and functions as reactive group for conjugation to other materials.

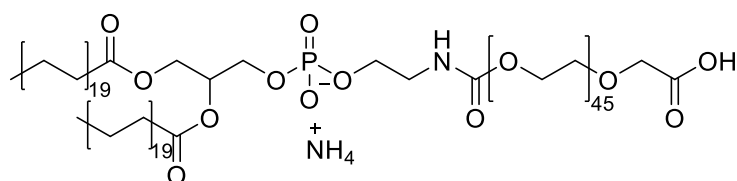


Figure 2-8: Chemical structure of DSPE PEG 2000 COOH

Other strategies rendering compounds used as contrast agents biocompatible are the encapsulation in liposomal and dendrimer coatings, or using different polymers (e.g. polyoxazolines, poly (amino acids) and polyglycerols) and biomimicking stealth coatings (e.g. red blood cell membranes). However, due to their potential toxicity, newly developed contrast agents require risk assessment in order to study potential toxic effects caused by them. Some organic dyes, like indocyanine green, have been approved by the FDA to be safe for the use in humans, posing no acute toxicity. Nanoparticles like gold nanoparticles and carbon nanotubes have previously been utilized in *in vivo* studies displaying little acute toxicity at the concentrations used. However long term accumulation of these compounds may introduce unforeseen toxic effects. The next section gives examples of compounds that have been used as contrast agents for PA imaging, describing their synthesis, properties and gives examples of *in vivo* studies using these compounds.

2.3 Exogenous contrast agents

For a material to be utilized as a PA contrast agent for *in vivo* applications, several physical, optical and safety requirements need to be fulfilled. However, for a strong PA signal generation optical properties, like ϵ , and thermodynamic properties, like the conversion efficiency from light to heat and subsequently to an acoustic pressure, are of great importance.

In the past, a broad array of materials has been proposed as contrast agent for PA imaging. Examples are nanoparticles such as gold nanorods, carbon nanotubes and polymeric nanoparticles, organic dyes and quantum dots. The following gives an overview of various

organic dyes and nanoparticles that previously have been proposed as contrast agent for molecular PA imaging. The section on nanoparticles is further divided into gold nanoparticles, carbon nanotubes, polymeric- and other nanoparticles, which are compounds that have been used frequently for the application as contrast agent in molecular PA imaging. A table giving an overview of the properties of the various types of exogenous contrast agents for molecular PA imaging including advantages and disadvantages is provided at the end of this chapter.

2.3.1 Organic dyes

Plant-based dyes, like indigo and saffron, have been used for thousands of years for different purposes such as the dyeing of textiles. The raw material needed for production of the valuable dyes was commercially harvested from the flowers like the saffron crocus (*crocus sativus*) and the true indigo (*indigofera tinctoria*). Due to the long history of the usage of dyes by humans, numerous natural and synthetic dyes with a wide range of optical properties have been developed. They are used in various fields of applications such as textile dyes, paints and inks, cosmetic products⁴¹, laser dyes⁴², biological staining⁴³ as well as contrast agent in the field of biomedical and medical imaging. Methylene blue is a well-known example of a dye used as a staining agent in biomedical research and with clinical applications. This cyanine dye, in its hydrated form, is certified by the Biological Stain Commission⁴³, and is used to stain the nuclei of cells *in vitro* and *in vivo*. The chemical structure of the methylene blue is depicted in Figure 2-9.



Figure 2-9: Chemical structure of methylene blue.

Conjugated π -systems are responsible for the colour of organic dyes due to their ability to absorb light via electronic transitions. Chemically, conjugated π -systems are alternating single and double bonds found for example in aromatic rings like benzene and linear molecules like 1,3-pentadiene. Within such a system, the p-orbitals of each of the atoms involved interact with each other, resulting in the delocalization of the electrons in those orbitals, forming π -bonds between them. In conjugated π -systems the electrons move freely between any of the atoms involved, resulting in a thermodynamically low energy system. These systems allow for electronic transitions of different kinds, commonly from one conjugated π -systems to another, but other transitions are possible. Thus, if a photon of a wavelength matching the band gap of the molecule is incident on such a system it is likely to be absorbed, promoting an electron to a higher energy level, also known as excited state of a molecule. The bigger the conjugated π -system present, the smaller the band gap and the longer the wavelength of the light that can be absorbed by it. This explains the spectral position of the absorption band of organic dyes, for

Table 2-1: Examples of commercially available dyes, their manufacturers and optical properties. The values for λ_{Ex} , λ_{Em} , ϵ and Φ_f are taken from Manufacturer data. λ_{Ex} = Peak absorption wavelength; λ_{Em} = Peak emission wavelength, Φ_f = quantum yield.

Dye	Manufacturer	λ_{Ex} [nm]	λ_{Em} [nm]	ϵ [cm ⁻¹ M ⁻¹]	Φ_f
Alexa Fluor 700	Molecular Probes	702	775	2·10 ⁵	25
Alexa Fluor 750	Molecular Probes	749	775	2.9·10 ⁵	12
DyLight 800	Thermo Fischer Scientific	777	794	2.7·10 ⁵	3
IRDye 800RS	LI-COR	778	794	2.5·10 ⁵	5-10
ATTO 700	Atto-Tec	700	719	1.2·10 ⁵	25
ATTO 740	Atto-Tec	740	764	1.2·10 ⁵	10

However, there are innumerable synthetic procedures for the preparation of various types and colours of dyes. Some of the reactions performed to synthesize specific dyes are rather complex, whilst others are straight forward. An example of a synthesis route of commonly used indicator dyes, such as methyl yellow, methyl orange and methyl red has been used for decades and is briefly described below. The synthesis of methyl yellow is a two-step synthesis consisting of (a) the formation of a diazonium ion and (b) the coupling of two diazonium ion with each other in a reaction called azo coupling (see Figure 2-11).

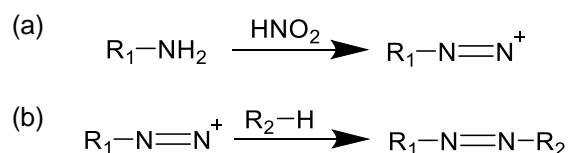


Figure 2-11: General synthesis of an azo dye. The synthesis consists of two steps: the formation of a reactive diazonium ion (a) and the azo coupling (b).

2.3.1.2 Properties

Heptamethine dyes like indocyanine green and aromatic compounds like methylene blue have frequently been utilized as contrast agents for molecular PA imaging. Other dyes used for this purpose are cyanine dyes like Cy5 (Figure 2-12), derivatives of cyanine dyes and aromatic compounds like AlexaFluor dyes (Thermo Fisher Scientific Inc., IL, USA), DyLight (Thermo Fisher Scientific Inc., IL, USA) and Black Hole Quencher dyes (Biosearch Technologies, CA, USA) or derivatives of porphyrin, a component of haemoglobin⁴⁴. Due to their extended conjugated π -electron system these organic dyes exhibit relatively strong absorption (typically in

the range of $\epsilon = 10^5 \text{ cm}^{-1}\text{M}^{-1}$) in the visible to near-infrared of the electromagnetic spectrum and a discrete band with a full width half maximum in the range of 20-100 nm.

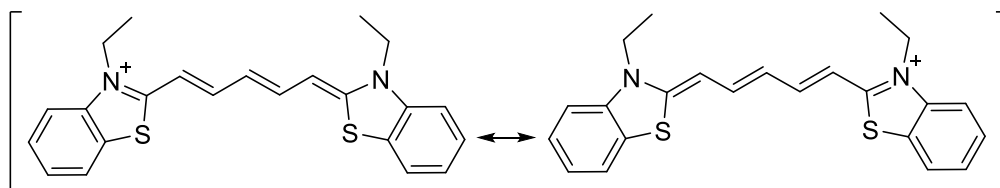


Figure 2-12: Resonance structure of an example of a cyanine dye (Cy5).

Organic dyes are very small (~0.5 nm) compared to other contrast agents proposed for PA imaging, such as nanoparticles (10-150 nm) or quantum dots (5-60 nm), and therefore are able to perfuse through the tissue more rapidly^{45,46}. Additionally, their relatively low toxicity (indocyanine green and methylene blue are approved by the US Food and drug administration for clinical use⁴⁷) makes them promising candidates for the application as PA contrast agents. However, organic dyes are prone to photobleaching, the photon induced destruction of chemical bonds, which alters their absorption characteristic irreversibly. This phenomena is undesired in PA imaging and occurs due to the greater reactivity of an enhanced molecule in a singlet or a triplet state after intersystem crossing⁴⁸. Other factors reducing the PA signal generation ability of organic dyes are fluorescence and ground state depopulation. The PA signal generation efficiency of fluorescent organic dyes is reduced by its radiative component, the quantum yield, because the emitted light does not contribute to the generation of heat - the E_t is reduced. However, many organic dyes, especially those with absorption in the near-infrared, tend to have quantum yields below 10% and therefore a significant proportion of the absorbed light contributes to the PA signal generation. Ground state depopulation on the other hand reduces the acoustic signal amplitude due to a lack of excitable molecules in the ground state. This effect can occur when the life-time of the excited state exceeds the pulse repetition time of the excitation source⁴⁹.

Another property of organic dyes is their tendency for self-association, which is due to strong intermolecular forces between the molecules. This can lead to the formation of aggregates with altered optical properties, compared to the monomeric species. These aggregates are classified by two different formations called J- or H-aggregates and can be identified by a spectral shift of the position of the absorption and emission bands of an aggregated molecule compared to its monomeric species⁵⁰. J-aggregates are characterised through a shift to longer wavelength, whilst H-aggregates exhibit an optical blue shift (see energy diagram in Figure 2-13).

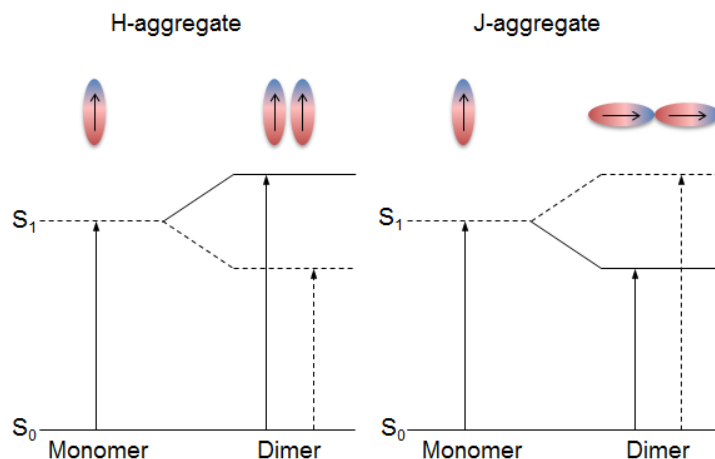


Figure 2-13: Band structure of H- and J-aggregates. The energy level of S_1 increases in H-aggregates compared to the monomeric species and results in a shift of the absorption and emission band to shorter wavelength. J-aggregates result in a shift of the absorption and emission band to longer wavelength.

Red or blue shifts of chromophores can also be observed with varying solvents. This phenomenon however is due to the changing polarity of the solvents. The extent of the shift depends on the electronic structure of the dye molecule and the polarity of the solvent and is typically in the range of tens of nanometres. An unforeseeable change, due to photobleaching, ground state depopulation or J- and H-aggregates, of the optical properties of an optical contrast agent for biomedical imaging can influence the resulting images significantly and therefore need to be considered. Some of the properties of two commercial available organic dyes, called Atto740 and HiLyte 750, are shown in Table 2-2. The dyes demonstrate a moderately strong absorption in the near-infrared with thermalisation efficiencies of 90% and 88%, respectively. However, the organic dyes are prone to photobleaching and possibly change their absorption spectra upon aggregation. Although their optical properties are inferior compared to other compounds, organic dyes have frequently been utilised as contrast agent for molecular PA imaging. A number of studies using organic dyes for this purpose have been summarised below.

Table 2-2: Properties of two commercial available organic dyes with absorption in the near-infrared - Atto 740 and HiLyte 750. The values for λ_{\max} , ϵ_{\max} , the E_t and the photobleaching have been taken from the supplier's website.

Property	Atto 740	HiLyte 750
λ_{\max}	740 nm	750 nm
ϵ_{\max}	$1.2 \cdot 10^5 \text{ M}^{-1} \text{ cm}^{-1}$	$2.7 \cdot 10^5 \text{ M}^{-1} \text{ cm}^{-1}$
E_t	90%	88%
Photobleaching	$7 \% \text{ h}^{-1}$	$18 \% \text{ h}^{-1}$
Aggregation	Possible	Possible
Linker molecule for targeting	Yes	Yes

2.3.1.3 Application in biomedical imaging

In 2004, Wang and co-workers used indocyanine green and indocyanine green stabilized by PEG to generate PA images of the vascular of a rat's brain⁵¹. They demonstrated for the first time the ability of indocyanine green to generate PA signals *in vivo*. In another study, the same group demonstrated the ability of a targeting peptide/indocyanine green conjugate to target for the vasculature of a tumour expressing $\alpha_v\beta_3$ *in vivo* and were able to visualise angiogenesis⁵². Much greater contrast using indocyanine green was achieved by Zerda et al, conjugating indocyanine green molecules to single walled carbon nanotubes, targeted to the tumour vascular in xenograft mice. Due to the high concentration of the dye at the surface of the nanoparticle, the carbon nanotube/indocyanine green probes exhibit, compared to plain single carbon nanotubes, an absorption coefficient 20 times greater at the peak absorption of indocyanine green at 780 nm, proving sub-nM sensitivity⁵³. Li et al demonstrated the feasibility of IRDye800 conjugated to a targeting peptide to act as contrast agent for molecular PA imaging in an *in vivo* study on nude mice inoculated with U87 glioblastoma xenografts⁵⁴. IRDye800 is a derivative of indocyanine green with $\epsilon = 1.6 \cdot 10^5 \text{ cm}^{-1} \text{ M}^{-1}$ at 785 nm. For the *in vivo* experiments Li et al conjugated the organic dye to a cyclic peptide (cyclo(Lys-Arg-Gly-Asp-Phe)) targeting for $\alpha_v\beta_3$ integrin. In their study, Li *et al* were able to demonstrate the targeting ability of the contrast agent, imaging the IRDye800 attached to the newly formed blood vessels surrounding the tumour. In another study by Song and co-workers, the ability of methylene blue to increase the PA signal contrast of the sentinel lymph nodes in an animal model has been shown⁵⁵. They calculated to be able to detect methylene blue at concentrations of 0.28 mM at depth of 20 mm. In a different study, Ke *et al* demonstrated the ability of methylene blue to generate PA signals at an imaging depth of up to 8 cm⁵⁶. Therefore they used a tube phantom filled with a solution of methylene blue (30 mM) and imaged through chicken breast using a PA imaging setup. Black hole quencher dyes and AlexaFluor dyes are further examples of organic absorbers that have been used for *in vivo* PA imaging studies. Levi *et al* demonstrated the

ability of an activatable PA probe for the detection of matrix metalloproteinase (MMP-2 and MMP-9), a biomarker for malignant thyroid lesions⁵⁷. Therefore, two different dye molecules (BHQ3 and Alexa750) were linked to each other via a linker-peptide. The linker-peptide is cleaved in the presence of MMP-2 and MMP-9, separating the two dyes. They were able to demonstrate, that after cleaving by MMP-2 and MMP-9 the Alexa750 accumulates in the cells in proximity to the lesion, whilst BHQ3 is cleared from the organism. Before cleavage the PA signals generated by the probe were due to the two dyes and spectrally differ from the cleaved probe accumulated in the targeted cells. In their study Levi *et al* were able to show enhanced PA signals generated by the activatable probes in comparison to non-activatable probe composed of the same dyes but using a different peptide linker.

2.3.2 Nanoparticles

Particles with a size between 1 to 150nm are called nanoparticles (see Figure 2-14 for a comparison of various small particles and nanoparticles), which often display different properties compared to the bulk material.

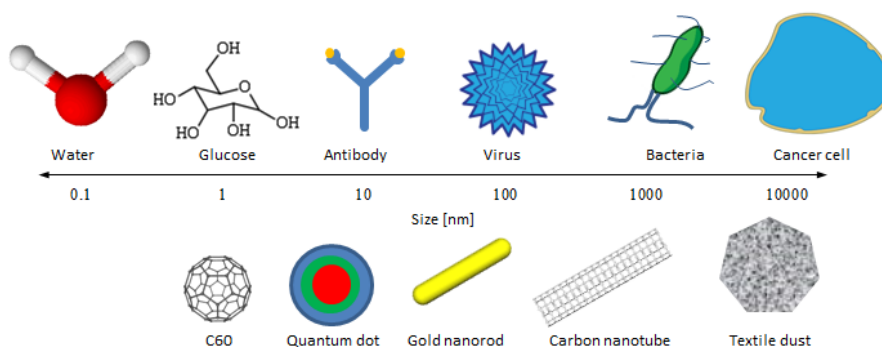


Figure 2-14: Sizes of different Biological nano sized materials, man-made nanoparticles and other materials.

They can be found in nature in form of volcanic ash, ocean sprays, clouds and clay⁵⁸. However, man-made nanoparticles have been used since the 5th century B.C. as additive to the amorphous matrix of glass-ware. A well-known example is the Lycurgus Cup, which was manufactured in the 5th to 4th century B.C. Its colour effect can be attributed to gold and silver nanoparticles of about 40 nm in diameter incorporated in the glass matrix. However, the source of the colour effect of the additive in the glass matrix was not understood and the production of a pure sample of nanoparticles not yet achieved.

The first pure nanoparticle sample was synthesized by Michael Faraday in the mid-19th century using chloroaurate (AuCl_4^-) and phosphorus in carbon disulfide⁵⁹. About half a century later, Wilhelm Ostwald suggested that the novel properties of particles arise from their surface atoms, which make up a great proportion of the particle⁶⁰. Since then, the properties of nanoparticles

have been intensely studied and are now well understood. Today, a variety of synthesizing methods enables the production of nanoparticles of different sizes and morphology, with narrow particles size distributions and various surface coatings.

2.3.2.1 Synthesis

Nanoparticles can be synthesised using two different approaches: the top-down and the bottom-up approach (see Figure 2-15).

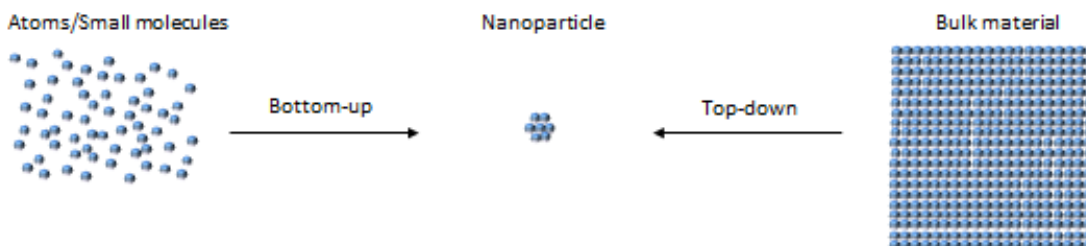


Figure 2-15: Schematic showing the bottom-up and the top-down approach for the synthesis of nanoparticles.

The top-down approach uses bulk-sized precursors which are reduced in size to gain nano-sized materials. Lithography, such as photolithography and electron-beam lithography, etching and mechanical milling are such top-down approaches commonly applied to produce nano-sized materials. However, these methods are expensive and can take a long time. The bottom-up approach utilizes atoms or molecules as building blocks to form the desired nanostructure. The formation of nanoparticles in a bottom-up approach usually involves chemical reactions or a self-assembly mechanism. An example of the bottom-up assembly is the synthesis of gold nanoparticles, such as gold nanorods. The nanoparticle formation can be mediated using a chloroauric acid (HAuCl_4)-cetrimonium bromide (CTAB) complex which is reduced by ascorbic acid to AuCl_2^- -CTAB (see Figure 2-16a). In a second step AuCl_2^- -CTAB is further reduced to elementary gold forming the nano-construct (Figure 2-16b)⁶¹.

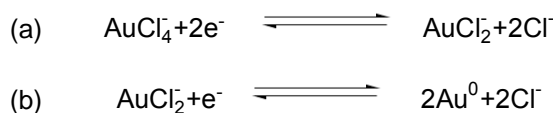


Figure 2-16: Reactions involved for bottom-up synthesis of gold nanorods. Two step reduction of chloroauric acid to elementary gold, forming the nano-construct.

Other bottom-up nanoparticle synthesis routes are self-assembly, emulsion-solvent evaporation and precipitation techniques. These methods are used to produce small nanoparticles with narrow size distributions^{62,63}. The bottom-up approach is compared to the top-down approach

less expensive and less time consuming and therefore more appropriate for the production of nanoparticles.

2.3.2.2 Properties

For nanoparticulated compounds the electronic and optical properties are governed solely by quantum mechanical effects⁶⁴. Therefore, size and morphology of such particles determine their optical and physical properties. Two renowned examples demonstrating size and shape dependent properties are quantum dots and gold nanoparticles. Murray and Kagan synthesized cadmium selenide quantum dots with various diameters in the range of 1.7-150 nm and measure their absorption spectra. They were able to show a red-shifted of the absorption maxima with increasing particle diameters⁶⁵. The same effect can be observed for gold nanoparticles as their optical properties are dependent on the size and shape of the compound⁶⁶⁻⁷⁰. Another important feature of nano-sized particles is their large surface to volume ratio. An example illustrating this property is given in ⁵⁸. Carbon micro particles with a diameter of 60 μm and a weight of 0.3 μg have a relatively small surface area of 0.01 mm^2 , orders of magnitude smaller than their nano-sized counterparts with diameters of 60 nm, which have a surface area of 11.3 mm^2 . Due to their great surface-area nanoparticles pose much higher chemical reactivity compared to bulk materials and therefore often require encapsulation, coatings or other surface modifications to be applicable for specific applications. Atoms localised at the surface of nanoparticles have less neighbouring atoms compared to atoms in the bulk and thus inherent a smaller binding energy. As a result nanoparticles have lower melting points, which decreases with particle size⁷¹.

2.3.2.3 Application in biomedical imaging

Due to their outstanding electrical and optical properties, the use of nano-sized contrast agents in biomedical imaging is in many cases advantageous compared to molecular or micro-sized imaging agents. Various nanoparticle-based contrast agents have been successfully applied in combination with imaging modalities such as X-ray based imaging^{72,73}, positron emission tomography^{74,75}, single photon emission computed tomography⁷⁶, magnet resonance imaging⁷⁷⁻⁷⁹, ultrasound imaging⁸⁰⁻⁸², fluorescence imaging⁸³⁻⁸⁶ and PA imaging^{3,22,31,87,88}. For molecular PA imaging gold nanoparticles, carbon nanotubes and polymeric nanoparticles are the most frequently used nano-sized imaging agents and are described in more detail below. Therein their properties, various syntheses pathways as well as their application in molecular PA imaging are detailed.

2.3.3 Gold nanoparticles

As mentioned above, gold nanoparticles have been utilized in since the 5th century B.C. Today gold nanoparticles are produced commercially in various shapes and sizes and can be functionalised to suit specific applications. Gold nanoparticles are utilized in various fields, such as medicine, electronics and catalysis. For PA imaging the most prevailing properties of gold

nanorods are their strong, tuneable optical absorption and their high thermalisation efficiency. In addition, gold nanoparticles are considered to be of relatively low toxicity. However, to avoid unintended aggregation and increase circulation time in blood the particles are often coated with a biocompatible layer such as a PEG coating. A disadvantage of gold nanorods and other complex gold constructs is their potential to overheat and change shape, which permanently changes their absorption spectra.

2.3.3.1 Synthesis

Today, a wide variety of synthesizing methods enables the production of gold nanoparticles with different sizes, various geometrical shapes and surface-modifications, yielding gold nanoparticles like gold nanospheres⁸⁹, gold nanocages (hollow colloid with porous walls)^{4,90,91}, gold nanowires (quasi one-dimensional gold structures)⁹², gold nanorods^{68,93–96}, gold nanoparticle clusters⁹⁷ and gold nanoshells (dielectric covered with a gold layer)^{98,99}.

For the preparation of gold nanoparticles chloroauric acid is dissolved in a solvent and rapidly stirred whilst a reducing agent is added, reducing the gold from Au^{3+} to Au^+ . Au^+ is further reduced by other gold ions present in the mixture, in a reaction called disproportionation reaction to form elementary gold (Au^0). Other gold ions are reduced at these elementary gold atoms, causing the growth of the gold cluster, forming a nanoparticle. To avoid the aggregation of the gold clusters formed stabilizing agents are introduced to the mixture during nanoparticle formation. The Turkevich method uses citric acid for the reduction of hydrogen tetrachloraurate and for the stabilisation of the gold nanoparticles formed during the procedure. Another popular method for the production of gold nanoparticles is the Frens method, which allows synthesising gold nanoparticles of diameters in the range of 10-100 nm.

2.3.3.2 Properties

Gold nanoparticles have gained great attention in the field of medical and biomedical imaging due to their outstanding optical properties, in particular the surface plasmon resonance, which gives rise to strong optical absorption (in the range of $10^9 \text{ cm}^{-1}\text{M}^{-1}$) with tunable absorption peak from the visible to the near-infrared⁶⁷. Some properties of two different gold nanoparticles are shown in Table 2-3.

Table 2-3: Properties of two commercial available gold nanoparticles - gold nanospheres (GNS) and gold nanorods (GNR). The values for λ_{\max} , ϵ_{\max} , the thermalisation efficiency and the photostability have been taken from the supplier's website. The fluence threshold is the fluence required to melt the particle - causing reshaping and coalescence of the molten metal particles.

Property	GNS	GNR
λ_{\max}	600 nm	800 nm
ϵ_{\max}	$1.2 \cdot 10^{10} \text{ M}^{-1} \text{ cm}^{-1}$	$1.6 \cdot 10^9 \text{ M}^{-1} \text{ cm}^{-1}$
Thermalisation efficiency	99%	99%
Fluence threshold ¹⁰⁰	-	6 mJcm^{-2}
Aggregation	Possible	Possible
Linker molecule for targeting	Yes	Yes

Surface plasmon resonance is the collective oscillations of charged particles at a metal - dielectric interface and depends on the particle shape and composition as well as on the dielectric constant of the medium it is embedded in¹⁰¹. This phenomenon enables optical absorption, due to the coupling of light to the collective oscillation of the electrons in the conduction band of the particle. The effect depends on the size and morphology of the nanoparticle and therefore nanoparticles like in gold nanorods exhibit surface plasmon resonances at different energy levels, resulting in two absorption bands. The more intense peak at longer wavelength is called the longitudinal mode and is associated with the coupling of light to the surface plasmon resonance occurring along the longitudinal axis. The second peak is called the transverse mode and is associated with the coupling of light to the surface plasmon resonance occurring along the transverse axis. The position of the absorption peak in the electromagnetic spectrum can conveniently be controlled by tuning the dimensions of the plasmonic particle. For example a gold nanorod with a longitudinal surface plasmon resonance with an absorption peak in the visible (550 nm) has an aspect ratio (lengths of the particle divided by the width of it) of about 1.5, whilst a gold nanorod with an aspect ratio of 6 absorbs in the near-infrared (1000 nm). For gold nanospheres, as a rule of thumb, ϵ increases roughly cubically with particle radius. However, once the plasmonic particle is in the excited state, via induction of the coherent oscillation there are several pathways for the de-excitation of the nanoparticle. The relaxation of the excited gold nanoparticle is the loss of coherent oscillation and can be induced by the emission of a photon or via direct heat transport via collisions of the electrons of the nanoparticle with electrons of the surrounding material or with the ionic core of the particle. For gold nanoparticles, the relaxation pathway via fluorescence is limited as fluorescence quantum yield are usually about 0.1%. The relaxation via collisions thermalizes the absorbed energy and occurs on a picosecond timescale. However, the heat energy transferred

to the crystal lattice of the nanoparticle can take several seconds to dissipate to the surrounding medium. If the generated heat within the nanoparticle fails to dissipate to the surrounding medium at a fast enough rate, the temperature of the particles can rise above their melting temperature, causing shape and size changes, altering the optical properties of the nanoparticle.

2.3.3.3 Application in biomedical imaging

Gold nanorods have been utilized as contrast agents in a number of biomedical studies. For instance, Liao et al used gold nanorods in PA flow measurements^{102–104} and demonstrated the feasibility of the compound as contrast agent for molecular PA imaging^{93,94,96} using human epidermal growth factor receptor 2 and CXCR4-chemokine receptor 4 as targeting moieties. In their imaging study, the researchers were able to show a four times increased PA signal generated by the antibody conjugated gold nanorods, compared to a control⁹⁴. Similar results have been presented by Bayer et al in a multiplexed imaging study using Silica coated, targeted gold nanorods¹⁰⁵. In a publication in 2011 Adarwal et al demonstrated that, gold nanorods attached to a radiolabel (¹²⁵Iodine) can be used as multimodal contrast agent for combined PA and nuclear imaging¹⁰⁶. Wilson et al successfully demonstrated the feasibility of a dual PA/ultrasound contrast agent consisting of gold nanorods incorporated in perfluorocarbon liquid nanodroplets¹⁰⁷. In their study, perfluorocarbon was used as a volatile compound which when heated by the nanoparticles forms bubbles, generating strong contrast for ultrasound imaging. In another study Wang et al were able to image the cerebral cortex of a rat *in vivo* using gold nanocages¹⁰⁸. They calculated the detection limit of the gold nanocages at an imaging depth of 33 mm to be 0.7 nM¹⁰⁹. Gold nanospheres have been utilized as biodegradable nano-clusters exhibiting absorption in the near-infrared¹¹⁰. The nano-clusters were made from gold nanospheres of diameters smaller than 5 nm and a biodegradable polymer stabilizer. The biodegradable polymer dissolves in acidic conditions, allowing for the controlled excretion of the gold nanospheres from the body, eliminating concerns about long term toxicity.

2.3.4 Carbon nanotubes

Rolled, one-atom-thick graphene sheets are called carbon nanotubes. The cylindrical allotropes of carbon exist in two basic configurations: Single and multi-walled carbon nanotubes. Single walled carbon nanotubes are made of one graphene layer wrapped to form a cylinder, whilst multi walled carbon nanotubes consist of either multiple layers of concentric cylinders or one sheet of carbon atoms wrapped around one axis - forming a spiral-shaped profile (Figure 2-17).

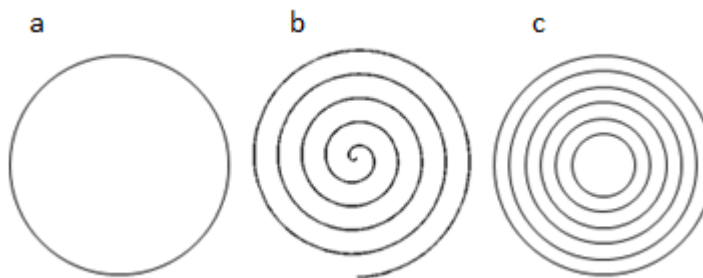


Figure 2-17: Profile of single-walled carbon nanotube (a) and multi-walled carbon nanotubes with a spiral profile (b) and concentric cylinders (c).

2.3.4.1 Synthesis

The first carbon nanotubes were synthesized using arc-discharge evaporation technique. Therefore a high current is generated between two graphite electrodes in the presence of a metal catalyst in a high pressure argon filled vessel. The arc-current induces the growth of carbon nanotubes on the negative electrode of the apparatus. With this technique multi-walled carbon nanotubes with diameters ranging from 4-30 nm and a length of up to 1 μm can be synthesized. The production of single-walled carbon nanotubes has been achieved via laser vaporisation technique using carbon-nickel-cobalt as feedstock¹¹¹. Today, arc-discharge evaporation and laser vaporisation are still used for the bulk production of carbon nanotubes, but are not favourable due to a lack of control over the growth rate, generating nanotubes with a broad particle size distribution. Another procedure for the synthesis of carbon nanotubes is chemical vapour deposition. For the synthesis a gaseous or volatile feedstock of carbon (e.g. ethylene) decomposes in a process catalysed by metallic nanoparticles such as alumina-supported iron nanoparticles¹¹². Chemical vapour deposition enables the production of both single- and multi-walled carbon nanotubes and allows for higher control over the morphology, size and structure of the resulting nanotubes. However, even chemical vapour deposition techniques deliver mixtures of carbon nanotubes which require grading via techniques such as size-exclusion chromatography or electrophoresis.

2.3.4.2 Properties

Carbon nanotubes can be classified using chiral indices (m,n) which refer to unit vectors of the equal length, positioned at a 60° angle to each other. The length of the unit vectors m and n are the length from carbon 1 to carbon 3 and at a 60° angle carbon 1 to carbon 5 as shown in Figure 2-18a. The sum of the m and n indices describe the circumference of the carbon nanotube and thus allows predicting their diameter. The chiral angle (angle between a_1 and C_n) can vary between 0° (zigzag configuration, with chiral indices $(n,0)$) to 30° (armchair configuration, with chiral indices (n,n)) as shown in Figure 2-18b.

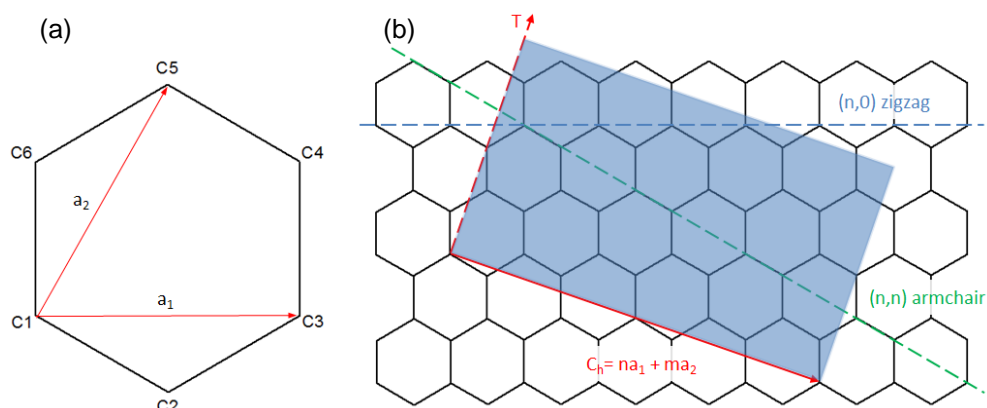


Figure 2-18: Basic arrangement of carbon atoms in carbon nanotubes and graphene-sheets (a). a_1 and a_2 are the unit vectors and C1-6 the positions of the individual carbon atoms. (b) shows three different examples for carbon nanotube folding, using various chiral indices: Zigzag configuration (chiral indices $(n,0)$; blue dotted line), armchair configuration (chiral indices $(n = m)$; green dotted line) and an example of a graphene-sheet with the chiral indices $(4,2)$. C_h is the resulting vector (red arrow) and T the resulting tube axis (red dashed arrow).

Like the configuration of graphene sheets, carbon atoms within the carbon nanotube structure are sp^2 -hybridized. Wrapping the sheets of graphene and therefore forming carbon nanotubes introduces new energy levels, whose energy increases with decreasing tube diameter. These newly introduced energy levels are due to steric interactions between the π -orbitals and the σ -orbitals of the carbon atoms¹². Depending on the chiral indices of the carbon nanotubes their electronic properties resemble metallic or semiconducting behaviour. In general, a single walled carbon nanotube in armchair configuration shows metallic behaviour whilst most other configurations lead to semiconducting nano-materials. The optical properties of the one dimensional tubes are due to electronic transitions between so called non-continuous one-dimensional density of states. Sharp peaks of density of states found in one-dimensional materials are called Van Hove singularities (see Figure 2-19) and give rise to sharp optical transitions with peak absorption in the visible and near infrared region of the electromagnetic spectrum.

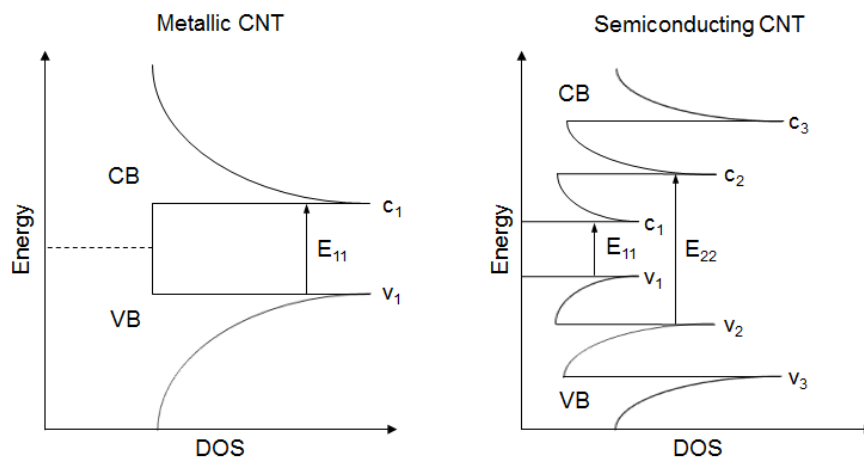


Figure 2-19: Examples of electronic transitions of metallic and semiconducting carbon nanotubes. E_{11} = First van Hove optical transition; E_{22} = Second van Hove optical transition; CB = Conduction band; VB = Valence band; DOS = Density of states.

2.3.4.3 Application in biomedical imaging

Even though there are still toxicity concerns regarding the safety for use in the human body, carbon nanotubes have been applied in numerous preclinical studies, including molecular PA imaging, making use of their relatively strong absorption (typically in the range of $10^6 \text{ M}^{-1} \text{ cm}^{-1}$) and good photostability. In 2007 Zharov et al applied carbon nanotubes for the first time for PA flow cytometry *in vivo*¹¹³. A different group conjugated PEG coated carbon nanotubes with cyclic Arg-Gly-Asp peptides in order to target for the neovascular of a tumour. They were able to demonstrate the ability of the carbon nanotube/peptide conjugate to target the vascular of the tumour using molecular PA imaging³⁴. In 2011, Kim et al introduced gold coated carbon nanotubes which due to the surface plasmon resonance exhibit a strong, narrow absorption band in the near-infrared²⁴. They also were able to demonstrate molecular targeting using the gold coated carbon nanotubes conjugated to a peptide and the feasibility of the compound for molecular PA imaging.

2.3.5 Polymeric nanoparticles

A polymer is a macromolecule composed of a large number of repeated sub-units of molecules. Polymers inheriting alternating multiple and single bonds along their polymeric-backbone are called conjugated polymers. Due to hybridization of the atoms involved in the conjugated backbone of the polymer, π -bonds are formed introducing new material properties, such as a band gap. Due to the band gap introduced via the alternating π -bonds, conjugated polymers are also called semiconducting polymers. The distance over which the polymer has uninterrupted alternating double and single bonds is defined as the conjugation length of the polymer. This new class of materials quickly found applications and was used to engineer organic light-emitting diodes^{114,115}, solar cells^{116,117} and most recently semiconducting polymers, in the form

of nanoparticles, have been introduced as a contrast agent for medical imaging¹¹⁸⁻¹²⁰ and cancer therapy^{121,122}. An example of such a semiconducting polymeric material used in nano-sized form for medical imaging purposes is PCPDTBT (Poly[2,6-(4,4-bis-(2-ethylhexyl)-4H-cyclopenta [2,1-b;3,4-b']dithiophene)-alt-4,7(2,1,3-benzothiadiazole)]), see Figure 2-20 for the chemical structure.

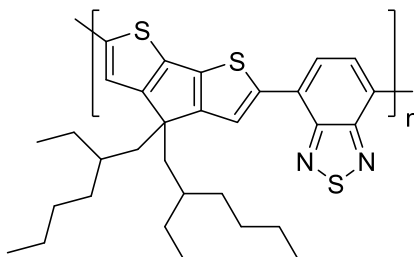


Figure 2-20: Chemical structure of the polymeric semiconductor PCPDTBT.

2.3.5.1 Synthesis

Several methods have been developed to generate nanoparticles made from various polymeric materials. The formulation of polymeric nanoparticles can be accomplished in either of two ways: i. via polymerisation of the desired monomer species to generate particles of the desired size or ii. by forming nano-sized particles from readily polymerised polymers. The formulation involving polymerisation can be performed via suspension, dispersion or emulsion polymerisation techniques. An example of a polymeric nanoparticle grown from the monomer species are polystyrene nanoparticles. The formulation of polymeric nanoparticles using readily formulated polymers can be performed via methods such as the nano-precipitation, mini-emulsion or self-assembly methods. Most methods for the preparation of polymeric nanoparticles require a surfactant for the stabilisation of the nanoparticles in aqueous solvents. The nanoparticle formation via the nano-precipitation method is based on the nucleation of small aggregates of polymers, followed by aggregation of these nuclei, whilst the mini-emulsions method is based on the ouzo-effect - the formation of small thermodynamically stable droplets. The formation of small droplets can be accomplished via agitation, for example using a sonicator. The shear force required for the formation of nano-sized droplets needs to match the Laplace pressure π_L of the droplets and can be estimated using:

$$\pi_L = \frac{2\sigma}{a} \quad \text{Equation 2-2}$$

where σ is the interfacial tension and a is the radius of the droplet. After formulation of the nano-sized droplets containing the polymer molecules, the disperse phase solvent is removed via evaporation - forming polymeric nanoparticles. These methods allow preparing polymeric nanoparticles with narrow particle-size distribution and various surface modifications.

2.3.5.2 Properties

When forming solid polymers, steric interactions between the long polymer molecules commonly result in a porous structure, which can be loaded with small molecules such as organic dyes and drugs. For this reason polymeric nanoparticles have gained great attention in the field of biomedicine for targeted delivery of drugs and combined imaging and treatment of diseases. A common approach for delivering drugs and combined imaging is to entrap both a drug-payload and a contrast agent tailored for a specific imaging modality in a polymeric vesicle targeted to a specific site within an organism.

Nanoparticles made from semiconducting polymers provide an intrinsic optical contrast with absorption bands in the visible to the near-infrared, enabling PA signal generation without the need to load the particles with another chromophore. An example of the properties of nanoparticles made from commercial available semiconducting polymers PCPDTBT and polypyrrole (PPy) is show in Table 2-4.

Table 2-4: Properties of nanoparticles made from two commercial available semiconducting polymers - PCPDTBT and polypyrrole. The values for λ_{\max} , ϵ_{\max} and the thermalisation efficiency have been taken from reference ¹¹⁸ and ¹¹⁹.

Property	PCPDTBT	PPy
λ_{\max}	680 nm	808 nm
ϵ_{\max}	$5 \cdot 10^7 \text{ cm}^{-1}\text{M}^{-1}$	$2.4 \cdot 10^{10} \text{ cm}^{-1}\text{M}^{-1}$
Thermalisation efficiency	99%	100%
Aggregation	Possible	Possible
Linker molecule for targeting	No	No

The optical properties arise from their inherent characteristic typical for semiconducting materials, a band gap. For polymeric semiconducting nanoparticles, the spectral position and intensity of the absorption band depends on the semiconducting polymer used to formulate the nanoparticles as well as on the electronic properties of the surface molecules and therefore can be tuned by changing the chemical composition of the polymers and the surface molecules used for the preparation of the particles. Polymeric semiconducting nanoparticles exhibit strong absorption in the range of $\epsilon = 10^7\text{-}10^{10} \text{ cm}^{-1}\text{M}^{-1}$ and strong thermalisation efficiencies and consequently strong PA signal generation.

2.3.5.3 Polymer nanoparticles in biomedical imaging

Examples of polymeric nanoparticles utilized in biomedical imaging are polystyrene-¹²³⁻¹²⁵, polyallylamide-^{126,127} serum albumin-nanoparticles^{128,129} and various other polymeric

nanoparticles^{130–133}. Encapsulation of a compound in a polymeric matrix for optical imaging modalities can be advantageous for various reasons such as an improved photostability¹³⁴, improved biocompatibility and solubility¹²⁴ and red-shifting of absorption and emission spectra via the formation of J-aggregates to gain absorption in the near-infrared¹²⁷ have been reported. Nanoparticles called porphysomes are another class of light absorbing materials that has been used as PA contrast agent. Porphysomes are porphyrin based nano-vehicles with strong absorption in the near-infrared. The extinction coefficient of these particles is comparable to gold nanorods and has been estimated to be $2.9 \cdot 10^9 \text{ cm}^{-1}\text{M}^{-1}$ at 680 nm. A study by Lovell et al demonstrated the use of porphysomes for PA lymph node mapping as well as for the photothermal destruction of tumours in xenograph bearing mice¹³⁵. Another example of polymeric nanoparticle proposed as contrast agent for molecular PA imaging is the based on the conjugated polymer termed PFTTQ (poly[9,9-bis(4-(2-ethylhexyl)phenyl)fluorene-alt-co-6,7-bis(4-(hexyloxy)phenyl)-4,9-di(thiophen-2-yl)-thiadiazoloquinoxaline]), which has been used to study the brain vasculature of rats¹³⁶. In this study, Liu et al were able to demonstrate moderate absorption with $\epsilon = 4.6 \cdot 10^5 \text{ cm}^{-1}\text{M}^{-1}$ in the near-infrared (700-850 nm), good photostability and low toxicity *in vivo*.

2.3.6 Other nano-materials

Various other nano-sized compounds such as copper sulphide nanoparticles and silver nanoparticles have been proposed as contrast agent for molecular PA imaging. These materials exhibit surface plasmon resonance effect and therefore high optical absorption and strong PA signal generation with tuneable absorption. Consequently, copper sulphide nanoparticles and silver nanoparticles have been evaluated as contrast agents for molecular PA imaging. Copper sulfide nanoparticles for instance exhibit increased photostability compared to e.g. gold nanorods and were successfully applied for PA imaging of a mouse brain⁸⁷. ϵ of the copper sulfide nanoparticles has been estimated to be $2.6 \cdot 10^7 \text{ cm}^{-1}\text{M}^{-1}$ in the near-infrared at about 1064 nm. Another example of a successfully implemented nano-sized contrast agent used for molecular PA imaging has been proposed by Jokerst et al in 2014⁸⁸. The contrast agent proposed is based on cellulose and demonstrated strong optical absorption ($\epsilon = 8.7 \cdot 10^9 \text{ cm}^{-1}\text{M}^{-1}$) in the near-infrared ($\lambda_{\text{max}} = 700 \text{ nm}$) and showed strong PA signal generation allowing to discriminate the compound from the background in *in vivo* experiments. An important feature of this novel contrast agent is its low toxicity and its ability to biodegrade.

The following table (Table 2-5) is provided in order to give an overview of the properties of the various types of contrast agents for molecular PA imaging.

Table 2-5: Overview of exogenous contrast agents for PA imaging.

Type	Organic dyes	Gold nanoparticles	Carbon nanotubes	Polymeric nanoparticles	Other nanoparticles
Example	ICG	Gold nanorods	HIPco SWCNT	Polypyrrole	Copper sulfide nanoparticles
ϵ_{\max}	$<10^6 \text{ cm}^{-1} \text{ M}^{-1}$	$<10^{11} \text{ cm}^{-1} \text{ M}^{-1}$	$<10^7 \text{ cm}^{-1} \text{ M}^{-1}$	$<10^{10} \text{ cm}^{-1} \text{ M}^{-1}$	$<10^8 \text{ cm}^{-1} \text{ M}^{-1}$
E_t	Varies	~100%	~100%	May vary with composition	~100%
Morphology	Molecular structure	Various shapes	Tubular structure	Spherical	Often spherical
Size	$<2 \text{ nm}$	~10-200nm	Diameter 0.7-1.2nm Length: ~100nm-1 μm	~10-200nm	~10-200nm
Advantages	<ul style="list-style-type: none"> - Low toxicity - Due to small size good tissue penetration, biodistribution and fast clearance 	<ul style="list-style-type: none"> - Often very high PA signal generation efficiency - Large surface area/porous matrix allowing for targeted drug delivery and imaging 			
Disadvantages	<ul style="list-style-type: none"> - Low ϵ_{\max} - Groundstate bleaching and aggregation may alter optical properties - Poor photostability profile 	<ul style="list-style-type: none"> - Often toxicity concerns - Often poor biodistribution - Difficulties with reproducibility, purification and stability 			

Chapter 3

Characterisation of the photoacoustic spectroscope

3.1 Introduction

The ability of compounds to generate PA contrast is frequently evaluated using purely optical methods. This however fails to account for relevant thermodynamic properties involved in the PA signal generation process, such as E_t and Γ . To address this a primary aim of this work is to set-up an apparatus and propose methods, which allows to determine all the parameters involved in the PA signal generation. Therefore, after introducing molecular PA imaging, the following chapter describes the design and characterisation of a PA spectroscope used throughout this thesis and details the validation of the methods used for the determination of the parameters involved in the PA signal generation

The following chapter describes an experimental arrangement, termed PA spectroscope, for the measurement of the PA amplitude and μ_a spectra, the determination of ϵ , E_t , Γ and the photostability of light absorbing compounds such as organic dyes and nanoparticles. This includes a detailed description of the individual components of the PA spectroscope, their fabrication and an analysis of their properties. The second part of this chapter describes the methods used to determine the PA amplitude and μ_a spectra, ϵ , E_t , Γ and the photostability of liquid samples, the validation of these methods and the assessment of the limitations .

3.2 Photoacoustic spectroscopy

This section describes the individual components of the PA spectroscopy used throughout this thesis. Based on laser generated ultrasound generated by a sample, the PA spectroscopy uses an ultrasound transducer in combination with an analogue-to-digital converter in order to record time-domain PA signals. These signals are used for the evaluation of the suitability of the chromophore as contrast agent for molecular PA imaging. The design, construction and characterisation of components, such as a PVDF based ultrasound transducer and the sample cuvette, as well as the performance of the PA spectroscopy as a completed unit are detailed.

A schematic of the PA spectroscopy used is depicted in Figure 3-1. The main components are: i) a laser system for the excitation of the sample, ii) a sample cuvette enabling optical excitation of a sample solution and the transmission of acoustic pressures generated, iii) an ultrasound transducer for the detection of the generated PA signal, iv) an analogue-to-digital converter to convert the electrical signal detected by the ultrasound transducer; and v) a computer to save and evaluate the measured signals.

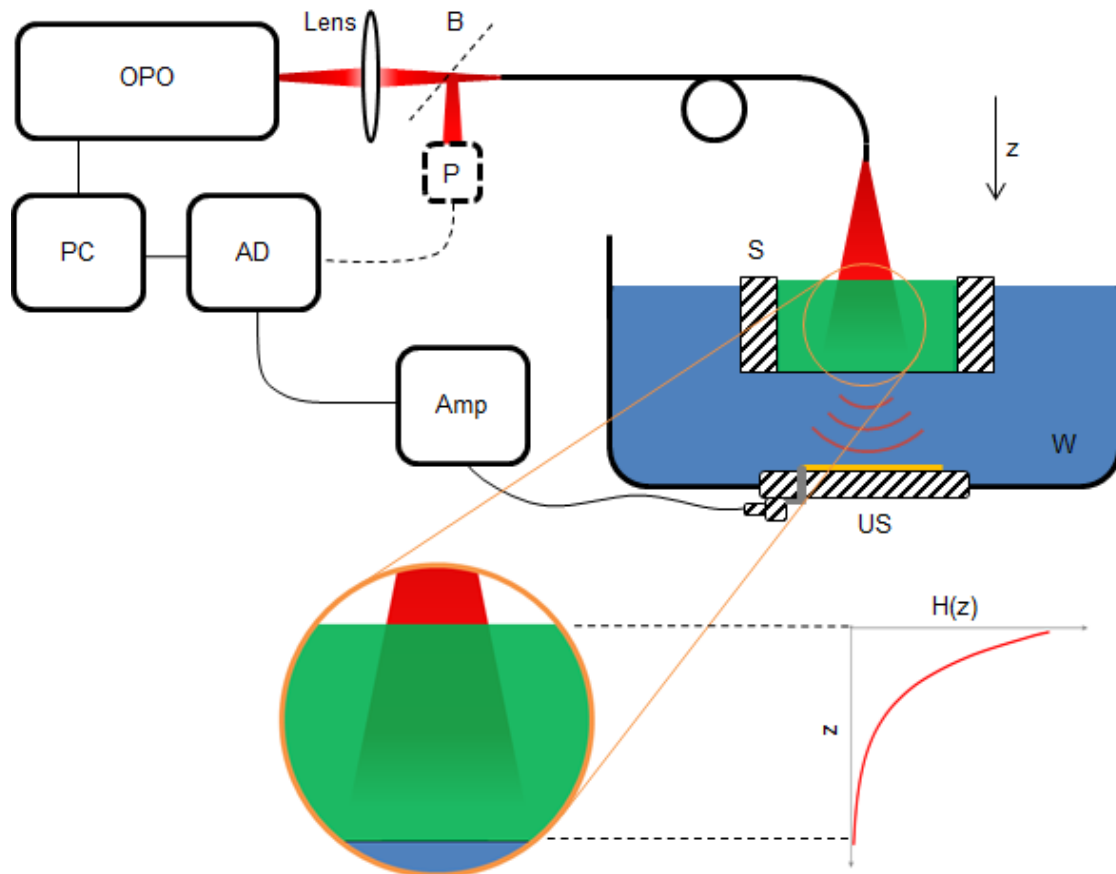


Figure 3-1: Schematic of instrumentation used for PA characterisation measurements (top) and a zoom of the sample cuvette (bottom left) with a diagram showing the exponential decay of the light intensity traveling through a purely absorbing medium (bottom right). OPO = Excitation laser system; P = Integrating sphere with photodiode; B = Beam splitter; S = Sample cuvette; W = Water tank; US = Ultrasound transducer; AD = Analog-to-digital converter. Depending on the laser system used the AD is either a digital oscilloscope or a data acquisition card installed on a PC. Also depending on the laser system the beam splitter and the photodiode were replaced by a laser inbuilt power meter. z = depth; $H(z)$ = Absorbed energy density as a function of depth.

3.2.1 Laser systems

The laser system used for the PA spectroscopy experiments described within this thesis is a Nd:YAG pumped optical parametric oscillator (OPO) laser, either tuneable from 400-2100 nm, with a pulse length of 7 ns (VISiR, GWU Spectra-Physics, CA, USA) or tuneable from 420-2500 nm with a pulse length of <8 ns (Spitlight 600, Innolas Laser GmbH, Germany). The PA signals generated using the two different laser systems compared well to each other and therefore the lasers were used as availability permitted. Fused silica optical fibres, with a diameter of 1.5 mm were used to guide the laser light towards the sample contained in the sample cuvette.

3.2.2 Sample cuvette

The sample cuvettes used during the experiments are homemade and consist of a block of Perspex with approximate side length of $45 \times 35 \text{ mm}^2$. A photograph of a cuvette containing an absorber is presented in Figure 3-2.

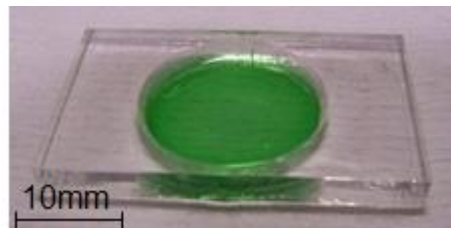


Figure 3-2: Photograph of a homemade cuvette containing an aqueous solution of IR-820.

The thickness of the different cuvettes varied between 2 and 20 mm in order to realise different light path lengths. Adapting the light path is useful for weak absorbers, in order to decrease light transmission through the sample cuvette and the generation of a parasitic PA signal at the surface of the ultrasound transducer. A hole was drilled in the centre of the block of Perspex using different drill diameters for various cuvettes with different capacities. Subsequently, a polyethylene film (40 x 30 mm, 50 μm thickness) was cemented to the bottom side of the Perspex block using UV-curing glue, sealing one side of the hole. The polyethylene film was thought to be sufficiently thin and exhibit an acoustic impedance close to that of water and hence was assumed to be acoustically transparent. Depending on the diameter of the drill-hole and the thickness of the Perspex block, the voids can be filled with a sample volume between 100 μL and 3 mL. Judging from the signal amplitude, the best results were obtained using a cuvette with a large drill-hole and a large sample volume. In addition, when the irradiated by the excitation laser beam the walls of the cuvette can generate a parasitic signal which interferes with the PA signal. To avoid this, when using the cuvettes with small drill-hole diameters, the fibre tip is positioned very close to the surface of the sample solution within the cuvette. In that case, in order to reduce photobleaching effects the fluence is required to be reduced using optical density filters, leading to a reduced PA signal amplitude. In addition to this the meniscus of the liquids in small volume cuvettes can distort the PA signals generated and introduce errors. For this reason, the cuvettes with a large sample volume were used throughout most parts of this thesis.

The meniscus of the sample solution depends on the cohesive and adhesive forces of the bulk solution. Figure 3-3 shows a concave (a) and convex (b) meniscus.

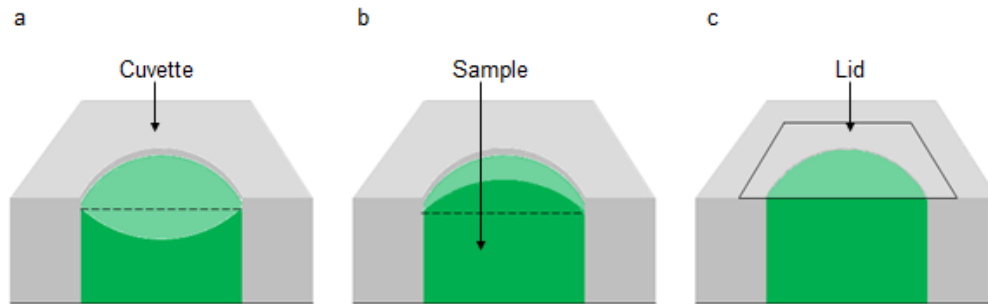


Figure 3-3: Schematic of liquids in a container forming either a concave (a) or a convex (b) meniscus. A practical solution to avoid the formation of such a meniscus is to completely enclose the liquid with a lid (c).

For PA spectroscopy measurements, the formation of a concave or a convex meniscus is undesirable due to the lens effect of such a surface and the distortion of the signal by acoustic pressure waves generated at different heights of the meniscus. In this case, a useful solution to avoid the formation of a meniscus is the use of a lid, enclosing the liquid (as shown in Figure 3-3c). In practice, a thin (50 μm), transparent polyethylene film was placed on top of the liquid if the formation of a meniscus was apparent.

3.2.3 PVDF ultrasound transducer

PVDF is a material commonly used to fabricate ultrasound transducers, due to its piezoelectric and acoustic properties (see Chapter 1 for a more detailed description). Unlike piezoceramic materials, PVDF as a transducer material has the advantage that it provides a broad band frequency response, a low noise equivalent pressure and has a well matched acoustic impedance to tissue¹³⁷. Especially the well behaved frequency response provided by PVDF transducers was the motive to choose PVDF as a transducer material for the ultrasound transducers used in the PA spectroscope, allowing for an accurate representation of the time-resolved PA wave. This is particularly important for the estimation of μ_a , because it is determined by fitting an exponential to the time-domain PA signals. If these signals are distorted errors in the estimation of μ_a will arise. The fabrication and analysis of the properties of PVDF ultrasound transducers used in the PA spectroscope is described below.

3.2.3.1 Fabrication

The basic components of the ultrasound transducers prepared for the PA spectroscopy setup are the sensing PVDF film and a block of Perspex used as a backing substrate. The substrates used are rectangular in shape with the side lengths of 30 mm and 45 mm and thicknesses varying between 7-23 mm. PVDF films of varying thicknesses (52 and 110 μm) were cut into square pieces of side length between 1 mm and 10 mm. Different thicknesses and side length of the PVDF films were analysed in order to achieve a transducer with an appropriate

compromise between high sensitivity, a broad frequency response and high directional sensitivity. Gold coatings on each side of the PVDF film enable electrical connection to the polymeric backbone. For the electrical connection between the transducer and the analogue-to-digital converter, a BNC connector was cemented to the back of the substrate. Initially the electrical contact between the BNC connector and the gold surfaces of the PVDF film were made via fine copper wires. Therefore one of the wires was passed through a thin drilled hole in the centre of the PMMA-substrate, connecting the PVDF film with the BNC connector (see Figure 3-4 left). However, in later designs of the PVDF-transducer (see Figure 3-4 right), the drill hole was omitted because it can result in acoustic scattering which results in non-uniform frequency response characteristics. For the design without the hole, the electrical connection between the BNC connector and the PVDF film was realised using a thin layer of electrically conductive silver ink (see Figure 3-4 right).

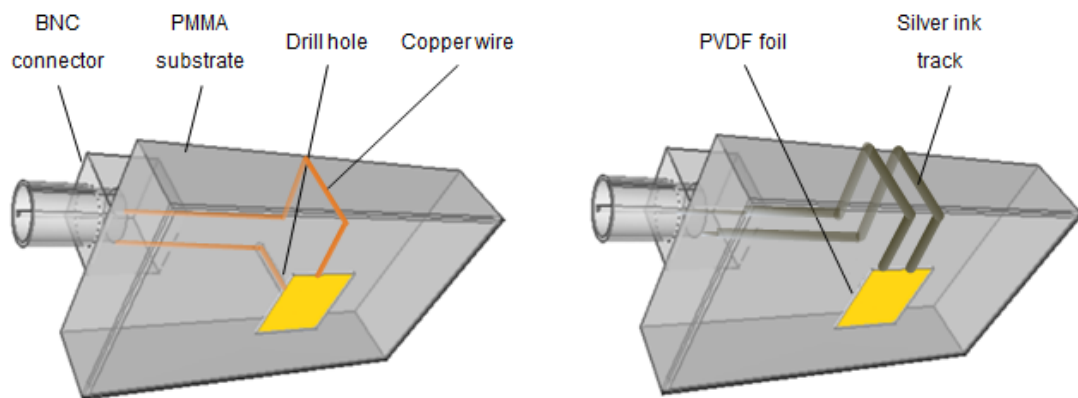


Figure 3-4: Two designs of the PVDF ultrasound transducers. Initial design (left) using a drilled hole for the electrical connection between the PVDF film and the BNC connector. The final design (right) uses a silver ink track for the electrical connection.

To achieve this, a small spot of silver ink was applied to a small area between the PVDF film and the substrate before the film was cemented to the substrate using UV-curing glue. Subsequently, a silver ink track was applied to the substrate, electrically connecting the silver ink spot between the PVDF film and the substrate and the BNC connector at the back of the substrate. A second layer of UV curing glue was applied to the edges of the PVDF film for electrical insulation between the edges of the gold-coating. For the electrical connection between the exposed side of the PVDF film and the BNC connector, a second silver ink track was applied between the contact of the BNC connector and a corner of the exposed side of the PVDF film. After drying, the silver ink tracks were insulated using a layer of UV curing glue. To reduce the pickup of electrical noise, the surface of the ultrasound transducer was covered in silver ink. The exposed side of the PVDF transducer was electrically grounded via the BNC shield, whilst the side facing the substrate was electrically connected to the centre pin of the BNC connector. The substrates used are made to be mounted in a fitting window at the bottom

of a water tank, using a rectangular rubber gasket between the window and the transducer. The ultrasound transducers were electrically connected via a low noise voltage amplifier with a gain of 20/40 dB, a bandwidth of 200 MHz and an input impedance of 1 M Ω (HVA-200M-40-F, Femto, Germany) to a data-acquisition card (PCIe6323, National Instruments) or a digital multi-channel oscilloscope (TDS5034B, Tektronix, OR, USA) for digitisation of the analogue signal and to enable downloading of the data to a PC.

After manufacturing a number of ultrasound transducers their acoustic properties were measured as described below. Initially the sensitivity of the transducers was determined by referencing their output to that of a calibrated hydrophone. Subsequently, the frequency response and directivity of the ultrasound transducers were measured.

3.2.3.2 Sensitivity of the ultrasound transducers

The sensitivity of the transducer is expressed by the noise equivalent pressure (NEP), which describes the minimum detectable pressure. The expected signal amplitude generated using the PA spectroscopy is in the order of a few kPa, and therefore high sensitivity is desirable. In order to determine the NEP of the PVDF ultrasound transducers prepared, the transducer output was referenced to that of a calibrated needle hydrophone. A calibrated needle hydrophone (MCX121, Precision Acoustics, UK) was used to provide an acoustic pressure reference and a planar PZT ultrasound transducer (V381-SU, Panametrics, UK) with a centre frequency of 3.5 MHz driven by an ultrasound pulser (UPG004, Precision Acoustics, UK) was employed as an acoustic source. The signals generated by the PVDF transducer were amplified using a low noise amplifier (352A-1-B, Analog Modules, US) and digitised using an oscilloscope (TDS 784D, Tektronix, US). For the measurements, one of the PVDF ultrasound transducers prepared was mounted in a water tank and the ultrasound pulser driven PZT transducer was placed a short distance in front of it. The acoustic source and the PVDF transducer were aligned by monitoring the amplitude of the received signal to adjust the position from maximum signal amplitude, moving the sound source on a mechanically x-y translation stage. Subsequently the PVDF transducer was replaced by the calibrated needle hydrophone. Great care was taken to keep the alignment of the two ultrasound transducers identical. Using the calibration data of the needle hydrophone allows estimating the NEP of the individual PVDF ultrasound transducers, by dividing the root mean square (RMS) noise value by the calibration sensitivity of the PVDF transducer. The results of the NEP measurements for some of the PVDF ultrasound transducers over a 20 MHz bandwidth are shown in Table 3-1.

Table 3-1: NEP of various PVDF ultrasound transducers.

Transducer No.	PVDF thickness [μm]	PVDF side length [mm]	NEP [kPa]
1	52	1.2	20.7
2	52	2	37.4
3	52	4	3.7
4	52	5	3.6
5	52	8	2.9
6	52	10	1.9
7	110	5	5.2
8	110	10	1.6

The NEP measured for different PVDF ultrasound transducers ranges between 1.6 kPa and 37.4 kPa. As expected, the measured NEP decreases with increasing element size and thickness of the transducers. Exceptions to this, such as the increased NEP of transducer 7, may be due to the alignment of the PVDF ultrasound transducers prepared with respect to the source. Due to the large extent of the PVDF films, the PVDF ultrasound transducers exhibit a highly directional response and therefore a small angle between the transducer and the source causes a loss in sensitivity. Another reason for the increased NEP of some of the transducers may be poor electrical connection between the PVDF film and the BNC connector. Due to the low NEP the geometry with a side length of 10mm was chosen for further experiments.

3.2.3.3 Frequency response of the ultrasound transducers

For PA spectroscopy, the frequency response of an ultrasound transducer is an important measure because insufficient bandwidth introduces errors and leads to the underestimation of μ_a and the PA amplitude. The bandlimiting effect cannot directly be observed from the time-domain PA signals and to investigate this, the frequency response of the PVDF transducer was measured.

3.2.3.3.1 Estimation of frequency content of photoacoustic signals

PA signals typically have broadband frequency content with a bandwidth extending to several tens of MHz. Therefore ultrasound transducers for PA spectroscopy are required to provide a similar broadband frequency response in order to reproduce the input signal without distortion. For a rough estimation of the bandwidth requirements for an acoustic transducer for PA spectroscopy a simple model was employed to simulate PA signals. Therefore, PA signals

corresponding to homogenous purely absorbing solutions with μ_a between 1 and 50mm^{-1} were modelled (see Figure 3-5 left) using the equation for the initial pressure distribution¹³⁸. This simple model assumes a purely absorbing homogeneous solution which upon laser excitation generates planar waves which are detected without attenuation, edge-waves, reflections or other effects. Despite its simplicity, the model is sufficient to deliver an approximately indication of the bandwidth requirements. After modelling the time-domain signals, they were Fourier transformed in order to obtain their frequency spectra (see Figure 3-5 right).

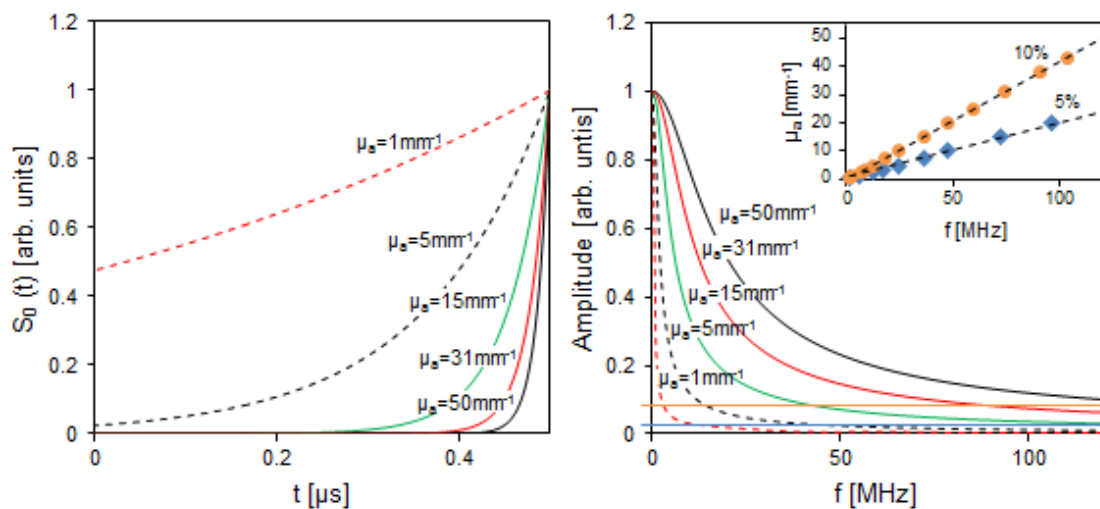


Figure 3-5: Modelled PA signals generated in homogeneous purely absorbing solutions with μ_a varying between 0 and 50mm^{-1} (left). Modelled frequency spectra (right) of the PA signals shown on the left. The orange line indicates 10% and the blue line 5% of the power density. The points at which the lines cross the curves were plotted in the inset (top right), which shows μ_a versus the bandwidth (frequency) at 10% (orange points) and 5% (blue squares) of the amplitude.

Figure 3-5 (right) shows the frequency content of modelled PA signals corresponding to homogenous purely absorbing solutions. The inset on the top right shows a plot of μ_a versus the frequency at which the amplitude of the signal falls to 5% or 10% of its value at 0 Hz. The plot shows that solutions exhibiting strong absorption ($>30\text{mm}^{-1}$) generate PA signals with high frequencies exceeding 50 MHz. For example the modelled signal using a μ_a of 50mm^{-1} reaches 10% of its maximum power density value at about 115 MHz. For μ_a values below 15mm^{-1} the frequency content of the signals is significantly lower - the amplitude for $\mu_a = 15\text{mm}^{-1}$ reaches 10% of its maximum value at 36 MHz. From this simple model it can be concluded that a transducer with a bandwidth of about 30 MHz should be sufficient for the accurate estimation of the PA signal amplitude and μ_a of absorbers with μ_a values up to about 15mm^{-1} .

After modelling the frequency content of signals of various μ_a values and gaining an insight into the frequency content of PA signals, the frequency response of the PVDF transducer was modelled and subsequently measured experimentally as described in the following section.

3.2.3.3.2 Modelling of the ultrasound transducer frequency response

The model used for the theoretical frequency response was adopted from ¹³⁹ and matched to fit the PVDF transducer properties. Matlab was employed to code the model of the theoretical frequency response ($P_1(k)$). Due to the large extent of the sensitive area of the PVDF transducers, radial resonance modes and the effect of acoustic diffraction around the edge of the film can be neglected. We further assumed negligible acoustic attenuation in the PVDF and adhesive film and matching acoustic impedance between the two, therefore neglect any reflections from these interfaces. In order to model the frequency response, the following equation (adopted from ¹³⁹) was used:

$$|P_1(k)| = \frac{T\sqrt{2}}{kl} \sqrt{\frac{(R_0^2+1)+4R_0 \cos k(l+2l_g) \sin^2\left(\frac{kl}{2}\right) - (1+R_0^2) \cos kl}{1-2R_0R_2 \cos 2k(l+l_g) + (R_0R_2)^2}} \quad \text{Equation 3-1}$$

where T is the pressure amplitude transmission coefficient, due to an acoustic impedance mismatch between the adhesive layer and the sensing layer; R_0 is the pressure amplitude reflection coefficient, due to an acoustic impedance mismatch between the adhesive layer and the backing material; R_2 is the pressure amplitude reflection coefficient, due to an acoustic impedance mismatch between the sensing layer and the surrounding medium (water); k is the acoustic wave number; l is the thickness of the sensing film and l_g is the thickness of the adhesive layer.

After modelling the frequency response of the manufactured PVDF transducer was determined empirically as described in the next part. For comparison the modelled and empirical frequency responses are overlaid with each other.

3.2.3.3.3 Measurement of the frequency response

For the generation of the PA signals with high frequency content a laser generated ultrasound source was used. To achieve this, a Perspex block (55 x 45 x 7 mm³) was spray-painted on one side with a thin layer of black paint. The Perspex block was placed 15 mm above the PVDF transducer in a water bath, with the painted side facing towards it. A fused silica fibre, of 1.5 mm inner diameter, was mounted about 20 mm above the Perspex substrate surface of the black-absorber, delivering 7 ns laser pulses at an excitation wavelength of 750 nm. The acoustic signals generated upon excitation in the thin layer of black paint were averaged over 100 laser pulses using a digital-oscilloscope connected to a computer. A broadband Fabry-Perot sensor (>100 MHz) with a spacer thickness of about 7 μm was used to provide a reference

measurement of the acoustic source. For a detailed description of the working principle of the Fabry-Perot sensor see reference ¹⁴⁰. Replacing the PVDF-transducer with the Fabry-Perot sensor without changing any distances or positions in the setup ensures identical experimental conditions. The signals of the Fabry-Perot sensor were also averaged over 100 laser pulses. An example of a time-domain signal recorded using the two different transducers is shown in Figure 3-6.

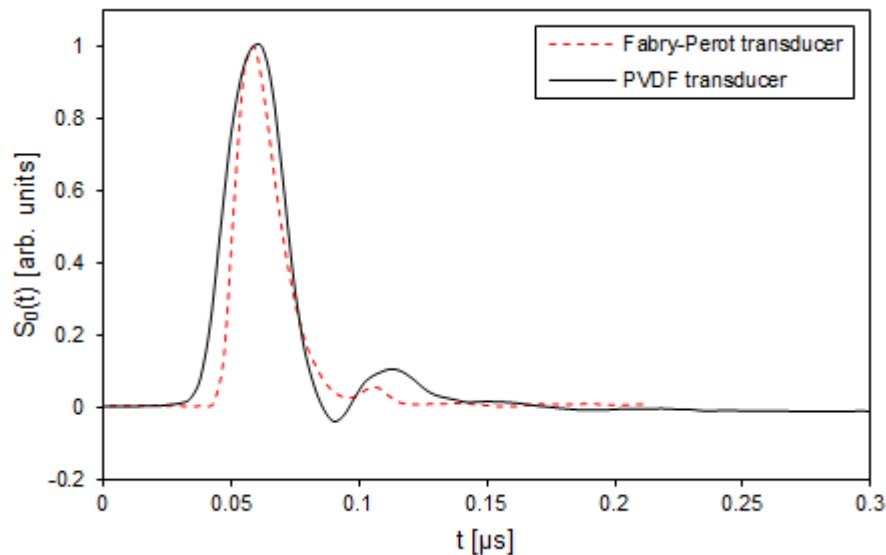


Figure 3-6: Laser generated ultrasound signals recorded using a Fabry-Perot sensor (red dotted line) and a PVDF transducer (black line).

The time domain signals measured using the Fabry-Perot sensor and the PVDF transducer, seen above, were Fourier transformed to obtain their frequency spectra. Dividing the frequency spectrum of the PVDF transducer with the frequency spectrum of the reference Fabry-Perot sensor, results in the normalised frequency response of the PVDF transducer. Both, the frequency spectra of the two ultrasound receivers and the normalised frequency response of the PVDF transducer are shown in Figure 3-7.

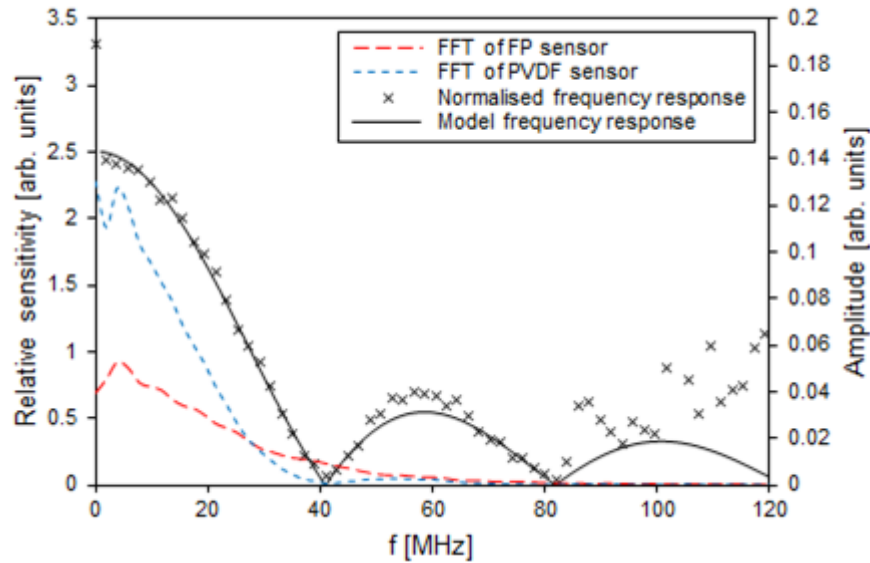


Figure 3-7: Measured normal incidence frequency response of a PVDF ultrasound transducer of 52 μm thickness (black crosses) and comparison to the modelled frequency response (black line). The modelled data was obtained by modelling Equation 3-1. Also shown is the Fourier transformation of the signal recorded using the Fabry-Perot sensor (FP, red dashed line) and the PVDF transducer (blue dashed line).

The results of the measured normalised frequency response of the PVDF transducer and the modelled data show excellent agreement for the lower frequencies, with little deviation up to about 80 MHz. Some minor deviations from the modelled data are apparent at about 60 MHz. At frequencies beyond 80 MHz the deviation of the measured data compared to the model data further increases. These discrepancies start to appear at higher frequencies (>40 MHz) at which uncertainties due to low SNR and the alignment of the acoustic source and the ultrasound transducer have a significant impact on the relative sensitivity. The PVDF transducer analysed in the example above has a -3 dB bandwidth of 23 MHz. These results are encouraging and show that, based on the estimation made by modelling the frequency content of PA signals in section 3.2.3.3.1 (Figure 3-5), the PVDF transducers have the potential to detect PA signals generated by chromophores with μ_a up to about 15 mm^{-1} without excessively bandlimiting the signal.

3.2.3.4 Directivity of the ultrasound transducer

In order to achieve high sensitivity an ultrasound transducer with large element size was chosen for the PA spectroscope. However, this has the disadvantage that it makes the transducer highly directional with a frequency response that exhibits strong angular dependence. Thus, small angular misalignments can result in distortion to the signal and thus errors in the estimation of μ_a and the PA amplitude. To investigate the angular dependence of the signal characteristics, the directivity of the PVDF transducer was measured. This measurement gives

an indication of the angular alignment accuracy required to achieve a truthful representation of the PA signal.

3.2.3.4.1 Experimental setup

In order to measure the directional response of the PVDF transducers a mechanical rotation stage was employed, allowing adjustment of the angle between the ultrasound source and detector, without changing the distance between the two. A schematic of the setup is depicted in Figure 3-8.

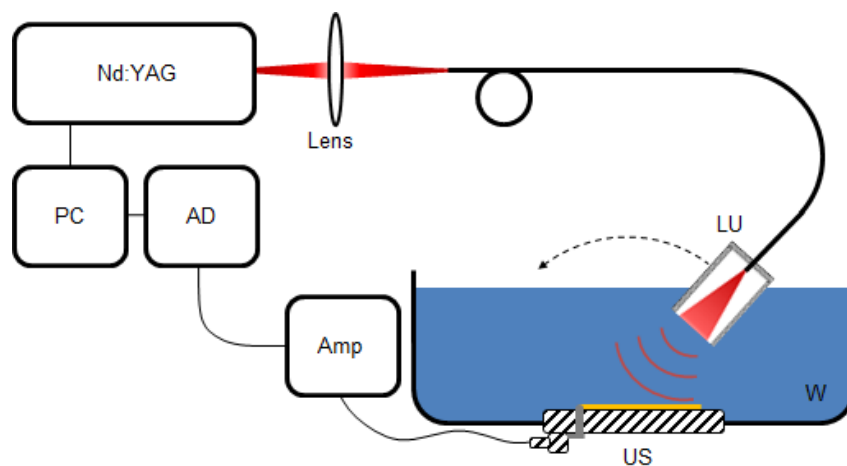


Figure 3-8: Setup used for the measurement of the directional response of the ultrasound transducer. LU = Laser generated ultrasound source made from black painted PMMA disc mounted in a cylindrical housing for the generation of ultrasound, mounted on a motorised rotation stage. Nd:YAG = Nd:YAG Q-switched laser; W = Water tank; US = ultrasound transducer; AD = Analog-to-digital converter; Amp = Amplifier.

For the measurements a rotation stage powered by a servo motor (Kinesis, UK) was used, allowing for the accurate movement of the ultrasound source under computer control. The ultrasound source used throughout the directivity experiments is based on laser generated ultrasound. A Nd:YAG Q-switched laser, with a pulse duration of <7 ns and 20 Hz pulse repetition rate, emitting at a wavelength of 1064 nm, was used as a light source. The emitted light was guided via a 1.5 mm fused silica glass fibre to irradiate a PMMA disc of 25 mm diameter and 8 mm thickness which has been spray-painted black. The disc was mounted in a cylindrical housing. The PVDF transducers were mounted at the bottom of the water tank. The ultrasound source and the PVDF transducer were aligned based on the time of arrival of the ultrasound signals generated at different angles. The position of the ultrasound source was adjusted until the time of arrival of the acoustic signal was equal at all angles. Due to spatial limitations of the experimental setup, the measurements were limited to the range of 30° from 15° to -15° . Subsequent to the alignment, signals were recorded at angles ranging from 15° to -15° in 0.1° steps, averaging over five laser pulses before being recorded. At the position of 0°

the ultrasound source was located about 50 mm directly above the centre of the PVDF transducer. The resulting signals and spectra as well as the evaluation of the effective radii of the ultrasound transducer are shown below.

3.2.3.4.2 Results

A selection of time-domain PA signals recorded at different angles, using the setup described above, is shown in Figure 3-9. The signals in were plotted with a time delay in order to better visualise the individual signals. The inset in Figure 3-9 shows the decreasing peak signal amplitude with increasing angle.

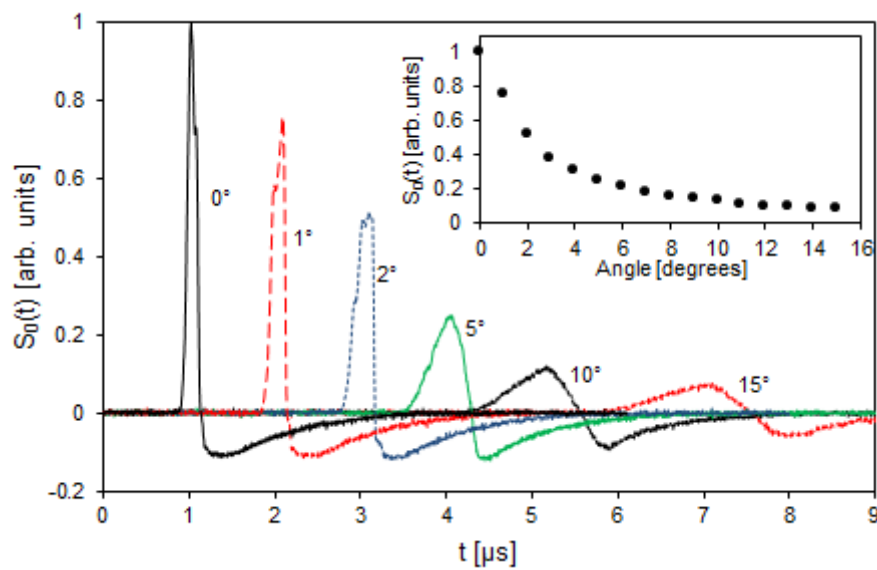


Figure 3-9: Signal amplitude recorded at various angles using the PVDF transducer. The inset shows a plot of the peak signal amplitude versus the angle of incidence.

As expected from a spatially averaging ultrasound transducer, the results shown in Figure 3-9 demonstrate a decrease in the signal amplitude with increasing angle. The results also show a broadening of the signals with increasing angle. To gain further insight into this, the signals recorded at different angles (Figure 3-9) were Fourier transformed into the frequency domain as shown in Figure 3-10.

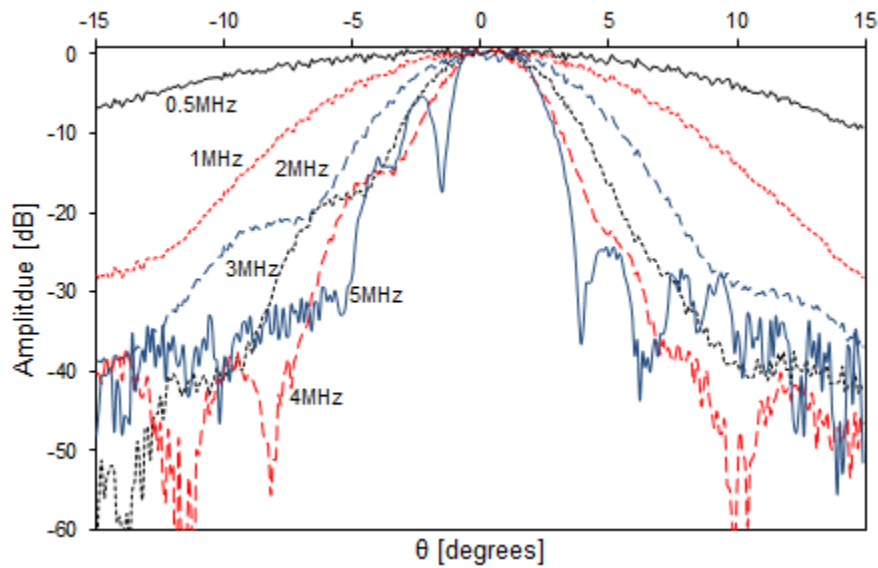


Figure 3-10: Measured directivity as a function of frequency at angles ranging from -15° to 15° of a PVDF transducer with a thickness of $52\ \mu\text{m}$ and dimensions of $9 \times 9\ \text{mm}^2$.

The directivity profile of the PVDF transducers, depicted in Figure 3-10, shows the Bessel function like behaviour of a spatial averaging, especially for the lower frequencies. The asymmetry of the directivity profiles presented is likely to be due to an inaccurate alignment of the ultrasound source with respect to the transducer.

By fitting the first-order Bessel function $D(\theta)$ of a circular plane receiver (Equation 3-2) to the measured directional response (Figure 3-10), an estimation of the effective radius was obtained.

$$D(\theta) = \frac{2J_1(k a \sin(\theta))}{k a \sin(\theta)} \quad \text{Equation 3-2}$$

where θ is the angle, J_1 is the first order Bessel function, k is the angular wavenumber and a the effective radius of the acoustic aperture of the transducer. The radius (a) was used as a fitting parameter. Due to the asymmetry of the measurements, the directivity function was fitted to the positive angles only. The angular response of the ultrasound transducer averaged over both sides and the resulting fitted Bessel functions are shown on the left in Figure 3-11. On the right of the same figure a plot of the effective radii of the PVDF transducer as a function of frequency is presented.

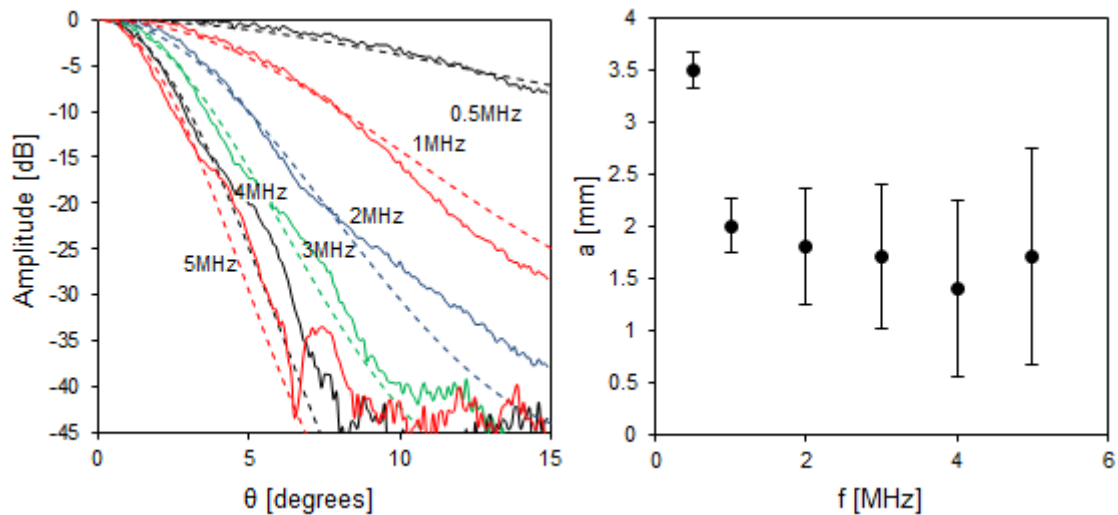


Figure 3-11: Left: Fitted Bessel functions (dashed lines) to the angular response of the PVDF transducer (full lines). Right: Effective radius of the PVDF transducer as a function of frequency. The error bars are the average standard deviation of the Bessel function from the angular response of the PVDF transducer.

The amplitude of the angular response of the ultrasound transducer (shown on the left in Figure 3-11) decreases rapidly with increasing frequency, which is consistent with the broadening of the time-domain signals. For frequencies up to 3 MHz the first-order Bessel function of circular plane receivers fits reasonably well with the data obtained experimentally up to about 15°. For higher frequencies (>3 MHz) the theoretical and the experimental data start to deviate strongly from each other for angles greater 5°. The results show, that ultrasound transducer analysed does not behave like a circular planar receiver, which may be explained by its rectangular dimensions. The model corresponding to a circular planar receiver was used as it functions as a standard model for comparison of acoustic transducers. The aim of the directivity measurements was to get a rough indication of the importance of the angular alignment and therefore the model used is sufficient. The plot on the right in Figure 3-11 shows the effective radius of the PVDF transducer as a function of frequency. The effective radius rapidly falls with increasing frequency from about 3.5 mm at 0.5 MHz to 2 mm at 1 MHz, levelling out at about 1.8 mm. The discrepancy between the effective radius and the physical size of the PVDF film may be explained by the simple model of a circular purely spatially averaging receiver that Equation 3-2 implies. Despite this the results of the directivity measurements are sufficient to conclude that the signal amplitude (Figure 3-9) and the bandwidth (Figure 3-11) of the ultrasound transducer drastically decrease with increasing angle of detection.

In summary, this section was dedicated to get a measure of the directional response of the PVDF transducer and its effective element size in order to understand the influence on the PA signal. The results have shown that the measured PA amplitude and the PA frequency component vary with the detection angle. Even at small angles the signal amplitude decreases

significantly, especially for higher frequencies (>3 MHz), for example at 1° the signal amplitude is reduced between 14 and 23% in the plotted frequency range (0.5 -5 MHz). Misinterpretation of PA signals arriving at an angle are the consequence of the large element size, which was approximated to be about 1.8 mm. This however does not restrict the application of the PVDF transducers in the PA spectroscopy setup described above, but emphasize the importance of careful angular alignment between the acoustic source and the ultrasound transducer.

3.2.3.5 Summary

PVDF based ultrasound transducers for the application in the PA spectroscopy setup described in this thesis were designed, manufactured and characterised in terms of their acoustic performance. In the first instance the sensitivity of the transducers was analysed using a reference transducer. The results show moderate sensitivity in the low kPa range. Subsequently, the frequency response and the directivity profile of the transducers were analysed. The experiments demonstrate the expected broad-band frequency response and decreasing sensitivity with angle. The results show, that using a PVDF film of a thickness of 52 μm and a side length of 10 mm, a -3 dB bandwidth of 23 MHz and a NEP of 1.9 kPa over 20 MHz can be achieved, suggesting the system can be used to measure μ_a up to about 15 mm^{-1} . However, the transducers are, due to their large effective element size (1.8 mm), very sensitive to signals arriving at an angle and therefore alignment of source and receiver will be important for accurate PA measurements. Overall the investigations indicate that the PVDF transducer manufactured exhibit sufficient sensitivity and bandwidth for the application in PA spectroscopy and therefore the PVDF ultrasound transducer with a thickness of 52 μm and a side length of 10x10 mm^2 was used throughout the thesis.

3.3 Validation

After describing the individual parts of the PA spectroscopy and the analysis of their properties, the remainder of this chapter details the validation of the methods used to determine μ_a , E_t and Γ . Initially, the determination of the PA amplitude and μ_a from time-domain PA signals is described. This includes a description of the properties of PA signals generated using the PA spectroscopy, the methods used for the determination of the two parameters and the analysis of the limitations of these measurements. The next sections introduce the methods used for the determination of E_t and their validation using reference fluorophores and the determination of Γ . Finally, the method for the determination of photobleaching profiles was demonstrated followed by a conclusion, summarising the achievements.

3.3.1 Instrumentation

For the validation of the PA spectroscopy and the methods used for the analysis of the properties of the chromophores, spectrophotometers and a Fabry-Perot ultrasound sensor

based PA scanner were employed. The instrumentation used for this purpose is described below.

3.3.1.1 Spectrophotometer

In order to validate the spectra generated using the PA spectroscopy, the results were compared to the μ_a values and absorption spectra measured using spectrophotometry. Various systems were used, depending on availability. Initially, optical absorption data was generated using a tungsten halogen white light source (HL 2000-FHSA, Ocean Optics, FL, USA) irradiating a 1 mm path-length cuvette made from optical glass (Hellma analytics, Mühlheim, Germany). The transmitted light is detected by a spectrophotometer with a detection range between 200 nm and 1000 nm (Maya pro 2000, Ocean Optics, FL, USA) and the data saved *via* USB connection onto a computer. The source and the spectrophotometer were controlled using a Labview code written in house by Dr. Thomas Allen (UCL, Department of Medical Physics and Biomedical Engineering) and the evaluation of the data was done using Matlab. In addition to the Ocean Optics spectrophotometer a commercial UV/Vis/NIR spectrophotometer (Perkin Elmer 750s) was employed, which allows for the detection of transmitted light in the wavelengths range between 200 nm and 2500 nm.

3.3.1.2 Fabry-Perot ultrasound sensor based PA scanner

Fabry-Perot sensors were used when reference measurements with transducers exhibiting increased bandwidth compared to the PVDF transducers were needed. The setup used for the experiments is described in detail in ¹⁴⁰. For the experiments a Fabry-Perot sensor with a bandwidth >200 MHz is mounted into the bottom of a water tank. The laser for the interferometer interrogation is a fibre-coupled tuneable continuous-wave external cavity laser (Thorlabs, ECL5000DT). Photoacoustic signals are generated using absorbing materials placed above the Fabry-Perot transducer, acoustically coupled via water contained in the water tank. Liquid samples - typically a volume of 1.5 mL - were contained within a cuvette (shown in Figure 3-2), which was placed 10 mm above the surface of the transducer. For the signal generation, the samples are irradiated by an OPO laser (see Chapter 3.2.1). The light output of the OPO laser used is delivered using an optical fibre in order to irradiate the samples at normal incidence and source and ultrasound-detector are placed on opposite sides of the sample cuvette. After setting up the transducer, alignment with the x-y scanner and biasing of the sensor by tuning the interrogation laser wavelength, the excitation laser is fired and the photoacoustic waveforms are acquired, and downloaded using a Labview code written in house by Dr. Edward Zhang (UCL, Department of Medical Physics and Biomedical Engineering). Data was acquired using single point measurements - without scanning the interrogation laser across the Fabry-Perot element - and, if not quoted otherwise, averaged over 100 laser pulses before the data was saved for further data processing.

3.3.2 Determination of μ_a and the PA amplitude from PA signals

3.3.2.1 Properties of signals generated using the PA spectroscope

Short pulses (ns) of laser light excite a homogeneous, purely absorbing sample contained within the cuvette. The sample absorbs the light and converts the absorbed energy to an acoustic pressure wave, which propagates through the medium towards the PVDF transducer causing it to produce an electrical signal proportional to the acoustic pressure. The signal is then recorded using a digital-oscilloscope. An example of a typical signal measured using the PA spectroscopy setup is shown in Figure 3-12. The initial light intensity incident on the sample solution decays exponentially as it travels through the sample solution. In purely absorbing solutions this can be described by:

$$H(z) = \Phi_0 e^{-\mu_a z} \quad \text{Equation 3-3}$$

where $H(z)$ is the absorbed energy density as a function of depth z , Φ_0 is the fluence at the surface of the medium and μ_a is the absorption coefficient of the medium. The light travelling through the sample solution decays at a rate depending on μ_a of the substance and is related to the molar extinction coefficient $\epsilon = \mu_a c^{-1}$, where c is the concentration of the chromophore within the sample solution. Subsequent to the absorption of the light, the chromophore relaxes to its ground state, transferring its energy to the surrounding medium, generating an acoustic pressure wave. The generated acoustic pressure wave propagates within the medium eventually arriving at the ultrasound transducer. Here, the pressure wave is converted to an electrical signal which is digitized using an analogue-to-digital converter. The characteristic exponential rise of the signals recorded in this manner, is the result of the absorption characteristic displayed by the chromophores within the sample solution and thus allows recovering the absorption coefficient as shown in Figure 3-12

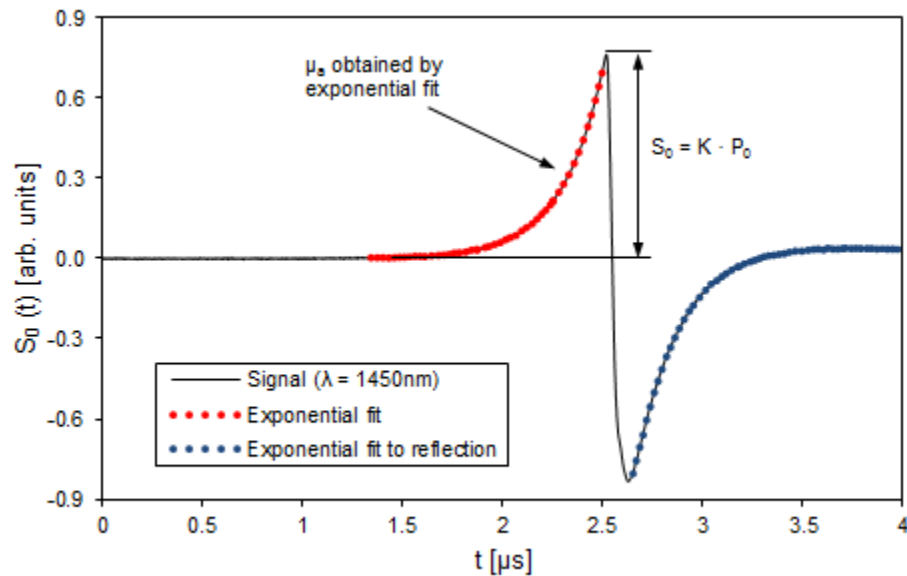


Figure 3-12: Example of PA signal generated by water irradiated with laser light of a wavelength of 1450 nm (solid, black line) showing the corresponding exponential fit (dashed, red line) used to determine the absorption coefficient and the PA amplitude S_0 . The dashed blue line is the exponential fit to the reflection of the signal.

The signal displayed in Figure 3-12 was recorded using the setup described above. The absorber in this case is water, excited with laser light at a wavelength of 1450 nm. The negative component of the signal at 2.5-4 μs is caused by the reflection of the PA signal due to an impedance mismatch at the air-liquid boundary (if no lid is used) or the air-polymer boundary (if a polymer film is used as a lid) at the sample cuvette. In order to show, that the negative component of the PA signal is due to the reflection caused by the impedance mismatch at the air-liquid boundary and not due to any other effects, an exponential fit to this part of the signal was computed. The absolute μ_a values estimated for the PA signal and its reflection compare well to each other, suggesting that the negative component of the detected pressure wave is due to the reflection at the air-liquid boundary. To further demonstrate this, the impedance mismatch on top of the cuvette was eliminated. For the experiment an aqueous solution of an organic dye (IR 820) was inserted into the sample cuvette which is sealed with a lid (as seen in Figure 3-2c) and a signal is recorded using an excitation wavelength (820 nm) at which IR 820 absorbs strongly and the absorption of water can be neglected. The second signal is recorded under the same conditions, but a 1 cm thick layer of water was placed on top of the sample cuvette. Adding water on top of the cuvette minimises the impedance mismatch between the sample and the surrounding, allowing the PA signal to travel in the opposite direction of the ultrasound transducer before being reflected at the air-water boundary. The resulting PA signals are shown in Figure 3-13.

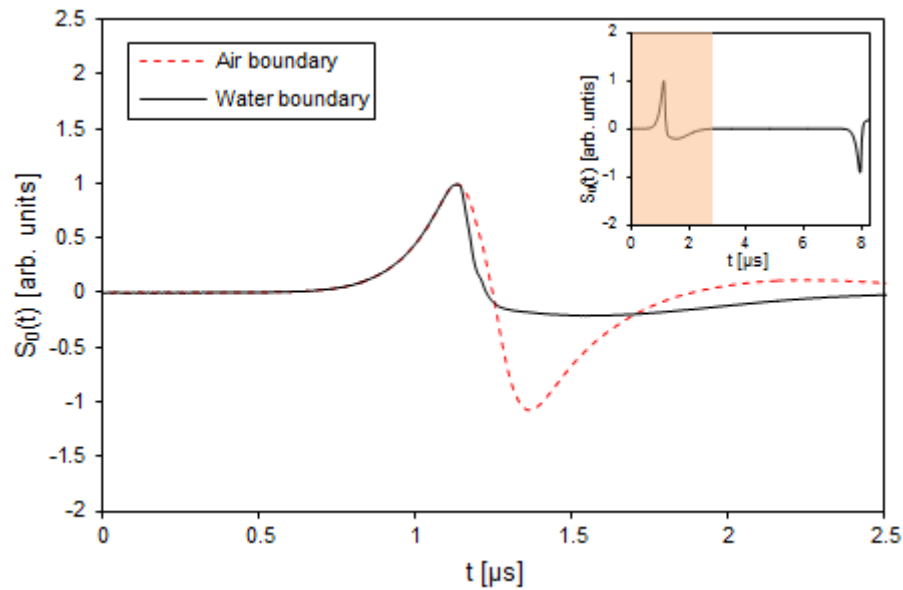


Figure 3-13: Comparison of PA signals recorded using an enclosed cuvette filled with an aqueous solution of IR 820. The chromophore solution within the sample cuvette is either bordering air (red dashed line) or water (black line) on the top of it. The inset on the bottom left shows the signal generated using the impedance matching layer on top of the cuvette on a greater time-scale.

Comparing the shape of the two signals shows that the negative component, due to the reflection of the signal, is missing in the signal generated using the impedance matching layer on top of the sample cuvette. This is due to the increased time needed for the signal to travel to the water-air boundary, before it is reflected back and reaches the transducer. The time delayed reflection of this signal is shown in the inset in Figure 3-13. The signal recorded without the water layer on top of the sample cuvette shows the same characteristic reflection of the PA signal at the air-liquid (chromophore solution) boundary as seen in Figure 3-12. However, the exponential rise of the two PA signals shown in Figure 3-13, compare well to each other. This demonstrates that the PA signals are not corrupted by their reflection.

After this initial analysis of the time-domain PA signals generated using the PA spectroscopy, the method for the determination of the PA amplitude and μ_a from these signals were examined in detail as described below.

3.3.2.2 Method used for the determination of the PA amplitude and μ_a

Assuming thermal and stress confinement, a homogeneous, purely absorbing medium and a collimated pulsed light beam for excitation, the initial axial pressure distribution $P_0(z)$ of the acoustic wave generated by the PA spectroscopy, can be described by

$$P_0(z) = \Phi_0 \mu_a e^{-(\mu_a \cdot z)} E_t \Gamma \quad \text{Equation 3-4}$$

where Φ_0 is the incident fluence and z is the axial distance from the surface of the absorber. After propagating a short distance the pressure wave is detected by the PVDF ultrasound transducer. Assuming the acoustic wave propagates as a plane wave with negligible acoustic attenuation, the initial compressive part of the signal detected by the transducer $S_0(t)$, can be related to the initial pressure distribution as follows¹³⁸,

$$S_0(t) = \Phi_0 \mu_a e^{-(\mu_a c_s(t-t_0))} E_t \Gamma K \quad \text{Equation 3-5}$$

where c_s is the speed of sound of the medium, t_0 is the time at which the signal amplitude is at its maximum and K is a scaling factor which represents the acoustic sensitivity of the system. Figure 3-12 shows a typical signal generated in a pure absorber in this way.

Two parameters can be extracted from each of the PA-signals recorded, namely (i) the signal amplitude and (ii) μ_a . The parameters were extracted as shown in Figure 3-12; μ_a was obtained by fitting Equation 3-5 to the initial compressive part of the measured PA signal (for $t < t_0$) using the non-linear least squares fit method. To do so, the signals were plotted on a logarithmic scale and a linear fit was used to determine the slope. The value for μ_a is calculated by taking the ratio of the slope of the linear fit and the speed of sound. PA amplitude and μ_a spectra can therefore be generated by recording PA signals at different wavelengths.

The fluence output of the OPO laser systems varied with wavelengths, which distorts the PA amplitude spectra. Therefore, it is necessary to correct for the wavelength dependency of the fluence as described in the next section.

3.3.2.3 Correcting for wavelength dependence of the fluence

In order to correct the measured PA amplitude values $S(\lambda)_{0, \text{Measured}}$ for the wavelength dependency of the fluence, the relative laser output power $O(\lambda)_{\text{Measurement}}$ was monitored and recorded for each wavelength during signal acquisition. When using the GWU laser, the light energy during the signal acquisition was measured using a photodiode within an integrating sphere (Tektronix, OR, USA). Therefore, a beam splitter (a glass slide) was placed in the laser beam. The glass slide was oriented so that a small proportion (~2%) of the laser light is directed to the optical input of the integrating sphere and is detected by the photodiode within. The output of the photodiode is monitored using a digital oscilloscope. The Innolas laser system on the other hand provides a measure of the laser energy via an internal power meter.

Subsequent to the acquisition of $S(\lambda)_{0, \text{Measured}}$ and $O(\lambda)_{\text{Measurement}}$, the light energy was monitored in a calibration step using the photodiode within the integrating sphere (GWU laser) or the internal power meter (Innolas laser) $O(\lambda)_{\text{Calibration}}$. In addition to this the light energy during the

calibration step was simultaneously monitored using an external power meter $M(\lambda)_{\text{Calibration}}$ giving a quantitative measure. For the quantitative determination of the laser power at the fibre tip an external power meter (Fieldmax II, Coherent, CA, USA) in combination with a photo-detector (PM30V1Q, Molectron/Coherent, CA, USA) were used during the calibration step. For the calibration, the fibre-tip is mounted in front of the photo-detector of the external power meter. Subsequently, the desired wavelength range was scanned whilst the readings of the external power meter ($M(\lambda)_{\text{Calibration}}$) and, depending on the laser system, the photodiode or the internal power meter readings ($O(\lambda)_{\text{Calibration}}$) were recorded simultaneously and saved to a calibration dataset. The calibration dataset consists of a file comprising a list of the wavelengths, $M(\lambda)_{\text{Calibration}}$ and $O(\lambda)_{\text{Calibration}}$. Equation 3-6 was used for the calculation of the corrected PA signal amplitude $S(\lambda)_{0,\text{Corrected}}$ accounting for the fluctuating light energy incident on the target.

$$S(\lambda)_{0,\text{Corrected}} = \frac{S(\lambda)_{0,\text{Measured}} \cdot O(\lambda)_{\text{Calibration}}}{M(\lambda)_{\text{Calibration}} \cdot O(\lambda)_{\text{Measurement}}} \quad \text{Equation 3-6}$$

For the evaluation of the corrected PA amplitude and μ_a an algorithm was coded in Matlab. The basic principle of the code is described below.

3.3.2.4 Algorithm used for the generation of PA amplitude and μ_a spectra

The algorithm used to extract both the μ_a and the PA amplitude from the individual signals of a measurement dataset to generate the PA spectra (PA amplitude and μ_a spectra) was coded in Matlab.

Initially a measurement dataset (Section 3.3.2.2) and a calibration dataset (Section 3.3.2.3) are imported to Matlab. The algorithm removes any dc offset in $S_0(t)$ and the variation of the fluence with wavelength using Equation 3-6. Subsequently, a plot of $S_0(t)$ as a function of t , for the entire wavelength range present in the measurement file, is displayed. Next, the code requires the user to manually select the time sequence containing the peak amplitude and the exponential rise of the PA signals for the determination of the PA amplitude and μ_a spectrum. The maximum $S_0(t)$ value (the PA amplitude) within the window chosen is saved and displayed as a function of wavelength (PA amplitude spectrum). For the calculation of μ_a the algorithm uses a time sequence limited to data points with an amplitude below 80% of the peak value of the exponential rise. These time sequences, used for the evaluation of μ_a of the individual signals, are displayed. The length of the resulting windows depends on the absorption of the sample and commonly ranges between 0.2 and 0.7 μs and consists of about 50-200 data points. Subsequently, the μ_a values of the individual signals are calculated as described in Section 3.3.2.2 and the correlation coefficient (R^2) was generated using a Matlab function. Finally, the resulting μ_a spectrum is displayed overlaid onto the PA amplitude spectrum for comparison. The results are saved on the computer in a file compiling a list of the wavelength, PA amplitude, μ_a

and SNR for analysis. Using the algorithm allows the user to determine PA amplitude and μ_a spectra of chromophores.

3.3.2.5 Limitations

Water has been well characterised in the past, and has E_t of 100% and high photostability making it a suitable reference absorber for the analysis of the limitations of the PA spectroscopy. Initially, to quantify the limitations of the PA spectroscopy, especially the upper and lower μ_a detection limits of the PA amplitude and μ_a measurements, ten PA amplitude and μ_a spectra were acquired in a wavelength range between 1400 nm and 2000 nm, with 5 nm steps, using water as a chromophore. μ_a of water in this wavelength range varies between 0.4 and 13 mm^{-1} . The resulting spectra were averaged and the standard deviation was calculated. For comparison, the spectrophotometer, referred to in section 3.3.1, was employed to acquire a transmission spectrum. The resulting averaged PA amplitude and μ_a spectrum and the transmission spectrum are shown in Figure 3-14. A plot of μ_a measured using the PA spectroscopy and the PA amplitude versus the μ_a measurements determined using the spectrophotometer is shown in the inset of the same figure.

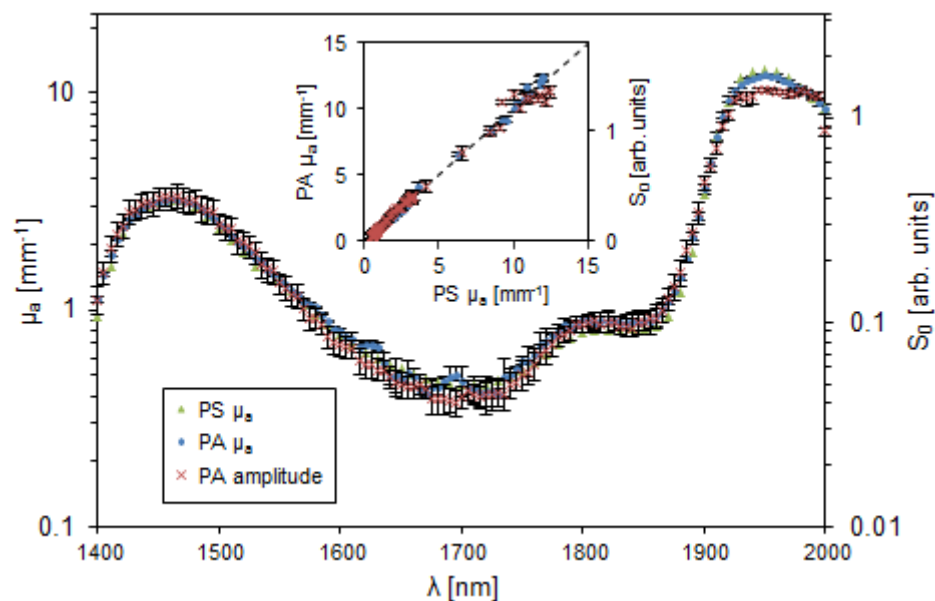


Figure 3-14: Near-infrared spectrum of water measured using the PA spectroscopy (blue circles μ_a and red crosses PA amplitude spectrum) and a spectrophotometer (PS; green triangles). The inset shows μ_a (blue circles) and PA amplitude (red crosses) measured using the PA spectroscopy versus μ_a measured using the spectrophotometer of water with wavelength between 1400 nm and 2000 nm. The dashed black line shows theoretical line of μ_a where μ_a measured using the PA spectroscopy is equal to that measured using the spectrophotometer. The error bars are the standard deviation of ten subsequent measurements. The maximum error is 15% and the minimum 3% of the spectrophotometer values.

The μ_a measurements agree well with the measured spectrophotometer transmission spectra over the whole range measured. Small deviations from the spectrophotometer measurements can be noted around 1700 nm, which is due to low PA SNR caused by the low μ_a of water in this wavelength range. For $\mu_a > 0.7 \text{ mm}^{-1}$ the deviation from the spectrophotometer measurements (measurement error) is less than 3% (assuming the spectrophotometer measurements represent the known μ_a values) and ten repeats of the PA measurements result in standard deviations of the μ_a values of less than 5%. However, the measurement error and the standard deviation for $\mu_a < 0.7 \text{ mm}^{-1}$ ($\lambda = 1620\text{-}1770 \text{ nm}$) both increase to maximum 23% and 19% due to low SNR, respectively. The measured PA amplitude spectrum follows the general trend of the spectrum generated using the spectrophotometer. However, from about 1930 nm to 1980 nm, when the absorption of water exceeds 10 mm^{-1} , the error in the PA amplitude values increases and the values consistently under-read. In this wavelength range (1930-1980 nm) the PA amplitude remains almost constant, whilst the PA μ_a and spectrophotometer readings increase to a maximum at about 1950 nm. The standard deviations of ten PA amplitude measurements in this range is lower (<6%) compared to the standard deviations of the values with μ_a below 10 mm^{-1} (<15%). Deviations of the PA amplitude from the spectrophotometer readings are in the range of 10% in the spectral range from 1930 nm to 1980 nm and less than 5% in the spectral range from 1400 nm to 1930 nm. The deviation in the wavelength range from 1930 nm to 1980 nm is assumed to be due to the limited bandwidth of the ultrasound transducer. This effect in particular depresses the peak amplitude, whilst the initial part of the exponential rise of the PA signal isn't affected. Hence the μ_a readings are more accurate for $\mu_a > 10 \text{ mm}^{-1}$. The influence of the bandwidth is explained in more detail later in this section.

To understand the source of the measurement errors, various experiments were executed. In the first instance the relationship between the accuracy of the measurements and the SNR was established. PA signals were generated at various wavelengths and fluences and the μ_a and SNR were determined. Choosing various wavelengths along the water spectrum gives μ_a values ranging from 1 mm^{-1} to 13 mm^{-1} . Even this range is higher than the range expected in a typical in vivo situation, it is sufficient to provide valuable information about the ability of contrast agents to generate PA signals. Varying the wavelength and reducing the fluence of the laser beam results in SNR values between 3 dB and 60 dB and allows determining the minimum SNR required for an accurate determination of μ_a . The fluence was reduced by partially obstructing the laser beam, using a beam-shutter. The blade of the beam-shutter obstructing the light can be set to values between 0 (fully open) and 100 (fully closed). For the experiments at reduced SNR the beam-shutter was set to values between 0 and 80. The resulting μ_a is plotted versus the SNR and can be seen in Figure 3-15.

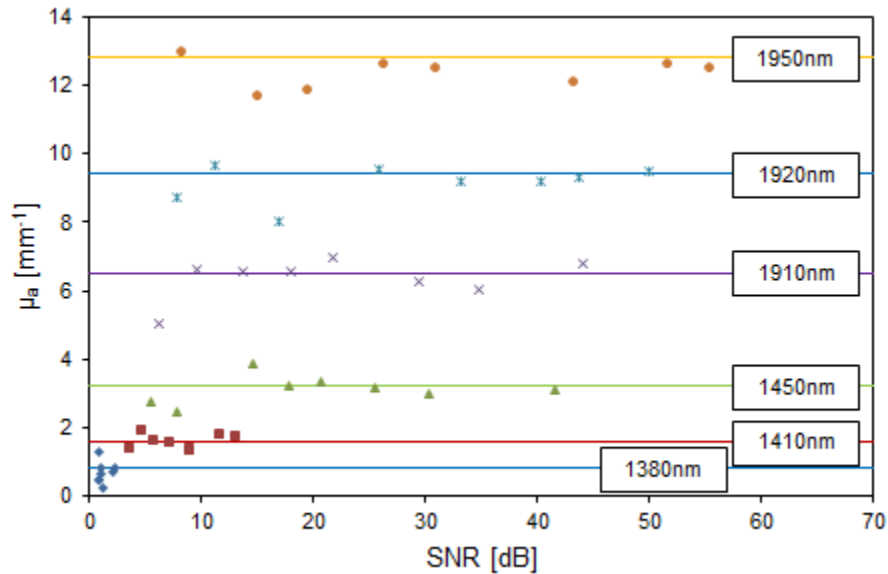


Figure 3-15: μ_a versus SNR measured using water irradiated by different wavelength at varying fluences. These wavelengths were chosen in order to gain different values of μ_a in the range of 1-13 mm^{-1} . The solid lines are the true μ_a values measured using the spectrophotometer. The symbols are the measured values at a specific wavelength and fluence.

The μ_a values measured using the PA spectroscopy are, apart from some outliers, generally in good agreement with the true values obtained using transmission spectroscopy. However, with decreasing SNR the spread around the true value increases. The values of μ_a measured with SNR >20 dB show deviations from the true value of less than 6%, whilst the deviation increases to up to 19% for SNRs between 4 dB and 20 dB. μ_a readings at SNR lower than 4 dB become unreliable and the spread from the true value exceeds 70% for some of the data points. Therefore it can be concluded, that the minimum required SNR for the determination of μ_a with reasonable accuracy is >4 dB. This also explains the deviation of the μ_a spectrum measured using the PA spectroscopy from the transmission spectrum around 1700 nm where the absorption of water is low as shown in Figure 3-14. However, it does not explain the discrepancy in the 1930-1980 nm range shown in Figure 3-14 since the SNR is high in this wavelength range due to strong absorption. In order to investigate this more comprehensively, the measurements were repeated using an organic dye (IR 820) which provides a greater range of μ_a than water. The dye was dissolved in deionised water at concentrations to gain solutions exhibiting μ_a between 0.01 and 42 mm^{-1} at its absorption peak at 820 nm. The μ_a and the PA amplitude were measured using the PA spectroscopy and the results plotted versus the μ_a calculated from literature values using $\mu_a = \epsilon c^{-1}$ with $\epsilon_{820\text{nm}} = 2.3 \cdot 10^5 \text{ cm}^{-1}\text{M}^{-1}$. The results are shown in Figure 3-16. Figure 3-17 shows the deviation of μ_a and the PA amplitude values measured using the PA spectroscopy compared to the values based on the known ϵ .

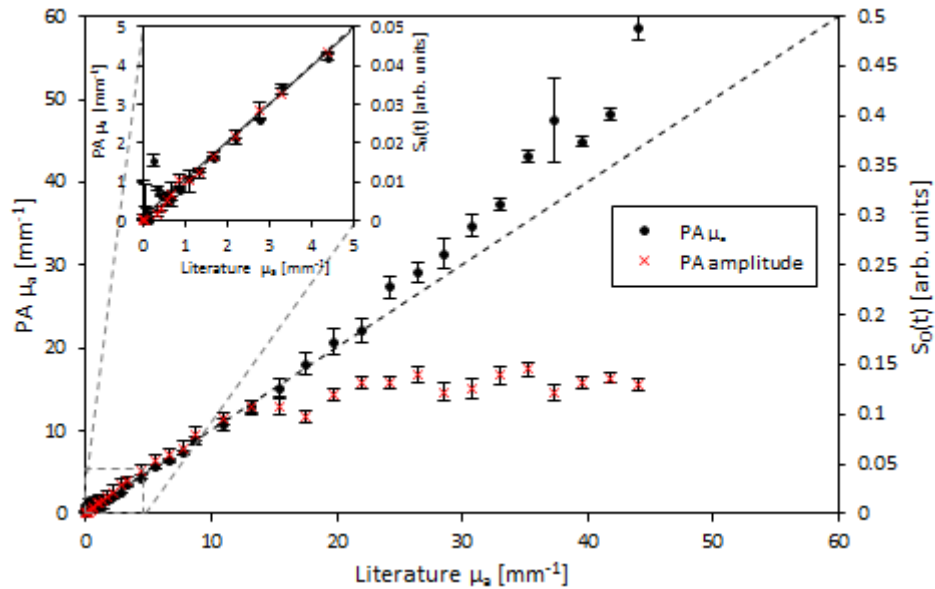


Figure 3-16: μ_a (black dots) and PA amplitude (red crosses) measured using the PA spectroscopie versus μ_a based on the known ϵ of IR 820 at its absorption maxima ($\epsilon(820 \text{ nm}) = 2.3 \cdot 10^5 \text{ M}^{-1} \text{ cm}^{-1}$). The inset on the top left is a zoom into the area indicated by the grey dashed box.

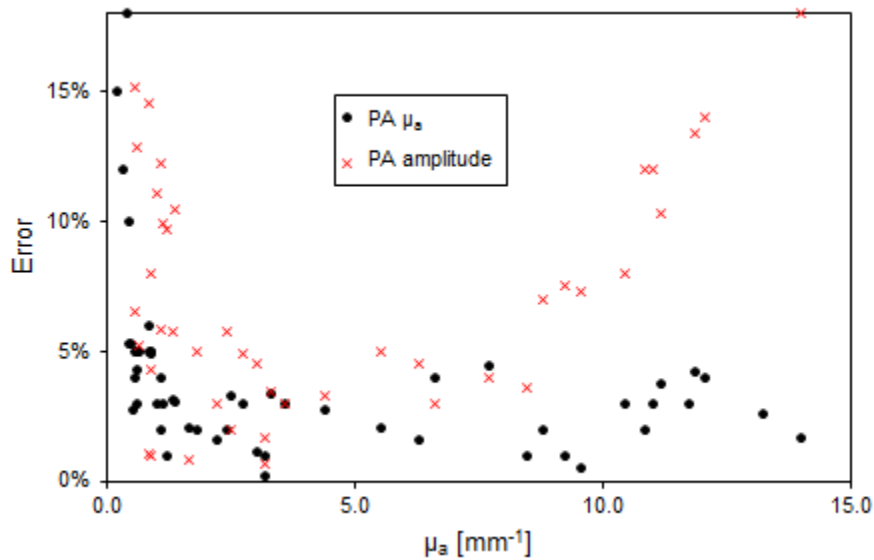


Figure 3-17: Error in % of μ_a and the PA amplitude measured compared to the calculated values over the μ_a .

Figure 3-16 shows good agreement between the μ_a measured using the PA spectroscopie and the literature values up to about 25 mm^{-1} . In the range $0.5\text{-}22 \text{ mm}^{-1}$ μ_a measurements are accurate to about 5% and show standard deviations of less than 5%. The deviation of the measured μ_a from the μ_a calculated from the literature values outside of the μ_a range of 0.5-

22 mm^{-1} increases to up to 35%. The results shown in Figure 3-16 and Figure 3-17 indicate a lower detection limit of about 0.5 mm^{-1} and an upper detection limit of 10 mm^{-1} for the PA amplitude measurements with deviations of less than 5% compared to the trend of the literature values.

As mentioned previously, the upper detection limit of the PA amplitude measurements is thought to be due to the limited bandwidth of the ultrasound transducer used. To test this hypothesis the measurements were repeated using Fabry-Perot sensors with significantly larger bandwidths than the PVDF sensor. Two Fabry-Perot sensors were used. One had a bandwidth of 200 MHz the other 60 MHz. The results are shown in Figure 3-18.

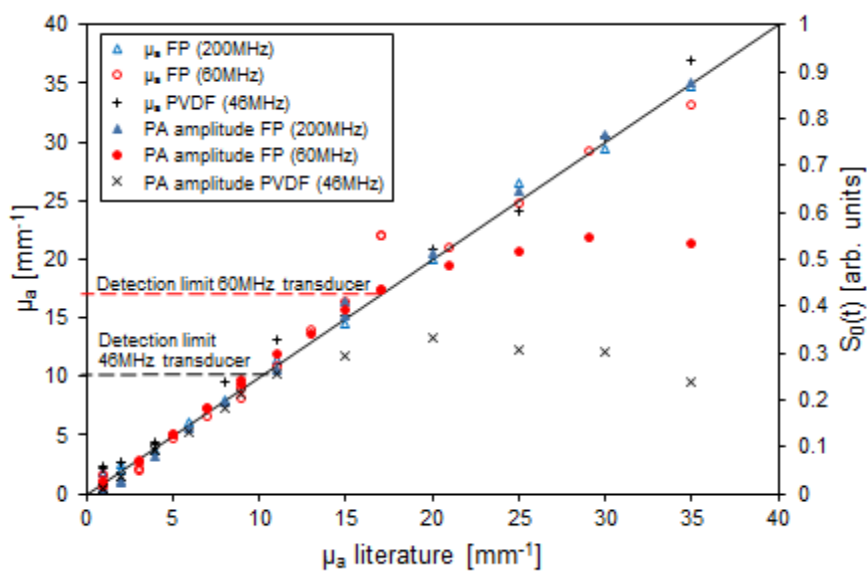


Figure 3-18: Comparison between Fabry-Perot sensors (200 MHz and 60 MHz) and the PVDF ultrasound transducer. The dashed horizontal lines indicate the upper detection limits for the PA amplitude measurements for the PVDF transducer and the $40 \mu\text{m}$ thick Fabry-Perot transducer.

The resulting PA amplitude and μ_a values obtained using the broad band (200 MHz) Fabry-Perot sensor are in good agreement with the literature values and follow the expected linear trend throughout the whole measurement range. However, the PA amplitude measured using the Fabry-Perot sensor with an estimated bandwidth of 60 MHz and the PVDF transducer show deviations from the expected linear trend and start to under-read at 18 mm^{-1} and 11 mm^{-1} , respectively. This discovery points towards insufficient bandwidth of the PVDF-transducer (and 60 MHz Fabry-Perot sensor) failing to accurately detect the high frequency content generated at high μ_a , leading to the under-reading of $S_0(t)$ when succeeding $\mu_a = 11 \text{ mm}^{-1}$. The detection limits of μ_a and the PA amplitude using the PA spectroscope described above are summarised in Table 3-2.

Table 3-2: Detection limit of the PA spectroscope.

Measurement type	Range of detection	Accuracy	Resolution
PA μ_a	0.5-25 mm ⁻¹	+/-5%	+/-3%
PA amplitude	0.5-10 mm ⁻¹	+/-5%	+/-8%

After showing the ability to accurately determining the PA amplitude and μ_a within the detection range stated above the ability to estimate E_t from time resolved PA signals generated using the PA spectroscope was analysed and validated. The results are described in the following section.

3.3.3 Determination of the thermalisation efficiency

Using PA spectroscopy for the purpose of determining the efficiency of an absorbing compound to generate heat requires a reference measurement. Two methods - one self-referencing and one requiring a reference absorber - for the determination of E_t are described and validated below. A light absorbing compound dissolved in a solvent at concentrations sufficient for accurate detection using the PA spectroscope is an example of a sample solution and the pure solvent can be used for the reference measurement.

3.3.3.1 Reference-absorber method

In order to obtain E_t an approach in which two PA signals are acquired is used. One signal is generated in the sample of interest and the other is generated in a reference absorber of known E_t and Γ . The peak amplitude of the signal generated in the sample at t_0 is given by

$$S_{0,s} = \Phi_0 \mu_{a,s} E_{t,s} \Gamma_s K \quad \text{Equation 3-7}$$

For the reference the signal peak amplitude at t_0 is given by

$$S_{0,r} = \Phi_0 \mu_{a,r} E_{t,r} \Gamma_r K \quad \text{Equation 3-8}$$

Symbols indexed by the letter r refer to reference measurements whilst symbols indexed by the letter s refer to sample measurements. It is assumed that the values of Φ_0 and K are the same for both measurements and thus cancel out when the ratio of the two signal amplitudes is taken

$$\frac{S_{0,s}}{S_{0,r}} = \frac{\mu_{a,s} E_{t,s} \Gamma_s}{\mu_{a,r} E_{t,r} \Gamma_r} \quad \text{Equation 3-9}$$

Rearranging Equation 3-9 allows calculating $E_{t,s}$ via:

$$E_{t,s} = \frac{S_{0,s}/\mu_{a,s}}{S_{0,r}/\mu_{a,r}} \frac{E_{t,r}\Gamma_r}{\Gamma_s} \quad \text{Equation 3-10}$$

Providing $E_{t,r}$, Γ_r and Γ_s are known, $E_{t,s}$ can therefore be obtained from Equation 3-10 by measuring the PA amplitudes and μ_a of both sample and reference signals using the PA spectroscope. In this study, water was used as a reference absorber because it is known to exhibit only non-radiative relaxation pathways and therefore $E_{t,r} = 1$ can be assumed. In addition Γ_r can be calculated from the known thermodynamic properties of water and the value of $\Gamma_{\text{H}_2\text{O}}=0.12$ is stated in the literature¹⁴¹.

3.3.3.2 Self-referencing method

For the method described above, knowledge of Γ_s is still required. In some cases it can be assumed to be known. For example if the sample comprises a small amount of dye dissolved in a solvent such as water or methanol to form a weakly concentrated solution, Γ_s can reasonably be assumed to be that of the solvent and calculated from its thermodynamic properties providing they are known. For many solvents, such as water or methanol, they are. However, in other cases, for example a highly concentrated dye or salt solution, Γ may have been modified by the presence of the solute to the extent that it is significantly different from that of the solvent. In these cases, either an independent measure of Γ_s is required or the following approach which obviates the need for knowing Γ_s can be employed. The method is termed self-referencing method because the reference signal can be acquired by simply tuning the laser wavelength to the absorption peak of the solvent and therefore both of the required signals can be obtained without changing the sample. This self-referencing method requires that there is a wavelength λ_0 at which the absorption of the sample chromophore is negligible but significant in the solvent. At λ_0 , E_t is therefore that of the solvent (since only it absorbs at this wavelength) and denoted $E'_{t,s}$ whereas Γ remains that of the sample:

$$S_{0,s}(\lambda_0) = \Phi_0 \mu_{a,s}(\lambda_0) E'_{t,s} \Gamma_s K \quad \text{Equation 3-11}$$

The measurement at λ_0 acts as a reference measurement, in line with Equation 3-8, but eliminating the need to replace the sample with the reference absorber. By taking the ratio of Equation 3-11 and Equation 3-7, not only do Φ_0 and K cancel but so too does Γ_s since it is the same for both measurements. $E_{t,s}$ is therefore given by

$$E_{t,s} = \frac{S_{0,s} \mu_{a,s}(\lambda_0)}{S_{0,s}(\lambda_0) \mu_{a,s}} E'_{t,s} \quad \text{Equation 3-12}$$

Note of course that this approach requires knowledge of the E_t of the solvent. However, in the case of many commonly used solvents, such as water, methanol or ethanol which do not exhibit radiative relaxation, this can be assumed to be unity. The advantage of this approach is that

there is no requirement to know Γ and the two measurements can be made simply by changing the wavelength. There is therefore no requirement to remove the sample from the cuvette and replace it with a reference absorber which may introduce errors if the alignment of the cuvette that contains the sample changes between the two experiments.

3.3.3.3 Validation

Both methods were validated using solutions of absorbers with known E_t . Therefore, in the first instance, the rhodamine B and rhodamine 6G were analysed. The two rhodamine dyes were used because they exhibit concentration dependant radiative relaxation and have been well characterised previously. Therefore, E_t of rhodamine B dissolved in methanol and rhodamine 6G dissolved in water was calculated, using the two methods described above and the results were compared to literature values of Φ_f via $E_t = 1 - \Phi_f$ where Φ_f is the fluorescence quantum yield. For the reference measurement using a sample dissolved in methanol $\lambda_0 = 1550$ nm was chosen whilst $\lambda_0 = 1400$ nm was chosen for samples dissolved in water. The signals of rhodamine b and rhodamine 6G were acquired at λ_{max} at 550 nm and 520 nm, respectively. The resulting values of E_t were converted to Φ_f values and plotted in Figure 3-20. Figure 3-19 shows a plot of PA signals generated in two different dyes at different concentrations which results in different values of E_t . IR 780 has a concentration independent E_t of 100% and was included in the figure for comparison.

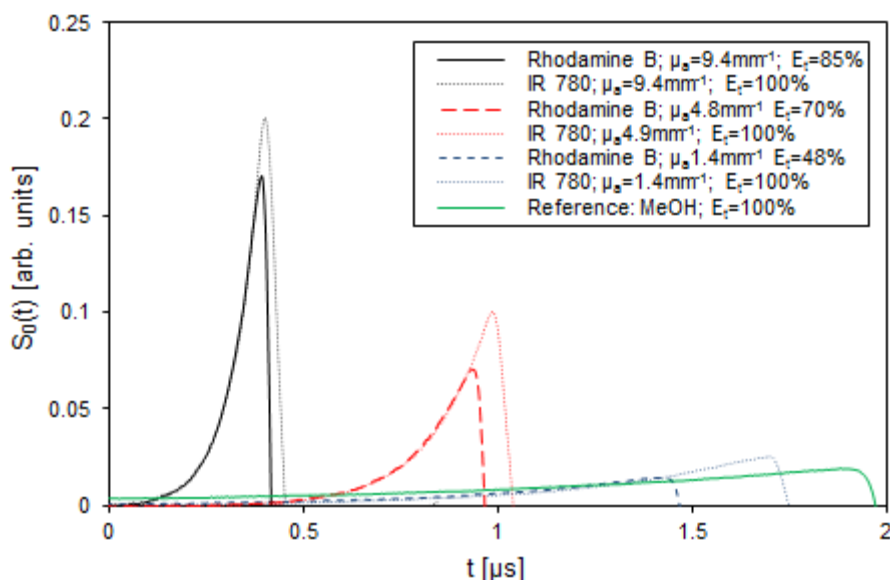


Figure 3-19: Comparison between signals generated by rhodamine B at different concentrations, yielding E_t values between 48% and 85%, and methanol (MeOH) at 1550 nm ($E_t = 100\%$). Signals of IR 780 ($E_t \sim 100\%$) at different concentrations were included for comparison.

The PA signals shown in Figure 3-19 demonstrate the decrease of the signal amplitude of three signals acquired in rhodamine B in methanol at different concentrations showing the influence of the changing E_t , in comparison to a chromophore (IR 780) that has a concentration independent E_t of $\sim 100\%$. The chromophore IR 780 was dissolved in methanol at concentrations to gain solutions exhibiting absorption coefficients similar to the absorption coefficient of rhodamine B. In order to show the decreased PA amplitude and to compare the exponential rise, pairs of signals of two chromophores exhibiting similar absorption but different E_t values were overlaid as shown in Figure 3-19. The results show that the PA amplitude of the signals generated using rhodamine B is decreased compared to the amplitude of the signals generated using IR 780. This discrepancy is caused by the reduced E_t of rhodamine B compared to IR 780. Examining the relative difference of the PA amplitude of rhodamine B and IR 780 at a given absorption coefficient reveals its correlation with E_t . For example the maximum PA amplitude of rhodamine B with $\mu_a = 9.5 \text{ mm}^{-1}$ and $E_t = 85\%$ compared to IR 780 ($\mu_a = 9.6 \text{ mm}^{-1}$; $E_t \sim 100\%$) is reduced by about 15%, whilst the PA amplitude of rhodamine B with $\mu_a = 1.43 \text{ mm}^{-1}$ and $E_t = 48\%$ compared to IR 780 ($\mu_a = 1.45 \text{ mm}^{-1}$; $E_t = 100\%$) is reduced by about half.

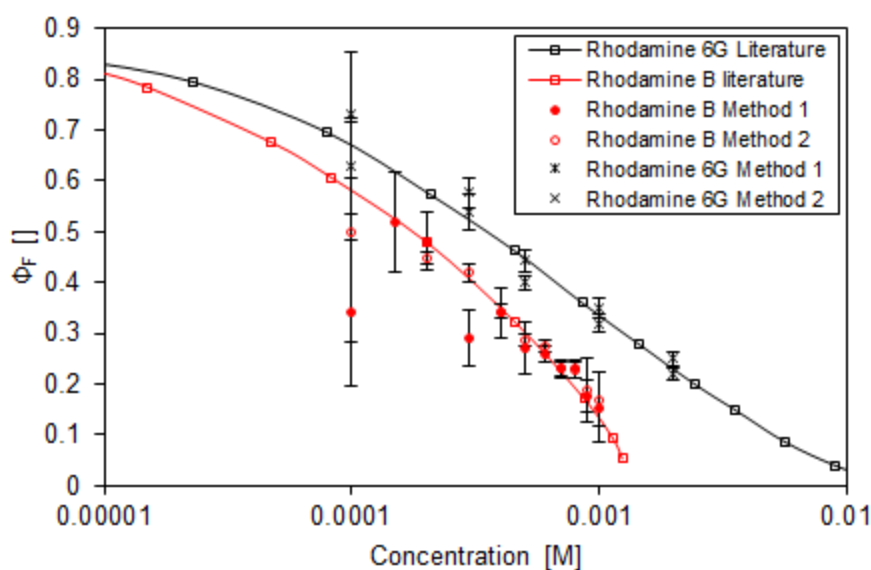


Figure 3-20: Φ_F of rhodamine B (red circles) and rhodamine 6G (black stars and crosses) versus the concentration, estimated using the reference-absorber method (method 1) and the self-referencing method (method 2). Literature values are plotted for comparison (lines with squares). The error bars are the standard deviation of five measurements.

To show the dependence of E_t on concentrations more comprehensively, measurements were made at various concentrations using method 1 (using a reference absorber) and method 2 (self-referencing method) and compared to literature values. As shown in Figure 3-20 E_t values measured using both methods are in close agreement (error $<5\%$; standard deviation $<5\%$) with literature values up to Φ_f of about 0.55. The points at 100 μM (with literature values of $\Phi_f = 0.59$ for rhodamine B and $\Phi_f = 0.68$ for rhodamine 6G) show much greater error and standard

deviation, especially for the method relying on a reference measurement in the pure solvent, method 1. The increased error is due to low SNR, which is caused by a combination of high Φ_t (=low E_t) and the low absorption of the diluted solution.

The experiments using the two rhodamine dyes successfully demonstrated the ability to quantify E_t . The next section discusses the method used for the estimation of Γ .

3.3.4 Determination of the Grüneisen coefficient

The dual wavelength method for the determination of E_t can also be used to estimate Γ of the sample solution, although this still requires a second measurement in a reference absorber such as water. This necessitates knowledge of the thermalisation efficiency of the solvent $E'_{t,s}$. However, as stated above this is often known and in the case of common solvents such as water or methanol it is equal to one. If $E_{t,s} = E_{t,r}$ can be assumed to be known, the Grüneisen coefficient of a sample solution Γ_s can be calculated using Equation 3-13. A light absorbing compound dissolved in a solvent at concentrations sufficient for accurate detection using the PA spectroscope is an example of a sample solution and the pure solvent can be used for the reference measurement.

$$\Gamma_s = \frac{S_{0,s}/\mu_{a,s}}{S_{0,r}/\mu_{a,r}} \Gamma_r \quad \text{Equation 3-13}$$

3.3.4.1 Validation

In order to show the ability of the method for determining Γ , the two solvents ethanol and methanol were used because their E_t can reasonably be assumed to be 100%. In addition, Γ of pure methanol and ethanol can be obtained using thermodynamic data found in literature via

$$\Gamma = \frac{\beta c_s^2}{c_p} \quad \text{Equation 3-14}$$

where β is volume thermal expansion coefficient, c_s is the sound speed and c_p is the heat capacity at constant pressure. In order to form solutions of different Γ the alcohols were mixed with water at various concentrations and Γ of the mixtures and the pure solutions was determined using Equation 3-13. For the comparison, Γ of the pure alcohols was calculated using thermodynamic data and Equation 3-14. The value of $\Gamma = 0.12$ for water was taken from literature¹⁴¹. Figure 3-21 shows the results of the Γ measurements of the pure and the diluted alcohol/water mixtures.

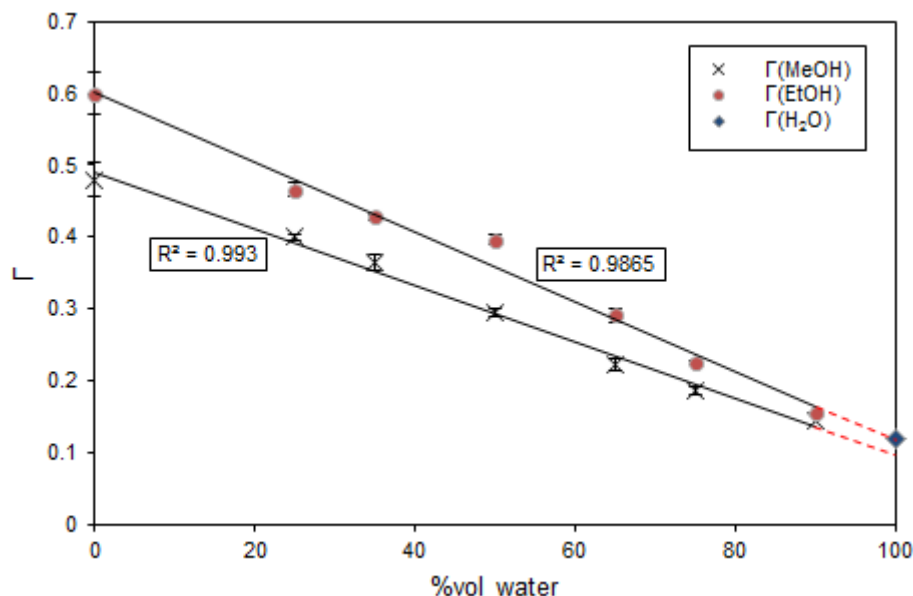


Figure 3-21: Γ versus %vol. of water in methanol and ethanol. The black lines represent the linear trend of the two alcohol/water mixtures, with variances of $R^2 = 0.993$ for methanol/water and $R^2 = 0.9865$ for ethanol/water. The dashed red lines are an extension of the linear trend lines.

Figure 3-21 shows a decrease of the measured Γ values of methanol and ethanol with increasing water content. The measured values of Γ follow a linear trend with high correlation ($R^2 = 0.993$ and $R^2 = 0.9865$ for methanol and ethanol respectively) and show standard deviations of less than 5% throughout the whole measurement range. Extending the lines of the linear trend towards a water content of 100%, as demonstrated by the dashed red lines in Figure 3-21, shows that both lines intercept roughly with the literature value of water at about $\Gamma = 0.12$. The discrepancy of the extended trend line of methanol from the literature value is due to measurement errors. The measured and calculated values of Γ for the pure alcohols are in close agreement with the values calculated using Equation 3-14: 0.47 (+/- 4%) and 0.48 for methanol and 0.60 (+/- 2%) and 0.61 for ethanol. These results show, that the method proposed allows the accurate determination of Γ of liquids such as methanol and ethanol. Furthermore, if a linear trend of Γ of mixtures of the alcohol with varying water content can be assumed, the method enables the estimation of Γ of mixtures of liquids.

3.3.5 Determination of photobleaching profiles

The ability of the PA spectroscope to record the photobleaching profile of sample chromophores under laser irradiation was verified using an organic dye. Irradiating an organic dye with light of a specific wavelength excites an electron, inducing a singlet state of the molecule. The molecule reaches the triplet state via intersystem crossing, reversing the spin of the excited electron. Photobleaching can occur from both of these states (singlet and triplet state) due the enhanced reactivity of excited molecules and results in either a structural change of the molecule due to a

chemical reaction or a change in the electronic structure of the molecule. In order to test the ability of the PA spectroscope to record the photobleaching characteristics of organic dyes, a sample was prepared by dissolving an organic dye (rhodamine B) in deionised water at a concentration of 0.6mM. For the measurements the samples were continuously irradiated ($18 \cdot 10^3$ laser pulses; pulse length < 8 ns; PRF = 10 Hz) with laser light with wavelength matching the peak absorption of the sample (550 nm). PA signals were recorded at regular intervals and averaged over 30 laser pulses. To avoid evaporation of the solvent, the photobleaching experiments were performed using an enclosed cuvette as shown in Figure 3-3c. The PA amplitude plotted over the number of laser pulses received by the sample solution shows the photobleaching profile of the rhodamine B sample (see Figure 3-22).

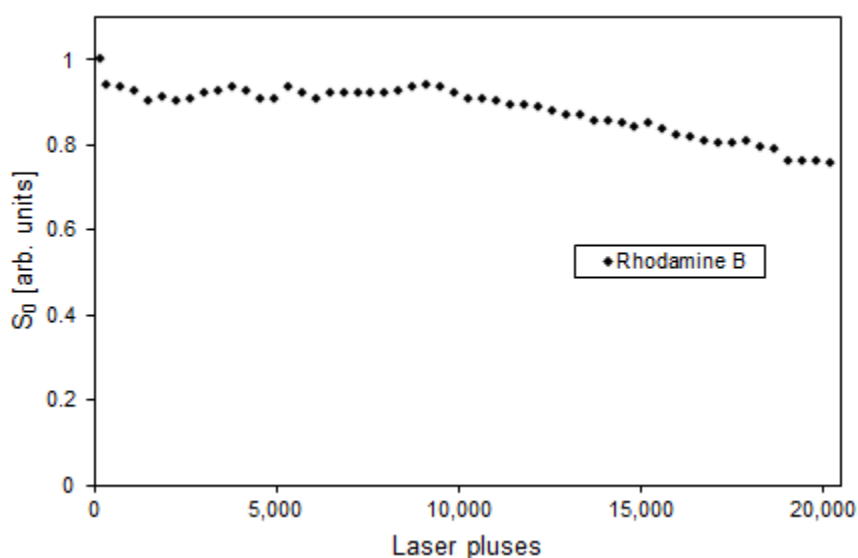


Figure 3-22: Photobleaching characteristic of rhodamine B, irradiated over 20,000 laser pulses with a wavelength of 550 nm.

The photobleaching profile of rhodamine B measured by irradiating the sample with about 20,000 laser pulses is shown in Figure 3-22. The photobleaching profile of the sample shows a constant decrease of the PA amplitude, losing about 25% of the initial signal amplitude. This initial test shows that it is possible to investigate the photobleaching profile of chromophores using the PA spectroscope.

3.4 Conclusion

In summary, a PA spectroscope in combination with the methods proposed enables to comprehensively analyse the parameters involved in the PA signal generation process, therefore fulfilling aim (i) and (ii) stated in Section 1.3. Using the methods proposed allows for the analysis of μ_a , E_t and Γ as well as the PA amplitude and μ_a spectra and the photostability of

a chromophore. Consequently, the PA spectroscopy and the methods proposed are a useful tool for the identification of the most promising chromophores for the application as contrast agent for molecular PA imaging. The highlights and key findings of the individual sections of this chapter are summarised below.

The first part of this chapter provides a detailed description of the PA spectroscopy used throughout this thesis. This includes the thorough description of the individual components of the PA spectroscopy, their fabrication and the analysis of their limitations. The results of the analysis of the limitations of the PVDF transducer show, that using a PVDF film of a thickness of 52 μm and a side length of 10 mm, a -3 dB bandwidth of 23 MHz and a NEP of 1.9 kPa over 20 MHz can be achieved. Based on a simple estimation, the PVDF transducer analysed has the potential to detect PA signals of up to 15 mm^{-1} without excessively bandlimiting the signal. However, the directivity measurements demonstrated the importance of the alignment of the acoustic source and the ultrasound transducer.

At the beginning of the second part of this chapter the limitations of the PA spectroscopy to determine the PA amplitude and μ_a spectra was analysed. The results show, that in a range from 0.5 mm^{-1} to 25 mm^{-1} the μ_a can be determined with an accuracy of +/- 5% and a resolution of +/-3%, whilst the measurements of the PA amplitude get bandlimited and therefore the detection range has a reduced upper detection limit of 10 mm^{-1} with the same accuracy and a resolution of 8%. The results are summarised in Table 3-2. The results are encouraging, showing that the apparatus exhibits a sufficient dynamic range and accuracy for the measurement of PA amplitude and μ_a spectra of solutions of light absorbing compounds. Even though the detection range (0.5-10 mm^{-1}) corresponds to concentrations of contrast agents significantly higher in many cases than used in a typical in vivo situation, the PA spectroscopy measurements provide valuable information about their ability to generate PA signals.

After describing the limitations of the PA spectroscopy to determine the PA amplitude and μ_a , methods for the full analysis of the PA signal generation of light absorbing compounds were proposed and validated. In the first instance two methods, for the analysis of the thermalisation of the absorbed light energy (E_t) using the PA spectroscopy were demonstrated. The results of the E_t measurements indicate that E_t values as low as 50% can be analysed. The accuracy of the measurements was found to be about 5%, given that the detection limits of the PA spectroscopy were met. The methods pose a useful tool for the characterisation of contrast agents for PA imaging. However, the methods also have the potential to have an impact on other fields of application, for example the determination of E_t of organic dyes, nanoparticles or quantum dots exhibiting strong absorption, which are difficult to analyse using conventional techniques such as optical fluorescence spectroscopy, due to errors introduced by reabsorption of the emitted light.

In the next part of this chapter a method for the determination of Γ was described and validated using mixtures of alcohol (methanol and ethanol) in water. The results are in good agreement with the expected values and the literature, with an accuracy <4% and therefore demonstrate the feasibility of the method.

Lastly the ability of the PA spectroscopy to record the photobleaching profile of chromophores was demonstrated using a solution of rhodamine B.

Overall the PA spectroscopy exhibits a sufficient range of detection, with high resolution and accuracy, for the generation of PA amplitude and μ_a spectra of organic dyes and nanoparticles. Using the methods in combination with a PA spectroscopy allows determining the parameters involved in the PA signal generation μ_a , E_t and Γ as well as the photostability of a compound. Therefore the PA spectroscopy allows to fully analyse compounds for their ability to generate PA signals and determine their usefulness as contrast agents for molecular PA imaging.

Chapter 4

Characterisation of contrast agents

4.1 Introduction

In the recent past, numerous light absorbing materials have been proposed as contrast agent for molecular PA imaging. Their potential to generate PA contrast is frequently evaluated using purely optical methods such as absorption spectroscopy. This practice however fails to account for relevant thermodynamic properties involved in the PA signal generation process, such as E_t and Γ . An example pronouncing the importance of the analysis of the PA signal generation process is gold nanoparticles with different surface coatings, which exhibit significantly different PA signal amplitudes upon excitation even though their optical properties are identical. This chapter aims to analyse a number of potential PA contrast agents more thoroughly, using the PA spectroscopy. This work will help identifying the suitable contrast agents for the purpose of molecular PA imaging. The analysis using the PA spectroscopy is limited to the evaluation of the parameters involved in the PA signal generation process and therefore the selection of contrast agents is only based on the strength of the PA signal they are likely to generate *in vivo*. For a successful application of a contrast agent other factors also need to be considered, such as biocompatibility, toxicity, size, morphology, surface charge etc., which is beyond the scope of this work.

For the analysis methods were employed evaluating the PA amplitude and μ_a spectrum as well as quantifying ϵ , E_t , Γ and the photostability of the samples as described in Chapter 3. In addition, the samples were analysed using transmission spectroscopy. In order to determine size, morphology and stability a selection of the nanoparticles was analysed using TEM, DLS and ζ -potential measurements. The samples analysed include commercially available organic

dyes and nanoparticles such as gold nanorods and carbon nanotubes as well as various home-made semiconducting polymeric nanoparticles. As described earlier in this thesis, various optical and thermodynamic effects can influence the ability of a compound to generate a PA signal, demonstrating the necessity of determining all the parameters involved in the PA signal generation process when analysing PA contrast agents. A good example for this is the significantly increased PA signal amplitude of gold nanoparticles with identical optical properties but different surface coatings¹. In order to identify effects altering the ability to generate PA signals the nanoparticles, especially the semiconducting polymeric nanoparticles, were chosen for the analysis using the PA spectroscope. This analysis might help understanding the PA signal generation process of nanoparticulated contrast agents in more detail.

After listing the materials used, the following chapter details the results of the individual measurements performed with the aim of finding materials exhibiting strong PA signal generation. Initially the determination of the particles size, morphology, polydispersity as well as the ζ -potential of the nanoparticulated samples prepared is detailed. Subsequently, the results of the optical and PA spectra, ϵ , E_t , Γ and photostability measurements of all the various organic dyes and nanoparticles are presented. The chapter concludes with the identification of a selection of compounds exhibiting strong PA signal generation and therefore have the potential to be applied as contrast agent for molecular PA imaging. This identification is based exclusively on the ability of the samples to generate strong PA signals, rather than any other properties such as biocompatibility or size.

4.2 Materials

Chromophores used in this chapter were chosen for their potential use as contrast agent for *in vivo* PA imaging. Carbon nanotubes, methylene blue, fluorescein, cresyl violet, rhodamine b, rhodamine 6G, IR 780, IR 820 as well as the solvents ethanol, methanol and dimethyl sulfoxide were purchased from Sigma Aldrich (UK). Gold nanorods were purchased from Nanopartz (USA), BHQ-3 from Biosearch Technologies (USA), Dylight800 from Thermo Scientific (UK), QXL680 from AnaSpec Eurogentec Inc. (USA). The polypyrrole sample was received from a collaborating research group (Dr. Steve Matcher; Sheffield University). The organic dyes, nanoparticles and solvents have been used without any purification before use. The organic dyes were weight in and mixed with a solvent to gain the desired concentration. The liquid gold nanorod and polypyrrole sample were diluted using deionised water. The procedure to gain stable solutions of carbon nanotubes is described in the appendix. Polymeric nanoparticles based on PCPDBT were synthesised as described in ¹¹⁸ and the appendix. The polymeric nanoparticles based on based on diketopyrrolopyrrole (DPPTT-T and DPPTT-S) or Indolophthalazine-6,13-dione thiophene (INDT-T, INDT-S and INDT-BT) used throughout this study were synthesized and purified as described in the next part. Figure 4-1 shows the chemical

structure and an image of the coloured solutions of a selection of chromophores. A full list of contrast agents analysed is provided in Table 4-1.

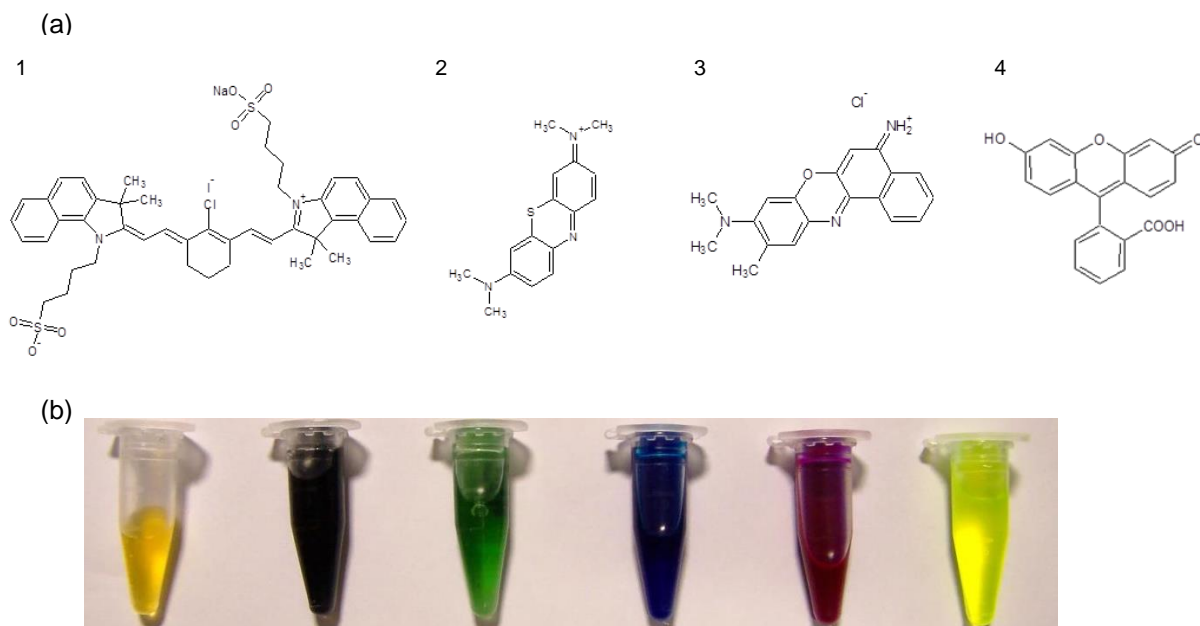


Figure 4-1: (a) Chemical structure of IR 820 (1), methylene blue (2), cresyl violet (3) and fluorescein (4). (b) Image of a selection of nanoparticles and organic dyes within sample containers. From left to right the sample containers are filled with gold nanorods, carbon nanotubes, IR 820, methylene blue, cresyl violet and fluorescein solutions.

Table 4-1: List of contrast agents analysed.

Contrast agent	λ_{\max}	Contrast agent	λ_{\max}
Carbon nanotubes	450	IRDye800CW	780
Fluorescein	490	DPPTT-S	780
Cresyl violet	590	INDT-T	780
Methylene blue	610	INDT-S	790
QXL 680	670	Gold nanorods	800
BHQ-3	670	INDT-BT	800
PCPDTBT	700	IR-820	810
IR-780	760	DPPTT-T	810
Dylight 800	770	Polypyrrole	1300

4.2.1.1 Preparation of DPPTT-T, DPPTT-S, IND-T-BT, IND-T-S and IND-T-T nanoparticles via miniemulsion

Polymers based on diketopyrrolopyrrole (such as DPPTT-T and DPPTT-S; the chemical structures are shown at the bottom in Figure 4-2) or Indolo-naphthyridine-6,13-dione thiophene (such as IND-T-T, IND-T-S and IND-T-BT; the chemical structures are shown at the top in Figure 4-2) have little solubility in any other organic solvent than dichloromethane (CHCl_2) and chloroform (CHCl_3). All of the polymers were synthesised in house and provided by Dr. Hugo Bronstein (UCL, Department of Chemistry). The synthesis of the diketopyrrolopyrrole based polymers can be found in ¹⁴² and the synthesis of the IND-T-S can be found in ¹⁴³. The synthesis of IND-T-T and IND-T-BT will be reported elsewhere.

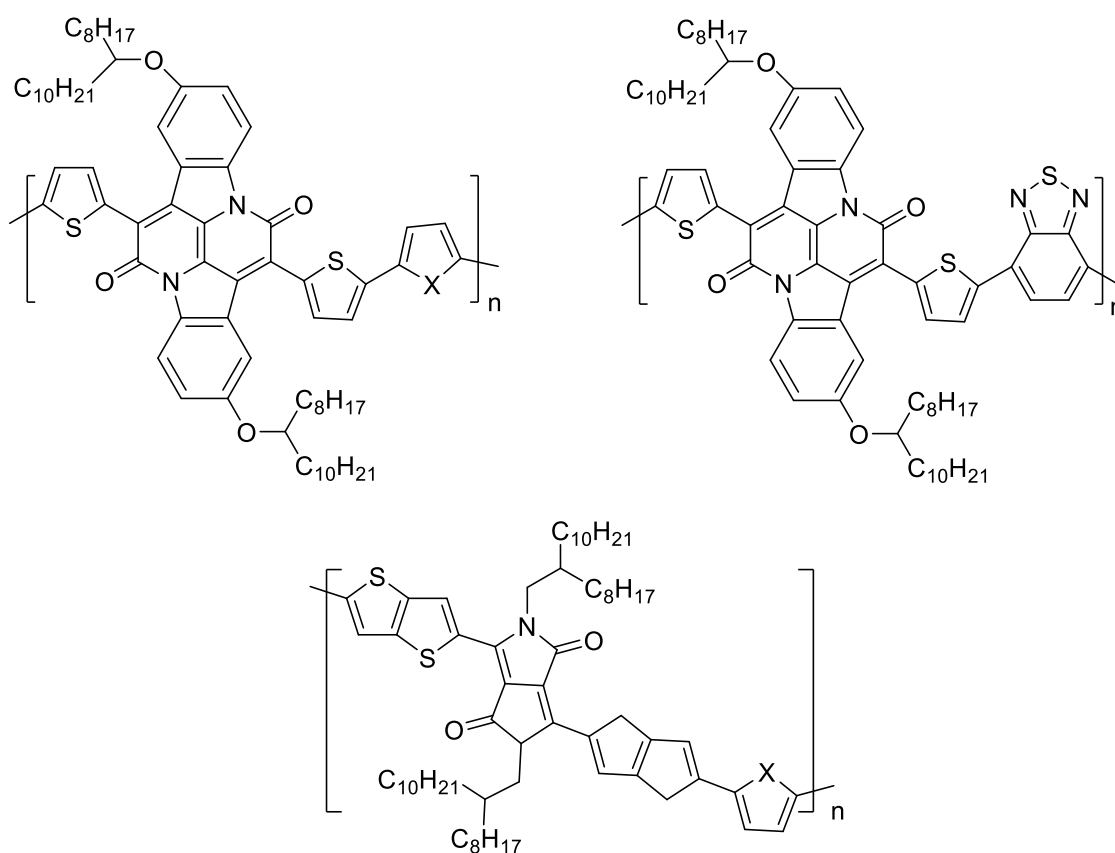


Figure 4-2: Chemical structure of semiconducting polymers. Top left: IND-T-T: X=S; IND-T-S: X=Se; Top right: IND-T-BT; Bottom: DPPTT-T: X=S; DPPTT-S: X=Se.

Due to the low solubility of these organic solvents in water a different procedure for the formation of nanoparticles was applied, called miniemulsion. Therefore, 2.5 mg of DPPC were dispersed in 2.5 mL of deionised water and vortexed for 1min before the mixture was sonicated for about 3 min in a sonicator bath. The polymers (DPPTT-T, DPPTT-S, IND-T-BT, IND-T-S and IND-T-T) were dissolved in CHCl_3 to obtain a final concentration of 0.6 gL^{-1} of each of the polymers in the organic solvent. To ensure the full solvation of the polymers, each of the polymer mixtures was heated to reflux to obtain green (DPPTT-T and DPPTT-S) to dark blue

(INDT-T, INDT-S and INDT-BT) solutions. Subsequently, 160 μL of one of the dissolved polymers was pre-emulsified in the aqueous surfactant mixture by stirring with a magnetic stirrer for 5 min at 1000 rpm. Next, the emulsion was subjected to high power sonication (10 W RMS) for 30 s using a probe sonicator. After formation of the miniemulsion, the power output of the probe sonicator was reduced to 5 W RMS and the mixture subjected to cycles of 30 s sonication and 10 s of resting with the probe sonicator turned off. After about 5 min, the opaque solution begins to clear, resulting in a clear coloured solution. Then, the solution was placed in a water-bath and kept at 60 $^{\circ}\text{C}$ for about 2 h in order to evaporate the remaining organic solvent. Lastly, the aqueous suspension of polymeric nanoparticles was filtered through a 0.22 μm polyethersulfone syringe driven filter and washed three times with deionised water using centrifugal filters with an MWCO of 30 kDa under centrifugation at 4,000 rpm for 3 min at 4 $^{\circ}\text{C}$. After the washing step the nanoparticles were resuspended in deionised water using an ultra-sonication bath.

4.2.1.1.1 Observations

The preparation of the π -conjugated polymeric nanoparticles using the miniemulsion technique results in green-blue dispersions of sizes in the range of 100-250 nm with PDIs varying between 0.2 and 0.3. Heating of mixture via the probe sonicator can lead to premature evaporation of the CHCl_3 before formation of the nanoparticles, causing the separation of the polymer from the dispersion visible as a dark green/blue film at the side of the sample vial. In such case, the sonication was stopped and 160 μL of CHCl_3 were added to the mixture before starting the procedure from the pre-emulsifying step. Due to the low solubility of the polymers used even in chlorinated solvents such as CHCl_3 , careful preparation of the polymer solutions is of great importance for the success for the preparation of the π -conjugated polymeric nanoparticles using the method described. Polymer molecules which are not in solution with the organic solvent will not be present in the nano-sized droplets to form the nanoparticles and are likely to aggregate at the stirrer or the walls of the sample vial. Nanoparticles made from π -conjugated polymeric via miniemulsion prepared with a badly prepared polymer mixture results in a pale green/blue suspension.

4.3 TEM measurements

The imaging modality TEM uses the transition of an electron beam through a thin sample to form an image, which is magnified and focused using electron lenses and visualised using CCD cameras or a fluorescent screen. Using this technique allows to analyse topography, morphology, composition and crystallinity of very small features down to the atomic level with resolutions $<1\text{nm}$. The main components of a TEM are: an electron gun, electron lenses, apertures, electron detectors and a sample holder. For a measurement an electron beam is

generated, using an electron gun, which is directed towards the detector unit. The beam passes through a series of condenser lenses focusing the electron beam onto the sample holder. The sample holder allows inserting a sample grid, containing the sample, into the electron beam path. The sample grid is about 2.5mm in diameter and consists of a fine mesh made from metals such as copper or platinum. In the bright field mode of a TEM, contrast is formed by the absorption of electrons in the sample. Therefore atoms with a higher atomic number and thick samples generate strong contrast and appear dark on the TEM images, whilst atoms of low atomic number and thin samples regions appear bright. After interacting with the sample, the electron beam passes through a series of electron lenses, called the projector lenses, in order to magnify and focus the image onto the detector. Depending on the detector type, images are displayed on a computer screen or a fluorescent screen. During the experiments, the whole electron path is evacuated and kept under vacuum ($\sim 10^{-4}$ Pa) in order to decrease resistance between the cathode and the anode of the electron gun and to avoid collision of electrons with gas molecules, thus increasing the mean free path of the electrons.

For the analysis of the morphology of the nanoparticles via imaging a TEM (JEOL CX100, JOEL, USA) with an accelerating voltage of up to 100 kV and a maximum resolution of 0.2 nm was applied. The TEM is equipped with a fluorescent screen and a photographic camera with 66x231.1 mm² negatives. After developing, the negatives were scanned (2080x7280 pixels) in order to generate digital images. The sample grids were made from copper. The nanoparticles were used without any staining or preparation prior to the application to the sample grids. For the application of the nanoparticles to the grid, a small amount (~ 10 μ L) of a dilute aqueous dispersion of nanoparticles was applied to a sample grid. After application of the samples, the grids were partially covered with a lid and left to stand overnight for the liquid to evaporate. The next day, the dry sample grid was placed in the sample holder using tweezers before the sample holder was placed in vacuum port of the TEM. Examples of the resulting TEM image are shown in Figure 4-3.

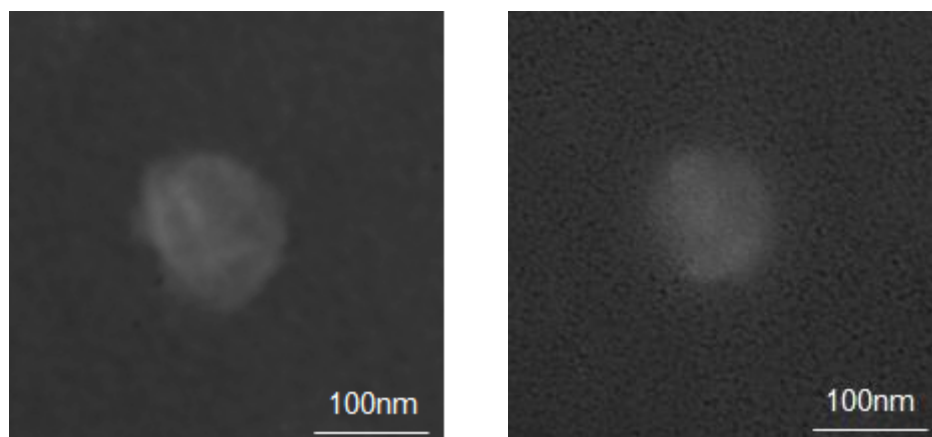


Figure 4-3: TEM images of DPPTT-T (right) and DPPTT-S (left) nanoparticles.

The TEM images generated didn't show great contrast which was expected due to the comparable small atomic weight of the carbon atoms making up the polymers. To gain higher contrast, the particles can be stained using atoms with high atomic weight such as uranium (in the form of uranyl acetate) or tungsten (in the form of methylamine tungstate). However, the results obtained are sufficient to identify an almost spherical shape of the polymeric nanoparticles prepared and to compare the size measured by TEM imaging to the estimation using DLS.

4.4 Dynamic light scattering measurements

DLS is a well-established method for determination of the size and size distribution of molecules and particles sub-micrometre to nanometre in extent. The measurements are based on Rayleigh scattering and the Brownian movement of small particles in solution. In practice, a sample is irradiated by polarized laser light with a specific wavelength, typically 255 nm. The light is scattered by the sample, passes a monochromator and the scattered light pattern is detected dynamically by photo-multipliers. A scattering pattern is formed due to constructive and destructive interference of the scattered light. Analysing the fluctuations of the detected scattering patterns allows generating an autocorrelation function. This autocorrelation function typically decays over time due to decorrelation of the signals caused by the Brownian movement of the particles present in the sample. A population of very small molecules leads, compared to bigger particles, to a faster decorrelation of the scattered intensity, which is due to the increased Brownian movement with decreasing particles size. Therefore, information relating to the time scale of the movement of the particles present in the sample is contained within the scattering intensity fluctuations detected. The correlation function extracted from the scattering intensity fluctuations typically shows an exponential decay which is related to the motion of the particles and thus to their size. In the case of a monodisperse sample the decay is a single exponential, however in most cases the sample contains particle species of different sizes and thus the autocorrelation function is a sum of the individual exponential decays, each related to the various sizes of the particles. Using the correlation function generated, various mathematical methods have been developed to gain information about size and size-distribution of the particles contained in the sample. The size-distribution is a measure of the heterogeneity of the particle size in a sample and can be expressed by the polydispersity index (PDI).

For the experiments, 10 μL of a nanoparticle sample solution was diluted in a sample cuvette (BRAND disposable PMMA cuvettes, Sigma Aldrich) with about 1 mL distilled water, to gain a colourless homogeneous sample. The preparation of the sample by diluting is critical to avoid particle-particle collisions. In order to remove dust and other artefacts from the water, it was filtered through a syringe filter with a pore size of 230 nm prior to use. DLS and ζ -potential measurements presented in this thesis were performed on a Malvern Zetasizer Nano

(ZSZEN3600, Malvern Instruments Ltd, UK) using a 30 mW laser diode for excitation at 658 nm and a detection angle of 173 °. Each measurement is repeated five times if not quoted otherwise. The cumulant method was used to analyse the generated data and quantify the size and the size distribution of the measured sample. The resulting particle size distribution of some nanoparticles samples are shown in Figure 4-4.

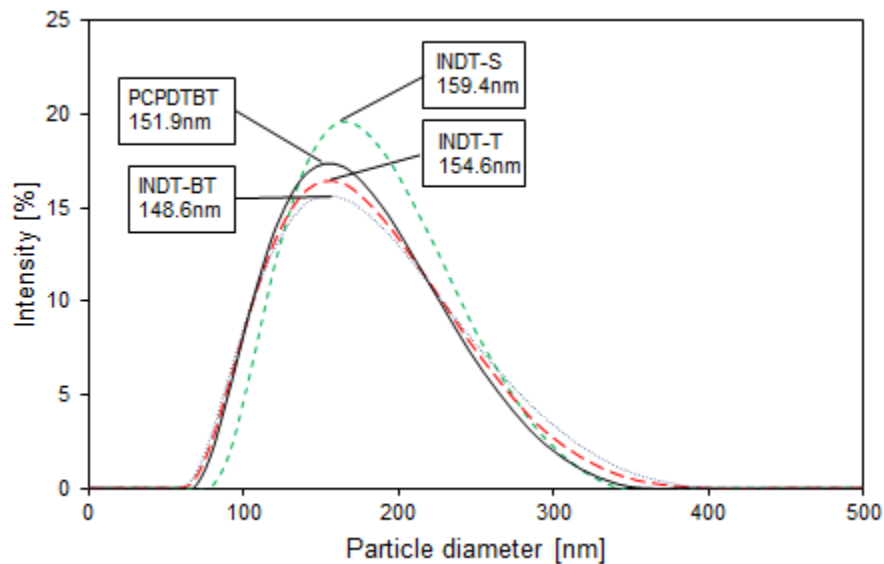


Figure 4-4: Particle size distribution INDT-X and PCPDTBT. The numbers below the labels are the z-average values - the average particle size measured in nm.

Table 4-2 shows the particle diameter and the PDI of various polymeric nanoparticles prepared as described in Chapter 4 of this thesis such as polystyrene nanoparticles (PS), poly (allylamine) nanoparticles (PAA) and the semiconducting polymeric nanoparticles PEDOT:PSS nanoparticles (PEDOT:PSS), PCPDTBT nanoparticles (PCPDTBT), DPPTT-x nanoparticles (DPPTT-S and DPPTT-T) and INDT-x nanoparticles (INDT-S and INDT-T). The measurements were performed as described above and repeated n times with different sample batches.

Table 4-2: Average particle size and PDI of various home-made polymeric nanoparticles. The numbers in brackets are the number of sample batches analysed n, followed by the standard deviation of the average particle size.

Nanoparticle	Particle diameter [nm]	PDI
PS	56 (n=2; +/-1%)	0.07
PAA	183 (n=4; +/-6%)	0.18
PEDOT:PSS	569 (n=2; +/-72%)	0.53
PCPDTBT	151(n=3; +/-5%)	0.18
DPPTT-S	287 (n=2; +/-8%)	0.35
DPPTT-T	236 (n=3; +/-8%)	0.26
INDT-S	159 (n=3; +/-10%)	0.25
INDT-T	154 (n=3; +/-12%)	0.34
INDT-BT	149 (n=3; +/-8%)	0.19

4.5 ζ -potential measurements

In a colloidal dispersion, such as nanoparticles homogeneously dispersed in a solvent, particles may adhere to on another, forming aggregates which precipitate out and under the influence of gravity collect at the bottom of the container. This process is called flocculation. If the density of the aggregates is lower than the density of the solvent, the phases separate and the aggregates collect at the surface of the solvent. This process is called creaming. The ζ -potential is used to optimise formulations of emulsions and suspensions of small particles and gives information about tendencies for aggregation and long term stability. Changing chemical composition or modification of the surface allows adjusting the surface charge of the particle as well as the ζ -potential to gain the desired stability of the colloidal dispersion. The ζ -potential describes the potential difference between the interfacial double layer of particles and the dispersion medium they are contained in, as indicated in Figure 4-5. The potential difference is caused by the electrical charge in the stern layer of the particles and the charged ions in bulk solution.

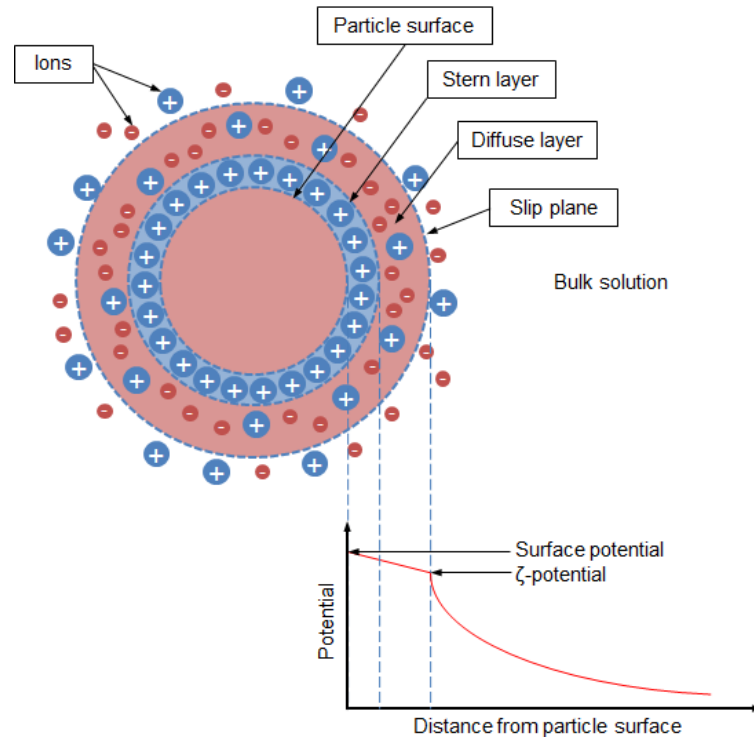


Figure 4-5: Diagram showing an example of a spherical particle, dispersed in solution, surrounded by the various layers of ions (top) and the potential differences as a function of distance from the particle surface.

For the measurement of the ζ -potential of a dispersion, an electric field is applied across the liquid sample. Depending on the ζ -potential the particles in the dispersion migrate towards the electrode of opposite charge, with a velocity proportional to the ζ -potential. The velocity of this movement can be evaluated using electro-phoretic light scattering. Electro-phoretic light scattering is based on dynamic light scattering (see above) and generates a decorrelation function which allows determining the velocity of the movement of particles in suspension. Therefore a laser beam irradiates a sample dispersion contained in an electro-phoresis cell and the scattered light is detected by photo-multipliers. With the knowledge of the viscosity and the dielectric permittivity of the sample the ζ -potential can be calculated from the particle velocity using the Smoluchowski theorem. As mentioned above, the ζ -potential allows predicting the tendency for aggregation and long term stability of colloidal dispersions. Generally, the higher the values of the ζ -potential lead to better long term stability and inhibition of aggregation of small particles contained in the sample dispersion. This is due to increased electrostatic repulsion between the adjacent particles. If the ζ -potential is small between (0 and +/-10 mV), attractive forces may exceed the electrostatic repulsion between the particles, causing them to aggregate.

In practice the ζ -potential measurements were performed using a Malvern Zetasizer Nano (ZSZEN3600, Malvern Instruments Ltd, UK) using a 30 mW laser diode for excitation at 658 nm and a detection angle of 173 °. Samples were prepared by diluting 10 μ L of the sample

suspension with 1 mL of filtered (230 nm syringe filter) deionised water. The samples were injected into a disposable folded capillary cell (DTS1070, Malvern Instruments Ltd, UK). After placing in the sample chamber, the temperature of the sample was adjusted to 24 °C and held constant during the measurements. The results of the ζ -potential measurements of various polymeric nanoparticle samples are shown in Table 4-3. Particle size and PDI of the same samples were measured subsequently to the ζ -potential measurements. The resulting size and PDI may differ from the results shown in Table 4-2, because different samples were used for the two measurements.

Table 4-3: Particle diameter, PDI and ζ -potential of various polymeric nanoparticles. PCPDTBT-DPPC: PCPDTBT nanoparticles with DPPC as a stabiliser; PCPDTBT-Maleimide: PCPDTBT nanoparticles with DPPC as a stabiliser and 5mol% PEG-2000-Maleimide; PCPDTBT-COOH: PCPDTBT nanoparticles with DPPC as a stabiliser and 5mol% PEG-2000-COOH.

Nanoparticle in aqueous suspension	Particle diameter [nm]	PDI	ζ-potential [mV]
PCPDTBT-DPPC	145	0.20	-37.8 (+/-7%)
PCPDTBT-Maleimide	153	0.24	-19.2 (+/-13%)
PCPDTBT-COOH	171	0.27	-22.8 (+/-9%)
INDT-S	159	0.25	-25.6 (+/-19%)
INDT-T	120	0.23	-29.8 (+/-18%)
INDT-BT	160	0.25	-31.0 (+/-10%)

The ζ -potential measurements of the various nanoparticles show values between 19 and 37 mV with standard deviations in the range of 7-19% (n = 3). Particles covered purely by DPPC such as the PCPDTBT-DPPC, INDT-S, INDT-T and INDT-BT show higher values compared to the nanoparticles covered by a mixture of PEG linkers and DPPC. This can be explained by the positive charge introduced by the PEG linkers to the negatively charged particle surface, reducing the overall negative charge. Generally, particles with a ζ -potential between 10 mV and 30 mV are considered to be of moderate stability. Therefore even the particles stabilised using the PEG linkers are sufficiently charged for them to exhibit strong repulsion from each other and consequently reasonable stability. In order to further analyse the long term stability of the nanoparticles suspensions, DLS measurements of three PCPDTBT nanoparticles stabilised by three different surfactant mixtures (pure DPPC; DPPC/DSPE-PEG(2000)-COOH and DPPC/DSPE-PEG(2000)-Maleimide) were monitored over four days. The results are shown in Figure 4-6. After preparation and in between the DLS measurements, the samples were kept in

the fridge at 4 °C. Before the DLS measurements the samples were allowed to warm up to room temperature and were agitated by vortexing for about 30 s.

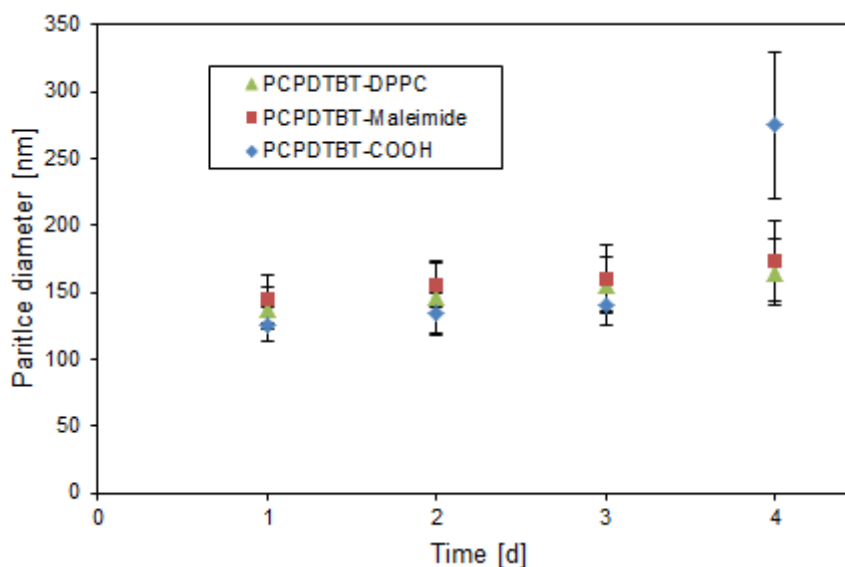


Figure 4-6: Particle diameter over time of three PCPDTBT nanoparticles samples with different surface modifications.

The resulting size measurements show, that all nanoparticles samples are stable over three days, increasing by less than 6% in particle diameter overnight. However, at day four a significant increase (~50%) of the particle size can be observed for the PCPDTBT-COOH sample, whilst the other two samples increase their size compared to the previous day by about 7%. The increasing size of the nanoparticles is due to aggregation and may be prevented by changing the surfactants. However, the stability posed by the nanoparticles suspensions over three days is sufficient for the PA analysis of the sample and therefore the surfactant system hasn't been altered.

4.6 Spectrophotometer measurements

For comparison to the spectra generated using the PA spectroscopy, optical transmission spectra were generated using spectrophotometers as described in Chapter 3. Depending on availability either a Cary 100 UV-Vis spectrophotometer or a Perkin Elmer 750s were used. Therefore about 300 μ L to 1 mL of the liquid samples were filled into quartz cuvette (Hellma Analytics, UK) with a path length of either 1 mm or 10 mm and placed in the sample holder of the spectrophotometer. The path length of the cuvette and settings of the spectrophotometer were used as required, depending on the absorption characteristics of the sample.

4.7 Photoacoustic spectroscopy and extinction coefficient measurements

4.7.1 Photoacoustic spectra

The PA amplitude and μ_a spectra of the various potential contrast agents for PA imaging were measured as described in Chapter 3. At wavelengths at which the sample exhibits very low absorption, the SNR is very low and the exponential rise of the PA signals is corrupted by noise to such an extent that fitting an exponential to the signals becomes increasingly difficult, leading to unreliable readings of μ_a . At wavelengths at which the sample exhibits absorption values close to zero, light passes the cuvette generating a PA signal at the surface of the ultrasound transducer. This parasitic signal disturbs the signal generated by the sample and makes the measurement unreliable. When this occurs, the Matlab code used for the estimation of μ_a tends to fit an exponential decay to the parasitic signal, leading to a negative μ_a . When plotting the PA amplitude or μ_a spectrum these false readings were ignored. For comparison to the PA spectra, spectrophotometer measurements were made, using the same samples. Therefore sample solutions providing sufficient absorption for sufficient SNR for the PA spectroscopy measurements but with sufficient transmittance for the photo-detector of the spectrophotometer were made up. To decrease the influence of ground state bleaching due to long relaxation times of the excited state induced by photoisomers and aggregates of organic dyes, the fluence of the excitation laser of the PA spectroscope was reduced using optical density filters for the measurements of organic dyes. The values for ϵ were calculated from the μ_a values provided by PA spectroscopy and spectrophotometer measurements. The molar ϵ for the polymeric nanoparticle IND-T-BT was estimated from the ϵ based on weight and the literature value of the molecular weight¹¹⁸ of a similar polymeric nanoparticle (PCPDTBT). This estimation can be made because the IND-T-BT nanoparticles exhibit similar size and size distributions compared to the PCPDTBT nanoparticles and the chemical structures of the polymers IND-T-BT and PCPDTBT are comparable. ϵ spectra measured using the PA spectroscope and a spectrophotometer of a selection of nanoparticles and organic dyes are shown in Figure 4-7.

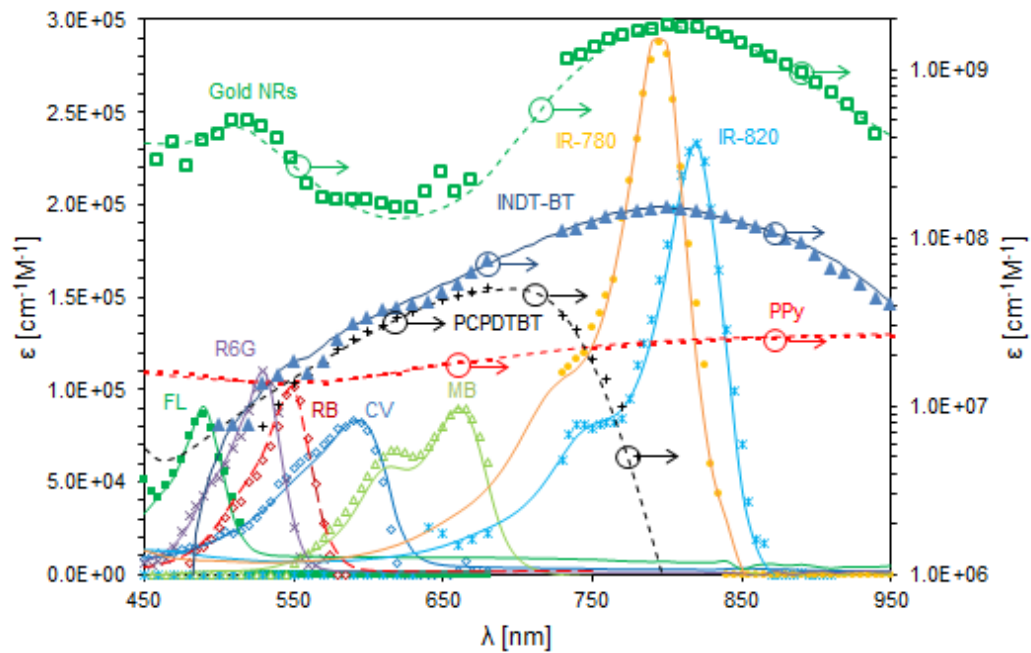


Figure 4-7: Extinction spectra of various chromophores, measured using the PA spectroscope (symbols) and reference measurements using the spectrophotometer (lines). FL = Fluorescein; R6G = Rhodamine 6G; RB = Rhodamine B; CV = Cresyl violet; MB = Methylene blue; PCPDTBT = PCPDTBT nanoparticles; PPy = Polypyrrole nanoparticles; Gold NRs = Gold nanorods. Note: The extinction coefficients of the nanoparticles (PCPDTBT, PPy, IND-T-BT and gold nanorods) are plotted on a logarithmic scale, corresponding to the right hand axis.

Figure 4-8 shows the ϵ spectra of a selection of nanoparticles made from semiconducting polymers. For comparison between the polymeric nanoparticles, ϵ was plotted in $\text{cm}^{-1}\text{lg}^{-1}$ rather than $\text{cm}^{-1}\text{M}^{-1}$. This is due to the unknown molar concentration of the nanoparticles within the samples. In the case of the semiconducting polymers the mass based ϵ can provide a more accurate comparison due to minor differences in size (ranging from 125-160 nm) and particles size distribution.

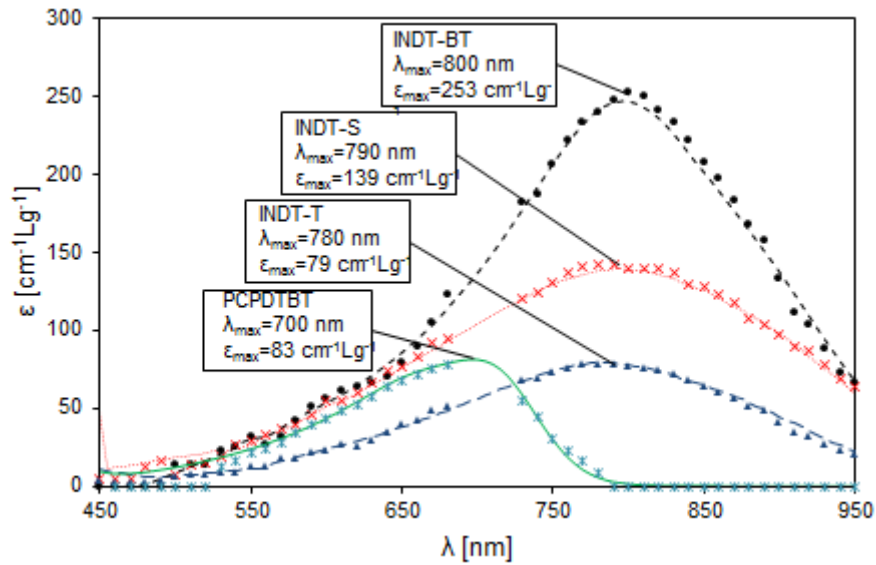


Figure 4-8: Extinction spectra of various nanoparticles, measured using the PA spectroscopy (symbols) and reference measurements using the spectrophotometer (lines).

4.7.1.1 Observations

Generally, the ϵ spectra measured using PA spectroscopy, shown in Figure 4-7 and Figure 4-8, agree very well with the spectra generated using a spectrophotometer. Missing points in the PA spectra between 680 nm and 720 nm are due to degenerate wavelength of the OPO excitation laser. The most obvious deviations from the spectrophotometer values appear when the absorption of the sample is low, which can be attributed to low SNR of the PA signals. The difference between the spectra generated by the two measurements close to 450 nm is due to the power output of the laser, which is reduced by about 45% (compared to 500 nm). As a result of the reduced fluence of the excitation light, the SNR generated by the sample solutions also reduces, increasing the measurement error. The minute discrepancies between the PA spectrum and the results of the spectrophotometer chromophores such as rhodamine B, cresyl violet, methylene blue and gold nanorods are due to measurement errors. These errors tend to occur at wavelengths at which the sample exhibits relatively low μ_a values and therefore low SNR. The secondary peak of the organic dyes can be attributed to the aggregation of the molecules due to the high concentrations used for the experiments. The monomer species of methylene blue, for example, has a single peak at about 660 nm. As described in Chapter 2 of this thesis, with increasing concentration of the organic dye, intermolecular forces between the molecules let to the formation of aggregates in the form of dimers. In the case of the methylene blue dimer, the monomer molecules are orientated on a parallel axis, causing an increase of the band gap of the electronic states responsible for its absorption. Consequently the absorption peak of the methylene blue aggregates is blue shifted with its maximum at about 610 nm. The discrepancies between the PA spectrum and the spectrophotometer measurements around the dimer peak of methylene blue at 610 nm may be due to measurement errors, but could also be

partially due the different relaxation pathway of the dimer species of methylene blue compared to its monomer species¹⁴⁴. The difference between the PA spectrum and the spectrophotometer measurement of methylene blue around the maximum wavelength of absorption of the dimer species around 610 nm might therefore be partially due to an increased quantum yield compared to the monomer species. Generally, deviations of the PA spectra from the spectrophotometer readings within the detection range were due to the measurement errors of the PA spectroscopy and are within 5%.

4.7.2 Extinction coefficient

For the calculation of ϵ the μ_a value was determined using PA spectroscopy and divided by the used concentration. Literature values were used for comparison. The results are shown in Table 4-4. Table 4-5 shows the results of the ϵ measurements of the nanoparticles made from different π -conjugated semiconducting polymers (see Chapter 3), gold nanorods and carbon nanotubes. Literature values for ϵ for most of the samples listed in Table 4-5 are not available due to the novelty of the nanoparticles. Therefore, the results generated using the PA spectroscopy were compared to spectrophotometer measurements only.

Table 4-4: Comparison between measured and literature ϵ of various chromophores. * ϵ from suppliers documentation.

Chromophore	$\epsilon_{\text{Literature}}$ [$\text{cm}^{-1}\text{M}^{-1}$]	λ_{max} [nm]	ϵ_{PA} [$\text{cm}^{-1}\text{M}^{-1}$]	ϵ_{trans} [$\text{cm}^{-1}\text{M}^{-1}$]	Error [%]
Methylene blue ¹⁴⁵	$7.5 \cdot 10^4$	610	$8.0 \cdot 10^4$	$7.9 \cdot 10^4$	1
QXL 680 ²⁶	$1.1 \cdot 10^5$	670	$1.2 \cdot 10^5$	$0.8 \cdot 10^5$	33
Dylight 800 ²⁶	$2.7 \cdot 10^5$	770	$2.4 \cdot 10^5$	$3.4 \cdot 10^5$	29
BHQ-3 ²⁶	$4.2 \cdot 10^4$	670	$9.6 \cdot 10^4$	$5.9 \cdot 10^4$	39
IRDye800CW*	$2.4 \cdot 10^5$	780	$2.3 \cdot 10^5$	$2.0 \cdot 10^5$	13
IR-780*	$2.5 \cdot 10^5$	760	$2.9 \cdot 10^5$	$2.9 \cdot 10^5$	0
IR-820*	$2.0 \cdot 10^5$	810	$2.3 \cdot 10^5$	$2.2 \cdot 10^5$	4
Rhodamine B ¹⁴⁵	$1.1 \cdot 10^5$	550	$1.0 \cdot 10^5$	$1.0 \cdot 10^5$	0
Rhodamine 6G	$1.2 \cdot 10^5$	520	$1.1 \cdot 10^5$	$1.1 \cdot 10^5$	0
Cresyl violet*	$8.2 \cdot 10^4$	590	$8.0 \cdot 10^4$	$8.6 \cdot 10^4$	7
Fluorescein ¹⁴⁵	$9.1 \cdot 10^4$	490	$8.6 \cdot 10^4$	$8.9 \cdot 10^4$	3
Gold nanorods*	$4.0 \cdot 10^9$	800	$1.7 \cdot 10^9$	$1.8 \cdot 10^9$	6
Carbon nanotubes ¹⁴⁶	$7.9 \cdot 10^6$	450	$7.8 \cdot 10^5$	$9.7 \cdot 10^5$	20

Table 4-5: Comparison between ϵ of various chromophores measured using the PA spectroscope (ϵ_{PA}) and the spectrophotometer (ϵ_{trans}).

Nanoparticle	λ_{max} [nm]	ϵ_{PA} [cm ⁻¹ Lg ⁻¹]	ϵ_{trans} [cm ⁻¹ Lg ⁻¹]	Error [%]
Gold nanorods	800	19	20	5
Carbon nanotubes	450	45	55	18
PCPDTBT	700	83	86	3
DPPTT-S	780	39	40	3
DPPTT-T	810	42	41	2
Polypyrrole	1300	69	72	4
INDT-S	790	139	142	2
INDT-T	780	79	78	1
INDT-BT	800	253	247	2

4.7.2.1 Observations

The calculated ϵ values are, for most of the chromophores, within 5% of the measured spectrophotometer values (see Table 4-5) or within 10% of the literature ϵ values (see Table 4-4). The deviations of the PA ϵ values measured and the spectrophotometer values are due to measurement errors caused by the PA spectroscope and are within the error (5%) stated for the PA spectroscope working range (see Chapter 3). Exceptions to this are the chromophores QXL 680, Dylight 800 and BHQ-3 which have been analysed using a preliminary version of the PA spectroscopy setup and could not be repeated due to a lack of material. The discrepancy between the PA measurements and the spectrophotometer measurements of IRDye800CW are caused by the low absorption of the sample analysed. The low absorption was due to a very dilute sample, which generated PA signals of low SNR and therefore increasing the measurements error. The deviation from the literature values can have various reasons, for instance differences in the purity of the sample, inaccurate dilution or different measurement temperatures between the measurements. The only exceptions are the ϵ value for the gold nanorod sample, with a deviation >10% from the literature value, and the ϵ value for the carbon nanotube sample, with a deviation >10% from the transmission spectroscopy value. The value for ϵ of the gold nanorods provided by the supplier ($4 \cdot 10^9 \text{ cm}^{-1}\text{M}^{-1}$) is more than twice as high as the measured values (PA spectroscopy: $1.7 \cdot 10^9 \text{ cm}^{-1}\text{M}^{-1}$ and spectrophotometer: $1.8 \cdot 10^9 \text{ cm}^{-1}\text{M}^{-1}$). This may be caused by a dilution error due to the small sample size. The deviation of ϵ value for the carbon nanotubes measured using PA spectroscopy from the

spectrophotometer measurements may be due to an unstable sample. The carbon nanotubes may be aggregating and form a precipitate due to insufficient stabilisation through the surfactants. This process has a bigger impact on the PA spectroscopy measurements, than the spectrophotometer measurements, for two reasons. First, due to the geometry of the sample cuvette used for the PA measurement, formed aggregates have a bigger impact of the signal generated, because a film of strongly absorbing material, such as a thin film of carbon nanotubes generates a signal, which overlays with the signal generated by the dispersion itself, introducing errors to the estimation of μ_a . Second, the PA measurements took slightly longer and therefore aggregation could occur over a longer period of time, further enhancing the parasite signal generated by the aggregates.

4.8 Thermalisation efficiency measurements

The two methods used for the determination of E_t , namely i) self-referencing method and ii) solvent referencing method, are described in the method section of Chapter 3. After measuring the spectra of the various chromophore samples, they have been analysed for their efficiency to convert absorbed light into heat. Therefore the chromophores were dissolved in various solvents at concentrations to form solutions of absorption values within the detection limit of the PA spectroscope. The resulting values of E_t using the two methods and values found in literature are shown in Table 4-6.

Table 4-6: Results of E_t measurements using various chromophores. Literature values for E_t of the polymeric nanoparticles marked with an x were due to the novelty of the nanoparticles not available.

Chromophore	Solvent	Concentration	E_t self-referencing method	E_t solvent referencing method	E_t literature value
Gold nanorods	H ₂ O	0.5 μ M	100% +/- 11% (n=3)	100% +/- 11% (n=3)	100% ¹⁴⁷
Methylene blue	EtOH	300 μ M	100% +/- 5% (n=5)	98% +/- 6% (n=5)	96% ¹⁴⁸
IR-780	MeOH	50 μ M	99% +/- 4% (n=8)	95% +/- 2% (n=5)	99% ¹⁴⁹
IR-820	MeOH	50 μ M	92% +/- 8% (n=15)	95% +/- 8% (n=15)	96% ¹⁵⁰
Fluorescein	NaOH/H ₂ O	300 μ M	71% +/- 3% (n=6)	72% +/- 2% (n=6)	75% ¹⁵¹
Cresyl violet	MeOH	500 μ M	58% +/- 6% (n=17)	51% +/- 4% (n=17)	51% ¹⁵²
Polypyrrole nanoparticles	H ₂ O	1gL ⁻¹	100% +/- 8% (n=10)	100% +/- 7% (n=10)	x
PCPDTBT nanoparticles	H ₂ O	0.1gL ⁻¹	99% +/- 6% (n=3)	100% +/- 4% (n=3)	x
DPPTT-S nanoparticles	H ₂ O	0.1gL ⁻¹	101% +/- 2% (n=2)	103% +/- 3% (n=2)	x
DPPTT-T nanoparticles	H ₂ O	0.1gL ⁻¹	99% +/- 1% (n=2)	100% +/- 2% (n=2)	x
INDT-S nanoparticles	H ₂ O	0.04gL ⁻¹	98% +/- 2% (n=2)	99% +/- 1% (n=2)	x
INDT-T nanoparticles	H ₂ O	0.04gL ⁻¹	100% +/- 6% (n=2)	101% +/- 6% (n=2)	x
INDT-BT nanoparticles	H ₂ O	0.04gL ⁻¹	99% +/- 5% (n=2)	102% +/- 7% (n=2)	x

4.8.1 Discussion

Table 4-6 shows the results of the E_t measurements using the two methods discussed in Chapter 3 with various organic dyes and nanoparticles. Some of the sample chromophores exhibit significant fluorescence quantum yields and therefore reduced E_t values. However, the measured values of E_t compare well to the values found in literature with maximum deviations of 13%. The standard deviation s of a number of measurements n was calculated using

$$s = \sqrt{\frac{\sum_{i=1}^n (x_i - \bar{x})^2}{n-1}} \quad \text{Equation 4-1}$$

where x_i is the individual measurement and \bar{x} is the average over all the measured E_t values. The standard deviation of the various values is within 8%, except for the gold nanorod measurements. The slightly higher standard deviation for the gold nanorod values is caused by the small sample volume used for the experiments. Due to the small sample volume (200 μl) the light path for the PA signal generation was limited, resulting in a short time signature and a short exponential rise with fewer points for the exponential fitting. Therefore the non-linear least squares fit to the exponential rise of the PA signal has a greater standard deviation compared to the measurements using a larger sample volume and therefore a longer light path and more points for the exponential fit. Literature values for the polymeric nanoparticles, such as polypyrrole, PCPDTBT and in house made DPPTT-X and INDT-X polymers are not available. However, the energy-gap law predicts an exponential increase in non-radiative decay rate of the excited states with decreasing band gap. The polymeric nanoparticles examined in this study all exhibit very small band gaps of about 1.5 eV. In addition to that, fluorescence spectroscopy and fluorescent imaging measurements (data not shown) of the nanoparticles solutions have shown no significant fluorescence and therefore $E_t = 100\%$ can be assumed. The PA measurements of E_t of the polymeric nanoparticles confirm this assumption - all measured values trend around 100%. Values smaller than 100% and the values of INDT-S, INDT-T and INDT-BT bigger than 100% are due to the measurement accuracy of the PA spectroscopy, introducing an error of about 5% for the PA amplitude and μ_a determination. The resulting accuracy of the E_t values of the polymeric nanoparticles is within 3% if $E_t = 100\%$ is assumed.

4.9 Grüneisen coefficient measurements

The method for the determination of Γ , as well as the validation of the method is detailed in Chapter 3. It has been shown, that Γ can be quantified with an accuracy of +/-5% using mixtures of either methanol in water or ethanol in water.

In order to further demonstrate the method for the determination of Γ , solutions of various concentrations of either copper chloride (CuCl_2 ; 70-430 gL^{-1}) or nickel chloride (NiCl_2 ; 250-480 gL^{-1}) were prepared and analysed as described in Chapter 3. CuCl_2 and NiCl_2 were chosen

for these experiments due to their concentration dependence of Γ , which follows a linear trend as demonstrated previously¹⁵³. The results of the measurements are shown in Figure 4-9.

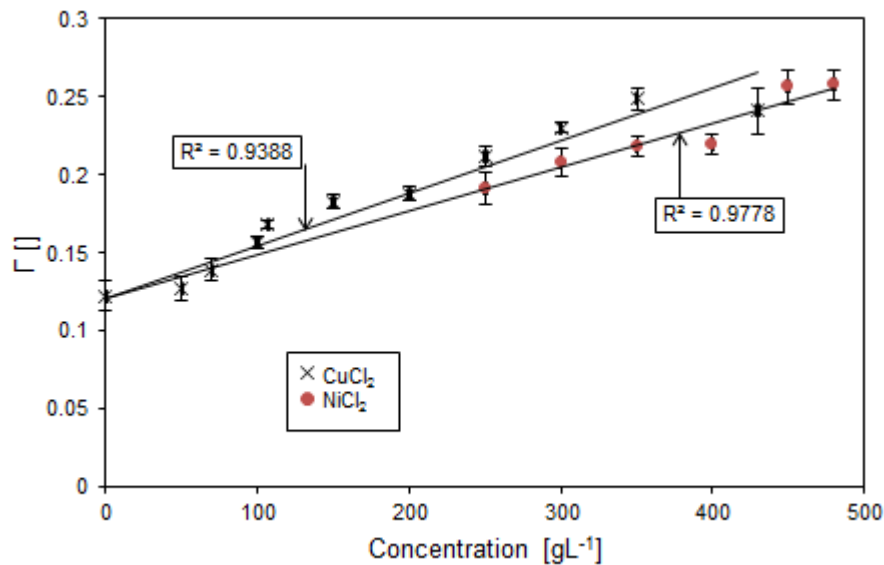


Figure 4-9: Γ versus the concentration of CuCl_2 (black crosses) and NiCl_2 (red dots) in water and Γ of pure water.

The results presented in Figure 4-9 show a linear increase of Γ with concentration of the dissolved chlorine salts of the transition metals Cu^{2+} and Ni^{2+} in water. As expected, Γ increases with increasing concentration of dissolved salt in aqueous solution in the measured concentration range of 70-480 gL^{-1} . The measured values align with linear trend lines originating from $\Gamma = 0.12$ with R^2 values of 0.9388 and 0.9778 for CuCl_2 and NiCl_2 , respectively. The standard deviation of the values range from 2-11% and are high for NiCl_2 due to its low ϵ and therefore low SNR even at the high concentrations measured. The measurements at the very high concentrations ($>400 \text{ gL}^{-1}$) using CuCl_2 and NiCl_2 show increased standard deviations and decreased accuracy. This is thought to be due to the limited bandwidth of the PVDF transducer used for the detection of the PA signals resulting in less accurate determination of the PA amplitude and μ_a , leading to a higher standard deviation and error of the estimated Γ . The increased standard deviation in the lower concentration range for both of the salt solutions can be assigned to low SNR due to low absorption.

Subsequently to the measurements of Γ of solutions of CuCl_2 and NiCl_2 , various solutions of organic dyes and dispersions of nanoparticles were analysed using the same method. Sample solutions are comprised of IR 780 in methanol and ethanol and IR 820, polypyrrole, PCPDTBT and IND-T in deionised water. The results are shown in Table 4-7.

Table 4-7: Measurements of various sample chromophores in solution of concentrations.

Chromophore	Solvent	Concentration	Γ_{measured}	Γ_{expected}
IR 780	Methanol	50M	0.61 (+/-7%)	0.60
IR 780	Ethanol	100M	0.51 (+/-9%)	0.48
IR 820	Water	120M	0.12 (+/-4%)	0.12
Polypyrrole	Water	0.2gL ⁻¹	0.13 (+/-3%)	0.12
PCPDTBT	Water	0.1gL ⁻¹	0.12 (+/-9%)	0.12
INDT-T	Water	0.04gL ⁻¹	0.11 (+/-8%)	0.12

The measured Γ values shown in Table 4-7 are in good agreement with the expected values at the low concentrations used. Assuming a Γ for the diluted sample of that of the pure solvent (Γ_{expected}), the measurements show a maximum error of about 8% with standard deviations for three measurements ranging from 3-9%. The increased standard deviations for IR 780, PCPDTBT and INDT-T are due to low SNR of the signals generated by either the chromophore solutions used or the solvent at the wavelengths used.

4.9.1 Temperature dependence of the Grüneisen coefficient

4.9.1.1 Water as a chromophore

In order to further demonstrate the ability of the PA spectroscopy to quantify Γ , the influence of different temperatures on the heat transfer and therefore Γ was analysed. Water as a chromophore was used for these experiments due to its loss of thermal expansion at about 4 °C¹⁵⁴. In addition water has been intensely studied and the value of Γ at different temperatures T_r can be calculated using the empirical formula shown in Equation 4-2. The change of Γ of water with temperature is a non-linear function and can be calculated using the speed of sound, heat capacity and thermal expansion coefficient over the temperature range desired. In the temperature range measured (4-23 °C), the linear equation¹⁵⁵ used below is sufficient due to the close to linear trend of Γ versus temperature in the measurement range.

$$\Gamma(\text{H}_2\text{O})=0.0043+0.0053T_r \quad \text{Equation 4-2}$$

The influence of the temperature on Γ and therefore on the PA amplitude generated by a water sample irradiated with laser light with a wavelength of 1450 nm was analysed using the PA spectroscopy. The sample contained in the cuvette was pre-cooled in a fridge before placing in an ice cooled water bath in the PA spectroscopy. The temperature was monitored using a thermocouple connected to a thermometer (2000T Digital Thermometer, Digitron, UK). The PA

amplitude and μ_a of the cool solution and at various temperatures during the warming up period of the sample until reaching room temperature were determined. In order to demonstrate the influence of the temperature on Γ , the latter was calculated using the method described in Chapter 3 and Equation 3-14. For the signal generation, the sample was irradiated with laser light of a wavelength of 1450 nm, matching the absorption maxima of water in that region. For comparison to literature values, Γ was calculated as described in ¹⁵⁶, using Equation 4-2. The results are plotted in Figure 4-10.

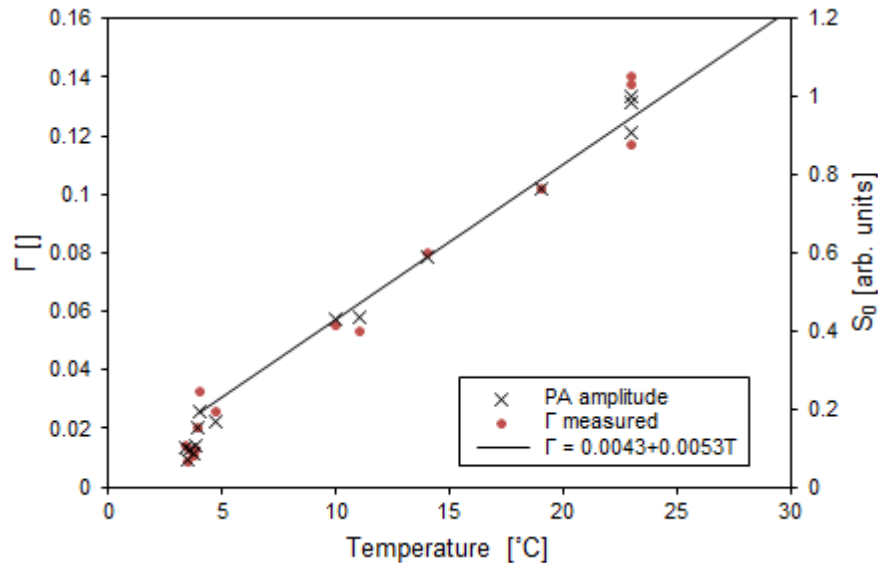


Figure 4-10: Results of the Γ measurements (red dots) compared to literature values (black line) at temperatures ranging from about 4 °C to 23 °C. The plot also shows the decreasing PA amplitude (black crosses) in the temperature range measured.

4.9.1.1.1 Observations

Figure 4-10 shows good agreement between the Γ estimated using the method described in Chapter 2 and the literature values. The normalised PA amplitude also follows the linear trend of the Equation 4-2, whilst the μ_a measurements are constant with temperature, due to the unchanged optical properties (data not shown). The great spread of the measurements close to 4 °C is due to low SNR of the PA signal generated at this temperature. The low signal amplitude at temperatures close to 4 °C is due to the thermal expansion of water, which decreases with decreasing temperatures, resulting in PA signal amplitudes just above the noise floor. The relationship between Γ and β can be seen in Equation 3-14. However, even though water exhibits no thermal expansion at about 4 °C small PA signals were still generated at this temperature. This can be attributed to external heating of the sample solution by the light source increasing the temperature and therefore increasing the thermal expansion coefficient.

4.9.2 Wavelength dependence of the Grüneisen coefficient

After measuring Γ of various solutions of chromophores and nanoparticle dispersions and the analysis of the temperature dependence of Γ , it was investigated if a mixture of multiple chromophores or nanoparticles with separate absorption bands may exhibit different efficiencies converting heat to stress and therefore exhibit a wavelength dependence of Γ . An example where this effect may be observed are gold nanoparticles with varying coatings such as gold nanoparticles covered in a silica shell compared to plain gold nanoparticles. It has been shown that the silica coating alters the thermal coupling of the nanoparticles and therefore alters Γ ¹⁵⁴. If the two species of gold nanorods (silica coated and plain) would exhibit separate absorption bands, the measurement of Γ of a mixture of the two nanoparticle species may demonstrate wavelength dependence. Another example where this might be observed is a mixture of nanoparticles and organic dyes or other chromophores.

In order to analyse the wavelength dependence of Γ of a sample mixture, various solutions of chromophores were studied. Initially, to investigate this, the Γ spectrum of a solution of IR 820 dissolved in water at a concentration of 400 μM was determined. The two chromophores in this initial test are water and the organic dye IR 820. In order to generate the Γ spectrum, initially Γ was determined at λ_{max} of IR 820 (820 nm) as described in Chapter 2. Next, the ratio of PA amplitude to μ_a at each wavelength of the measured wavelength range was calculated, normalised to the value at λ_{max} and multiplied by Γ previously calculated for λ_{max} . The results are shown in Figure 4-11.

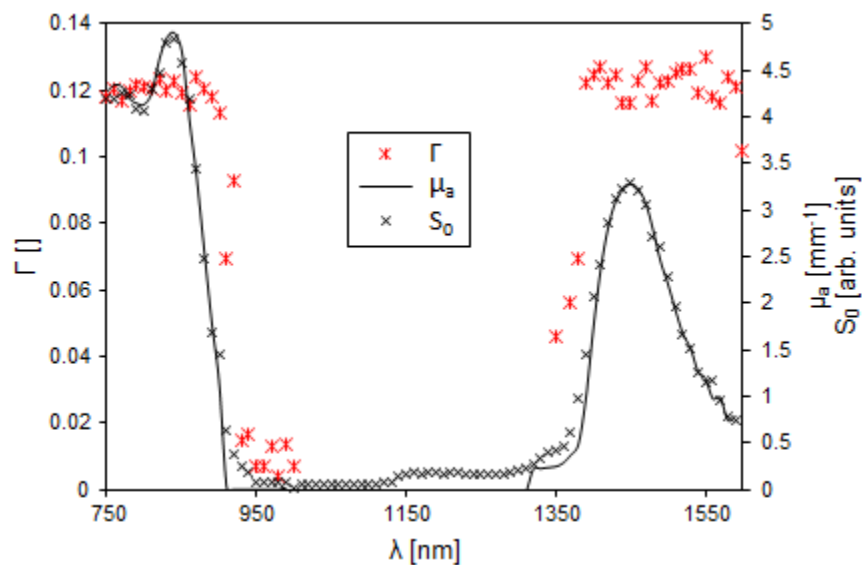


Figure 4-11: Γ (red stars), PA amplitude (black crosses) and μ_a (black line) spectra of IR 820.

Figure 4-11 shows that in the wavelength range from 750-880 nm and 1390-1590 nm Γ is relatively constant. The deviation from the value of Γ of water ($\Gamma(\text{H}_2\text{O}) = 0.12$) are no more than 7% over this wavelength range. Strong deviations from this constant value of Γ can be observed in the wavelength range from 880-1390 nm. These values are measurement errors due to low SNR.

Next, in order to further analyse the possibility of a wavelength dependence of Γ , aqueous solutions of CuCl_2 were employed because the salt is known to alter the value of Γ of a solution, which has been demonstrated above (Figure 4-9). Water was used as the second chromophore in the mixture, consistent with the previous experiment. Γ spectra of the mixture were generated at room temperature and at 4 °C in order to evaluate the influence of the reduced thermal expansion coefficient of water at this temperature on the measured Γ . The PA amplitude, μ_a and Γ spectra generated at the two temperatures are shown in Figure 4-12.

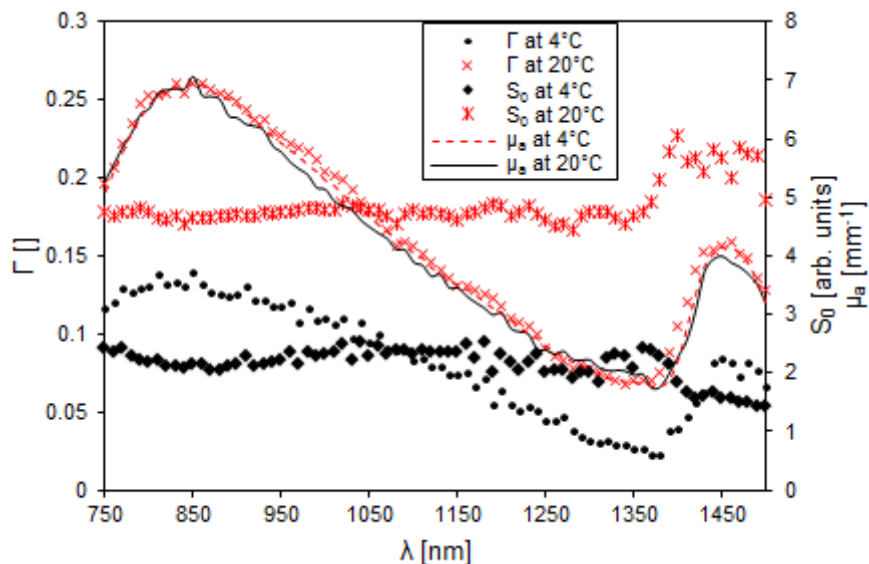


Figure 4-12: PA amplitude (red crosses), μ_a (red dashed line) and Γ (red stars) spectra of CuCl_2 (200 gL^{-1}) in water at 20 °C compared to PA amplitude (black crosses), μ_a (black line) and Γ (black squares) spectra of CuCl_2 (200 gL^{-1}) in water at 4 °C.

The resulting PA amplitude and the μ_a spectrum at 20 °C agree well with each other and the μ_a spectrum at 4 °C. However, the PA amplitude at 4 °C is reduced by about 50% at the wavelength of peak absorption of the salt (850 nm) and the solvent (1450 nm), see Figure 4-12. Minor differences in amplitude and shape of the μ_a spectrum can be attributed to low SNR generated at the lower temperatures. The difference in the PA amplitude at the two temperatures can be explained with the decreased Γ at the lower temperatures - at 4 °C $\Gamma(\text{CuCl}_2) = 0.08$ compared to $\Gamma(\text{CuCl}_2) = 0.17$ at room temperature (see also Figure 4-10). However, the calculated Γ values show spectral features, especially near the absorption maxima of the solvent from about 1380-1500 nm. Comparing Γ in the spectral range of 750-

1370 nm to Γ in the spectral range from 1380-1500 nm shows a change in the amplitude of the values differing by 14% and 20% at room temperature and at 4 °C, respectively. Additional to the feature at the peak absorption of the solvent, a subtle dip around λ_{max} of the metal ion (Cu^{2+}) around 820 nm is apparent.

To further investigate these spectral features of Γ , CuCl_2 was dissolved in a series of organic solvents including methanol, ethanol, isopropanol, dimethyl sulfoxide and acetone in order to exploit the different values of Γ of the solutions produced. Subsequently, PA amplitude, μ_a and Γ spectra of the different samples were generated and the resulting spectra were overlaid as shown above. In addition to this the PA amplitude spectra of the pure solvent were generated for comparison. The results are shown in Figure 4-13.

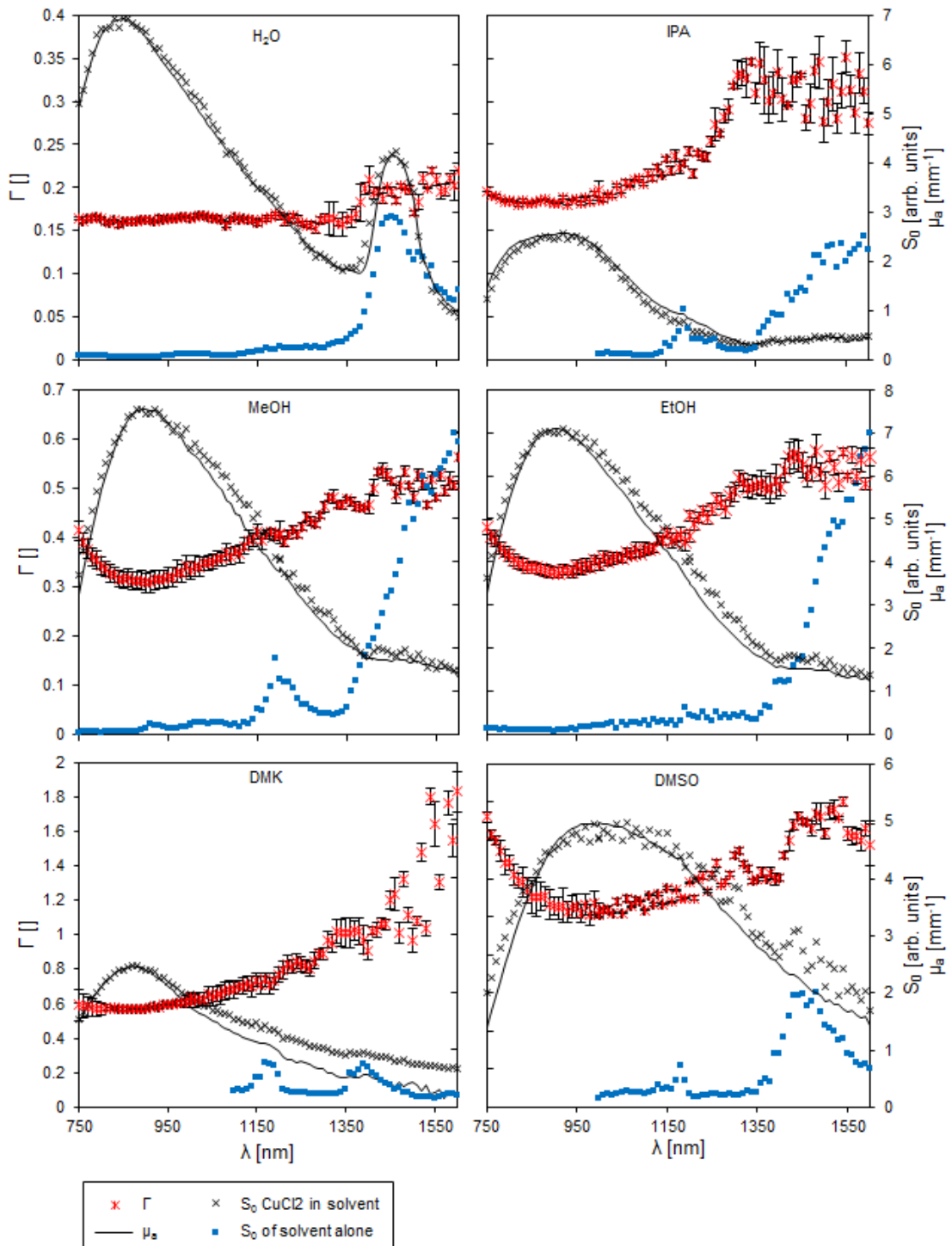


Figure 4-13: Γ (red stars), PA amplitude (black crosses) and μ_a (black line) spectra of the CuCl₂ solutions using various solvents and PA amplitude spectra of the pure solvents used for the experiments (blue squares). The solvents used were water (H₂O), isopropanol (IPA), methanol (MeOH), ethanol (EtOH), acetone (DMK) and dimethyl sulfoxide (DMSO).

4.9.2.1 Observations

Figure 4-13 shows the resulting spectra of CuCl_2 in various solvents, including the calculated Γ values for wavelength between 750 nm and 1600 nm. The change in the wavelength of maximum absorption of CuCl_2 is due to the variable electronic environment provided by the solvents of Cu^{2+} . The PA amplitude of the pure solvent shows a peak at the longer wavelength which often can't be made out in the PA amplitude spectra or the μ_a spectra of the CuCl_2 mixtures (see for example the ethanol and methanol measurements at about 1550 nm Figure 4-13). This is due to the scaling. The trend of the spectral features of Γ compare well to the features indicated in Figure 4-12. Particularly striking is the increased Γ at wavelength between 1300 and 1600 nm in the measured range. Γ of the isopropanol/ CuCl_2 mixture changes by about 50% from the minimum ($\Gamma(820 \text{ nm}) = 0.27$) to the maximum ($\Gamma(1550 \text{ nm}) = 0.53$) value. The change of Γ over a wavelength range of 750 to 1250 nm ($\Gamma(750\text{-}1250 \text{ nm}) = 0.3$) compared to the change over the range of 1300 to 1600 nm ($\Gamma(1300\text{-}1600 \text{ nm}) = 0.47$) is about 36%. Another feature of the Γ spectrum is the dip around λ_{max} of the metal ion at 820 nm, which also can be made out for all the other mixtures of the copper ions in the range between about 820-920 nm.

4.9.2.2 Discussion

The change of Γ with wavelength and its spectral features can possibly be explained by considering the behaviour of ions in solution, such as copper, nickel or chlorine ions in aqueous solution or in an organic solvent. For example, when dissolved in an aqueous solution, CuCl_2 is solvated by the water molecules forming copper (Cu^{2+}) and two chlorine ions (Cl^-), which are solvated by a number of water molecules forming clusters which are called clathrates. A clathrate consists of an atom or molecule which is trapped by other molecules. A scheme of an example of a clathrate, consisting of a hydrated metal ion, is shown in Figure 4-14.

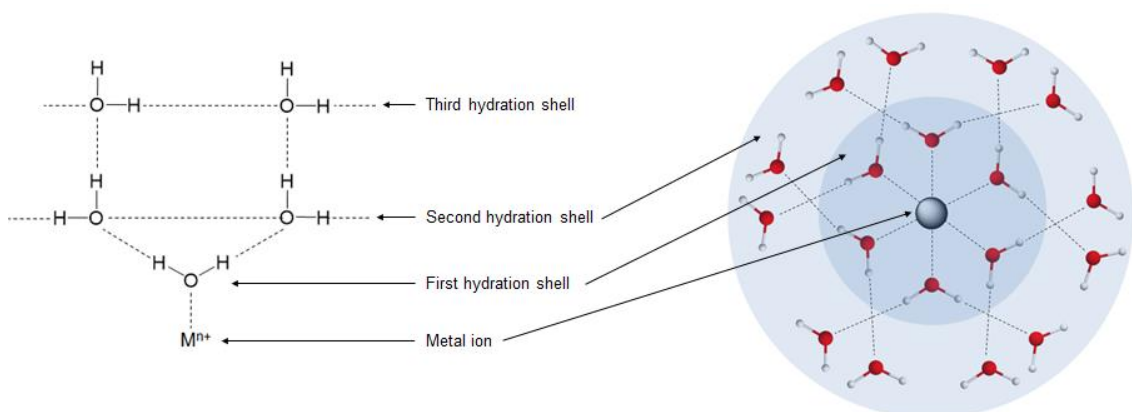


Figure 4-14: Scheme of the hydrogen bonding pattern in the first three hydration shells (left) and an example of a metal ion trapped by water molecules (right). The red spheres in the scheme on the right represent oxygen atoms, the white spheres hydrogen atoms and the grey spheres the metal ion. Dashed lines represent hydrogen bonds.

A well-known example of a clathrate is the methane clathrate, also known as frozen methane. The clathrates consist of methane molecules trapped by hydrogen bonded water molecules. Another example is clathrates consisting of ions trapped by solvent molecules. The process of entrapping ions by the solvent molecules is called solvation or, in the case of water as a solvent, hydration. The solvation process and the resulting clathrates have been closely examined in the past, using various methods, such as infrared spectroscopy¹⁵⁷, magnet resonance spectroscopy¹⁵⁸, Raman spectroscopy^{159,160}, electro-osmosis¹⁶¹ and gel exclusion chromatography¹⁶², in order to acquire information about the number of solvent molecules influenced by the ions and their spatial distribution around the central ion. The influence of an ion in solution on the solvent depends on factors such as size and charge of the ion¹⁶³. It has been proposed, that an ion can influence solvent molecules in a range of up to several hundreds of nanometres, involving 10^3 - 10^8 solvent molecules¹⁶⁴ in layers (in aqueous solution called hydration shells) around the central ion, resulting in an increased local density of solvent molecules around the ions compared to the rest of the bulk solution. The solvent molecules are affected in various ways, such as induced charge transfer, changing of the dipole orientation and distorting of the hydrogen-bond network in the bulk¹⁶⁵. The effects of these interactions are predominant in the first hydration shell and can be observed by the elongation of the oxygen lone pair orbitals along the ion-oxygen direction and the influence on the hydrogen bonding electrons, resulting in a strong polarisation of the molecules¹⁶⁶. In addition, recently, Ahmed et al were able to show that the water molecules involved in formation of the hydration shell are vibrationally decoupled from their neighbouring bulk water molecules¹⁵⁹. These properties of clathrates may be the reason for the observed wavelength dependency of Γ of the solutions (Cu^{2+} ions in various solvents) shown in Figure 4-12 and Figure 4-13. In particular the increased local density of solvent molecules surrounding the central ion of a clathrate compared to the bulk solution might explain the observed wavelength dependence of Γ , because the density has a direct influence on Γ via

$$\Gamma = \frac{\beta K_S}{C_p \rho} \quad \text{Equation 4-3}$$

where K_S is the adiabatic bulk modulus and ρ is the density. As a result of the changed local density due to the formation of clathrates, the two absorbing species (Cu^{2+} and the solvent) in the spectral region measured (750-1500 nm), exhibit different efficiencies converting heat to stress as shown by plotting the Γ spectra in Figure 4-12. At about 4 °C the density of water is at its maximum and the thermal expansion at its minimum. At this temperature (4 °C), Cu^{2+} clathrates are more efficient converting the thermalized energy to stress than the bulk water. The effect can be observed in Figure 4-12, showing the increased Γ values in the spectral region around the clathrate absorption peak (750-1300 nm) compared to the spectral region around the solvent absorption peak (1350-1500 nm) at 4 °C. However, at 20 °C the thermal expansion of water is increased and thus the conversion from heat to stress is more efficient,

shown by the values of Γ in the spectral region from 1350-1500 nm. Even though the spectral features of Γ are in the same position, the amplitude of the measurements of Γ at 4 °C differs significantly from the measured Γ at 20 °C. At 20 °C the average Γ of the aqueous Cu^{2+} solution is increased due to the increased thermal expansion of water. However, apart from the changing amplitude, a blue shift of the maximum Γ by more than 500 nm is noticeable. In the case of the solution at 4 °C the efficiency of the bulk water to convert heat to stress is lower compared to the ability of the clathrates. At increasing temperatures the situation is reversed and at 20 °C the amplitude is greater around the water absorption peak (1450 nm) than around the ion absorption peak (850 nm). It can therefore be concluded that the conversion from heat to stress is more efficient in the bulk water compared to the Cu^{2+} clathrates at increased temperatures.

The same holds true for solutions of CuCl_2 in organic solvents. Figure 4-13 shows the Γ spectrum measured using CuCl_2 in water, isopropanol, methanol, ethanol, acetone and dimethyl sulfoxide. The spectral features of Γ shown are comparable to those identified in Figure 4-13 and could also be explained by the formation of clathrate like structures. These structures and the bulk solvent exhibit a different efficiency converting heat to stress likely to be caused by the increased local density of solvent molecules surrounding the metal ions compared to the bulk solvent.

Another feature presented in Figure 4-13 is the intermediate peak in the Γ spectra. For example the Γ spectrum of isopropanol shows an intermediate peak at about 1200 nm, which is due to the increased influence on Γ of the solvent, caused by the absorption peak of isopropanol in this spectral region (see PA amplitude measurement of pure IPA - blue squares in Figure 4-13). At wavelengths where both absorbing species pose significant absorption, the values of Γ depends on both species and thus introduces features such as the intermediate peak at around 1200 nm in the Γ spectrum of Cu^{2+} in isopropanol. Similar results have been obtained using other organic solvents such as methanol, ethanol, dimethyl sulfoxide and acetone, which are also shown in Figure 4-13.

4.10 Photostability measurements

4.10.1 Photobleaching

In order to analyse the ability of the chromophores used throughout this study to generate PA signals under continuous exposure to pulsed laser light with a fluence of about 2 mJcm^{-1} the PA spectroscopy was employed, using the method described in Chapter 3 of this thesis. Therefore sample solutions composed of either nanoparticles or organic dyes were exposed to laser light with a wavelength tuned to the peak absorption of the individual sample over a period of 20,000 laser pulses. In order to maintain the same conditions for all the samples, the solutions were

diluted to concentrations to gain constant values of μ_a ($\sim 6 \text{ mm}^{-1}$). An exception to this was the gold nanorod sample, which was used at the concentration it was received, exhibiting a μ_a of about 1 mm^{-1} . The photobleaching profile of a selection of chromophores is shown in Figure 4-15.

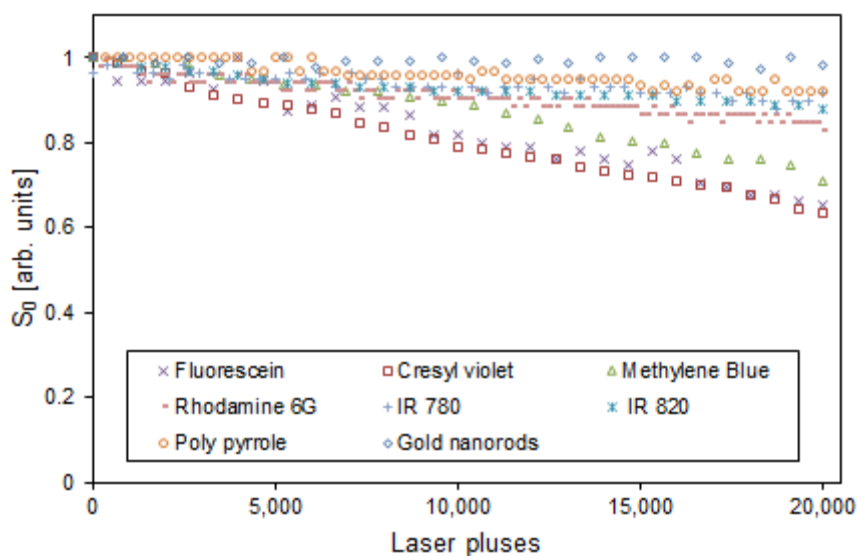


Figure 4-15: Photobleaching profile of gold nanorods, methylene blue, fluorescein, cresyl violet, IR 780, IR 820, rhodamine B, rhodamine 6G and polypyrrole nanoparticles.

The decrease of the PA amplitude after 20,000 laser pulses varies between 29% (methylene blue) and 1% of (gold nanorods). The most radical change of the PA amplitude under the exposure of 20,000 laser pulses can be made out from the photobleaching profile of the chromophores fluorescein and cresyl violet. Figure 4-15 shows the PA amplitude of both chromophores decreased by more than one third of its initial value; fluorescein 35% decrease and cresyl violet 37% decrease. The other chromophores analysed are less susceptible to changes in the PA amplitude upon prolonged pulsed laser light irradiation. The reason for this might be found in the chemical structure of the individual organic dyes, each exhibiting intrinsic rates for intersystem crossing (k_{isc}) after excitation. Intersystem crossing is the electronic transition of an excited electron to the triplet state responsible for the degradation of the dye molecule. Therefore, if a dye molecule favours relaxation from an excited state via the triplet state of the molecule, the probability for a chemical reaction with components in the environment - the photo induced degradation of the dye molecule - increases. For fluorescein¹⁶⁷ $k_{isc} = 6.6 \cdot 10^6 \text{ s}^{-1}$ is compared to the k_{isc} value of rhodamine dyes¹⁶⁸ $k_{isc} = 2.5 \cdot 10^6 \text{ s}^{-1}$ high, which explains the increased susceptibility of fluorescein for photobleaching shown in Figure 4-15. Another reason for the difference in the photostability of the various organic dyes might be the individual quenching rate of the molecules. When the triplet state of a dye is quenched the dye molecule returns to its ground state without exhibiting an electron transfer which would

introduce the photobleaching mechanism. Two major pathways for the depopulation of the triplet state are the reaction between a triplet state dye and another dye molecule and the reaction between a triplet state dye molecule with oxygen. It might be reasoned, that a steric hindrance posed by the some dye molecule prohibits the electron transfer with other dye molecules and favours physical quenching by oxygen. This might be the reason for why dyes such as IR 820 exhibit enhanced photostability compared to other dyes such as rhodamine 6G and fluorescein.

After measuring the photobleaching profiles of various samples, gold nanorods were analysed in more detail. Nanoparticles, in particular gold and silver nanoparticles are prone to light induced shape and size changes, which alters their optical properties. This effect can be observed when such noble metal nanoparticles are exposed to high fluences. The light fluence at which this effect starts to occur and the influence on the PA signal generation by this effect were analysed as described in the next section.

4.10.2 Photo induced melting of (noble metal) nanoparticles

When noble metal nanoparticles absorb light, their temperature can reach melting temperature within a few picoseconds¹⁶⁹. If the temperature reaches the melting temperature of the nanoparticles, they change their shape and size through aggregation. Gold nanorods have been reported to change aspect ratio before transforming into a nanodot shape^{170,171}. Compared to the bulk material the melting temperature decreases with particle diameter. The decreased melting temperature can be explained by the reduced cohesive energy of atoms at the surface of a material compared to atoms of the bulk of the material. These surface atoms require less energy to change from their solid state to the liquid state. Nanoparticles are defined by their great surface to volume ratio, which means they mainly consist of surface atoms. This explains their decreased melting temperature, which can be reduced by hundreds of degrees compared to bulk materials.

In order to estimate the fluence threshold at which a sample of nanoparticles starts to melt, the PA spectroscopy was employed. The estimation of this threshold is based on the detection of a change in the optical properties which occurs when the nanoparticles reach their melting temperature. Therefore, in the first instance PA spectra at various fluences were recorded using samples of gold nanorods (Nanopartz, US) of an aspect ratio of 4.1 and a maximum longitudinal surface plasmon resonance at 808 nm at a concentration of 3 nM. The samples were placed in the cuvette and covered with a mask. The mask consists of a thin, square piece of polyethylene; spray painted with black paint and a hole of 5mm diameter in the centre of it and was used to ensure constant diameter of the excitation light. In order to vary the fluence incident on the sample, the distance between the mask and the tip of the glass fibre used for excitation was varied. The fluence incident on the samples was estimated by replacing the cuvette with a power meter covered with the same mask. For the measurements, PA signals were recorded at

excitation wavelengths between 720 nm and 1000 nm, beginning with the longer wavelength at 1000 nm and scanning in 10nm steps towards the short wavelengths. The signals were averaged over 100 laser pulses. The resulting PA amplitude spectra recorded at various fluences are shown in Figure 4-16.

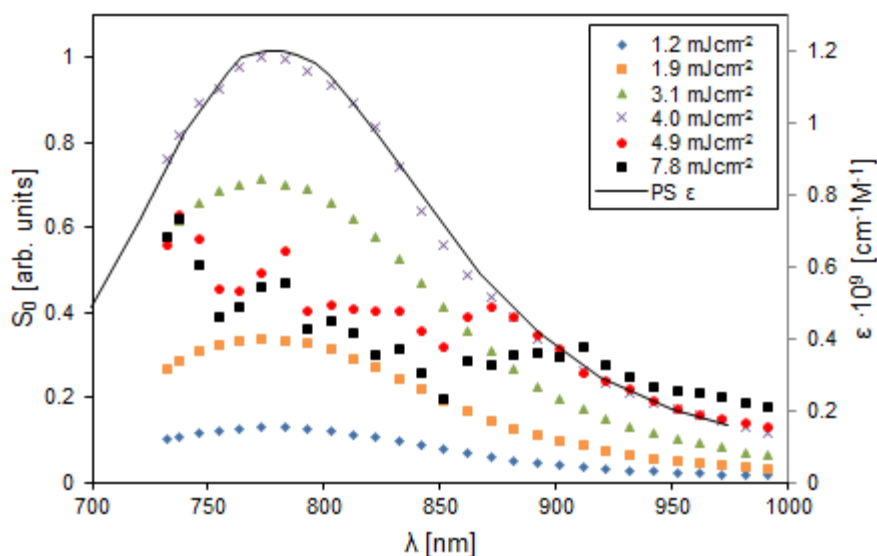


Figure 4-16: PA amplitude spectra recorded at fluences between 1.2 mJcm^{-2} and 7.8 mJcm^{-2} . The solid line is the ϵ spectrum measured using a spectrophotometer (PS). The PA amplitude spectra recorded at 4.9 mJcm^{-2} and 7.8 mJcm^{-2} do not show the characteristic absorption peak at about 800 nm, due to photo induced melting of the nanorod samples.

The spectra generated using low fluences ($<4.9 \text{ mJcm}^{-2}$), presented in Figure 4-16 show an absorption peak at about 800 nm, caused by the longitudinal surface plasmon resonance of the nanorods. However, the spectra recorded at higher fluences (4.9 mJcm^{-2} and 7.8 mJcm^{-2}) strongly deviate from the expected absorption profile. Due to the direction of the scan (from long to short wavelengths) the spectra recorded at 4.9 mJcm^{-2} and 7.8 mJcm^{-2} matches the spectra recorded at lower fluences between 1000 nm and 870 nm and 1000 nm and 910 nm, respectively. Once the particles are strongly absorbing (at wavelength above 870 nm and 910 nm at 4.9 mJcm^{-2} and 7.8 mJcm^{-2} , respectively), the optical properties of the sample changes irreversibly. This behaviour is due to the melting of the nanorods, which results in decreased PA amplitude and an altered shape of a time resolved PA signal. The PA signals recorded with intact gold nanorod dispersions show a smooth exponential rise, whilst the initial increase of the PA signals generated by a gold nanorod sample irradiated with fluences exceeding the threshold is distorted and the peak amplitude is of lower amplitude (see Figure 4-17). The distorted amplitude spectra recorded (Figure 4-16) and the PA signals shown below indicate a fluence threshold for the gold nanorod sample of about 4.9 mJcm^{-2} , which needs to be considered when using gold nanorods as a contrast agent, to avoid photo induced melting.

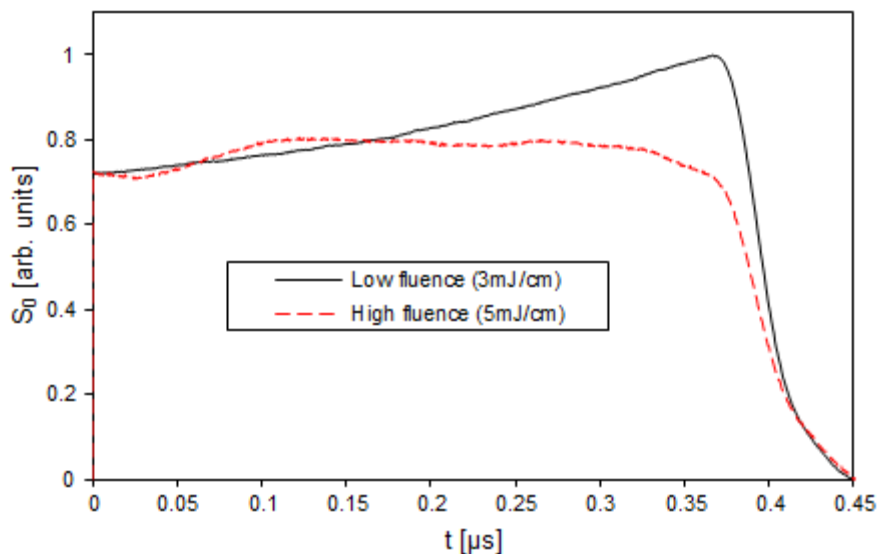


Figure 4-17: PA signals recorded using gold nanorods irradiated by laser light with a wavelength of 820 nm and a light fluence of 3 mJcm^{-1} (black line) and 5 mJcm^{-1} (red dashed line).

In order to estimate the fluence at λ_{max} (810 nm) at which the gold nanorods change their optical and PA properties, samples were exposed to laser light of varying fluences and the PA amplitude was recorded. Signals were averaged over 100 laser pulses before recording. The fluence was tuned from 2 mJcm^{-2} to about 6 mJcm^{-2} . The measured PA amplitude values were plotted over the fluence and the results are shown in Figure 4-18.

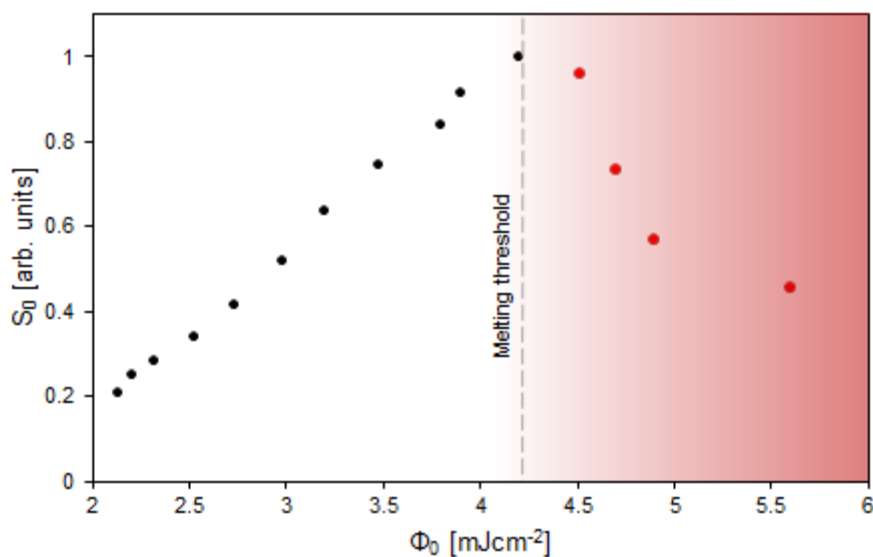


Figure 4-18: PA amplitude of gold nanorods at fluences between 2 mJcm^{-2} and 6 mJcm^{-2} . Signals were recorded at the wavelength of peak absorption - 810nm.

The results presented in Figure 4-18 indicate a fluence threshold at the peak absorption of the gold nanorod sample of 4.3 mJcm^{-2} . The threshold at the peak absorption of the nanorods is lower than previous estimation (4.9 mJcm^{-2}), which can be explained by the increased light energy absorbed by the gold nanorods at the wavelength of peak absorption. This absorbed energy is available for the melting process, therefore lowering the fluence threshold.

4.11 Conclusion

In this chapter various organic dyes and nanoparticles for the potential application as contrast agents for molecular PA imaging were analysed for their PA properties using the PA spectroscopy and the methods described in Chapter 3 of this thesis. The samples analysed consist of either organic dyes or nanoparticles with strong absorption in the visible to near-infrared. Nanoparticles analysed included gold nanorods, carbon nanotubes and various polymeric nanoparticles prepared as described in Chapter 4.

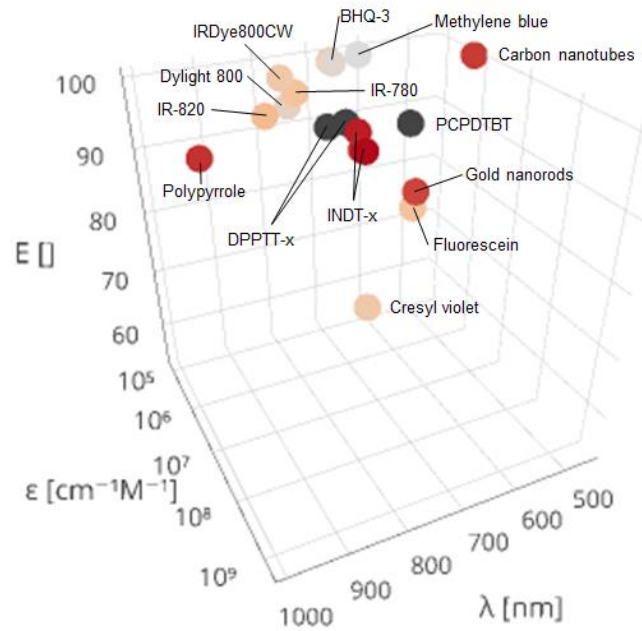
One of the most important properties of contrast agents for molecular PA imaging is its ability to generate strong PA signal upon excitation with light in the near-infrared. Therefore, initially the PA amplitude and μ_a spectra and the $\epsilon(\lambda_{\text{max}})$ were determined. The spectra show that chromophores, such as IR 820, gold nanorods and IND-T-BT, exhibit an absorption peak in the near-infrared at about 820 nm - ideal due to enhanced penetration depth of light into tissue at this wavelength (optical window of tissue). The wavelength of peak absorption of the other chromophores analysed is often located far outside of this window and range from 490-780 nm. Chromophores such as the polypyrrole nanoparticles show very broad absorption bands. The resulting spectra as well as the results of the ϵ measurements show, that the nanoparticles analysed exhibit very strong absorption compared to the organic dyes. Especially the gold nanorod sample ($\epsilon(\lambda_{\text{max}}) = 1.7 \cdot 10^9 \text{ cm}^{-1}\text{M}^{-1}$) as well as the polymeric nanoparticles, in particular the IND-T-BT nanoparticles ($\epsilon(\lambda_{\text{max}}) = 1.5 \cdot 10^8 \text{ cm}^{-1}\text{M}^{-1}$), show $\epsilon(\lambda_{\text{max}})$ orders of magnitude greater than the organic dyes analysed ($\sim 10^5 \text{ cm}^{-1}\text{M}^{-1}$). After generating the PA spectra and determining the extinction coefficient of the organic dyes and the nanoparticles, their ability to thermalize the absorbed light energy was analysed. Therefore E_t was measured using the two methods proposed (Table 4-6). Cresyl violet and fluorescein show significant losses via fluorescence whilst the remaining organic dyes and the nanoparticles analysed exhibit E_t values of about 100% and therefore are well suited for the conversion of the absorbed light energy to heat.

Subsequently, the results of the measurements of Γ of various sample solutions are presented, indicating no significant deviation from the value of Γ of the pure solvents (Table 4-7). However, upon further analysis of Γ of mixtures of light absorbing compounds a wavelength dependence of Γ was identified. The photostability measurements showed significant photobleaching of

some of the organic dyes (e.g. cresyl violet and fluorescein), while other organic dyes as well as the nanoparticles analysed exhibited little or no photobleaching.

Figure 4-19a shows a plot of E_t versus ϵ and λ_{\max} of the contrast agents analysed. The plot enables identifying suitable contrast agents for a given application. Both, the nanoparticles (coloured dots) and the organic dyes (pale coloured dots), cover a broad spectrum of λ_{\max} . However, the organic dyes appear, compared to nanoparticles, predominantly in the background of the plot, which demonstrates the superior PA signal generation properties of nanoparticulated contrast agents compared to contrast agents based on organic dyes. Organic dyes generally have lower ϵ values than the nanoparticles characterised and often exhibit low E_t values (Cresyl violet and Fluorescein). This can be made out by the position of the organic dyes in the lower background of the plot below compared to the nanoparticles which are found in the top front. The two 2D plots shown in Figure 4-19b have been included in order to make it easier to identify suitable contrast agents for a given application. Contrast agents of suitable λ and ϵ can be identified in the plot on the left and contrast agents of suitable Γ on the right in Figure 4-19b.

a)



b)

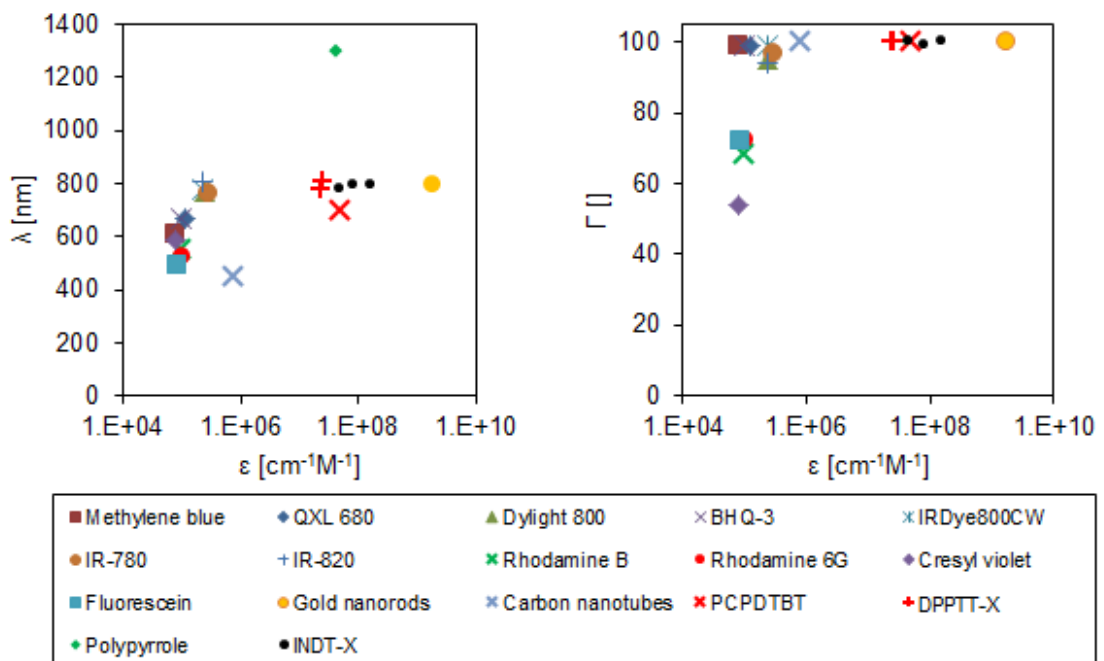


Figure 4-19: Plot of E_t versus ϵ and λ_{max} of the contrast agents characterised.

In summary, among all the chromophores analysed, gold nanorods and the π -conjugated semiconducting nanoparticles - INDT-BT are in terms of the PA signal generation ability the most promising candidates for the potential application as contrast agents for molecular PA

imaging, demonstrating the strongest extinction coefficient in the near-infrared, high E_t (100%) values and little photobleaching.

Even though gold nanorods have a higher ϵ based on the molar concentration, due to the novelty of the nanoparticles made from the π -conjugated polymer, IND-T-BT nanoparticles were chosen for further *in vitro* and *in vivo* demonstrations, which are detailed in the next chapter.

Chapter 5

In vitro and in vivo analysis

5.1 Introduction

After preparation of the various nanoparticles described in Chapter 3 and identification of those with the ability to generate strong PA signals (Chapter 4), the performance of one of the most promising nanoparticles was analysed in preliminary *in vitro* and *in vivo* experiments. The absorber chosen for the *in vivo* experiments is the novel π -conjugated nanoparticle made from the polymer INDT-BT. PCPDTBT was employed for the *in vitro* targeting experiments. In this chapter the experimental details of the *in vitro* and *in vivo* analysis are described and the performance of the nanoparticles that were synthesised is evaluated.

In the first section of this chapter the *in vitro* experiments are detailed and the results of targeting experiments analysing the ability of the nanoparticles, conjugated to an antibody, to target for an antigen in an assay related to an enzyme-linked immunosorbent assay are described. The ability of the nanoparticles, conjugated either to antibodies or a targeting peptide, to target cells was then analysed *in vitro*. The results of these experiments are presented in the final part of the first section. The second section of this chapter describes the *in vivo* analysis of the INDT-BT nanoparticles. First the ability of the nanoparticles to generate sufficient PA signal for the detection in a highly vascularised environment was demonstrated by acquiring PA images before and after intratumoral injection of the nanoparticles in an animal model. After this the experimental details and the results of the subcutaneous injection of the nanoparticles are presented. The aim of this second *in vivo* experiment was to compare the signal amplitude generated at various wavelengths in the *in vivo* experiment to the spectra generated using PA spectroscopy and absorption spectroscopy.

5.2 *In vitro* targeting experiments

5.2.1 *In vitro* antigen targeting

In the first instance, in order to analyse the targeting ability of the IND-T nanoparticles conjugated to the antibody A5B7 either via DSPE-PEG(2000)-COOH or DSPE-PEG(2000)-maleimide), an assay related to a direct enzyme-linked immunosorbent assay (ELISA) was performed. A direct ELISA employs an antigen attached to the walls of a polystyrene plate for the detection of an antibody present in a sample. Only the antigen specific antibodies present in the sample are retained within the wells of the plate. A substrate added to the well reacts with an enzyme present on the antigen specific antibodies and allows for the detection of the antibodies often via a colour change. Fortunately, PCPDTBT readily provides strong absorption in the visible and therefore enables a colour change in an experiment with PCPDTBT/Antibody conjugates, eliminating the last step of the ELISA. PCPDTBT was used for the experiments due to sufficient availability of the material. However, the behaviour in an *in vitro* targeting experiment using the π -conjugated semiconducting nanoparticles made from PCPDTBT compared to those made from IND-T-X is likely to be identical as the morphology and surface of the nanoparticles are analogous. Therefore, a similar degree of successful targeting should be achieved when replacing the PCPDTBT nanoparticles with other semiconducting polymeric nanoparticles such as IND-T nanoparticles.

5.2.1.1 Experimental

For the *in vitro* antigen targeting experiments the procedure found in ¹⁷² was used as a guideline. All experiments were performed in 96 well polystyrene microplates (Pierce, Thermo Fischer Scientific, UK) and the detection of a colour change was achieved using a plate reader with a spectral range of 220-1000 nm (CLARIOStar, BMG Labtech, UK). The antigen employed for the experiments was a carcinoembryonic antigen (CEA, Sigma Aldrich, UK) and allows binding to A5B7. For the experiments the microplates were coated with 100 μ L of a PBS solution containing 10 μ g mL⁻¹ CEA and were left over night at 4 °C. Some of the wells were left blank for comparison. Next, the microplates were washed twice using PBS. Subsequently, binding sites that remain in the polystyrene microplate wells following the initial coating step were blocked using a mixture of powdered non-fat milk (5 wt%) and Tween20 (1 wt%) in PBS. Therefore 150 μ L of the blocking buffer was added to the wells after the washing step and were incubated for two hours at 4 °C. Subsequently, the blocking buffer was washed off by flushing the wells twice with about 200 μ L of PBS. Using the plate reader, absorption spectra of the wells were generated in a wavelength range of 350-900 nm. After measuring the absorption spectra, 100 μ L of the sample solutions were added to the wells before incubating for one or two hours, giving the antibody time to attach to the antigen on the polystyrene surface. The samples consisted of aqueous dispersions of the semiconducting nanoparticles made from the polymer PCPDTBT, conjugated to A5B7 antibodies via DSPE-PEG(2000)-COOH or DSPE-PEG(2000)-

maleimide) linkers. The concentration of the nanoparticles ranged from 10-40 mg l⁻¹. Finally, the wells were washed three times using Tween20 (2 wt%) in PBS and four times using deionised water. After the last washing step only the PCPDTBT/A5B7 conjugates that successfully attached to the antigen remained in well, whilst the other non-attached nanoparticles were washed out. Subsequently to the last step, the absorption spectra with a wavelength range of 350-900 nm of each of the individual wells were measured using the plate reader. In order to detect a colour change the spectra were compared to the spectra generated before applying the sample and to the spectra of the wells which were intentionally left uncoated.

5.2.1.2 Observations

PCPDTBT nanoparticles conjugated to A5B7 via two different linkers were analysed at various concentrations. After the last washing step of the procedure, all samples wells, even the wells treated with the highest concentration of PCPDTBT/A5B7, appeared clear and the blue/green stain of the nanoparticles had disappeared. The spectra of the individual wells showed the same result and even at the wavelength of peak absorption (680 nm) the absorption value measured was negligible. These results may indicate that the nanoparticles conjugates either haven't targeted the antigens or detached themselves from the target.

Because the antigen targeting experiment wasn't successful, PCPDTBT nanoparticles were conjugated to a peptide with the amino acid sequence CLARLLT, replacing the antibody A5B7. In order to analyse the targeting ability of the PCPDTBT/peptide conjugate, cell overexpressing EGFR were used. The experimental details are described in the next section.

5.2.2 Cell targeting experiments

In order to further analyse the ability of the π -conjugated nanoparticles for molecular targeting a different targeting strategy was employed. Therefore, a peptide was synthesised and conjugated to the PCPDTBT nanoparticles using two different linker molecules. Cells were employed for the targeting experiments because the synthesised peptides don't interact with the antigens used in the previous experiment. In addition, cells are a closer representation of the environment the particles are required to be detected in.

5.2.2.1 Experimental

For the cell targeting experiments two different colorectal cancer cells lines (SW 12.22 (ATCC, US) and LS17.40 (ATCC, US)) were employed due to the overexpression of EGFR. EGFR is a surface receptor which is targeted by both the synthesised peptide with the amino acid sequence CLARLLT and the antibody A5B7. The cells were provided by Dr. Peter Johnson (UCL, Cancer Institute) and the peptide was synthesised by Dr. Robin Bofinger (UCL, Department of Chemistry). The PCPDTBT nanoparticles used were conjugated to either the peptides or the antibodies utilising two different maleimide functionalised lipids: the novel

maleimide lipid (shown in Chapter 4 of this thesis) or DSPE-PEG(2000)-maleimide. For the analysis of the targeting experiments, samples made from PCPDTBT/A5B7 nanoparticles conjugated using DSPE-PEG(2000)-COOH were also included.

The cells were grown in cell culture flasks (Nunc EasYFlask, Thermo Fischer Scientific, UK). Before use, cells were counted using an automated cell counter (Countess, INVITROGEN, UK), diluted down to gain 1 mL solutions containing $1 \cdot 10^6$ cells using cell medium and transferred to centrifugal tubes. Subsequently, the sample solutions were added to the tubes before the mixtures were incubated for 1 h at 36 °C. For comparison, instead of a nanoparticles sample, PBS was added to a number of the cell solutions, creating a blank sample. The cells were incubated in the cell medium solution because high cell viability can be expected and for convenience. The nanoparticle sample solutions consisted of different volumes (100-500 μ L) of 30 mgL^{-1} of PCPDTBT nanoparticles conjugated to the peptide or A5B7 using the novel maleimide lipid, DSPE-PEG(2000)-maleimide or DSPE-PEG(2000)-COOH as a linker. After the incubation the cells were centrifuged at 1200 rpm for 3 min before being washed three times using PBS. After this process only nanoparticles retained by the cells are left in the tube whilst all the unbound nanoparticles should have been washed out. After the last centrifugation step the resulting cell pellets were analysed using PA spectroscopy and compared to the cells treated only with PBS. The cells were also analysed using a spectrophotometer. Therefore the cells were re-dispersed in 500 μ L deionised water before acquiring spectra in the wavelength range between 350 nm and 900 nm.

5.2.2.2 Observations

Both the PA spectroscopy measurements as well as the transmission spectra generated using the spectrophotometer show no significant change in the absorption of the samples compared to cells treated only with PBS (blank solution). Compared to the blank solution even at the absorption maxima of the nanoparticles at 680 nm no change in the absorption or the PA amplitude could be detected. This indicates that none of the nanoparticles incubated have been retained at the target. This was observed for all the samples analysed, including the samples incubated with a high volume of nanoparticles, as revealed by the PA spectroscopy measurements and the transmission spectra. As before, it can be observed, that the contrast is lost during the washing step - eliminating the unbound nanoparticles from the vial.

5.2.3 Conclusion

All the targeting experiments conducted indicated that the nanoparticle/targeting moiety conjugates weren't retained at the target. The results are consistent across all the measurement modalities used, such as spectrophotometers (plate reader and cuvette measurements) and the PA spectroscope. These disappointing results may be due to several factors, such as detaching of the linker molecule including the targeting moiety from the nanoparticles after binding to the target or impairment or loss of the binding function after conjugation. In order to improve the

targeting of the nanoparticles different linker systems, such as a peptide based linker as described in ¹⁷³, need to be analysed and the conjugation procedures need be improved to gain more control over the conjugation site. Crosslinking of the linkers may prohibit detaching of the linkers from the nanoparticle surface.

After analysis of the targeting ability of the π -conjugated polymeric nanoparticles, their ability to generate PA signals in an *in vivo* environment was verified. The experimental details of the *in vivo* experiments and the results are described below.

5.3 *In vivo* experiments

In vivo experiments were conducted in order to show the ability to detect the novel π -conjugated nanoparticles made from the polymer INDT-BT in living subjects using PA imaging. INDT-BT was chosen for these experiments due to its high ϵ . Two similar experiments were performed: (i) the intratumoral injection of an aqueous solution of the nanoparticles to a tumour grown on the flank of a mouse and (ii) a subcutaneous injection of a small volume of a solution containing the nanoparticles into the flank of a mouse. The initial experiment is designed to demonstrate the ability of the novel nanoparticle to be detected in a highly vascularised environment, whilst the latter serves to show the wavelength dependence derived from *in vivo* PA images.

A detailed description of the PA tomography system used for the detection of the nanoparticles can be found in ¹⁴⁰ and is briefly refer to in Chapter 3. For the excitation a 50 Hz tuneable fibre-coupled Q-switched Nd:YAG pumped OPO laser (premiScan, GWU and Quanta-Ray PRO-270, Newport Spectra Physics) was employed and a Fabry-Perot based ultrasound detection system with a -3 dB bandwidth of 22 MHz was used for the detection of the generated ultrasound. Excitation source and ultrasound transducer were operated in backward mode.

5.3.1 Intratumoral injection

In order to promote tumour growth, approximately $1 \cdot 10^6$ SW12.22 cells were subcutaneously injected into the right flank of an eight week old male NOD Scid gamma mouse. About 3 weeks after the injection the tumour had grown to a sufficient size for the experiment posing a volume of about 1 cm^3 . For the imaging experiments the mouse was anaesthetised using isoflurane in oxygen (4 % (vol/vol) at a flow rate of 2 Lmin^{-1} for induction and 1.5 % (vol/vol) at a flow rate of 1 Lmin^{-1} for maintenance). Before imaging the hair in the region surrounding the tumour was removed using hair removal cream. During the experiment the body temperature of the animal was maintained using a homemade temperature controller. The anaesthetised mouse was placed on a custom designed cradle and positioned on the scanner with the region of interest facing towards the Fabry-Perot sensor. Using the cradle ensured that the same field of view (14

x 14 mm² area) was imaged when placing the mouse on the scanner. Acoustic coupling between the mouse and the sensor was accomplished using ultrasound gel applied to the mouse skin. Images were acquired with the excitation laser tuned to 750 nm, 800 nm and 850 nm before and 1 h and 5 h after intratumoral injection of 50 μ L of 160 mgL⁻¹ IND-T-BT nanoparticles into the centre of the tumour. During injection the needle was retreated from the tumour in order to spread the nanoparticles throughout the tumour volume. PA images were reconstructed from the PA signals recorded using an algorithm based on time reversal as described in ^{174,175}. The resulting maximum intensity projection PA images are shown in Figure 5-1.

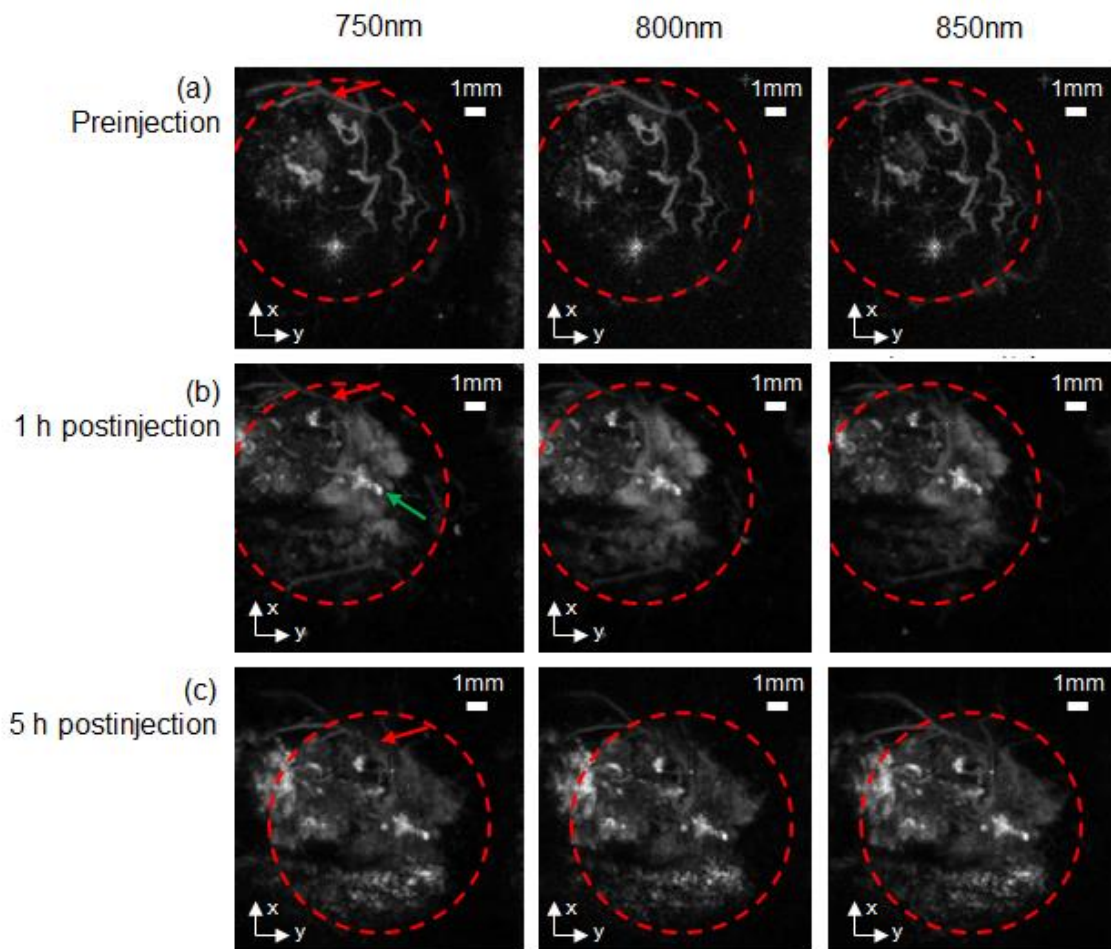


Figure 5-1: *In vivo* PA images (x-y maximum intensity projection; area 14 x 14 mm²) at excitation wavelengths of 750 nm, 800 nm and 850 nm before injection (a), 1 h (b) and 5 h post intratumoral injection (c). The red arrow shows the same blood vessel at the different time points, allowing to judge the position of the tumour on the PA scanner. The green arrow indicates the site of injection. The red dashed line shows the tumour margin.

5.3.1.1 Observations

The maximum intensity projections of an area of 14 x 14 mm² of the mouse flank pre-injection (Figure 5-1a), show the vasculature of the tumour. The absorption of haemoglobin is strong enough for PA signal generation across all the excitation wavelengths analysed. The tumour margins are indicated by the red dashed line. Figure 5-1b and c show the PA images post-intratumoral injection. The bright spot (indicated by the green arrow) close to the centre of the images indicates the site of injection. The post-injection images clearly show the contrast generated by the nanoparticles across all the wavelengths measured. Especially in Figure 5-1b strong contrast generated by the nanoparticles located in the extracellular space surrounding the site of injection can be seen. 5 h post-injection the nanoparticles seemed to have spread throughout the tumour volume. This can be seen close to the side of injection (Figure 5-1b and c). 1 h post-injection strong PA contrast close to the side of injection can be seen, whilst 5 h post-injection the nanoparticles have accumulate at the outer edge of the tumour, seen as contrast close to the bottom of the dashed red circle. The images suggest that the injected nanoparticles have spread throughout the tumour volume and a PA signal of the nanoparticles could be detected for at least 5 h post-injection. The PA images demonstrate that the novel π -conjugated IND-T-BT nanoparticles can be detected at a depth of about 2 mm in a highly vascularised environment, such as a tumour, using PA tomography.

In a second *in vivo* experiment the chromophore was injected subcutaneously into the flank of a mouse. The aim of this experiment was to create a well-defined volume of the chromophore solution in order to compare the signal amplitude at various wavelengths to the spectra generated using PA spectroscopy and transmission spectroscopy. The experimental details and the results can be found below.

5.3.2 Subcutaneous injection

For the second *in vivo* experiment using the novel π -conjugated IND-T-BT nanoparticles, 10 μ L of an aqueous solution containing 160 mgL⁻¹ of IND-T-BT nanoparticles was injected subcutaneously into the right flank of a 12 week old male NOD Scid gamma mouse. PA images were acquired pre- and post-injection using the method described above at ten wavelengths between 600 nm and 1000 nm. A selection of reconstructed images generated using 5 different excitation wavelengths (out of 10 acquired) is shown in Figure 5-2, revealing the presence of the nanoparticles after injection.

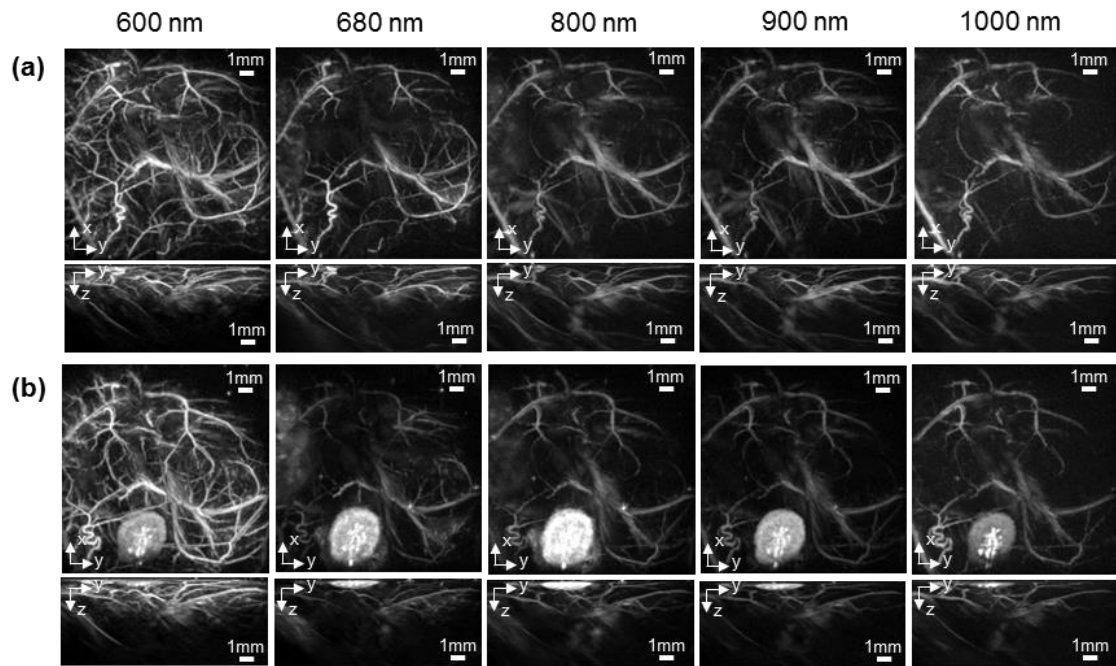


Figure 5-2: Multi wavelength *in vivo* photoacoustic showing spectral dependence of IND-T-BT nanoparticles and vasculature: Photoacoustic images (a) before (b) after subcutaneous injection of IND-T-BT nanoparticles in the flank of a mouse. x-y maximum intensity projections (top rows, area $14 \times 14 \text{ mm}^2$) and y-z maximum intensity projection (bottom rows, area $14 \times 6 \text{ mm}^2$) acquired at different excitation wavelengths are shown.

5.3.2.1 Observations

The PA images show that at 600 nm blood generates comparable PA signals to the nanoparticles, resulting in relatively low differential image contrast, whilst at 800 nm the nanoparticles provide stronger PA signal than blood. The contrast of the nanoparticles is still visible at long wavelengths (1000 nm), against the background of blood and increasing absorption water.

In order to compare the PA amplitude of the *in vivo* PA images generated in the wavelength range analysed with the spectra generated by PA spectroscopy and absorption spectroscopy, the image intensity in 3D over the regions corresponding to the nanoparticles was estimated. In order to correct for the variation in pulse energy of the laser at different wavelengths the image intensity was normalised by the integrated image intensity of the first slice of the 3D image where the particles are not present. The resulting *in vivo* wavelength dependence of the IND-T-BT nanoparticles, derived from the PA images, show in Figure 5-2, is presented in Figure 5-3. For comparison, spectra of IND-T-BT nanoparticles generated using PA spectroscopy and absorption spectroscopy are also plotted in the same figure.

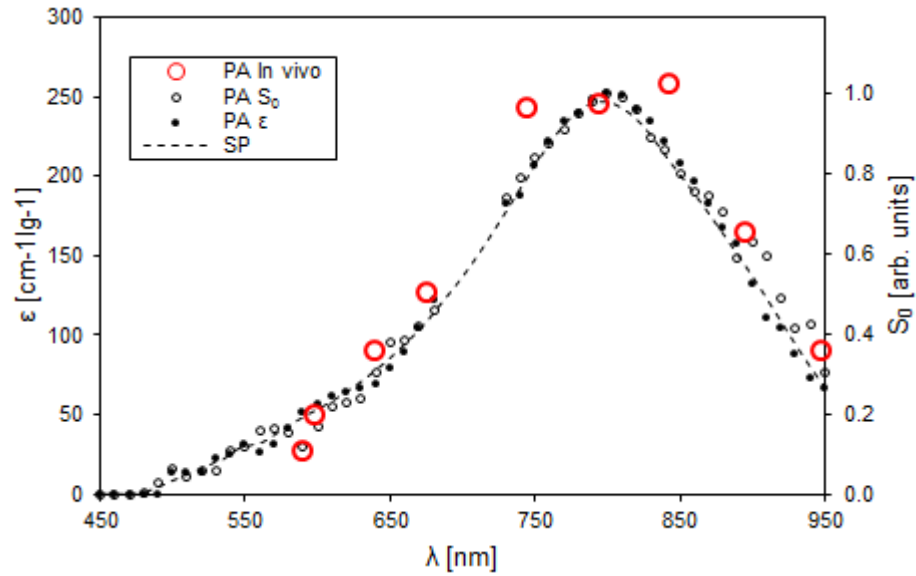


Figure 5-3: Normalised wavelength dependence of INDT-BT nanoparticles *in vivo*. The PA *in vivo* values (red circles) are the normalised image intensities of the 3D PA images (Figure 5-2) over the regions corresponding to the nanoparticles. PA S_0 (black circles) is the PA amplitude and PA ϵ (black dots) the extinction coefficient measured using PA spectroscopy. SP (dashed line) is the extinction coefficient spectrum measured using a spectrophotometer.

The *in vivo* wavelength dependence of the INDT-BT nanoparticles agrees well with the spectra generated using the PA spectroscopy and the spectrophotometer, also shown in Figure 5-3. The results shown in Figure 5-2 and Figure 5-3 illustrate the wavelength dependent differential contrast between the novel nanoparticles and the vasculature, which can be used to unambiguously discriminate the presence of the nanoparticles *in vivo*.

5.4 Conclusion

The results shown in Figure 5-1 and Figure 5-2 demonstrate the ability of the novel π -conjugated polymeric semiconducting nanoparticles to be detected at superficial depths in an *in vivo* environment using PA tomography. It has been shown, that even in the highly vascularised environment of a tumour, it is possible to distinguish the nanoparticles from the endogenous contrast. The preliminary *in vivo* experiments demonstrated that at 800 nm the INDT-BT nanoparticles exhibit a significantly stronger PA signal generation than haemoglobin at the concentration present at the injected site. This is due to the favourable properties of the novel nanoparticles, such as high extinction coefficient with an absorption maximum in the near-infrared in the optical window of low absorption of endogenous chromophores within human tissue, good thermalisation efficiency and photostability.

However, the targeting approach, using amphiphilic phospholipids to link the nanoparticles with targeting moieties, didn't show any significant retention of the nanoparticles at the target. These results were obtained either targeting for antigens in experiments similar to a direct ELISA or targeting for two different cell lines known to overexpress EGFR. The lack of retention of the nanoparticles at the target may be caused by a variation of sources, such as detaching of the linker molecule including the targeting moiety from the nanoparticles after binding to the target or impairment or loss of the binding function after conjugation. In order to optimise the nanoparticles for their ability for specific targeting, future work could include crosslinking of the linkers or using different linker systems, for example a peptide based linker or direct conjugation to the polymeric core of the nanoparticles.

Chapter 6

Conclusions

6.1 Conclusions

The work described in this thesis was aimed at identifying materials exhibiting strong PA signal generation upon excitation that could be suitable as contrast agents for molecular PA imaging. Therefore, a PA spectroscopy was designed and evaluated. Methods for the evaluation of all the parameters involved in the PA signal generation were proposed and verified using reference absorbers with well-known properties. In the next step, nanoparticles with suitable optical properties were synthesised and together with commercially available nanoparticles and organic dyes were analysed using the PA spectroscopy. Comparing the array of organic dyes and nanoparticles studied allowed appoint the compounds exhibiting strong PA signal generation, one of which was analysed in preliminary *in vitro* and *in vivo* experiments. This last part of the thesis summarises the findings, draws conclusions from each section and provides the reader with an outlook and suggestions for future work.

6.2 Summary of findings

6.2.1 PA spectroscopy and methods for the evaluation of the properties relevant for the PA signal generation of organic dyes and nanoparticles

After assessing the performance of the PA spectroscopy set-up described in Chapter 3, it was demonstrated that the PA spectroscopy enables accurate measurement ($\pm 5\%$) of μ_a in a range of $0.5\text{-}25\text{ mm}^{-1}$ with a resolution of $\pm 3\%$. PA amplitude measurements on the other hand are limited to a smaller range of detection ($0.5\text{-}10\text{ mm}^{-1}$, $\pm 5\%$ accuracy and $\pm 8\%$ resolution) due

to the limited bandwidth of the PVDF based ultrasound transducer used. The various PA spectra shown throughout this thesis confirm, that the detection range is sufficient for the intended application, allowing to generate PA amplitude and μ_a spectra of solutions of organic dyes and dispersions of nanoparticles in order to compare their performance.

However, in order to assess the performance of highly diluted samples or compounds exhibiting very weak absorption it would be advantageous to extend the lower detection limit for both the PA amplitude and μ_a . To achieve this, the parasitic PA signal generated at the surface of the ultrasound transducer needs to be reduced by reducing the excitation light reaching the ultrasound transducer. This could be realized by various measures, for example filling the water tank with a scattering medium instead of water or using an acoustically transparent mirror to reflect the excitation light away from the ultrasound transducer.

In addition, extending the upper detection limit, especially of the PA amplitude measurements, would be advantageous for measurements of mixtures of compounds exhibiting great differences in their absorption. An example for this is a mixture of gold nanorods with ϵ typically in the range of $10^9 \text{ cm}^{-1}\text{M}^{-1}$ and organic dyes with ϵ of about $10^5 \text{ cm}^{-1}\text{M}^{-1}$. At an equal molar concentration it is impossible to resolve the absorption maxima of the two compounds with the current PA spectroscopy set-up. In order to enable resolving the two absorption maxima of such a mixture, the dynamic range of the PA spectroscope needs to be improved. The lower detection limit can be decreased as mentioned above. To improve the upper detection limits of the PA amplitude and μ_a measurements, the bandwidth of the ultrasound transducer needs improvement. To increase the bandwidth of the ultrasound transducer, a thinner PVDF film could be applied as a sensing element. This measure reduces the NEP and therefore might compromise the lower detection limit. A different measure increasing the upper detection limit is to replace the piezoelectric transducer with a Fabry-Perot sensor, which have shown to exhibit very high bandwidths¹⁷⁶.

The second part of Chapter 3 describes the methods for the determination of E_t , Γ and the photostability profile of sample solutions consisting of organic dyes and nanoparticles. For the determination of E_t two methods were proposed and validated using solutions of rhodamine B and rhodamine 6G at various concentrations. The results were in good agreement with literature values and demonstrated, that E_t values as low as 50% can be measured. Because E_t impacts the PA signal generation efficiency the methods pose a useful tool for the characterisation of potential contrast agents for PA imaging. Furthermore the methods might be useful for other fields of application apart from examining the ability of a compound to generate PA signals, such as the determination of E_t of organic dyes, nanoparticles or quantum dots for example for biomedical fluorescence imaging or next generation barcodes (see Appendix for a detailed description). The PA measurement of E_t may also be advantageous compared to pure optical methods such as fluorescence spectrometers which require fluorescence standards for the quantification of E_t . Therefore the measurement of E_t using the PA spectroscope saves the cost for an expensive fluorescent standard and obviates errors introduced by this reference measurement. Furthermore the PA spectroscope enables the measurement of E_t of solutions

exhibiting strong absorption characteristics, which can be difficult to achieve using conventional fluorescence spectrometers. This is because purely optical methods require sample solutions of relatively low absorption in order to avoid excessive reabsorption of the emitted light before being detected by the photomultipliers. Therefore, the methods for the determination of E_t using the PA spectroscopy pose a useful tool for characterisation of fluorophores for various applications.

Chapter 3 also describes a method for the determination of Γ using the PA spectroscopy. The method was validated using mixtures of water and alcohol. The measured values of Γ of the pure solvents (methanol and ethanol) compared well with literature values whilst the resulting values for the mixtures followed the expected linear trend with a coefficient of determination (R^2) of about 0.99. Despite being an important measure involved in the PA signal generation, the measurement of Γ spectra of mixtures of light absorbing compounds has shown a wavelength dependency, which has been explained by the formation of clathrates and the characteristic change in local density of the solvent molecules surrounding the central atom of those clathrates. Therefore, the PA measurement of Γ may be a useful tool for the characterisation of the solvation process of ions or molecules in various solvents. These measurements could be generating valuable information about the density of solvent molecules of clathrates relative to the bulk solvent molecules and therefore help understanding the solvation process and the kinetics of chemical reactions.

Chapter 3 furthermore demonstrates an initial photostability experiment verifying the ability to investigate the photobleaching profile of nanoparticles and organic dyes using the PA spectroscopy. This measure allows for the estimation of the number of excitation cycles a compound can undergo before its optical properties irreversibly change. Therefore, the photobleaching profile is an important measure for molecular PA imaging, due to its impact on the signal generation. However, using PA spectroscopy for the purpose of determining the photobleaching of organic dyes, fluorophores and fluorescent reporter genes may be useful for the other fields such as biomedical research (i.e. quantitative PA imaging, fluorescence imaging and labelling), and industry (the development of organic light-emitting diodes and solar panels).

The ability of the PA spectroscopy to generate PA amplitude and μ_a spectra and to accurately determine ϵ , E_t , Γ and the photostability profile of nanoparticles and organic dyes has been demonstrated, fulfilling the primary aims (i) and (ii) of this project as stated in Chapter 1. The approach represents a simple and rapid method for comprehensively evaluating potential PA contrast agents for their ability to generate PA signals.

6.2.2 Synthesis of various nanoparticles and characterisation of potential contrast agents for molecular PA imaging

Various protocols have been used to generate a range of different nanoparticles, including copper sulphide nanoparticles, dye loaded PS nanoparticles, poly(allylamine) nanoparticles, PEDOT:PSS nanoparticles, polypyrrole nanoparticles, PCPDTBT nanoparticles, DPPTT-x nanoparticles and INDT-x nanoparticles. Some of the methods used were adapted from procedures found in literature, whilst for other preparations literature procedures only served as guidelines. Next, the prepared nanoparticles and an array of commercially available nanoparticles and organic dyes were examined using the PA spectroscopy in combination with the methods proposed for the analysis of the individual parameters involved in the PA signal generation, fulfilling the primary aim (iii) of this project as stated in Chapter 1. On the basis of this analysis gold nanorods and the novel π -conjugated nanoparticles made from the semiconducting polymer INDT-BT were found to be promising candidates for the application as contrast agents for molecular PA imaging, due to their strong ϵ , high E_t and a narrow absorption spectrum with an absorption maximum in the near-infrared in the optical window of human tissue. Gold nanorods are known to be prone to light induced overheating, causing a change in their optical properties, which has been confirmed in this thesis. Owing to this disadvantage the INDT-BT nanoparticles were further analysed in preliminary *in vitro* targeting experiments and *in vivo* imaging studies.

6.2.3 *In vitro* and *in vivo* experiments

For the *in vitro* analysis of the π -conjugated nanoparticles a number of experiments were conducted analysing the ability of the nanoparticle/targeting moiety conjugate to selectively be retained at the target. The results were obtained either targeting for antigens or targeting for two different cell lines using antibodies and peptides. Unfortunately no retention of the nanoparticles at the target could be observed. The lack of retention of the nanoparticles at the target may be caused by a variation of sources, such as detaching of the linker molecule including the targeting moiety from the nanoparticles after binding to the target or impairment or loss of the binding function after conjugation to the nanoparticles via the linkers.

The preliminary *in vivo* experiments demonstrated that at 800 nm the semiconducting polymeric nanoparticles based on INDT-BT exhibit a significantly stronger PA signal generation than haemoglobin, thus allowing to unambiguously distinguish the nanoparticles from the endogenous contrast. Even in a highly vascularised environment of a tumour, the novel nanoparticles can be visualised using PA tomography. These results can be attributed to the properties of the INDT-BT nanoparticles: high ϵ with an absorption maximum in the near-infrared (800 nm) in the optical window of human tissue and high E_t .

6.2.4 Summary

In summary, the work presented in this thesis suggests that using the PA spectroscopy in combination with the methods used allows determining all the parameters involved in the PA signal generation and therefore thoroughly analyse organic dyes and nanoparticles for their ability to generate PA signals.

After assessing the performance of the PA spectroscopy and validation of the methods, the PA spectroscopy was employed to determine ϵ , E_t , Γ and the photobleaching profile of various organic dyes and nanoparticles adding valuable information to the database of properties of such compounds. This allows choosing a compound for any specific application as contrast agent for molecular PA imaging based on the PA properties. Compounds analysed included commercially available organic dyes and nanoparticles as well as nanoparticles synthesised in house. The analysis showed that π -conjugated semiconducting nanoparticles based on the polymer IND-T-BT and gold nanorods exhibit exceptional strong PA signal generation upon excitation in the near-infrared - ideal for the application as contrast agent for molecular PA imaging. Subsequently the semiconducting polymeric nanoparticles were used in preliminary *in vitro* and *in vivo* experiments. Although the targeting strategy using the polymeric nanoparticles conjugated to either a full antibody or a small peptide were unsuccessful, the *in vivo* experiments demonstrated their ability to generate strong PA signals, allowing to unambiguously distinguish the nanoparticles from the endogenous chromophores such as haemoglobin.

6.2.5 Publications arising from this work

- Conference Proceeding (SPIE PhotonicsWest 2014):
Stahl, T., Allen, T., & Beard, P. (2014). Characterisation of the thermalisation efficiency and photostability of photoacoustic contrast agents. In A. A. Oraevsky & L. V. Wang (Eds.), *Proc. of SPIE, Photons Plus Ultrasound: Imaging and Sensing* (Vol. 8943, pp. 89435H-1 – 89435H-8). doi:10.1117/12.2039694
- Expanding on the conference proceedings a paper has been produced and is ready for submission to the Journal of Biomedical Optics (JBO): "PVDF-based photoacoustic spectroscopy – Methods for the evaluation of potential contrast agents for molecular photoacoustic imaging."
- A paper describing the synthesis and the characterisation of the novel π -conjugated polymeric nanoparticles based on the IND-T-x polymers has been submitted for review to the journal American Chemical Society (ACS) in August 2016: "Tuneable Semiconducting Polymer Nanoparticles with IND-T-Based Conjugated Polymers for Photoacoustic Molecular Imaging."

6.3 Suggestions for future work

6.3.1 Increasing the detection range of the PA spectroscopy

In order to improve the PA spectroscopy set-up an ultrasound transducer with increased bandwidth and NEP should be employed. Especially the bandwidth of the transducer used throughout this thesis may be improved. Increasing the bandwidth of the ultrasound transducer would allow accurately mapping of time-domain PA signals exceeding the current upper detection limit of both the PA amplitude and μ_a . This is especially important to improve the upper detection limit of the PA amplitude, which was determined to be significantly lower than the upper detection limit of μ_a measured using the PA spectroscopy. Increasing the bandwidth of the ultrasound transducer could be achieved by applying a thinner PVDF film as the sensing element or by using a different ultrasound sensor, such as a Fabry-Perot sensor which have been demonstrated to exhibit very high bandwidth >200 MHz¹⁷⁶.

In order to achieve a lower detection limit of both the PA amplitude and the μ_a measurements, first and foremost the parasitic signal generated at the surface of the ultrasound transducer needs to be reduced. The parasitic signal is generated at the surface of the transducers by the light that hasn't been absorbed in the sample solution in the cuvette. To avoid this, various approaches could be considered, for example: increasing the length of the light path through the sample cuvette, filling the water tank with a scattering medium such as intralipid instead of water or using an acoustically transparent mirror to reflect the excitation light away from the ultrasound transducer. In this thesis, in order to acquire PA signals of sample solutions with low absorption, neutral density filters were used to decrease the fluence of the laser before reaching the sample and the light path of the sample cuvette was increased, both reducing light passing through the cuvette and reaching the ultrasound transducer. These measures have reduced the parasitic signal, to gain the current lower detection limit of the PA amplitude and μ_a . Using a scattering medium for the attenuation of the excitation light or using a mirror reflecting light away from the transducer, has the potential to further reduce light reaching the surface of the ultrasound transducer, but may also introduce another source of parasitic PA signals similar to the signal generated at the surface of the ultrasound transducer. Another approach to avoid the generation of parasitic PA signals originating from the surface of the ultrasound transducer is to offset the transducer from the light path. This however requires a transducer with low directional sensitivity and may therefore compromise the NEP.

6.3.2 Improving the synthesis employed for the preparation of nanoparticles

Although a number of nanoparticles have been synthesised during the course of this thesis, many of the protocols employed yielded unstable dispersions of nanoparticles inadequate for the intended application as a contrast agent for molecular PA imaging. In order to further evaluate the PA properties of those nanoparticle species, the protocols used for the synthesis

need to be improved. This could involve applying different surfactants, increasing the ζ -potential of the particles and thus decreasing the tendency to aggregate.

Some of the protocols employed for the production of nanoparticulated chromophores yielded suspensions of low absorption. Especially the dye loaded PS nanoparticles suffered from leaching out of the dye molecules from the polymeric matrix and although the concentration of the nanoparticles was relatively high (0.5 wt%) the resulting solutions were of low absorption. To improve the absorption of this nanoparticle species, different dyes with low solubility in water should be employed, avoiding the leaching out of the dyes from the polymeric matrix.

6.3.3 Improving the molecular targeting ability

The targeting approach used didn't show any significant retention of the nanoparticles at the target. It was hypothesised, that this was caused by either the detaching of the linker molecule including the targeting moiety from the nanoparticles after binding to the target or impairment or loss of the binding function after conjugation. To improve this and to optimise the specific targeting, future work could include crosslinking of the linkers or using different linker systems, such as a peptide based linker¹⁷³ or directly linking the targeting moieties with the polymeric core. In order to rule out impairment or loss of the binding function of the antibodies used for the targeting, other methods for the conjugation should be employed in order to regioselective establish a link between the chromophore and the antibody, as described in ¹⁷⁷. Once the particles have been conjugated, their ability for molecular targeting should be analysed in ELISA type studies and cell conjugation studies as demonstrated.

6.3.4 Access the toxicity and improve clearance of the nanoparticles

In this thesis, the characterisation of the organic dyes and nanoparticles solely assessed the ability to generate PA signals upon excitation. The results of this characterisation clearly demonstrated that nanoparticles such as gold nanorods and semiconducting polymeric nanoparticles exhibit ϵ orders of magnitude stronger than organic dyes and high E_g , providing robust and strong PA signal generation. However, compared to organic dyes, nanoparticles are known to exhibit poor biodistribution and clearance profiles, increasing long-term toxicity concerns. Whilst small molecules such as organic dyes have shown to be excreted via renal clearance, nanoparticles commonly accumulate in liver and spleen. Therefore, nanoparticulated contrast agents offering both, strong signal generation and renal clearance, would have a significant advantage for clinical translation. Consequently, future work would involve assessing the biodistribution and the toxicological characterisation especially of the IND-T-BT nanoparticles. In order to improve the clearance profile and any acute toxicity concerns posed by the nanoparticles, new formulations of the nanoparticles and their surface coating may be required. In order to gain renal clearance an approach similar to that demonstrated by Tam et al¹⁷⁸ could be realised. They used biodegradable plasmonic nanoclusters containing gold nanoparticles with a diameter of 5 nm to generate PA signals in the near-infrared. Preparing

biodegradable nanoclusters containing semiconducting polymers (e.g. INDT-BT) might be a solution in order to gain strong PA signals and enable the controlled clearance from the organism.

Appendix

A1: Preparation of contrast agents

Introduction:

This chapter describes the methods for the preparation of various nanoparticles with promising properties as contrast agents for molecular PA imaging. This includes the preparation of the nanoparticle dispersions, as well as the conjugation to targeting moieties and fluorescent markers. The methods for the preparation of the nanoparticles and the conjugation reactions have been adapted from the literature and were refined to meet the requirements to generate contrast agents for PA imaging. For some preparation methods, such as the miniemulsion or the stabilising of carbon nanotubes, literature procedures only served as guidelines. In order to determine the stability of the samples, particle size and polydispersity of the nanoparticle dispersions generated were analysed directly after their preparation using DLS. The preparation of nanoparticle dispersions comprises carbon nanotubes, copper sulphide nanoparticles, dye loaded PS nanoparticles, poly (allylamine) nanoparticles, PEDOT:PSS nanoparticles, polypyrrole nanoparticles, PCPDTBT semiconducting polymer nanoparticles.

Methods

Preparation of stable aqueous suspension of carbon nanotubes

In order to measure the PA properties of carbon nanotubes, using the methods described in Chapter 3, a stable aqueous colloidal solution of the nanoparticles was required. Therefore, various surfactants were tested in order to stabilise the nanoparticles. The carbon nanotubes used for the experiments were single walled carbon nanotubes (SWCNT, Sigma-Aldrich, UK) with diameters in the range of 1.2-1.5 nm and multi walled carbon nanotubes (MWCNT) with diameters in the range of 6-9 nm and a length of 5 μm . In the first instance Tween20, a polysorbate surfactant, was chosen due to its stabilizing properties and its availability. Therefore, five samples of each of the nanotubes were prepared, each containing 1 mL of an aqueous solution of Tween 20 (Sigma-Aldrich, UK) at different concentrations, ranging from 1-15 vol%. Approximately 1 mg of carbon nanotubes (single walled or multi walled) were added to each of the solutions. After vortexing for 3 min the dispersion was left in an ultrasonic bath for 1 h at room temperature. The resulting mixtures were left to settle overnight. After about 15 h the carbon nanotube solutions were inspected. The carbon nanotubes in all five sample mixtures settled to the bottom of the flask forming a thin layer of colloids. However, the supernatant, consisting of an aqueous solution of Tween20, of the samples prepared using 10 and 15 vol% of the surfactant seem to contain a small amount of the nanotubes, which is evident due to the grey colouring compared to the other samples (see Table A1-1).

Table A1-1: Results from the initial attempt to form a stable colloid solution using single walled carbon nanotubes (SWCNT) or multi walled carbon nanotubes (MWCNT).

Sample	Stable solution	Properties of supernatant
1 mg SWCNT in 1 vol% Tween20	No	Opaque, white
1 mg SWCNT in 3 vol% Tween20	No	Opaque, white
1 mg SWCNT in 5 vol% Tween20	No	Opaque, white
1 mg SWCNT in 10 vol% Tween20	No	Opaque, grey
1 mg SWCNT in 15 vol% Tween20	No	Opaque, grey
1 mg MWCNT in 1 vol% Tween20	No	Opaque, white
1 mg MWCNT in 3 vol% Tween20	No	Opaque, white
1 mg MWCNT in 5 vol% Tween20	No	Opaque, white
1 mg MWCNT in 10 vol% Tween20	No	Opaque, grey
1 mg MWCNT in 15 vol% Tween20	No	Opaque, grey

However, the optical absorption of the supernatants, obtained using high concentration of the surfactant, was too low to be able to measure the PA properties. Therefore, a different approach using PEG methyl ether thiol ($M_n=2000$; Sigma-Aldrich, UK) was needed to give a stable aqueous colloidal solution.

A procedure similar to the procedure used here, can be found in ¹⁷⁹ and served as guideline for the stabilisation procedure. Therefore 14 mg of the single walled or the multi walled carbon nanotubes were added to 7 mL of an aqueous solution of PEG methyl ether thiol (20 gL^{-1}). After vortexing for 3 min the dispersion was left in an ultrasonic bath for about 2 h at about $30 \text{ }^\circ\text{C}$. The black colloidal solution was left overnight, before dialysis against deionised water, using dialysis tubing with a molecular weight cut off (MWCO) of 120 kDa (Merck Millipore, US). The resulting dark black solution, containing 2 gL^{-1} of carbon nanotubes, was stable over many days and showed absorption coefficients sufficient for PA analysis. However, a small amount of carbon nanotubes formed a precipitate visible as a dark black layer at the bottom of the sample container.

Preparation of copper sulphide nanoparticles

Copper sulphide nanoparticles were reported to act as efficient contrast agents for PA imaging, exhibiting strong absorption in the near-infrared due to surface plasmon resonance, with small diameters in the range of 10 nm. To analyse their properties the particles were prepared following the procedure described in ⁸⁷. Therefore 10 μL of an aqueous solution of 1 M sodium sulphide (Sigma-Aldrich, UK) was added to 1000 mL of an aqueous solution of 1 mmol copper chloride (Sigma-Aldrich, UK) and 0.68 mmol sodium citrate (Sigma-Aldrich, UK) under stirring at room temperature. To avoid oxidation of the mixture the reaction was performed in a sealed 3-neck round bottom flask under argon atmosphere and all liquids were either degassed via bubbling nitrogen through the liquid over night or the freeze-pump-thaw method in 3 cycles. After stirring the reaction mixture for 5 min at 1000 rpm it was heated to about $90 \text{ }^\circ\text{C}$ in an oil bath. Subsequently, about 15 min after the mixture reached $90 \text{ }^\circ\text{C}$, the reaction was terminated by cooling the flask to room temperature. In order to stabilise the nanoparticles in solution, 1 mg of PEG methyl ether thiol ($M_n=2000$; Sigma-Aldrich, UK) was added to the mixture and left overnight at room temperature under mild stirring (100 rpm).

Observations

Three batches of the copper sulphide nanoparticles were prepared as described above. All three dispersions generated were unstable, showing a dark green precipitate evident a few minutes after preparation. Measuring the average particle size and the PDI of the dispersion confirms this - aggregating nanoparticles with great average sizes ($>450 \text{ nm}$) and large PDI (>0.5). Due to these results the preparation of the particles was terminated. The lack of stability of the nanoparticle dispersion could be due to a various reasons such as insufficient surfactant surface coverage or oxidation of the sodium sulphide due to unsatisfactory degassing of the

solvents. However, even though the attempts were unsuccessful it is worth to further investigate this class of nanoparticles because they have been reported to exhibit strong PA signal generation. In addition to their PA properties, due to their size (~10 nm) copper sulphide nanoparticles bear the potential to be excreted from an organism via renal clearance which is a significant advantage for clinical translation.

Preparation of polymeric nanoparticles

Polymeric nanoparticles as contrast agent for molecular PA imaging are due to their ability to generate strong PA signals, their photostability, biocompatibility and low acute toxicity a promising alternative to nanoparticles such as gold nanorods. Polymeric nanoparticles are tuneable in size, morphology and optical properties and allow encapsulation of small molecules such as dyes or drugs. In order to explore the ability of this group of nanoparticles various polymeric nanoparticles loaded with dye molecules and semiconducting nanoparticles were prepared as described below. Initially, a swelling procedure, loading dye molecules to the polymeric matrix of PS nanoparticles was explored. Subsequently, in order to analyse the targeting ability of the dye loaded PS nanoparticles, they were conjugated to an antibody.

Swelling procedure to stain polystyrene nanoparticles

In order to generate contrast agents based on commercially available PS nanoparticles, a swelling procedure was applied, which allows loading the polymeric matrix of the particles with dyes, introducing the desired optical properties to the nanoparticles. The procedure was adapted from ¹⁸⁰. 50 nm diameter, PS nanoparticles with carboxylic acid surface modification and 50 nm diameter PS nanoparticles without surface modification were obtained from Kisker (Germany) and used without further purification. IR 780 and IR 820 - two commercially available dyes (Sigma-Aldrich, UK) were used for the swelling procedure. IR 780 was chosen for their low water solubility and IR 820 for its optical characteristics. For the swelling procedure the dyes were dissolved in tetrahydrofuran (THF) at concentrations of 1 mM. The PS nanoparticles (surface modified or plain) were loaded with the dyes via adding 100 μ L of the dye/THF solution to 600 μ L PS aqueous solution containing 0.5 wt% of particles. After incubation for 15-30 min 800 μ L of deionised water were added and the resulting mixture was vortexed for 30 s. Subsequently, the solution was centrifuged at 45,000 g for 40 min and washed three times using deionised water, before the nanoparticles were resuspended in deionised water under mild ultra-sonication. The resulting stained PS nanoparticles, containing either IR 780 or IR 820 were analysed using DLS, spectrophotometer and PA spectroscopy.

Observations

The loading procedure of organic dyes IR 780 and IR 820 to the polymeric matrix of PS nanoparticles yielded dark green dispersions. However, severe leaking of the dyes from the

polymeric matrix could be observed measuring the absorption spectra after preparation and each washing step, as shown in Figure A1-1 and Figure A1-2.

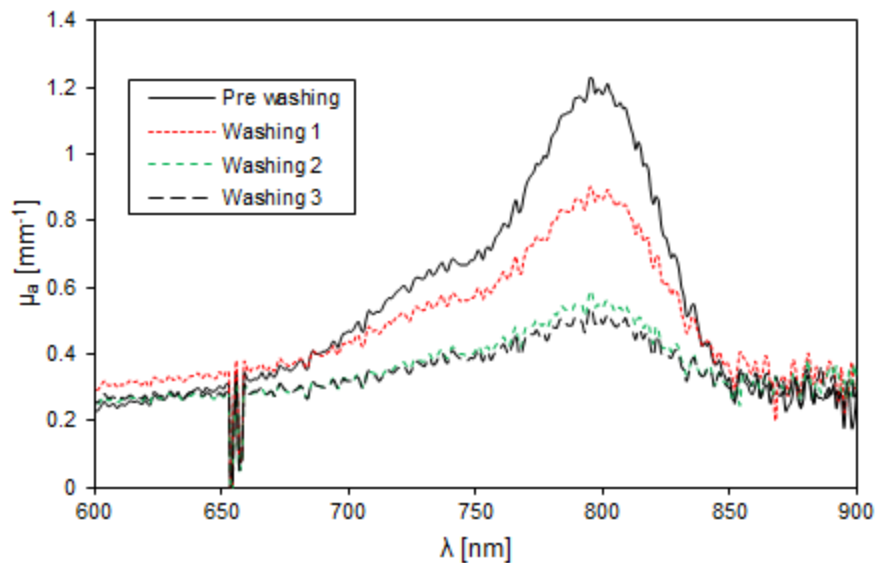


Figure A1-1: Absorption spectra of PS IR 780 before and after each washing step.

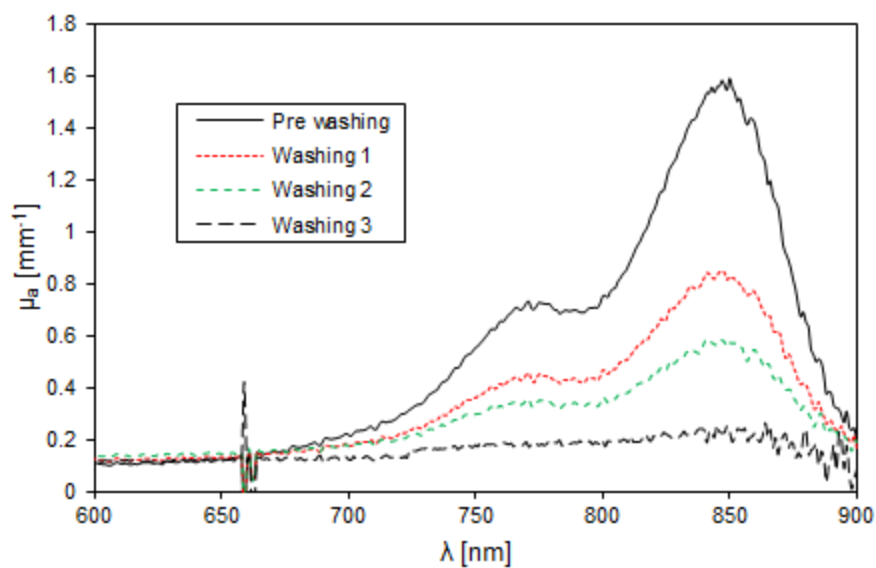


Figure A1-2: Absorption spectra of PS IR 820 before and after each washing step.

IR 780 (Figure A1-1) and IR 820 (Figure A1-2) both showed severe leakage from the nanoparticles. However, the leakage of IR 780 from the polymeric matrix is small compared to the other heptamethine dye used (IR 820). This can be appreciated when comparing μ_a before washing and after the last washing step - μ_a of the nanoparticles loaded with IR 780 decreased about 2.5 times, whilst the μ_a of the IR 820 nanoparticle sample decreased by about 8 times of its value before washing. This behaviour of IR 820 is explained by its good water solubility.

One remarkable observation can be made when comparing the spectra of IR 820 in aqueous solution with the PS nanoparticles loaded with the heptamethine dye - a redshift of the spectra by about 30 nm (see Figure A1-3). The decreased band gap of the dye loaded to the polymeric matrix, is due to the influence of the electronic environment the dye molecules are embedded in - the polymer matrix opposed to water molecules. The spectrum of the PS IR 780 nanoparticles on the other hand showed no deviation from the pure dye in solution. The difference can be explained by the polarity of the two molecules. IR 780 is less polar compared to IR 820 and therefore the band gap of IR 820 is influenced to a greater extent by other polar molecules, such as water. However, due to the loss through leaking of IR 820 from the PS nanoparticles after the swelling procedure only PS IR 780 nanoparticles were used for initial test of antibody conjugation to nanoparticles.

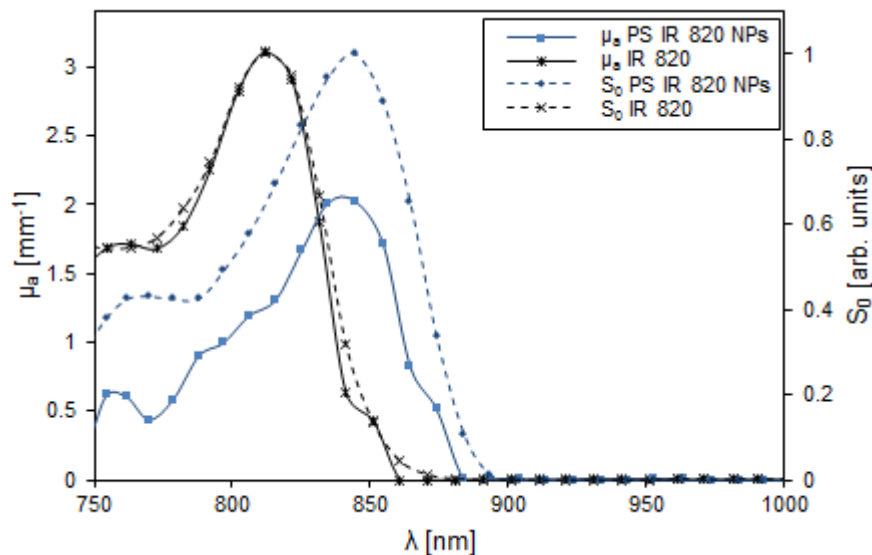


Figure A1-3: PA amplitude (S_0) of IR 820 (black dashed line with black crosses) and PS IR 820 nanoparticles (NPs) (blue dashed line with blue circles) and μ_a spectra of IR 820 (black line with black stars) and PS IR820 nanoparticles (blue line with blue squares), showing a red shift of about 30nm.

Antibody conjugation

The conjugation of antibodies to the dye loaded PS nanoparticles was performed using the PS nanoparticles with carboxylic acid surface modification (PS-COOH). The applied procedure for the crosslinking was adapted from ¹⁸¹. The antibody used (A5B7, UCB Pharma, UK) is an anti-CEA antibody targeting for epidermal growth factor receptors (EGFR). For the conjugation, 100 μ L of the PS-COOH loaded with IR 780 were added to 1 mL of a solution of 0.1 M 2-(*N*-morpholino) ethanesulfonic acid buffer (MES; pH 6) (see reaction equation Figure A1-4**Error! eference source not found.**).

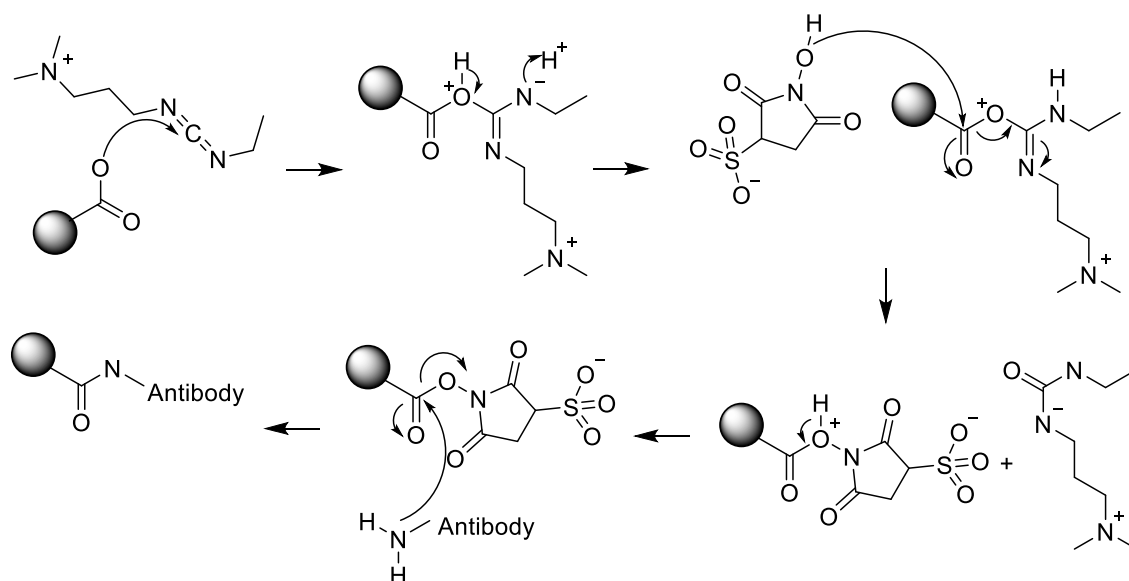


Figure A1-4: Antibody conjugation reaction using PS-COOH. The grey ball represents the PS nanoparticle. Reaction of the COOH functional group with EDC forming an intermediate, which subsequently reacts with sulfo-NHS. In the final step the formed PS-NHS conjugate reacts with the N-terminus or a lysine residue of an antibody to form the conjugate.

The resulting mixture was centrifuged at 4 °C and 14,000 rpm for 3 min. The supernatant was replaced by about 1 mL of MES buffer (pH 5) and vortexed before the buffer exchange was repeated. Subsequently, the pelleted fraction was incubated with 500 μ L of a mixture of 26 mM EDC and 10 mM sulfo N-Hydroxysuccinimide (sulfo-NHS) in 0.1 M MES buffer for 20 min at room temperature. In the next step in the antibody conjugation, the pH of the mixture was increased to 7.2 via buffer exchange - centrifugation (14,000 rpm, 30 min, 4 °C), subsequent elimination of the supernatant and the addition of deionised water (pH 7) to the pelleted fraction. Next, the as prepared nanoparticles were incubated with 200 μ L of 1 gL^{-1} A5B7 solution in PBS overnight, followed by a purification step. For the purification of the PS-COOH-A5B7 conjugates, the resulting solution was filtered twice using centrifugal filters with a MWCO of 150 kDa (Merck Millipore) at 1000 rpm for 5 min.

After procedure a pale green dispersions of A5B7 conjugated PS IR 780 nanoparticles was recovered. The dispersions were analysed for the particle size and the PDI using DLS after the final purification step. The DLS measurements show a strong increase in particle size from \sim 60nm to $>$ 1000 nm and an increased PDI from $<$ 0.1 to $>$ 0.4. Even though the procedure was modified in various ways, including the addition of additional surfactants, increasing of the buffer volumes and decreasing the antibody to nanoparticle ratio, the antibody conjugated PS-COOH

nanoparticles aggregated to form clusters of diameters >1000 nm and great polydispersity. Due to the high tendency for aggregation of the PS-COOH nanoparticles using the antibody conjugation procedure described and the leaking of the dyes from the polymeric core, the dye loaded PS nanoparticles were not further investigated.

Self-assembly synthesis of Poly (allylamine) nanoparticles

Another procedure for the formulation of dye containing polymeric nanoparticles was performed using poly (allylamine hydrochloride) (PAH) as a precursor. The original procedure by Yu et al can be found in ¹²⁶. For the synthesis, 20 μL of a cooled (4 °C) aqueous solution of 30 μM PAH (Alfa Aesar; $M_w=120,000-200,000 \text{ g mol}^{-1}$) of pH 4.3 was added to 120 μL of various concentrations (0.5-30 mM) of a cooled (4 °C) aqueous solution of disodium phosphate (Na_2HPO_4) and vortexed for 10 s. The ratio of negative charge of Na_2HPO_4 to positive charge added by PAH determines the growth rate and the final size of the particles and therefore was varied in order to obtain particles of about 100 nm in diameter (Table A1-2).

Table A1-2: Table of the various concentrations of PAH and Na_2HPO_4 used for the formulation of poly (allylamine hydrochloride) nanoparticles and the resulting particle size and PDI.

Experiment no.	c(PAH) [g L^{-1}]	c(Na_2HPO_4) [mM]	Particle diameter [nm]	PDI []
1	4	0.5	540	0.42
2	2	0.5	380	0.35
3	2	1	>1000	-
4	2	2	493	0.32
5	2	5	705	0.8
6	2	10	>1000	-
7	2	30	>1000	-

Subsequently to the mixing of the polymer and the salt, 1.2mL of deionised water was added followed by the addition of 120 μL of a cooled (4 °C) aqueous solution of 1 g L^{-1} ICG (Sigma-Aldrich, UK). The mixture was further vortexed for 10 s, before aging for 2 h at 4 °C in the fridge. The resulting suspension was then washed three times via centrifuging at 3,000 rpm for 2 h and resuspension in phosphate buffered saline (PBS; Sigma-Aldrich) before analysing their properties.

Observations

Various batches of the Poly (allylamine) nanoparticles were generated using the procedure described above. The size and the PDI were determined after step 1 in the synthesis and after the final washing step. Initially, after step 1 of the synthesis, the size of the nanoparticles generated were in the range of 100-250 nm with PDIs <0.3. However, after the final step of the synthesis, the nanoparticles substantially gained size and the suspensions became very poly-disperse with PDIs >0.5 (see Table A1-3).

Table A1-3: Size and PDI of poly (allylamine) nanoparticles after nanoparticle formation (step 1 of the synthesis) and after complete synthesis.

Sample	After nanoparticles formation		After complete synthesis	
	Size [nm]	PDI	Size [nm]	PDI
1	158	0.25	942	0.873
2	178	0.29	2325	1
3	195	0.18	1278	0.75

These results were obtained even with very low concentrations of Na_2HPO_4 present in the reaction mixture, which indicates aggregation rather than uncontrolled, continuous growth of the polymeric core. However, the dispersions seemed to be stable for a few minutes after agitation and did not immediately form a precipitate, allowing generating PA amplitude, μ_a and optical absorption spectra (Figure A1-5).

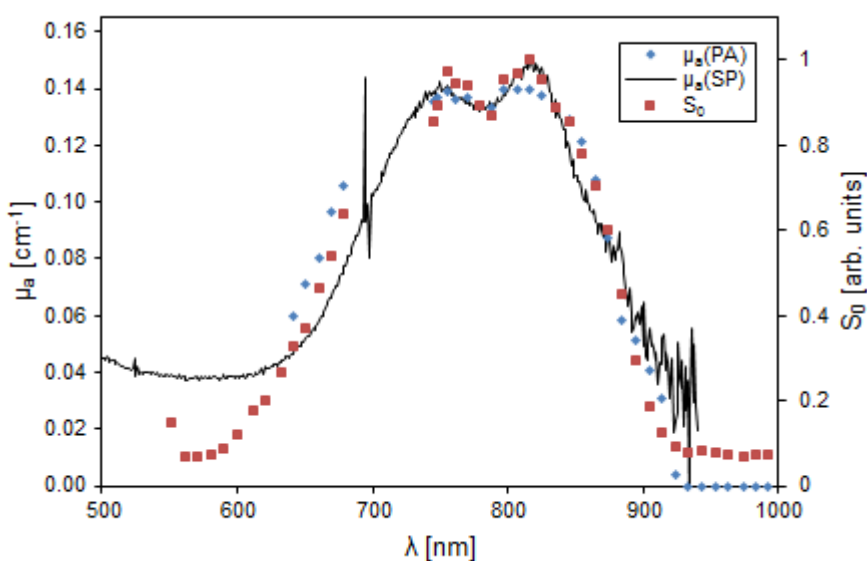


Figure A1-5: PA amplitude and μ_a measured using the PA spectroscope ($\mu_a(\text{PA})$) and transmission spectra ($\mu_a(\text{SP})$) of a batch of poly (allylamine) nanoparticles.

Figure A1-5 shows the PA amplitude, μ_a and transmission spectrum of a poly (allylamine) nanoparticles sample. The peak absorption at about 820 nm is ideal for the purpose of PA imaging due to the high penetration depth of light in tissue at this wavelength. However, the μ_a of the solutions is relatively low, even though high concentrations of (1 gL^{-1}) organic dye were used for the synthesis. This is probably due to a low loading efficiency of the dyes onto the polymeric matrix of the nanoparticles. Poor loading efficiency can be assumed because the dark green coloured solution becomes pale green after the final washing step. Even though the concentration of the nanoparticles in the resulting solution is unknown and therefore a direct comparison between the poly (allylamine) nanoparticles and other chromophores is difficult, judging from the μ_a spectra and the concentrations of polymer used for the synthesis a relatively low ϵ can be expected.

After various experiments, all resulting in unstable, pale dispersions of poly (allylamine) nanoparticles with sizes $>500 \text{ nm}$ and great poly- dispersity (>0.5), the synthesis was discontinued.

Semiconducting polymer Nanoparticles

Polypyrrole nanoparticles

Synthesis of polypyrrole nanoparticles were performed according to the procedure described in ¹⁸² and ¹¹⁹. Therefore, 0.75 g of poly (vinyl alcohol) (PVA, Mw $\sim 9,000 \text{ g mol}^{-1}$; Sigma-Aldrich, UK) were added to 10 mL deionised water under mild stirring (400 rpm) at $60 \text{ }^\circ\text{C}$. After about 1 h of stirring, the PVA mixture was taken from the hot-plate and 6.3 mg ($\sim 24 \text{ } \mu\text{mol}$) of solid iron(III) chloride hexahydrate powder (Sigma-Aldrich, UK) were added to the reaction mixture under stirring. The reaction mixture was left to cool down to room temperature. Approximately 30 min after the addition of iron chloride hexahydrate to the PVA solution was transferred to an ice bath before the addition of 7 mL of polypyrrole (5 wt% dispersion in water; Sigma-Aldrich, UK) via rapid injection to the stirred reaction mixture using a syringe. The polymerisation reaction was allowed to proceed for 24 h and the resulting dispersion was washed three times via centrifugation at 20,000 rpm for 2 h and resuspended in deionised water in order to eliminate excess PVA and iron salts from the polypyrrole nanoparticles suspension.

Observations

Immediately after the injection of the polypyrrole dispersion to the ice cooled PVA/iron chloride mixture, the mixture turned black. Once the reaction was left overnight and the stirrer was turned off, the mixture separated into two different phases. After washing the bottom phase using deionised water, the particles generated were difficult to resuspend and formed aggregates settling at the bottom of the centrifuge vial immediately after agitation. Analysis of the particle size and PDI using DLS, have been performed before and after the washing step, both revealing great particle sizes ($>500 \text{ nm}$) and PDIs (>0.7) for all the samples prepared. Due

to the difficulties preparing stable polypyrrole nanoparticles with sizes between 100 nm and 150 nm and small poly-dispersity and the gift of a sample of polypyrrole¹⁸³ nanoparticles fulfilling these requirements, received from a collaborating research group (Dr. Steve Matcher; Sheffield University), the synthesis of polypyrrole nanoparticles was discontinued. The PA amplitude, ϵ and transmission spectra of the polypyrrole sample received were measured. The results of these measurements are shown in Figure A1-6.

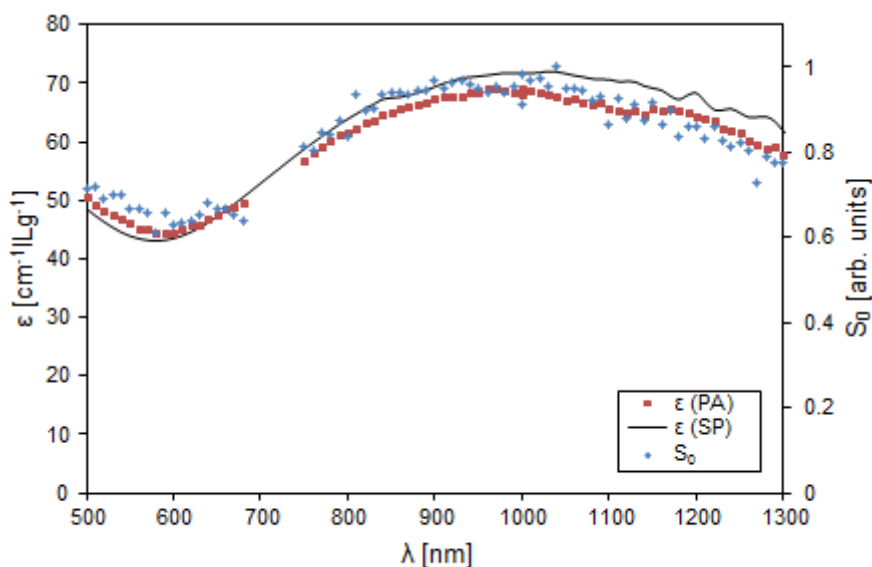


Figure A1-6: PA amplitude and ϵ measured using the PA spectroscopy ($\epsilon(\text{PA})$) and transmission spectra ($\epsilon(\text{SP})$) of the polypyrrole gifted by Sheffield University.

Figure A1-6 shows the PA amplitude, ϵ and transmission spectra of the polypyrrole sample with the wavelength of maximum absorption at about 1000 nm and extinction coefficients at this wavelength of $69 \text{ cm}^{-1}\text{Lg}^{-1}$ ($73 \text{ cm}^{-1}\text{Lg}^{-1}$ measured with the spectrophotometer).

Layer-by-layer self-assembly synthesis of PEDOT:PSS nanoparticles

Another semiconducting polymer that has been analysed for its properties as a nanoparticle for PA imaging is the polymer mixture poly(3,4-ethylenedioxythiophene):poly(4-styrenesulfonate) (PEDOT:PSS). It is made up from two polymers: sodium polystyrene sulfonate (a sulfonated polystyrene) and poly(3,4-ethylenedioxythiophene) (PEDOT; a semiconducting polymer), see Figure A1-7 or chemical structure of the two polymers.

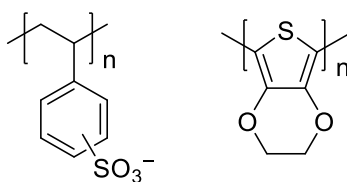


Figure A1-7: Chemical structure of polystyrene sulfonate (left) and PEDOT (right).

Nanoparticles made from PEDOT:PSS have first been introduced by Cheng et al as a photosensitive agent for photothermal therapy. For the detailed description of the synthesis of nanoparticles made from this semiconducting material see ¹²². Initially, 5 mL of 0.5 gL⁻¹ of a 1.3 wt% solution of PEDOT:PSS (Sigma-Aldrich; PEDOT to PSS ratio = 2:5) was added drop wise over 5 min to a stirred solution of 5 mL of 1 gL⁻¹ PAH (Sigma-Aldrich; Mw=70,000 gmoL⁻¹) using a syringe. To remove excess PAH after stirring the mixture for 6 h at room temperature with 150 rpm, the resulting suspension was dialysed against deionised water, using dialysis tubing with a MWCO of 100 kDa (Merck Millipore, US). The resulting mixture was added in drops over 30 min to 5 mL of an aqueous solution of poly (acrylic) acid (PAA, Mw=1800 gmoL⁻¹; Sigma-Aldrich) with a concentration of 2 gL⁻¹ under ultra-sonication. The mixture was left to stir for another 6 h before removing excess poly (acrylic) acid using dialysis tubing with a MWCO of 50 kDa (Merck Millipore, US). The pH of the resulting suspension was increased to pH 7.4 using sodium hydroxide (NaOH) and subsequently 5 mg of N-(3-dimethylaminopropyl-*n*-ethylcarbodiimide) hydrochloride (EDC) were added. The mixture was vortexed for 1 min and left at room temperature overnight. The next day, the suspension was washed using centrifugal filter with a MWCO of 300 kDa, resulting in a pure dark blue colloidal suspension of polymer stabilised PEDOT:PSS nanoparticles. In order to gain enhanced biocompatibility for the nanoparticles, an additional PEG layer was added. Therefore, 5 mL of 2 gL⁻¹ of a four-arm PEG-amine (Mw=10,000 gmoL⁻¹; see Figure A1-8 for chemical structure; Creative PEGworks, US) were added to the suspended nanoparticles under sonication.

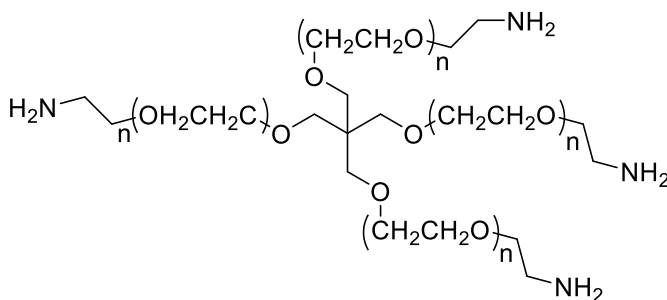


Figure A1-8: Chemical structure of four-arm PEG-amine.

After sonication for 30 min, 10 mg of EDC were added to the mixture and the pH was increased to pH 7.4 using about 5 mL of 0.1 M sodium phosphate buffer. The reaction mixture was left overnight followed by an additional dialysis against deionised water using dialysis tubing with a MWCO of 50 kDa. Finally, the resulting nanoparticle suspension was analysed using DLS, spectrophotometer and PA spectroscopy.

Observations

After the washing step using the centrifugal filter, a great proportion of the formed PEDOT:PSS nanoparticles aggregated in the filter membrane, allowing to recover only a pale blue/green suspension from the filtrate, even after the attempt to resuspend the particles. All attempts preparing PEDOT:PSS nanoparticles resulted in pale blue/green suspensions of nanoparticles of sizes > 500 nm with high PDIs (>0.6) and therefore was not investigated any further. PA and transmission spectra recorded, showed low μ_a (<0.7 mm^{-1}) and are due to low signal amplitude very noisy and therefore not included here.

Preparation of PCPDTBT nanoparticles via nanoprecipitation

Nanoparticles made from Poly[cyclopentadithiophene-alt-benzothiadiazole] (PCPDTBT) were prepared via nanoprecipitation which is also known as solvent displacement method, adapted from¹¹⁸. Therefore a preformed polymer precipitates from an organic solution in an aqueous environment forming nanoparticles which can be stabilised via surfactants present in the aqueous medium. The polymer used (PCPDTBT; M_w 20,872 g mol^{-1}) was obtained from Sigma-Aldrich (UK) and was dissolved in THF at a concentration of 0.25 g L^{-1} . THF was used due to its miscibility with water. The formation of nanoparticles using the nanoprecipitation method was instigated via the rapid injection of 1 mL of the polymer solution, with a syringe, into 9 mL of deionised water under continuous sonication using a probe sonicator (Q125; 3 mm tip diameter; QSonica, US) set to 6 W RMS. After 30 s of sonication 1 mL of a solution of 1,2-Dipalmitoyl-sn-glycero-3-phosphocholine (0.25 g L^{-1} ; DPPC; Avanti Lipids, US) in a 2:3 THF/water was injected to the sonicated solution in order to stabilise the formed nanoparticles. The mixture was kept under sonication for an additional 1 min at 6 W RMS before the sonicator-tip was removed from the mixture. For the final step the organic solvent was evaporated via heating the resulting solution in a water-bath to 45 °C and bubbling nitrogen through it. After about 2 h the aqueous suspension of PCPDTBT nanoparticles was judged to be free of THF, and was filtered through a 0.22 μm polyethersulfone syringe driven filter (Merck Millipore, US) and washed three times with deionised water using centrifugal filters with an MWCO of 30 kDa (Merck Millipore, US) under centrifugation at 4,000 rpm for 3 min at 4 °C. After the washing step the nanoparticles were resuspended in deionised water using an ultra-sonication bath. The resulting nanoparticles appear blue when in suspension and were analysed using DLS, TEM, spectrophotometer and PA spectroscopy.

Observations

The preparation of PCPDTBT nanoparticles using the nanoprecipitation technique described above results in blue dispersions of nanoparticles with sizes in the range of 100-200 nm and average PDI of about 0.2-0.3. The dispersions do not aggregate and are stable over days without significant change in size or PDI. After synthesis sometimes a small residues of PCPDTBT polymer can be found on the tip of the probe sonicator or occasionally on the rim of the sample vial. This incomplete incorporation of the polymer to the nanoparticle can be due to an insufficient concentration of surfactant and the consequently leaking out of the polymer from

the nano sized droplet before solvent evaporation. Another reason for the precipitate on the sonicator tip may be the increased temperature at the tip, which could lead to premature evaporation of the organic solvent and the resulting precipitation of the polymer. If precipitation occurred the samples were discarded.

Introducing fluorescent molecules to the semiconducting polymeric nanoparticles

In order to correlate the results of the *in vitro* and *in vivo* PA imaging experiments with fluorescence imaging, fluorescent dyes were introduced to the surface of the semiconducting polymeric nanoparticles. Therefore, up to 5 mol% of the surfactants used for the stabilisation of the polymeric core were replaced by 1,2-dioleoyl-*sn*-glycero-3-phosphoethanolamine-*N*-(lissamine rhodamine B sulfonyl) (DOPE-Rhodamine), which was added to the aqueous mixture. The preparation of the nanoparticles was performed as described above, using the DPPC/DOPE-Rhodamine mixture for the incorporation of the polymers. Size and PDI using the DPPC/DOPE-Rhodamine surfactant mixture had no significant influence on the particle size or the polydispersity of the samples compared to the nanoparticles made using only DPPC as a surfactant.

Observations

Even though Rhodamine B, the fluorescent dye incorporated in DOPE-Rhodamine, is of bright red/pink colour, once the lipid mixture is mixed with the π -conjugated polymers, the solutions appear blue/green in colour with no apparent difference to the pure polymer solutions. Also, fluorescence measurements using a spectrophotometer did not show any fluorescence when exciting at 560 nm and detecting in the spectral range between 580-700 nm. This could be either due to the absorption posed by the polymer in the spectral range of the emission band of DOPE-Rhodamine or due to the loss of the surfactant during the washing step. This however, could not be further investigated due to a lack of DOPE-Rhodamine, which was only sufficient for two experiments.

Conjugation of targeting moieties to semiconducting polymeric nanoparticles

For the conjugation of the semiconducting polymeric nanoparticles PCPDTBT and IND-T-BT to either a peptide with the amino acid sequence CLARLLT¹⁸⁴ or a full sized anti-CEA antibody (A5B7, MW~150 kDa), linker molecules were introduced to the surface of the nanoparticles, enabling covalent binding to the targeting moiety. The peptide was synthesised in house by Dr Robin Bofinger (UCL, Department of Chemistry). Both, the peptide and the antibody were chosen for their ability to target EGFR, a cell surface protein which is overexpressed in numerous cancer cell lines. The linker molecules were added at 1-3 mol% of the total surfactant concentration to the aqueous suspension of surfactants before the nanoparticles are formed as described above. Linkers used for the conjugation include a novel short PEG chain maleimide lipid (synthesised by Ivan Lam (UCL, Department of Chemistry)), 1,2-distearoyl-*sn*-glycero-3-phosphoethanolamine-*N*-[carboxy(polyethylene glycol)-2000] (ammonium salt) (DSPE-PEG(2000)-COOH, Avanti Lipids, US) and 1,2-distearoyl-*sn*-glycero-3-phosphoethanolamine-*N*-

[maleimide(polyethylene glycol)-2000] (ammonium salt) (DSPE-PEG(2000)-maleimide, Avanti Lipids, US). The synthesis of the novel short PEG chain maleimide lipids was carried out following the procedure in ¹⁸⁵ in which unsaturated lipids were synthesized. Their chemical structure is depicted in Figure A1-9.

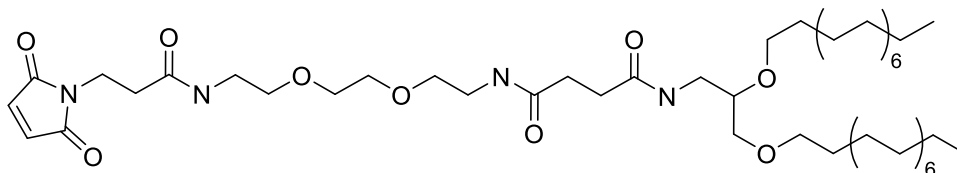


Figure A1-9: Chemical structure of the novel short PEG chain maleimide lipid.

It was envisaged that maleimide functionalised lipid (the novel maleimide lipid and DSPE-PEG(2000)-maleimide) would react with thiol groups present in the hinge-region of antibodies after selective reduction of disulphide bonds and on the cysteine building block of the peptide. DSPE-PEG(2000)-COOH would be activated and would then react with primary amines occurring on the N-terminus and on lysine residues of each polypeptide. Various protocols were utilized for the conjugation of the targeting moieties (peptide and antibody) to the polymeric semiconductor nanoparticles functionalised with the different linker molecules (short PEG chain maleimide lipid, DSPE-PEG(2000)-COOH and -maleimide).

Initially, for the conjugation of the short chain maleimide lipid, present in the stabilizing surfactant layer of the nanoparticles, to the antibodies, a partial reduction reaction using dithiothreitol (DTT) was adapted from ¹⁸⁶. Therefore, a PBS solution of A5B7 (3.9 gL^{-1} , 0.5 mL, pH 7.4) was added to DTT in PBS (0.4 gL^{-1} , 10 μL , 4 μg , 26 nmol, pH 8.0) and PBS buffer (0.5 mL, pH 8.0). The reaction mixture was allowed to stand for 2 h before purification using a 5 kDa size exclusion column (MiniTrap G-25, GE Healthcare, UK) and PBS buffer (pH 7.4) as eluent. Subsequently, the purified antibody solution was added to suspensions of the polymeric semiconductor nanoparticles functionalised with various concentrations of the short chain maleimide lipid (<5 mol% of the total surfactant concentration). The reaction mixture was left to stand for 1 h at room temperature before being washed with PBS using 30 kDa centrifugal filters at 4,000 rpm for 3 min at 4 °C and resuspended in PBS. The resulting suspension was stored at 4 °C until usage.

A second procedure for the conjugation of the targeting moieties to the nanoparticles used is based on the partial reduction of the disulphide bond present in the hinge-region of the antibodies using tris (2-carboxyethyl) phosphine hydrochloride (TCEP)¹⁷². The reaction mechanism is shown in Figure A1-10. Using TCEP as a reducing agent eliminates the purification step, essential in the previous procedure, and therefore decreases losses of nanoparticle conjugates within the size exclusion column. In a typical reaction 50 μL of an aqueous solution of TCEP (pH 8; 0.23 gL^{-1} ; five equivalents of A5B7) was added to 330 μL of

A5B7 in PBS (pH 8; 3.9 gL^{-1}) and the mixture subsequently incubated for 3 h at room temperature under mild agitation. After reduction of the disulphide bonds the mixture was added to 2 mL of a suspension of the polymeric semiconductor nanoparticles functionalised with the short chain maleimide lipid (3 mol% of the total surfactant concentration). For experiments using different concentrations of the PEG linker molecule the initial antibody volume was adjusted to remain the ratio of about 1:4 of linker molecules to antibody molecules. The reaction mixture was left to stand for 1 h at room temperature before being washed three times with PBS using 300 kDa centrifugal filters at 4,000 rpm for 3 min at 4 °C and being resuspended in PBS. In later experiments the washing step using centrifugal filters was replaced by dialysis over 24 h against deionised water using dialysis tubing with a MWCO of 300 kDa. The resulting suspension was stored at 4 °C until usage. The conjugation to the peptides to the nanoparticles was performed analogue to the procedure using TCEP as a reducing agent, except the volume of the antibody suspension was adjusted to suit the 1:4 ratio of linker molecules to peptides.

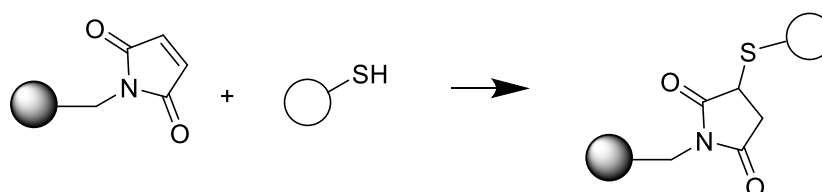


Figure A1-10: Conjugation reaction of semiconducting nanoparticles (grey ball) with sulfhydryl on a protein (plain circle).

The conjugation reaction using DSPE-PEG(2000)-COOH is mediated via crosslinking of the PEG-linker to *N*-hydroxysulfosuccinimide (sulfo-NHS) to form reactive NHS ester. Therefore, 4 mL of an aqueous solution of the semiconducting polymeric nanoparticles ($\sim 0.1 \text{ gL}^{-1}$), functionalised with 3 mol% of the total surfactant concentration with DSPE-PEG(2000)-COOH, was set to pH 6 using 2-ethanesulfonic acid (MES buffer). *N*-(3-Dimethylaminopropyl)-*N*-ethylcarbodiimide hydrochloride ($\sim 3.5 \text{ }\mu\text{g}$) and sulfo-NHS ($\sim 9 \text{ }\mu\text{g}$) were added to the suspension and the mixture vortexed for 30 s before incubation for 15 min. Next sodium bicarbonate (NaHCO_3) was used to raise the pH to 7.5 in order to favour the reaction of primary amines with the NHS ester on the surface of the nanoparticles. After, the addition of 1 mL of A5B7 (3.9 gL^{-1} ; pH 7.5) in PBS to the nanoparticle suspension, the mixture was incubated for 2 h at room temperature with occasionally shaking before dialysing the mixture against deionised water for 24 h, using dialysis tubing with a MWCO of 300 kDa.

Observations

The procedure initially tested, using DTT for the partial reduction of the disulphide bonds of the targeting moiety, yielded only very dilute dispersions of the nanoparticles. Most of the conjugated nanoparticles were lost during the purification step, using the size exclusion columns. When adding the sample to column a large amount of nanoparticles are retained within the column even when adding large volumes of eluent. This is evident by the colour of the

column, which changes from white to blue/green and retains coloured after adding the eluent. The remaining dilute nanoparticle dispersion was stable without forming any visible precipitate. Particle size and PDI measurements before (particle size 194 nm; PDI 0.24) and after (particle size 463 nm; PDI 0.32) the antibody conjugation show an increase of both measurements, which is due to aggregation of the nanoparticles.

The conjugation procedure using TCEP as an agent for the reduction of the disulphide bonds present in the targeting moiety eliminates the purification step via size exclusion column. The purification is not needed because after reducing the disulphide bond TCEP forms a phosphate, which does not interfere with the following procedure and can be found in similar form in the PBS buffer used throughout the procedure. DTT on the other hand forms cyclic disulphides, which interfere with the conjugation reaction and therefore need to be separated. However, the procedure using TCEP also includes a washing step, separating the antibody conjugated nanoparticles from the unbound antibodies. Initially centrifugal filters were used for this step. Unfortunately, a great proportion of the antibody/nanoparticle conjugate was lost due to aggregation in the filter and on the polymeric wall of the filter cup. When the flow of liquid through the filter was blocked by aggregates before completing the washing step, the filter was replaced by a new filter. The aggregates were difficult to recover and could not be resuspended in deionised water when scraped off the filter or the walls of the filter cup. The resulting suspension that could be recovered from the filter had a volume of about 200 μ L and was of pale blue colour. Particle sizes and PDI values generally increased from below 200 nm and <0.3 before conjugation to more than 300 nm and >0.4 after the conjugation to the antibodies. However, size and polydispersity of the nanoparticles before the washing step using centrifugal filters only slightly increases, compared to the original size of the nanoparticles. Due to these results the washing step via centrifugal filtration was replaced by a 24 h dialysis against deionised water using dialysis tubing with a MWCO of 300 kDa. The finally recovered dispersions were of blue/green colour with particle sizes below 250 nm and PDI in the range of 0.2-0.3. The dispersions were stored in the fridge at 4 °C and appeared to be stable for up to three days before a light film of precipitate started to build up at the bottom of the sample vial. Another procedure for the conjugation of the antibody to the nanoparticles was tested using carbodiimide and NHS-ester as crosslinkers. This procedure, targeting primary amines, also yielded blue/green coloured dispersions without apparent aggregation or other losses of nanoparticles during the conjugation. The dispersions were stored in the fridge at 4 °C and stable for up to three days before a light film of precipitate appeared at the bottom of the sample vial. This antibody conjugation procedure increased the size and PDI of the particle dispersion only by a small amount, usually the increase in size is less than 25 % and 15 % for the PDI e.g. from about 150 nm and 0.25 before the antibody conjugation to about 180 nm and 0.28.

Conclusion

Various methods have been used to generate a range of different nanoparticles, including copper sulphide nanoparticles, dye loaded PS nanoparticles, poly(allylamine) nanoparticles, PEDOT:PSS nanoparticles, polypyrrole nanoparticles, PCPDTBT nanoparticles, DPPTT-x nanoparticles and INDT-x nanoparticles. After preparation the nanoparticles were initially analysed for their particle sizes and polydispersity using DLS. Most of the procedures analysed yielded highly polydisperse dispersions of aggregating particles of sizes bigger (>200 nm) than the recommended size limitation for passive targeting via EPR (<200 nm). This is true for copper sulphide nanoparticles, poly(allylamine) nanoparticles, PEDOT:PSS nanoparticles and polypyrrole nanoparticles. Organic dye (IR 780 and IR 820) stained PS nanoparticles showed severe leaking of the dye, especially for IR 820, and yielded lightly coloured dispersions. The particles did not aggregate and the particle size and PDI are typically 60 nm and <0.1, depending on the PS nanoparticles source material. The nanoprecipitation and the miniemulsion method to generate PCPDTBT, DTPPP-x and INDT-x nanoparticles yield coloured nanoparticle dispersions with particle diameters in the range of 100-150 nm with PDI <0.3. The resulting dispersions of the various nanoparticles prepared were analysed using PA spectroscopy and transmission spectroscopy (for more details see Chapter 5). In addition to the DLS measurements and to determine the morphology of the nanoparticles, selected samples were imaged using TEM.

Finally, various reactions for the conjugation of the most promising nanoparticles prepared with targeting moieties such as small peptides or antibodies were tested. Initially, PS IR 780 was conjugated to an antibody. After the procedure for the conjugation of the nanoparticles to the targeting moiety, the particle size and the PDI drastically increased and rendered the dispersions unsuitable for in vivo experiments. In addition to this, the final dispersions of PS IR 780 conjugated to the antibody showed little colour. Therefore, the synthesis of targeted PS nanoparticles was discontinued. However, the synthesis of PCPDTBT and INDT-x nanoparticles conjugated to either antibodies or short peptides allowed recovering coloured dispersions of nanoparticles with acceptable particle sizes (<200 nm) and polydispersity (<0.3). The resulting dispersions of targeting moiety conjugated PCPDTBT and INDT-x nanoparticles were stable for up to three days when stored in the fridge at 4 °C.

A2: Commercial evaluation of semiconducting polymeric nanoparticles

Introduction

Nanoparticles are subject to a great number of studies touching on a broad spectrum of fields, for example biological and medical research and spectroscopic barcoding technology. The high interest in this group of materials is explained by the outstanding optical and physical properties exhibited by particles in this size regime. For the same reason nanoparticles bear great potential for commercial applications such as medical theranostic agents (combined diagnosis and treatment), molecular imaging probes and barcoding material for second generation barcoding - utilizing the unique optical fingerprint of various nanoparticles for the identification of goods. Over the last few years these and other factors have driven the demand for nanoparticulated materials. Consequently small businesses have emerged serving this market with specialized products like gold nanoparticles, latex nanoparticles and quantum dots tailored for medical and biomedical research. Fuelled by a number of factors, such as newly emerging imaging and treatment strategies, for example molecular PA imaging and photothermal therapy, the diversity of these products and the commercial demand has been consistently increasing and is expected to continue this trend in the foreseeable future.

Semiconducting polymeric nanoparticles represent an example of a group of materials that, owing to the novelty of the material, so far has not fully developed its full market potential. This novel group of nanoparticles exhibits outstanding optical and physical properties, typical for nanoparticles. Polymers forming the core of the particles can be chemically modified to suit various requirements. In addition to their inherent properties, semiconducting polymeric nanoparticles can be complemented by means of the incorporation of other molecules within their polymeric matrix, opening various potential fields of applications, such as multimodal imaging and targeted drug delivery. This set of properties and the high degree of flexibility allows defining practical applications for the class of semiconducting polymeric nanoparticles in various fields. Because of this, this chapter is intended to evaluate the commercial potential of

this class of nanoparticles. Synthesis, functionalization and characterisation of the nanoparticles have been described in detail in the previous chapters and therefore are omitted here. However, a short introduction to the class of semiconducting polymeric nanoparticles and their properties is provided which is intended to serve as a reminder, followed by the evaluation of their potential commercial applications. A schematic depicting the potential fields of application and the beneficial properties is shown in Figure A2-1.

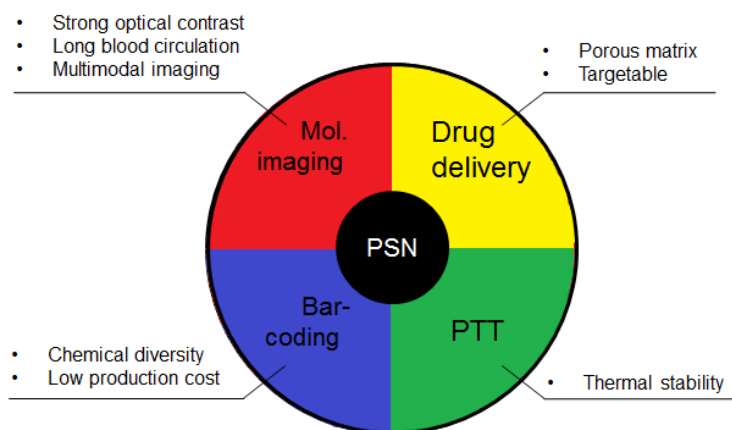


Figure A2-1: Potential commercial applications and properties of the PSNs desirable for each individual application. PTT = Photothermal therapy.

Furthermore the chapter on the commercial evaluation of the semiconducting polymeric nanoparticles includes the estimation of the costs involved founding a start-up company with the goal to produce the particles commercially and briefly overviews possible conflicts with existing patents and intellectual property laws.

Semiconducting polymeric nanoparticles

Semiconducting polymeric nanoparticles are a class of solid state nanoparticles with sizes tuneable between 10 and 200nm. They are made up from polymers with semiconducting properties, such as PCPDTBT (Poly[2,6-(4,4-bis-(2-ethylhexyl)-4H-cyclopenta [2,1-b;3,4-b']dithiophene)-alt-4,7(2,1,3-benzothiadiazole)]), in scalable processes known as nano-precipitation or via mini-emulsion. During the nano-formulation process the particles form and are coated in a surfactant-layer, making the particles water-dispersible. The properties of the semiconducting polymeric nanoparticles depend on the polymer and therefore can be tuned by chemical modification before formulation of the nanoparticles. This allows the absorption spectrum of semiconducting polymeric nanoparticles to be tuned from the visible to the near infrared of the electromagnetic spectrum. In addition to their tuneable absorption spectrum, various linkers can be introduced to the surfactant-layer of the particles enabling further chemical modification. Utilizing a suitable linker allows for the conjugation of various molecules to the semiconducting polymeric nanoparticles surface, such as antibodies for molecular targeting. Due to the porous nature of polymeric particles, semiconducting polymeric

nanoparticles also bear the potential to retain molecules within their matrix. The retention time of molecules within the polymeric matrix depends on the porosity and the chemical composition of the polymer making up the nanoparticles. Thus, the nanoparticles proposed here could be utilized for targeted drug delivery or multimodal molecular imaging, by loading the porous structure of the particles with drug or contrast agent molecules. Another advantage over other nano-particulated compounds for biomedical theranostic is the potential biodegradability of the semiconducting polymeric nanoparticles, avoiding the frequently observed accumulation of nanoparticles within liver and spleen. A scheme of the porous core of the semiconducting polymeric nanoparticles, stabilized by surfactants is depicted in Figure A2-2.

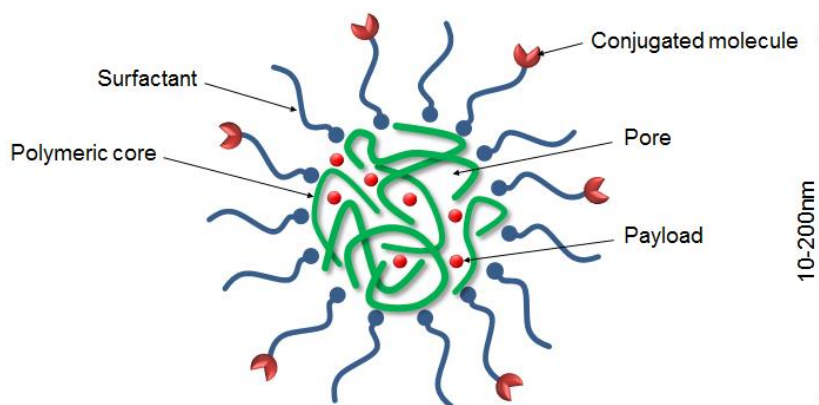


Figure A2-2: Schematic of cross section of a polymeric nanoparticle, showing the porous polymeric core (green lines) stabilized by surfactants (blue lines). The red shapes represent molecules such as antibodies, conjugated to the surfactants; the red spheres symbolize another material which is loaded and retained within the porous structure of the polymer.

The properties of the semiconducting polymeric nanoparticles are highly desirable in various fields for various purposes. Thus a detailed analysis of potential fields of applications has been carried out in the next chapter. Furthermore, to each potential application current commercial solutions are identified and evaluated, followed by a market analysis and a perspective for the nanoparticles proposed here.

Potential applications

Due to their flexibility - tuneable size, and absorption spectrum, ease of surface-conjugation and the ability to load the polymeric core with molecules - semiconducting polymeric nanoparticles have the potential to be utilized in a number of fields. This section is aimed to identify these fields of application, existing solutions and the market potential of the semiconducting polymeric nanoparticles, by reviewing commercial applications of similar nanoparticulated products and their projected markets. The first part of this chapter is dedicated to imaging and sensing using

the nanoparticles, the second part details their commercial applications as a therapeutic agent and finally analysing their potential as second generation barcoding material.

Imaging and sensing

Molecular imaging has become an important tool in the field of biomedical research for numerous applications such as the evaluation of the therapeutic effect of newly developed drugs, the validation of therapeutics before translation into a clinical setting, tumour characterization and tracer development. During the recent past, instrumentation with sufficient sensitivity and spatial resolution has been developed which in combination with targeted contrast agents allows for molecular imaging of small animals. Examples of molecular imaging modalities are PA imaging, fluorescence imaging and positron emission tomography (PET), each possessing its own characteristics. Combining imaging modalities often helps overcoming limitations set by the individual imaging technique, and thus instrumentation for multimodal imaging has been developed. However, molecular targeted contrast agents for these imaging modalities or combinations of them are not always commercially available, lack in performance, are hard to target or bear cytotoxic effects. Therefore, a commercial need for molecular targeted contrast agents for various imaging modalities and especially for multimodal imaging can be identified.

Semiconducting polymeric nanoparticles are due to their strong, tuneable absorption, tuneable size, biocompatibility, chemical variety and stability well suited contrast agents for molecular PA imaging. Depending on the polymeric precursor, the nanoparticles exhibit significant intrinsic fluorescence and are thus also useful probes for fluorescence imaging and combined PA and fluorescence imaging. The ability to load the polymeric matrix of the nanoparticles further allows incorporation of contrast agents for different imaging modalities, such as radioactive isotopes for PET. Additional contrast can also be accomplished via conjugation to the surface of the nanoparticles via linker molecules. Targeting modalities, for example in the form of an antibody or a peptide, are also conveniently mediated via introduction of a suitable linker during nanoformulation. The targeting moiety is attached to the linker in a subsequent step, providing a chemical bond without compromising its function. For an in vivo experiment, the semiconducting polymeric nanoparticles are injected into the bloodstream of the organism. Due to their size and surface charge, once injected they perfuse throughout the whole organism and successively accumulate at the target. In practice, images are frequently acquired pre-injection and at several time points post-injection to be able to see the successive accumulation of the contrast agent at the site of interest. In summary, the semiconducting polymeric nanoparticles pose a suitable solution as contrast agent primarily for optical absorption based biomedical molecular imaging modalities. However, as mentioned above, their intrinsic fluorescence and the ability to load additional contrast agents, allows for the nanoparticles to be used in a wider range of fields of medical imaging and thus can be regarded as a multimodal contrast agent.

Current method

Due to the intrinsic strong optical absorption of the semiconducting polymeric nanoparticles and their suitability as contrast agent for PA imaging, the first part of this chapter summarizes current solutions used to realise molecular PA imaging - refer to previous chapters for a more detailed description. The second part briefly introduces contrast agents for fluorescence imaging and, without going into detail, familiarises with contrast agents used for other imaging modalities which ultimately could be combined with PA and fluorescence imaging to realize multimodal imaging.

Molecular PA imaging

PA imaging is an imaging modality utilizing light to generate three dimensional images of tissue with high spatial resolution and penetration depth into tissue (several centimetres). Signal generation is based on the conversion of absorbed light to an acoustic signal mediated by a light absorbing compound. However, pathogens such as tumour cells pose little, if any, difference in absorption compared to their healthy counterparts and thus generate PA signal indistinguishable from each other. This limitation can be overcome via the introduction of exogenous contrast agents targeting for a specific pathogen and thus enable to distinguish diseased from healthy cells on a molecular level. This approach has the potential elevating PA imaging to a molecular imaging modality. Consequently, a number of studies including parts of this thesis have been motivated to analyse the performance of various contrast agents. Organic dyes and various types of nanoparticles, including gold nanoparticles, silver nanoparticles, iron oxide nanoparticles, carbon nanotubes and nano-diamonds are examples of materials which have been proposed for this purpose and have been analysed *in vivo*. However, apart from gold nanoparticles, none of the proposed absorbers has been successfully translated into a commercial product tailored for the use in molecular PA imaging. Nonetheless organic dyes are commercially available, for applications such as molecular fluorescence imaging. Well known vendors are LI-COR (US), Atto-Tec (Germany), Thermo Fisher Scientific (US) and Sigma Aldrich (US). The tendency to photobleach and the moderate extinction coefficient renders organic dyes not well suited as contrast agents for PA imaging. Gold nanoparticles on the other hand are better suited. Strong extinction coefficients with tuneable absorption spectrum, the lack of photobleaching and the ability to conjugate to a targeting moiety make gold nanoparticles a good choice for molecular PA imaging. Consequently, various gold nanoparticles products, including linker systems for the attachment of a targeting moiety, have been made commercially available by small ventures like Nanopartz Inc. (US) and Nanohybrids (US) and big concerns like Sigma Aldrich (US). However, a disadvantage especially of gold nano-constructs such as gold nanorods is the tendency to change optical absorption characteristics when exposed to excessive fluence. In summary, various contrast agents have been proposed for the molecular PA imaging with limited commercial outcome, except for gold nanoparticles which are available from a small number of suppliers.

Molecular fluorescence imaging

Fluorescence imaging is based on molecules which are excited by light of one wavelength and emit light of a different wavelength, known as fluorophore. The difference between the wavelength of maximum absorption and the wavelength of maximum emission is termed Stokes shift. As mentioned above, molecular fluorescence imaging can be achieved employing a fluorophore chosen from a wealth of fluorescent reporter technologies for tagging of cellular and subcellular processes *in vitro* and *in vivo*. Organic fluorophores are the traditional means for signal generation using fluorescence imaging. However, recently, quantum dots have been made commercially available, which surpass the optical properties of organic fluorophores. Quantum dots are semiconducting materials with diameters in the order of 10-100nm, exhibiting strong and tuneable absorption and fluorescence as well as great stoke-shifts and no photobleaching. However, due to their composition quantum dots are often regarded as cytotoxic and thus need to be encapsulated for certain applications. LI-COR (US), Atto-Tec (Germany), Thermo Fisher Scientific (US) and Sigma Aldrich (US) are examples of vendors, supplying a broad array of fluorophores and quantum dots with attached linker technology, for convenient conjugation to a targeting moiety.

Multimodal imaging

The ability to load the semiconducting polymeric nanoparticles with contrast agents of imaging modalities such as magnet resonance imaging (MRI), PET, single-photon emission computed tomography (SPECT) and computed tomography (CT) allows for multimodal imaging. Therefore the appropriate molecule is either embedded in their polymeric matrix or attached to their surface. Contrast agents such as gadolinium or paramagnetic iron oxide nanoparticles (MRI), fluorine (PET), indium (SPECT) and barium (CT) provide good contrast for the individual imaging modalities but often require chelation or entrapment due to their toxic effects on the body or to attach a molecule for molecular targeting. Thus, confining such molecules within the semiconducting polymeric nanoparticles matrix not only decreases their toxicity but allows for convenient conjugation to a targeting moiety and multimodal imaging exploiting the PA and fluorescence imaging contrast posed by the semiconducting polymer. Various products for each of the imaging modalities are commercially available, some approved for use in the clinics. Examples of clinically approved contrast agents are Dotagita (AFGA Healthcare) and MultiHance (Bracco) for MRI, and Hexabrix 320 (Mallinckrodt) for CT. However, the growing interest in multimodal imaging and the commercial availability of hardware for multimodal imaging calls for the development of improved molecular targeted contrast agents capable of generating sufficient signal for the imaging methods desired.

Market analysis

The market analysis of semiconducting polymeric nanoparticles is divided into two sections: The first documents the analyses of the market for molecular imaging probes in biomedical research

- with a focus on optical imaging probes including PA imaging - followed by evaluation of the market for clinical optical and multimodal imaging probes.

Contrast agents for biomedical molecular imaging

Biomedical molecular imaging has become an essential technique used in molecular biology and biotechnology laboratories, the pharmaceutical industry and medicine. Biomedical molecular imaging is a powerful tool helping understanding key molecular and biological processes and can be used to detect and analyse diseases. It has been widely used for applications such as the evaluation of the therapeutic effect of newly developed drugs, the validation of therapeutics before translation into a clinical setting and tumour characterization by means of *in vitro* techniques such as quantitative polymerase chain reaction or fluorescence activated cell sorting (both relying on fluorescence markers such as Sybr Green and MitoSOX Red) or *in vivo* imaging technologies such as molecular fluorescence imaging or fluorescence microscopy. The success of these molecular imaging techniques is reflected in the great number of publications in the field and in the diverse range of commercially available molecular probes, including organic dyes and inorganic nanoparticles, provided by various companies (see above). These optical probes have proven useful for imaging techniques like molecular fluorescence imaging. However, nanoparticulated materials often exhibit properties exceeding those of classical contrast agents and thus establish themselves on the market with increasing annual market share. Examples are gold nanoparticles and quantum dots. In addition, contrast agents for some novel imaging modalities, such as molecular PA imaging, are either insufficient or completely lack a commercial supplier. Owing to their excellent properties the class of semiconducting polymeric nanoparticles have the potential to fill this void as well as being utilized by other optical imaging modalities.

In a report from 2013 by BCC research¹⁸⁷, imaging agents for biomedical applications were estimated to reach a global market value of \$14.5 billion in the year 2017. This number was calculated from an annual growth rate of 7.8% from \$9.4 billion in 2011 and \$9.9 billion in 2012. According to the report, optical imaging agents made up about 35% (\$4.6 billion) of the total market volume in 2012 with an estimated annual growth rate of 7.3%, thus decreasing its share in this sector to 33% (\$4.9 billion) in 2017. It can be expected that a great percentage of the optical imaging agents sector is dominated by organic dyes, due to the wealth of fluorescent reporter technologies and established protocols based on organic dyes. However, the share of nanoparticles will increase owing to their superior properties, improvements and availability of nanoparticulated imaging agents and newly emerging imaging technologies such as PA imaging. This can be seen in the example of quantum dots as probes for molecular fluorescent imaging. In 2013, organic dyes had the biggest market share in this field; the share of quantum dots however is increasing at a higher annual growth rate - thus destined to surpass the market volume of organic dyes eventually. The increased usage of nanoparticles is also reflected in a report of BCC research published in 2014¹⁸⁸. In this report the global market for nanoparticles used in pharmaceuticals and biotechnology was quoted to be \$25 billion in 2013, \$29.6 billion in

2014 and was estimated to reach \$79.8 billion in 2019 assuming an annual growth rate of 22%. A different report by Markets and Markets¹⁸⁹ published in November 2015, projecting the market development of molecular imaging over the coming five years, estimates an annual growth rate of 9.3%, to reach a total volume of \$9.3 billion by 2020. The driving factors for this development are high rates of incidences of cancers and infectious diseases and newly emerging biomarkers and imaging technologies. Included in the report are instruments, imaging probes, services and software related to the field, with the imaging sector accounting for the largest share and highest annual growth rate. Gold nanoparticles are a class of nanoparticles with properties similar to those of PSNs: strong extinction coefficient with tuneable absorption peak and convenient targeting technology. Therefore, gold nanoparticles are a good surrogate to predict the future market of PSNs. A recent study (2015) by Grand view research¹⁹⁰ has analysed the global market for gold nanoparticles from 2009 to 2014. The study predicts the global market for gold nanoparticles, applied in the fields of medicine, electronics and catalysis, to reach \$4.86 billion by 2020. Driven by an increasing scope of medical applications and the appearance of novel commercially available gold nanoparticles based products, in 2013 the share of gold nanoparticles used for medical products accounted for over 50% of the total market and grew at an annual growth rate of 17% and is expected to continue to grow at a similar rate till 2020. Even though the market for the PSNs would initially be considerably smaller, the field of molecular biomedical imaging potentially offers a promising platform for commercial success.

In summary, all relevant markets, such as the market for molecular imaging agents, optical imaging as well as the market for nanoparticles used in biotechnology and pharmaceuticals are worth several billion USD and are growing with high annual growth rates. These dynamic markets are driven by various factors, such as high demand from biomedical research laboratories and pharmaceutical industry and new developments in instrumentation and contrast media. The increasing number of commercially available nanoparticles, their successful introduction to the field of molecular imaging and their annually increasing market share, illustrates the commercial potential of the semiconducting polymeric nanoparticles in the field of molecular imaging agents. When introduced to the market of biomedical imaging, semiconducting polymeric nanoparticles are likely to predominantly be used for molecular PA imaging and as molecular fluorescent tag. The market share in this field has the potential to grow to a billion dollar business, possibly to a comparable size to that of gold nanoparticles.

Contrast agents for clinical optical and multimodal imaging

Clinical optical imaging modalities allow for the early detection and staging of cancerous cells and other pathogens, important factors choosing a suitable treatment and ultimately influencing patient survival. Due to the limited penetration depth of the light into the tissue of interest, purely optical imaging modalities are restricted to certain applications. However, PA tomography allows extending the penetration depth by several centimetres. An example of an application for molecular targeted contrast agents for PA tomography is the detection and staging of breast cancers – one of the most widespread disease for woman in the UK - according to the NHS, every year about 50 thousand new breast cancer patients are being reported, only in the UK.

Currently breast cancer is detected using mammograms, ultrasound imaging and MRI. Molecular PA imaging bears advantages compared to these classical methods, such as combined high resolution and penetration depth, and therefore bears great potential to be utilized in the clinics for breast cancer detection and staging. Combining optical or optoacoustic imaging with other imaging modalities has the potential to further extend the clinical applications of PA contrast agents.

A report from 2014, published in the Business Standard¹⁹¹, estimated the growing market of clinical optical imaging, which includes PA imaging, to reach a share of \$2 billion by 2020. Assuming a market share of 10% of this figure for PA imaging underlines the enormous market potential of this imaging modality. A different, earlier report by Markets and Markets¹⁹² forecasting the global contrast agents market over a period from 2013 to 2017 estimated an annual growth rate of 6.8% to reach a total volume of \$8.6 billion in 2017 (from \$6.8 billion in 2012). In this report, imaging agents for modalities like X-ray, computed tomography and ultrasound imaging were included. The market share of contrast agents for ultrasound imaging is about 3% of this figure with an annual growth rate of 30%¹⁹³. Due to the novelty of the imaging modality contrast agents for PA imaging are likely to have a significant smaller share of this market. However, once established in the clinics and research centres, PA imaging could gain a market share comparable to that of ultrasound imaging.

The semiconducting polymeric nanoparticles are designed for molecular PA imaging and are due to their excellent PA properties likely to become a popular probe among other nanoparticulated contrast agents. Thus, when established in the clinics, molecular PA imaging using the semiconducting polymeric nanoparticles as contrast agent has the ability to improve diagnosis and therefore patient wellbeing and therefore has a great market potential - the comparable market for ultrasound imaging contrast agents is a multimillion dollar business. Additionally, incorporating of contrast agents to the PSNs polymeric matrix for multimodal imaging would further widen its clinical applications and commercial success. Thus, aiming to market the polymeric nanoparticles in a clinical environment bears great potential (see Figure A2-3 for markets relevant to semiconducting polymeric nanoparticles).

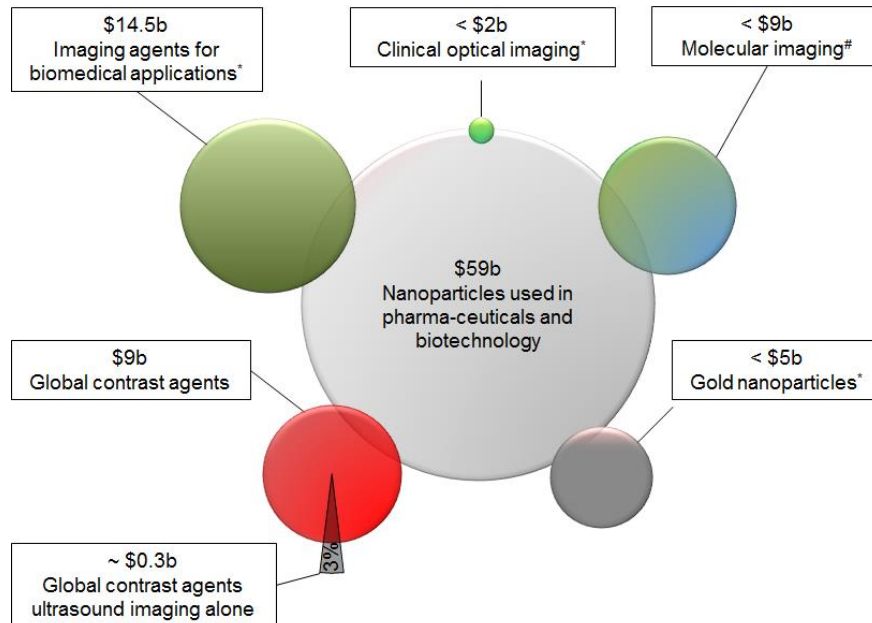


Figure A2-3: Volume of various biomedical and medical markets (in billion dollars) with potential application for PSNs.

Therapeutic applications

Photothermal therapy

Photothermal therapy is a minimal invasive therapy, using light to generate sufficient heat (temperatures above 48 °C) to eradicate diseased tissue such as malignant tissue. The process generating the increased temperatures is based on the absorption of light - often near-infrared laser light - by an absorber in proximity to the target, and the subsequent non-radiative relaxation. Recently, various studies showed successfully employed of nanoparticles for the localized heating of diseased tissue. Therefore, nano-sized absorbers, preferably with absorption in the near-infrared of the electromagnetic spectrum, are targeted to accumulate at a diseased area within an organism. After sufficient time for accumulation at the target and clearing from the blood stream, the diseased region is irradiated with light of wavelengths corresponding to the absorption spectrum of the nanoparticles. A short while after the start of the light treatment, the temperature around the nanoparticles is sufficiently high to cause irreversible damage to the diseased cells in their proximity. Nanoparticles mediated photothermal treatment has been successfully employed for the eradication of tumours, resulting in an increased survival rate. Nanoparticle mediated photothermal therapy is predestined for the combination with PA imaging due to the similar properties required from the contrast agent. A wide array of nanoparticles have been analysed for their feasibility as photosensitizer for photothermal treatment. Successful candidates exhibit properties such as high extinction coefficient, low fluorescence quantum yield, no photobleaching, sizes between 50 and 200 nm and the ability for molecular targeting. Semiconducting polymeric nanoparticles

readily provide all these properties and, therefore, have the potential to be utilized for this purpose.

Current method

Nanoparticles including gold nanoparticles, carbon nanotubes, quantum dots and various other nanoparticles have been proposed as photothermal photosensitizer. The advantage of targeted nanoparticles for photothermal therapy is the high specificity compared to non-targeted thermal treatment. Compared to photosensitizers based on organic dyes, nanoparticles are less sensitive to or exhibit no photobleaching. Various scientific papers have shown their targeting ability and the effectiveness of photothermal therapy mediated by such nanoparticles in *in vivo* experiments. Examples of molecular targeted nanoparticles are functionalised graphene nanoparticles and hollow gold nanoshells. Both systems were conjugated to antibodies, targeting for tumour cells. However successful, none of the proposed photosensitizers has been made commercially available, probably due to the novelty of the therapeutic technique. Currently, photothermal therapy is mainly used without exogenous photosensitizer - irradiating the diseased site with light of wavelength corresponding to the absorption of endogenous absorbers - but often in combination with other treatments. Applications range from the treatment of oral infections and eye surgery (such as central serous retinopathy treatment) to the treatment of cancer cells. A great number of both research based studies and clinical trials indicate a strong interest in photothermal therapy and will further drive its applications. Another driving factor is the availability of robust, inexpensive, handheld light sources.

Market analysis

Nano-sized, molecular targeted photosensitizers are going to have a profound impact on photothermal therapy - allowing for personalised cancer treatment. When commercially available, molecular targeted photosensitizers for photothermal therapy can be expected to be utilized in a broad spectrum of clinical applications, especially in the field of oncology, eventually replacing conventional treatments. The market for photosensitizers for photothermal therapy is probably going to be composed of a mixture of materials tailored for specific applications. Examples of promising materials are gold nanoparticles, carbon based materials (graphene nanoparticles, carbon nanotubes etc.) and polymeric nanoparticles.

According to a BCC research paper from 2012¹⁹⁴, the global market for nanoparticles used in theranostic applications in 2017 will have reached a volume of \$188 billion (from \$112 billion in 2012) based on an annual growth rate of 10.8% (see Figure A2-4).

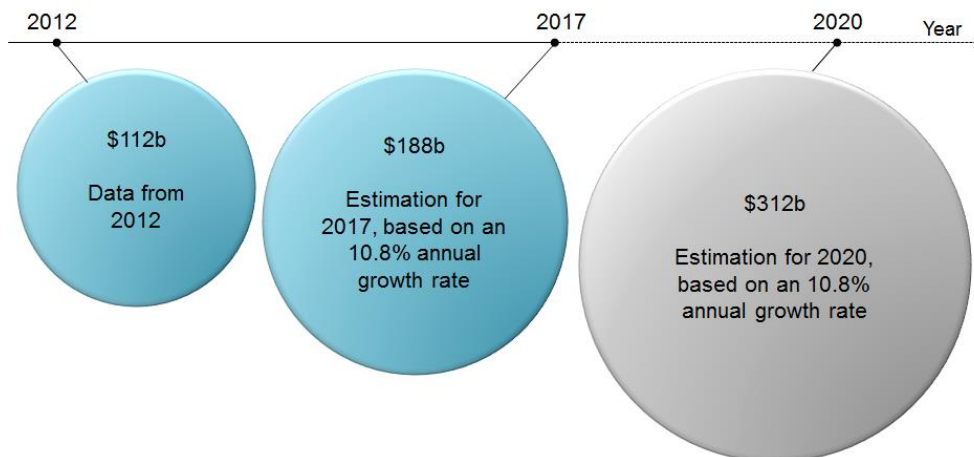


Figure A2-4: Market volume of nanoparticles used in theranostic applications (in billion dollars) from 2012 till 2020. The values for 2017 and 2020 are based on an annual growth rate of 10.8%.

The paper included biological nanomaterials – proteins and antibodies - as well as organic and inorganic synthetic nanoparticles such as quantum dots, gold nanoparticles, nanocrystals and polymeric nanoparticles. The biggest share of this market is likely to be taken by the biological materials, due to high material costs and their increased use for targeted drug delivery. However, once photothermal therapy is established in the clinics, targeted nanoparticulated photosensitizers for personalised therapy are expected to significantly increase their market share.

Drug delivery

Drug delivery is a heavily investigated field of research - especially for cancer therapy - aiming to direct therapeutic compounds directly to the disease, therefore, improving the effect of the administered bioactive compound and allowing decreasing its dosage, reducing side-effects. This can be achieved via the selection of safe and specific delivery routes, such as site specific application or targeted delivery using a targeting moiety. Due to the ability to molecular target the semiconducting polymeric nanoparticles the following covers only the targeted delivery using biomolecules such as peptides or antibodies. In general, for this approach the payload is incorporated in vesicles, such as liposomes, microspheres or dendrimers, which are targeted to a specific biomarker. The vesicles can release their payload via an external (e.g. light pulses) or endogenous trigger (e.g. by a change in the pH often found in cancerous tissue) or by leaking out.

Polymeric particles are known to have a porous structure. Molecules entering the pores formed by the particle can be retained via various processes, such as π - π stacking or via hydrogen bonds. In the case of the semiconducting polymeric nanoparticles the retention time of the molecules within the pores can further be influenced via the surfactant layer surrounding the

solid polymeric core. Thus, when targeted to a biomarker, a semiconducting polymeric nanoparticle system could be used for the controlled release of drug molecules at the target combined with multimodal molecular imaging.

Current method

Current targeted drug therapy is based on monoclonal antibodies and small inhibitors. Once administered, these drugs interfere with localised specific molecular targets within the body, which triggers a therapeutic effect. The therapeutic effect can be based on a great variety of mechanisms including cell signal transduction inhibiting, apoptosis inducing, angiogenesis inhibiting or the delivery of cytotoxic molecules to the diseased site. Herceptin, Avastin and Erbitux are examples of drugs approved by the American Food and Drug Administration and are currently used in the clinics. Commercial vendors of such drugs are Amgen (US), Ariad Pharmaceuticals (UK) and Merck (US). However, a new generation of targeted medicine is currently being tested in clinical trials. This second generation of targeted drugs utilizes nano-sized vesicles like liposomes, microspheres or dendrimers to deliver a payload to the desired site.

Market analysis

In 2015, Markets and Markets published a report on the global market for molecular targeted drug therapy¹⁹⁵, which estimated a market volume of \$1,048 billion for the same year, and calculated the market to reach \$1,505 billion by 2020, based on an annual growth rate of 7.5%. This enormous market and the annual growth rate can in part be explained by the growing number of patients and the high cost of these drugs, which annually sums up to \$50,000-100,000 per patient. Other driving factors are increase of chronic diseases and innovation and technological advancements. The high interest and the need for new cancer drugs is reflected in the number of Phase I, II and III clinical trials related to cancer treatments, which is in the tenths of thousands. Out of these trials a few hundred new treatments are expected to be translated successfully to the clinics, likely to generate an increasingly crowded pool of drugs. Even though the market is highly selective, semiconducting polymeric nanoparticles bear the potential to be utilized for drug delivery because of their great chemical flexibility and their ability to be molecularly targeted. The intrinsic absorption and fluorescence properties further allow imaging the region of interest, making drug loaded semiconducting polymeric nanoparticles a valuable theranostic agent.

Other applications

Barcoding

Barcoding is used to label, track and authenticate goods. In its traditional form of 1D or 2D printed optical labels barcodes have become ubiquitous in our everyday lives. However, printed barcodes are easily damaged, altered or falsified. For product manufacturers, law enforcement

and security agencies using traditional barcoding technology causes health and security issues, which led to the emergence of various tracking and anti-counterfeiting technologies. Electronic tags which interact with radio-frequencies, metal threads with specific material morphology and optically absorbing or fluorescent nanoparticles are examples of advanced barcoding technologies - see Figure A2-5 for a schematic of the working principle.

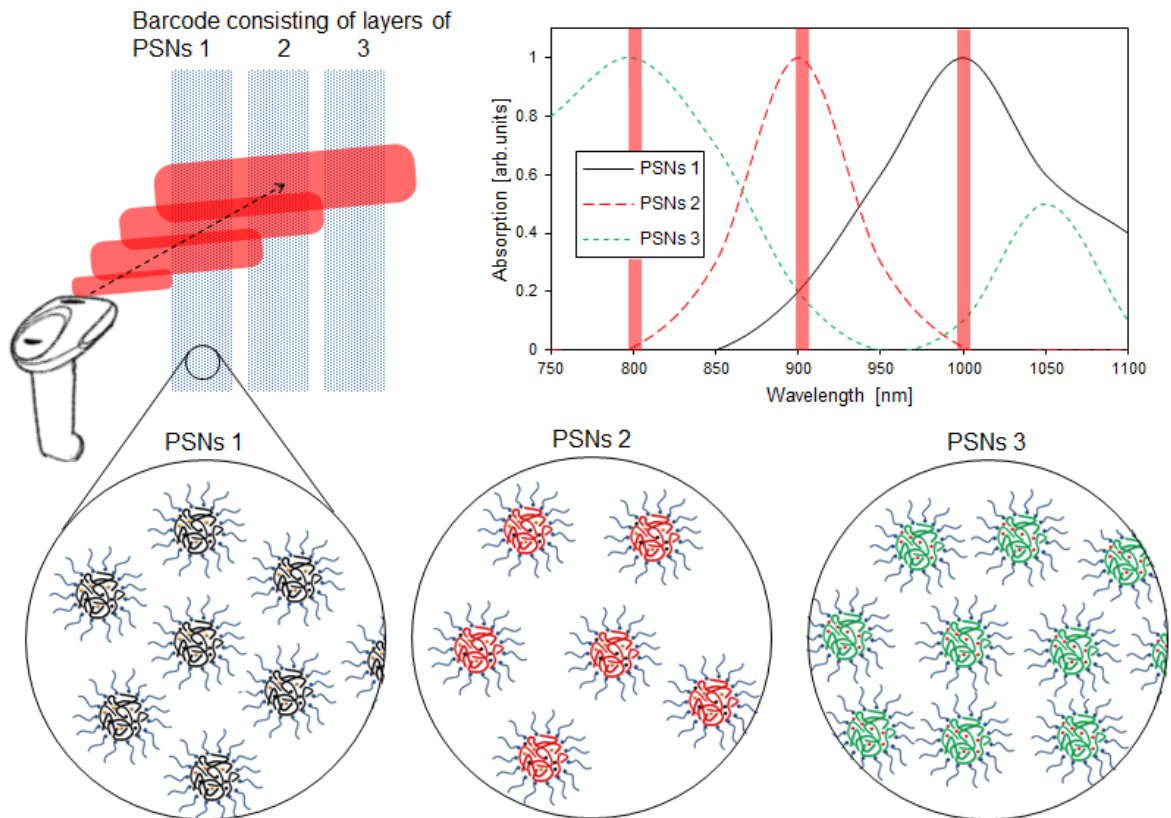


Figure A2-5: Working principle of second generation barcoding based on fluorescence nanoparticles (top left). There different types of nanoparticles (PSN 1, 2 and 3) are used to generate a specific fluorescent spectrum (top right) which can be read by a handheld spectroscope.

The following focuses only on the latter, because the semiconducting polymeric nanoparticles analysed in this chapter exhibit properties, such as tuneable absorption and fluorescence spectrum, suitable for the application as spectroscopic barcoding material. The absorption or fluorescent spectrum of the material or material mixture used, allows for the identification of the individual barcode by means of spectroscopy. Quantum dots and polystyrene nanoparticles loaded with organic dyes have been proposed as barcoding material. Semiconducting polymeric nanoparticles however have due to their outstanding properties the potential to be utilised for this application.

Current method

Current barcoding technology is based on the 1D or 2D printed labels read-out by optical scanners. Increasing security requirements for various applications of barcodes drive the need for alternative techniques. For that purpose mixtures of quantum dots or polymeric nanoparticles have been proposed as barcoding material in various publications. Suitable, barcode scanners based on optical techniques, such as fluorescence microscopy, are currently being developed. A commercial system allowing for the convenient detection of such novel barcodes is however not available yet, which could be due to the novelty of the technology. The commercialisation of this technology will enable a broad spectrum of nanoparticles to be utilised as a material for secure barcoding.

Market analysis

Next generation optical barcodes based on nanoparticles could be employed by governmental security agencies, law enforcement, pharmaceutical industry and product manufacturers, allowing for invisible barcodes, which could be incorporated directly into the product, minimizing counter fitting, destruction or loss of the barcode. A commercial solution nonetheless has not been marketed yet, although cheap optical parts (laser-diodes, CCD-chips etc.) for the design of a scanner for this kind of barcodes are available and nanoparticles, which could be used as barcodes, can be produced relatively inexpensive and in great quantities. Making barcoding more secure will ultimately drive the market towards this kind of barcodes. A report of BCC research from 2015¹⁹⁶ confirms this with their prognosis for the global market for anti-counterfeiting packaging for pharmaceutical and food industries for the next 5 years. The report estimates a market share of \$135.6 billion by 2020 (from \$74.2 billion) with an annual growth rate of 12.8%, revealing the great potential for next generation barcodes only in this sector of the market.

Production costs

Manufacturing costs, especially the cost for the production of the PSNs, is an important factor to consider when establishing a start-up company aiming at commercializing a product new to the market. Therefore, in the first instance an estimate of the material costs of the semiconducting polymeric nanoparticles is detailed in the following. Considerations for the establishment of a start-up company for the production of semiconducting polymeric nanoparticles are outlined in the second part of this section.

Production costs for the semiconducting polymeric nanoparticles

Most of the applications proposed above require conjugation of a biomolecule to the nanoparticle surface. Furthermore, other nanoparticles, such as gold nanoparticles, are

marketed in combination with biomolecule linker systems or in form of linker kits, which include the nanoparticle-linker conjugate and other chemicals and consumables for the conjugation of biomolecules. Therefore, the following estimates the material costs for the production of a batch of PSNs with a common linker system, using commercial products without the need for chemical modification or purification. A batch size of 10 mL with 0.25 g/L of semiconducting polymeric nanoparticles was chosen for the estimation of the production costs, due to the procedure used to generate the particles for this thesis - the resulting 2.5 mg of semiconducting polymeric nanoparticles is sufficient material for various applications such as molecular imaging. However, vendors often include a bigger batch in their portfolios, often 100 mg, for frequent users. Therefore, the estimation of the production costs for 100 mg of nanoparticles has been included (see Table A2-1).

Table A2-1: Break-down of the approximate materials cost for the preparation of a small batch (2.5 mg semiconducting polymeric nanoparticles) and a bigger batch (100 mg semiconducting polymeric nanoparticles). Prices are based on quotes from appropriate manufacturers.

Description	Cost [£]	
	for 2.5 mg	for 100 mg
Semiconducting polymer - for example PCPDTBT (0.25mg)	0.70	28
Surfactant - DPPC (0.25 mg)	0.12	4.8
Liker system - DSPE-PEG2000-COOH (0.1 mg)	0.54	21.6
Solvents: distilled Water, PBS, THF	0.10	4
Nitrogen for purging of the PSNs solution	0.01	0.4
Other consumables for the preparation via nano-precipitation	0.25	10
Glassware	0.34	13.6
Total	4.56	82.4

The procedure for the production of the PSNs can be up scaled and may even be modified for a continuous production rather than the production in batches, which could significantly lower the production costs whilst increasing the throughput. Another advantage is the long shelf life of the nanoparticles even at room temperature, minimizing wastage and thus economic losses. However, because the procedure for the production of the semiconducting polymeric nanoparticles is rapid and repeatable and can be realized in small quantities, the nanoparticles could be freshly prepared as required. This could help cutting or completely eliminate spending on storage and increase the control over temporal fluctuations in the demand for the product.

Startup costs

In addition to the material costs listed in Table A2-1, various running costs and one-off investments need to be considered when building a start-up company. These costs are summarized in Table A2-2.

Table A2-2: Approximate costs to establish a start-up company aiming to commercialise semiconducting polymeric nanoparticles. Prices are based on quotes from online vendors, estimations or based on quotes.

	Description	Cost [£]
Preparation of the nanoparticles	Probe sonicator (10W)	1,500
	Hot-plate/stirrer	350
	Schlenk line	500
Storage	Fridge	300
	Freezer	350
Development		30,000
Quality control (outsourced):	DLS	200
	TEM	500
Other	Laboratory space including fume hood (p.a.)	25,000
	Waste disposal (p.a.)	8,000
	Salaries (p.a.)	50,000
Total		116,700

Table A2-2 lists the various costs involved for the initiation of a start-up company aiming to produce semiconducting polymeric nanoparticles for biomedical medical imaging. This approximation includes one-off payments such as the costs for laboratory equipment and storage facilities, running costs such as the costs for outsourced quality control and the premises for the production. Initially the start-up would produce in small production-scale and gain customers. The production of small batches of 100 mg would allow supplying 500 samples of 1 gL⁻¹ with a volume of 200 µL. Initially, a start-up producing semiconducting polymeric nanoparticles would target for research institutes and analytical laboratories from the field of molecular PA imaging, due to the intrinsic properties of the particles. After an initial stage, when customers are aware of the product and orders being placed, the nanoparticle synthesis can be scaled up without further investment. The capital intended for further development is not critical

at the initial stage of the venture, but could be used to expand the impact of the product to other fields of application. Potential customers are shown in Figure A2-6.

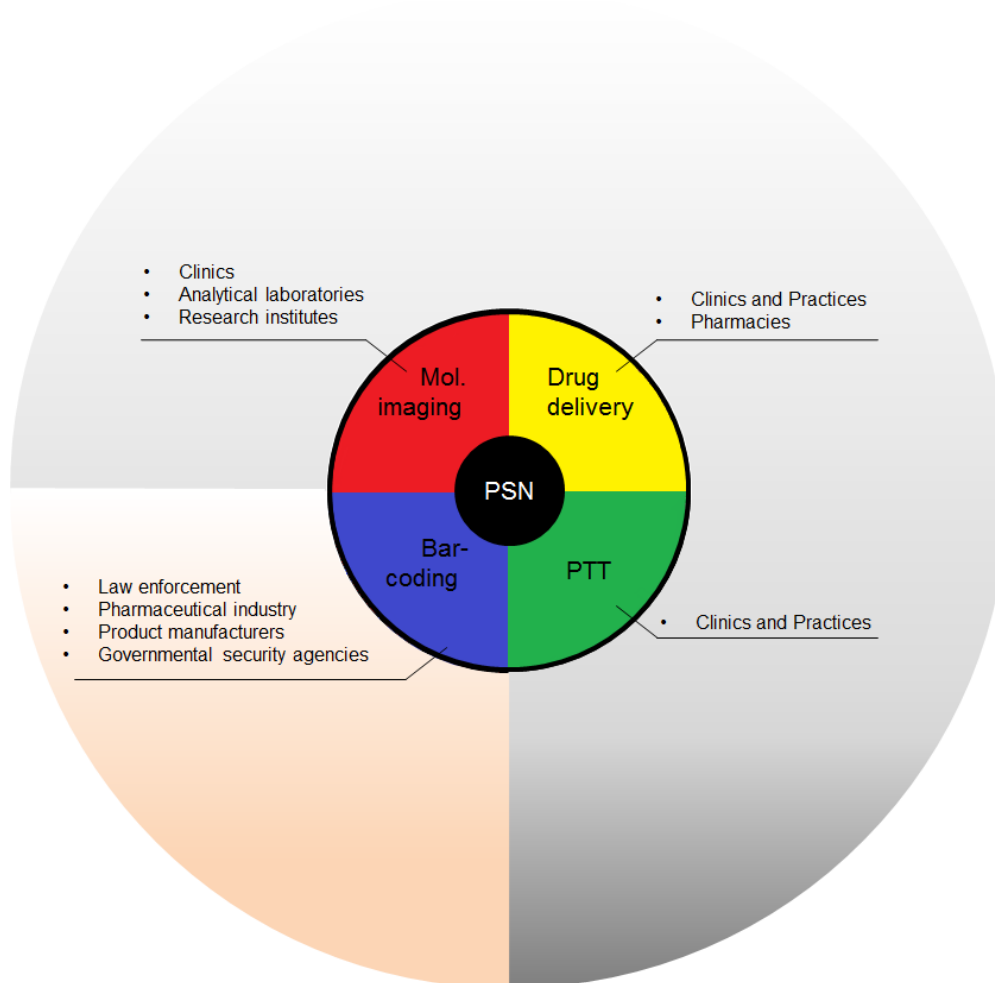


Figure A2-6: Potential customers for semiconducting polymeric nanoparticles.

However, a quarter of the total costs for the start-up are reserved for the development such as the development and chemical modification of the semiconducting polymers. In the first instance the outsourcing of the quality control may be sensible due to the low costs of the measurements but the high costs of the instrumentation (e.g. TEM ~£100,000). According to this estimation the costs for the initiation of a start-up company for the production of semiconducting polymeric nanoparticles are about £120,000. This price, however, may considerably increase due to the patent law, which may involve purchasing a licence which allows for the production of the nanoparticles. Therefore, a brief survey of intellectual property demands has been carried out in the next section. However, in order to determine the success of such a venture, a lawyer specialized in patent law needs to extend on the interpretation of the patents related to the semiconducting polymeric nanoparticles.

Intellectual property

Due to the ever increasing demand of molecular targeted contrast agents, numerous patents have been issued relating to these products. New patents are added frequently, as new synthesis methods and new materials allow for the development of novel imaging probes. Patents span from organic dyes for PA imaging¹⁹⁷ and microbubbles for combined ultrasound and PA imaging¹⁹⁸ to biodegradable cellulose nanoparticles for PA imaging¹⁹⁹. Despite being written to cover a broad spectrum of materials and methods, none of these patents will affect the commercialisation of the nanospheres for molecular PA imaging, because these patents do not cover nanoparticles made from semiconducting polymers. However, one patent²⁰⁰, issued at the beginning of 2015, describes molecular probes for PA imaging similar to those proposed here. Even though the particles described in the patent are used for molecular sensing, they employ reactive molecules for the detection of reactive oxygen species. This fundamentally differs from the targeting mechanism realised by the nanoparticles proposed within this document: targeting of molecular markers present, for example, on the surface of cancerous tumour cells by the means of proteins conjugated to the nanoparticle surface. Apart from the targeting mechanism, the particles proposed here also differ in their chemical composition compared to the particles described in the patent. The particles described herein are made of a different polymeric material, use a different coating, and are synthesised via a different method. However, a patent law expert needs to revise these patents and extend the search to avoid intellectual property violations. If, however, patents are in violation with the intention of the start-up company as proposed here, considerations can be made for either buying the patents from the holder or to buy a license to manufacture semiconducting polymeric nanoparticles.

Conclusion

In this chapter, four potential fields have been identified as possible future markets for the commercial application of the material class of semiconducting polymeric nanoparticles, which are: biomedical imaging and sensing, photothermal therapy, drug delivery and barcoding (see Table A2-3).

Table A2-3: Summary of the commercial potential for the applications evaluated.

Application	Customers	Stage	Comment
Contrast agent	<ul style="list-style-type: none"> • Clinics • Research laboratories • Analytical laboratories 	<p>Available for research purposes. The cost intensive translation from laboratory to the clinics, including various clinical trials, is required before the market is available to the semiconducting polymeric nanoparticles.</p>	<p>Well suited for PA and fluorescence imaging and combination of these with other contrast agents. Immediate commercial potential.</p>
Drug delivery	<ul style="list-style-type: none"> • Clinics • Practices • Pharmacies 		<p>Expensive translation from laboratory to the bedside. Semiconducting polymeric nanoparticles aimed for the personalised treatment market bears great potential, especially in combination with imaging.</p>
Photosensitizer (PTT)	<ul style="list-style-type: none"> • Clinics • Practices 		
Barcoding	<ul style="list-style-type: none"> • Law enforcement • Pharmaceutical industry • Product manufacturers • Governmental security agencies 	<p>Available for application. Little research needed. semiconducting polymeric nanoparticles could be spray-painted to the surface of objects for prove of concept.</p>	<p>Great market potential when second generation barcode readers and nanoparticle based barcoding materials are established.</p>

For the foreseeable future, the major application will be within the field of biomedical imaging and sensing. This expectation is based on the properties ideal for optical imaging modalities such as PA imaging. In addition to this the commercialisation of semiconducting polymeric nanoparticles as vesicle for targeted drug delivery or as photosensitizer for photothermal therapy is hampered by the high costs for the translation from the laboratory to the clinics - today the development of a new drug has been estimated to costs about \$1 billion per drug. Therefore, a start-up company would concentrate on developing a marketing strategy targeting the biomedical imaging and sensing market. However, with the emergence of second generation barcoding technology another field for the commercial application of the semiconducting polymeric nanoparticles is arising. The market volume of all these fields is enormous - multimillion dollar annual turnover with annual double digit growth rates.

Semiconducting polymeric nanoparticles are an addition to a pool of competitor materials, for example gold nanoparticles for biomedical imaging, which possess similar properties and therefore will share these markets. Nonetheless, when established, the semiconducting polymeric nanoparticles may have developed a market volume similar to that of gold nanorods, which over a short period of time has grown to a volume of about \$4 billion. The costs for a start-up company are relatively low as well as the production costs of the nanoparticles - therefore giving room for great profit. The success of such a venture depends greatly on the patents that protect the intellectual property of nanoparticles made from semiconducting polymers. Therefore, the relevant patents need to be explored in more detail by a patent law expert. In summary: The proposed nanoparticles can be mass produced at low costs and have great immediate commercial potential due to the volume of the targeted markets. However, patents will ultimately determine whether it is feasible to commercialize this product.

Bibliography

1. Chen, Y.-S. *et al.* Silica-coated gold nanorods as photoacoustic signal nanoamplifiers. *Nano Lett.* **11**, 348–54 (2011).
2. Beard, P. Biomedical photoacoustic imaging. *Interface Focus* **1**, 602–631 (2011).
3. Jokerst, J. V., Cole, A. J., Van de Sompel, D. & Gambhir, S. S. Gold Nanorods for Ovarian Cancer Detection with Photoacoustic Imaging and Resection Guidance via Raman Imaging in Living Mice. *ACS Nano* **6**, 10366–77 (2012).
4. Song, K. H., Kim, C., Cobley, C. M., Xia, Y. & Wang, L. V. Near-infrared gold nanocages as a new class of tracers for photoacoustic sentinel lymph node mapping on a rat model. *Nano Lett.* **9**, 183–8 (2009).
5. Pan, D. *et al.* Molecular photoacoustic imaging of angiogenesis with integrin-targeted gold nanobeacons. *FASEB J.* **25**, 875–82 (2011).
6. Wang, B. *et al.* Intravascular Photoacoustic Imaging of Macrophages using Molecular Targeted Gold Nanoparticles. *Proc. SPIE* **7564**, 75640A–75640A–7 (2010).
7. Brunker, J. & Beard, P. Pulsed photoacoustic Doppler flowmetry using time-domain cross-correlation: accuracy, resolution and scalability. *J. Acoust. Soc. Am.* **132**, 1780–1791 (2012).
8. Brunker, J. & Beard, P. Acoustic resolution photoacoustic Doppler flowmetry: practical considerations for obtaining accurate measurements of blood flow. in *Proc. of SPIE, Photons Plus Ultrasound: Imaging and Sensing* (eds. Oraevsky, A. A. & Wang, L. V.) **8943**, 89431K–1–89431K–7 (2014).
9. Zhang, H. F., Maslov, K., Stoica, G. & Wang, L. V. Functional photoacoustic microscopy for high-resolution and noninvasive in vivo imaging. *Nat. Biotechnol.* **24**, 848–51 (2006).
10. Bell, A. The production of sound by radiant energy. *Nature* **12 May**, 42–44 (1881).
11. Wang, L. V. & Wu, H.-I. *Biomedical Optics: Principles and Imaging*. (Wiley, 2007).
12. de la Zerda, A., Kim, J.-W., Galanzha, E. I., Gambhir, S. S. & Zharov, V. P. Advanced contrast nanoagents for photoacoustic molecular imaging, cytometry, blood test and photothermal theranostics. *Contrast Media Mol. Imaging* **6**, 346–69 (2011).
13. Franzen, S., Kiger, L., Poyart, C. & Martin, J. L. Heme photolysis occurs by ultrafast excited state metal-to-ring charge transfer. *Biophys. J.* **80**, 2372–85 (2001).
14. Wang, X. *et al.* Noninvasive laser-induced photoacoustic tomography for structural and functional in vivo imaging of the brain. *Nat. Biotechnol.* **21**, 803–6 (2003).

15. Zhang, H. F., Maslov, K., Stoica, G. & Wang, L. V. Functional photoacoustic microscopy for high-resolution and noninvasive in vivo imaging. *Nat. Biotechnol.* **24**, 848–51 (2006).
16. Laufer, J., Delpy, D., Elwell, C. & Beard, P. Quantitative spatially resolved measurement of tissue chromophore concentrations using photoacoustic spectroscopy: application to the measurement of blood oxygenation and haemoglobin concentration. *Phys. Med. Biol.* **52**, 141–168 (2007).
17. Oh, J.-T. *et al.* Three-dimensional imaging of skin melanoma in vivo by dual-wavelength photoacoustic microscopy. *J. Biomed. Opt.* **11**, 34032 (2006).
18. Zhang, E. Z., Laufer, J. G., Pedley, R. B. & Beard, P. C. In vivo high-resolution 3D photoacoustic imaging of superficial vascular anatomy. *Phys. Med. Biol.* **54**, 1035–1046 (2009).
19. Oh, J.-T. *et al.* Three-dimensional imaging of skin melanoma in vivo by dual-wavelength photoacoustic microscopy. *J. Biomed. Opt.* **11**, 34032 (2006).
20. Wang, X., Pang, Y., Ku, G., Stoica, G. & Wang, L. V. Three-dimensional laser-induced photoacoustic tomography of mouse brain with the skin and skull intact. *Opt. Lett.* **28**, 1739–41 (2003).
21. Roggan, A., Friebel, M., Dörschel, K., Hahn, A. & Müller, G. Optical Properties of Circulating Human Blood in the Wavelength Range 400–2500 nm. *J. Biomed. Opt.* **4**, 36–46 (1999).
22. de la Zerda, A. *et al.* Family of enhanced photoacoustic imaging agents for high-sensitivity and multiplexing studies in living mice. *ACS Nano* **6**, 4694–701 (2012).
23. Agarwal, A. *et al.* Dual-mode imaging with radiolabeled gold nanorods. *J. Biomed. Opt.* **16**, 51307 (2011).
24. Kim, J.-W., Galanzha, E. I., Shashkov, E. V, Moon, H.-M. & Zharov, V. P. Golden carbon nanotubes as multimodal photoacoustic and photothermal high-contrast molecular agents. *Nat. Nanotechnol.* **4**, 688–94 (2009).
25. Ha, S., Carson, A., Agarwal, A., Kotov, N. a & Kim, K. Detection and monitoring of the multiple inflammatory responses by photoacoustic molecular imaging using selectively targeted gold nanorods. *Biomed. Opt. Express* **2**, 645–57 (2011).
26. Levi, J. *et al.* Design, synthesis, and imaging of an activatable photoacoustic probe. *J. Am. Chem. Soc.* **132**, 11264–9 (2010).
27. Li, P.-C. *et al.* In vivo photoacoustic molecular imaging with simultaneous multiple selective targeting using antibody-conjugated gold nanorods. *Opt. Express* **16**, 18605–15 (2008).
28. Li, P.-C. *et al.* Photoacoustic imaging of multiple targets using gold nanorods. *IEEE Trans. Ultrason. Ferroelectr. Freq. Control* **54**, 1642–7 (2007).
29. Bayer, C. L. C. L. *et al.* Multiplex photoacoustic molecular imaging using targeted silica-coated gold nanorods. *Biomed. Opt. Express* **2**, 1828–1835 (2011).

30. Fan, Z. *et al.* Multifunctional plasmonic shell-magnetic core nanoparticles for targeted diagnostics, isolation, and photothermal destruction of tumor cells. *ACS Nano* **6**, 1065–73 (2012).
31. Homan, K. a *et al.* Silver nanoplate contrast agents for in vivo molecular photoacoustic imaging. *ACS Nano* **6**, 641–50 (2012).
32. Bhattacharyya, S. *et al.* Synthesis and Evaluation of Near-Infrared (NIR) Dye-Herceptin conjugates as photoacoustic computed tomography (PCT) Probes for HER2 Expression in Breast Cancer. *Bioconjug. Chem.* **19**, 1186–1193 (2008).
33. de la Zerda, A. *et al.* Ultrahigh sensitivity carbon nanotube agents for photoacoustic molecular imaging in living mice. *Nano Lett.* **10**, 2168–72 (2010).
34. De la Zerda, A. *et al.* Carbon nanotubes as photoacoustic molecular imaging agents in living mice. *Nat. Nanotechnol.* **3**, 557–62 (2008).
35. Meng-Lin, L. *et al.* Simultaneous Molecular and Hypoxia Imaging of Brain Tumors Using In Vivo Spectroscopic Photoacoustic Tomography. *Proc. IEEE* **96**, 481–489 (2008).
36. Tan, X. *et al.* A NIR heptamethine dye with intrinsic cancer targeting, imaging and photosensitizing properties. *Biomaterials* **33**, 2230–9 (2012).
37. Zhang, C. *et al.* A near-infrared fluorescent heptamethine indocyanine dye with preferential tumor accumulation for in vivo imaging. *Biomaterials* **31**, 6612–7 (2010).
38. Biswas, S., Dodwadkar, N. S., Sawant, R. R., Koshkaryev, A. & Torchilin, V. P. Surface modification of liposomes with rhodamine-123-conjugated polymer results in enhanced mitochondrial targeting. *J. Drug Target.* **19**, 552–561 (2011).
39. Steichen, S. D., Caldorera-Moore, M. & Peppas, N. a. A review of current nanoparticle and targeting moieties for the delivery of cancer therapeutics. *Eur. J. Pharm. Sci.* **48**, 416–427 (2012).
40. Hühn, D. *et al.* Polymer-coated nanoparticles interacting with proteins and cells: focusing on the sign of the net charge. *ACS Nano* **7**, 3253–63 (2013).
41. Levitan, H. Food, drug, and cosmetic dyes: biological effects related to lipid solubility. *Proc. Natl. Acad. Sci. U. S. A.* **74**, 2914–8 (1977).
42. Bass, I. L., Bonanno, R. E., Hackel, R. P. & Hammond, P. R. High-average-power dye laser at Lawrence Livermore National Laboratory. *Appl. Opt.* **31**, 6993–7006 (1992).
43. Sabnis, R. W. *Handbook of Biological Dyes and Stains: Synthesis and Industrial Applications.* (Wiley & Sons Inc., 2010). at <<http://www.scribd.com/doc/39254287/Handbook-of-Biological-Dyes-and-Stains-Synth-And-Indl-Appl>>
44. Abuteen, A. *et al.* The evaluation of NIR-absorbing porphyrin derivatives as contrast agents in photoacoustic imaging. *Phys. Chem. Chem. Phys.* **15**, 18502–9 (2013).
45. Song, K. H., Stein, E. W., Margenthaler, J. & Wang, L. V. Noninvasive

- photoacoustic identification of sentinel lymph nodes containing methylene blue in vivo in a rat model. *J. Biomed. Opt.* **13**, 54033 (2008).
46. Shashkov, E. V, Everts, M., Galanzha, E. I. & Zharov, V. P. Quantum dots as multimodal photoacoustic and photothermal contrast agents. *Nano Lett.* **8**, 3953–8 (2008).
 47. Landsman, M. L., Kwant, G., Mook, G. a & Zijlstra, W. G. Light-absorbing properties, stability, and spectral stabilization of indocyanine green. *J. Appl. Physiol.* **40**, 575–83 (1976).
 48. Widengren, J. & Rigler, R. Mechanisms of photobleaching investigated by fluorescence correlation spectroscopy. *Bioimaging* **4**, 149–157 (1996).
 49. Penzkofer, A. & Blau, W. Theoretical analysis of S1-state lifetime measurements of dyes with picosecond laser pulses. *Opt. Quantum Electron.* **15**, 325–347 (1983).
 50. Spano, F. C. & Silva, C. H- and J-aggregate behavior in polymeric semiconductors. *Annu. Rev. Phys. Chem.* **65**, 477–500 (2014).
 51. Wang, X. *et al.* Noninvasive photoacoustic angiography of animal brains in vivo with near-infrared light and an optical contrast agent. *Opt. Lett.* **29**, 730–2 (2004).
 52. Wang, L. *et al.* Combined photoacoustic and molecular fluorescence imaging in vivo. *Conf. Proc. IEEE Eng. Med. Biol. Soc.* **1**, 190–2 (2005).
 53. de la Zerda, A. *et al.* Ultrahigh sensitivity carbon nanotube agents for photoacoustic molecular imaging in living mice. *Nano Lett.* **10**, 2168–72 (2010).
 54. Li, M. *et al.* Simultaneous molecular and hypoxia imaging of brain tumors in vivo using spectroscopic photoacoustic tomography. *Proc. IEEE* **96**, 481–489 (2008).
 55. Song, K. H., Stein, E. W., Margenthaler, J. a & Wang, L. V. Noninvasive photoacoustic identification of sentinel lymph nodes containing methylene blue in vivo in a rat model. *J. Biomed. Opt.* **13**, 54033 (2012).
 56. Ke, H., Erpelding, T. N., Jankovic, L., Liu, C. & Wang, L. V. Performance characterization of an integrated ultrasound, photoacoustic, and thermoacoustic imaging system. *J. Biomed. Opt.* **17**, 56010-1-56010-6 (2012).
 57. Levi, J. *et al.* Molecular photoacoustic imaging of follicular thyroid carcinoma. *Clin. Cancer Res.* **19**, 1494–502 (2013).
 58. Buzea, C., Pacheco, I. I. & Robbie, K. Nanomaterials and nanoparticles: Sources and toxicity. *Biointerphases* **2**, MR17 (2007).
 59. Daniel, M.-C. & Astruc, D. Gold nanoparticles: assembly, supramolecular chemistry, quantum-size-related properties, and applications toward biology, catalysis, and nanotechnology. *Chem. Rev.* **104**, 293–346 (2004).
 60. Schmid, G. & Corain, B. Nanoparticulated Gold: Syntheses, Structures, Electronics, and Reactivities. *Eur. J. Inorg. Chem.* **2003**, 3081–3098 (2003).
 61. Pérez-Juste, J., Liz-Marzán, L. M., Carnie, S., Chan, D. Y. C. & Mulvaney,

- P. Electric-Field-Directed Growth of Gold Nanorods in Aqueous Surfactant Solutions. *Adv. Funct. Mater.* **14**, 571–579 (2004).
62. Tuncel, D. & Demir, H. V. Conjugated polymer nanoparticles. *Nanoscale* **2**, 484–94 (2010).
63. Vauthier, C. & Bouchemal, K. Methods for the preparation and manufacture of polymeric nanoparticles. *Pharm. Res.* **26**, 1025–58 (2009).
64. Yoffe, A. D. Low-dimensional systems: quantum size effects and electronic properties of semiconductor microcrystallites (zero-dimensional systems) and some quasi-two-dimensional systems. *Adv. Phys.* **42**, 173–262 (1993).
65. Murray, C. B., Kagan, C. R. & Bawendi, M. G. Synthesis and characterisation of monodisperse nanocrystals and close-packed nanocrystal assemblies. *Annu. Rev. Mater. Sci.* **30**, 545–610 (2000).
66. Orendorff, C. J., Sau, T. K. & Murphy, C. J. Shape-dependent plasmon-resonant gold nanoparticles. *Small* **2**, 636–9 (2006).
67. Jain, P. K., Lee, K. S., El-Sayed, I. H. & El-Sayed, M. a. Calculated absorption and scattering properties of gold nanoparticles of different size, shape, and composition: applications in biological imaging and biomedicine. *J. Phys. Chem. B* **110**, 7238–48 (2006).
68. Chang, S.-S., Shih, C.-W., Chen, C.-D., Lai, W.-C. & Wang, C. R. C. The Shape Transition of Gold Nanorods. *Langmuir* **15**, 701–709 (1999).
69. Chang, S.-S., Lee, C.-L. & Wang, C. R. C. Gold Nanorods: Electrochemical Synthesis and Optical Properties. *J. Phys. Chem. B* **101**, 6661–6664 (1997).
70. Link, S. & El-Sayed, M. a. Shape and size dependence of radiative, non-radiative and photothermal properties of gold nanocrystals. *Int. Rev. Phys. Chem.* **19**, 409–453 (2000).
71. Roduner, E. Size matters: why nanomaterials are different. *Chem. Soc. Rev.* **35**, 583–92 (2006).
72. Sudheendra, L. *et al.* NaGdF₄:Eu(3+) Nanoparticles for Enhanced X-ray Excited Optical Imaging. *Chem. Mater.* **26**, 1881–1888 (2014).
73. Hainfeld, J. F., Slatkin, D. N., Focella, T. M. & Smilowitz, H. M. Gold nanoparticles: a new X-ray contrast agent. *Br. J. Radiol.* **79**, 248–53 (2006).
74. Sun, G. *et al.* Strategies for Optimized Radiolabeling of Nanoparticles for in vivo PET Imaging. *Adv. Mater.* **19**, 3157–3162 (2007).
75. Stockhofe, K., Postema, J. M., Schieferstein, H. & Ross, T. L. Radiolabeling of Nanoparticles and Polymers for PET Imaging. *Pharmaceuticals* **7**, 392–418 (2014).
76. de Barros, A. B., Tsourkas, A., Saboury, B., Cardoso, V. N. & Alavi, A. Emerging role of radiolabeled nanoparticles as an effective diagnostic technique. *EJNMMI Res.* **2**, 39 (2012).
77. Hadjipanayis, C. G. *et al.* Metallic iron nanoparticles for MRI contrast enhancement and local hyperthermia. *Small* **4**, 1925–9 (2008).

78. Na, H. Bin, Song, I. C. & Hyeon, T. Inorganic Nanoparticles for MRI Contrast Agents. *Adv. Mater.* **21**, 2133–2148 (2009).
79. Tang, W. *et al.* Fe₅C₂ nanoparticles with high MRI contrast enhancement for tumor imaging. *Small* **10**, 1245–9 (2014).
80. Zheng, S.-G., Xu, H.-X. & Chen, H.-R. Nano/microparticles and ultrasound contrast agents. *World J. Radiol.* **5**, 468–71 (2013).
81. Chiriaco, F. *et al.* Epithelial cell biocompatibility of silica nanospheres for contrast-enhanced ultrasound molecular imaging. *J. Nanoparticle Res.* **15**, 1779 (2013).
82. Liu, J. *et al.* Nanoparticles as image enhancing agents for ultrasonography. *Phys. Med. Biol.* **51**, 2179–89 (2006).
83. Jetty, R. *et al.* Protein triggered fluorescence switching of near-infrared emitting nanoparticles for contrast-enhanced imaging. *J. Mater. Chem. B* **1**, 4542 (2013).
84. Asselin, J., Viger, M. L. & Boudreau, D. Metal-Enhanced Fluorescence and FRET in Multilayer Core-Shell Nanoparticles. *Adv. Chem.* **2014**, 1–16 (2014).
85. Wang, J. *et al.* Fluorophore-gold nanoparticle complex for sensitive optical biosensing and imaging. *Nanotechnology* **23**, 95501 (2012).
86. Krieger, J. W. *et al.* Imaging fluorescence (cross-) correlation spectroscopy in live cells and organisms. *Nat. Protoc.* **10**, 1948–1974 (2015).
87. Ku, G. *et al.* Copper sulfide nanoparticles as a new class of photoacoustic contrast agent for deep tissue imaging at 1064 nm. *ACS Nano* **6**, 7489–96 (2012).
88. Jokerst, J. V., Van de Sompel, D., Bohndiek, S. E. & Gambhir, S. S. Cellulose nanoparticles are a biodegradable photoacoustic contrast agent for use in living mice. *Photoacoustics* **2**, 119–127 (2014).
89. Ackerson, C. J., Jadzinsky, P. D., Sexton, J. Z., Bushnell, D. a & Kornberg, R. D. Synthesis and bioconjugation of 2 and 3 nm-diameter gold nanoparticles. *Bioconjug. Chem.* **21**, 214–8 (2010).
90. Kim, C. *et al.* In Vivo Molecular Photoacoustic Tomography of Melanomas Targeted by Bioconjugated Gold Nanocages. **4**, 4559–4564 (2010).
91. Chen, J. *et al.* Gold nanocages: Bioconjugation and their potential use as optical imaging contrast agents. *Nano Lett.* **5**, 473–7 (2005).
92. Kondo, Y. Synthesis and Characterization of Helical Multi-Shell Gold Nanowires. *Science (80-)*. **289**, 606–608 (2000).
93. Li, P.-C. *et al.* In vivo photoacoustic molecular imaging with simultaneous multiple selective targeting using antibody-conjugated gold nanorods. *Opt. Express* **16**, 18605–15 (2008).
94. Li, P.-C. *et al.* Photoacoustic imaging of multiple targets using gold nanorods. *IEEE Trans. Ultrason. Ferroelectr. Freq. Control* **54**, 1642–7 (2007).
95. Eghtedari, M. *et al.* High sensitivity of in vivo detection of gold nanorods

- using a laser optoacoustic imaging system. *Nano Lett.* **7**, 1914–8 (2007).
96. Chen, L.-C. *et al.* Enhanced photoacoustic stability of gold nanorods by silica matrix confinement. *J. Biomed. Opt.* **15**, 16010 (2010).
 97. Yoon, S. J. *et al.* Utility of biodegradable plasmonic nanoclusters in photoacoustic imaging. *Opt. Lett.* **35**, 3751–3 (2010).
 98. Ji, X. *et al.* Bifunctional Gold Nanoshells with a Superparamagnetic Iron Oxide-Silica Core Suitable for Both MR Imaging and Photothermal Therapy. *J. Phys. Chem. C. Nanomater. Interfaces* **111**, 6245 (2007).
 99. Xiang, L. *et al.* Gold nanoshell-based photoacoustic imaging application in biomedicine *. *Biophotonics, Nanophotonics Metamaterials, 2006* **1**, 76–79 (2006).
 100. Chen, Y.-S. *et al.* Silica-coated gold nanorods as photoacoustic signal nanoamplifiers. *Nano Lett.* **11**, 348–54 (2011).
 101. Perner, M. *et al.* Optically Induced Damping of the Surface Plasmon Resonance in Gold Colloids. *Phys. Rev. Lett.* **78**, 9–12 (1997).
 102. Li, P. C. *et al.* Photoacoustic flow measurements by use of laser-induced shape transitions of gold nanorods. *Opt. Lett.* **30**, 3341–3343 (2005).
 103. Wei, C.-W., Huang, S.-W., Wang, C.-R. C. & Li, P.-C. Photoacoustic flow measurements based on wash-in analysis of gold nanorods. *IEEE Trans. Ultrason. Ferroelectr. Freq. Control* **54**, 1131–41 (2007).
 104. Liao, C.-K., Huang, S.-W., Wei, C.-W. & Li, P.-C. Nanorod-based flow estimation using a high-frame-rate photoacoustic imaging system. *J. Biomed. Opt.* **12**, 64006 (2010).
 105. Bayer, C. L. C. L. *et al.* Multiplex photoacoustic molecular imaging using targeted silica-coated gold nanorods. *Biomed. Opt. Express* **2**, 1828–1835 (2011).
 106. Agarwal, A. *et al.* Dual-mode imaging with radiolabeled gold nanorods. *J. Biomed. Opt.* **16**, 51307 (2011).
 107. Wilson, K., Homan, K. & Emelianov, S. Biomedical photoacoustics beyond thermal expansion using triggered nanodroplet vaporization for contrast-enhanced imaging. *Nat. Commun.* **3**, 610–618 (2012).
 108. Yang, X., Skrabalak, S. E., Li, Z.-Y., Xia, Y. & Wang, L. V. Photoacoustic tomography of a rat cerebral cortex in vivo with Au nanocages as an optical contrast agent. *Nano Lett.* **7**, 3798–802 (2007).
 109. Cai, X. *et al.* In vivo quantitative evaluation of the transport kinetics of gold nanocages in a lymphatic system by noninvasive photoacoustic tomography. *ACS Nano* **5**, 9658–67 (2011).
 110. Yoon, S. J. *et al.* Utility of biodegradable plasmonic nanoclusters in photoacoustic imaging. *Opt. Lett.* **35**, 3751–3 (2010).
 111. Thess A, Lee R, Nikolaev Pavel, Dai H, Petit P, Robert J, Xu C, Hee Lee Y, Gon Kim S, Rinzler AG, Colbert DT, Scuseria GE, Tomanek D, Fischer JE, S. R. Crystalline Ropes of Metallic Carbon Nanotubes. *Science* (80-). **273**, 483–487 (1996).
 112. Dai, H. Carbon nanotubes: synthesis, integration, and properties. *Acc.*

- Chem. Res.* **35**, 1035–44 (2002).
113. Zharov, V. P. *et al.* Photoacoustic flow cytometry: principle and application for real-time detection of circulating single nanoparticles, pathogens, and contrast dyes in vivo. *J. Biomed. Opt.* **12**, 51503 (2012).
 114. Braun, D. & Heeger, a. J. Visible light emission from semiconducting polymer diodes. *Appl. Phys. Lett.* **58**, 1982 (1991).
 115. Burroughes, J. H. *et al.* Light-emitting diodes based on conjugated polymers. *Nature* **347**, 539–541 (1990).
 116. Ashraf, R. S. *et al.* Silaindacenodithiophene Semiconducting Polymers for Efficient Solar Cells and High-Mobility Ambipolar Transistors †. *Chem. Mater.* **23**, 768–770 (2011).
 117. McCulloch, I. *et al.* Design of semiconducting indacenodithiophene polymers for high performance transistors and solar cells. *Acc. Chem. Res.* **45**, 714–22 (2012).
 118. Pu, K. *et al.* Semiconducting polymer nanoparticles as photoacoustic molecular imaging probes in living mice. *Nat. Nanotechnol.* **9**, 233–9 (2014).
 119. Zha, Z. *et al.* Biocompatible polypyrrole nanoparticles as a novel organic photoacoustic contrast agent for deep tissue imaging. *Nanoscale* **5**, 4462–7 (2013).
 120. Song, X. *et al.* Ultra-Small Iron Oxide Doped Polypyrrole Nanoparticles for In Vivo Multimodal Imaging Guided Photothermal Therapy. *Adv. Funct. Mater.* **24**, 1194–1201 (2014).
 121. Geng, J. *et al.* Biocompatible Conjugated Polymer Nanoparticles for Efficient Photothermal Tumor Therapy. *Small* 1–8 (2014). doi:10.1002/smll.201402092
 122. Cheng, L., Yang, K., Chen, Q. & Liu, Z. Organic stealth nanoparticles for highly effective in vivo near-infrared photothermal therapy of cancer. *ACS Nano* **6**, 5605–13 (2012).
 123. Napp, J. *et al.* Targeted luminescent near-infrared polymer-nanoprobes for in vivo imaging of tumor hypoxia. *Anal. Chem.* **83**, 9039–46 (2011).
 124. Behnke, T. *et al.* Encapsulation of hydrophobic dyes in polystyrene micro- and nanoparticles via swelling procedures. *J. Fluoresc.* **21**, 937–44 (2011).
 125. Shi, D. *et al.* Fluorescent Polystyrene-Fe₃O₄ Composite Nanospheres for In Vivo Imaging and Hyperthermia. *Adv. Mater.* **21**, 2170–2173 (2009).
 126. Yu, J. *et al.* Self-assembly synthesis, tumor cell targeting, and photothermal capabilities of antibody-coated indocyanine green nanocapsules. *J. Am. Chem. Soc.* **132**, 1929–38 (2010).
 127. Song, X. *et al.* J-Aggregates of Organic Dye Molecules Complexed with Iron Oxide Nanoparticles for Imaging-Guided Photothermal Therapy Under 915-nm Light. *Small* 10–12 (2014). doi:10.1002/smll.201401025
 128. Li, F.-Q. *et al.* Preparation and characterization of sodium ferulate entrapped bovine serum albumin nanoparticles for liver targeting. *Int. J. Pharm.* **349**, 274–82 (2008).

129. Jeong, H. *et al.* Photosensitizer-conjugated human serum albumin nanoparticles for effective photodynamic therapy. *Theranostics* **1**, 230–9 (2011).
130. Gu, G. *et al.* PEG-co-PCL nanoparticles modified with MMP-2/9 activatable low molecular weight protamine for enhanced targeted glioblastoma therapy. *Biomaterials* **34**, 196–208 (2013).
131. Yang, Y. *et al.* Ultrabright and ultrastable near-infrared dye nanoparticles for in vitro and in vivo bioimaging. *Biomaterials* **33**, 7803–9 (2012).
132. Rossin, R., Muro, S., Welch, M. J., Muzykantov, V. R. & Schuster, D. P. In vivo imaging of ⁶⁴Cu-labeled polymer nanoparticles targeted to the lung endothelium. *J. Nucl. Med.* **49**, 103–11 (2008).
133. Rolfe, B. E. *et al.* Multimodal polymer nanoparticles with combined ¹⁹F magnetic resonance and optical detection for tunable, targeted, multimodal imaging in vivo. *J. Am. Chem. Soc.* **136**, 2413–9 (2014).
134. Krause, J., Imlau, M., Woike, T. & Schaniel, D. Improvement in photostability of solid state dye by oxygen removal. *Opt. Mater. Express* **2**, 71 (2011).
135. Lovell, J. F. *et al.* Porphysome nanovesicles generated by porphyrin bilayers for use as multimodal biophotonic contrast agents. *Nat. Mater.* **10**, 324–32 (2011).
136. Liu, J. *et al.* Conjugated polymer nanoparticles for photoacoustic vascular imaging. *Polym. Chem.* **5**, 2854 (2014).
137. Sherar, M. D. & Foster, F. S. The design and fabrication of high frequency poly(vinylidene fluoride) transducers. *Ultrason. Imaging* **11**, 75–94 (1989).
138. Laufer, J., Zhang, E. & Beard, P. Evaluation of Absorbing Chromophores Used in Tissue Phantoms for Quantitative Photoacoustic Spectroscopy and Imaging. *IEEE J. Sel. Top. Quantum Electron.* **16**, 600–607 (2010).
139. Beard, P. C., Perennes, F. & Mills, T. N. Transduction mechanisms of the Fabry-Perot polymer film sensing concept for wideband ultrasound detection. *IEEE Trans. Ultrason. Ferroelectr. Freq. Control* **46**, 1575–1582 (1999).
140. Zhang, E., Laufer, J. & Beard, P. Backward-mode multiwavelength photoacoustic scanner using a planar Fabry-Perot polymer film ultrasound sensor for high-resolution three-dimensional imaging of biological tissues. *Appl. Opt.* **47**, 561–577 (2008).
141. Yao, D., Zhang, C., Maslov, K. & Wang, L. V. Photoacoustic measurement of the Grüneisen parameter of tissue. *J. Biomed. Opt.* **19**, 17007 (2014).
142. Bronstein, H. *et al.* Thieno[3,2-b]thiophene-diketopyrrolopyrrole-containing polymers for high-performance organic field-effect transistors and organic photovoltaic devices. *J. Am. Chem. Soc.* **133**, 3272–5 (2011).
143. Fallon, K. J. *et al.* A Nature-Inspired Conjugated Polymer for High Performance Transistors and Solar Cells. *Macromolecules* **48**, 5148–5154 (2015).
144. Bergmann, K. & Konski, T. O. A spectroscopic study of methylene blue

- monomer, dimer, and complexes with montmorillonite. *J. Phys. Chem.* **67**, 2169–2177 (1963).
145. Prael, S. A. & Jacquess, S. Oregon medical laser center. (2012). at <omlc.ogi.edu>
146. Schöppler, F. *et al.* Molar Extinction Coefficient of Single-Wall Carbon Nanotubes. *J. Phys. Chem. C* **115**, 14682–14686 (2011).
147. Li, C.-Z., Male, K. B., Hrapovic, S. & Luong, J. H. T. Fluorescence properties of gold nanorods and their application for DNA biosensing. *Chem. Commun.* **1**, 3924–3926 (2005).
148. Olmsted, J. Calorimetric Determinations of Absolute Fluorescence Quantum Yields. *J. Phys. Chem.* **83**, 2581–2584 (1979).
149. Chapman, G., Henary, M. & Patonay, G. The effect of varying short-chain alkyl substitution on the molar absorptivity and quantum yield of cyanine dyes. *Anal. Chem. Insights* **6**, 29–36 (2011).
150. Conceição, D. S., Ferreira, D. P. & Ferreira, L. F. V. Photochemistry and Cytotoxicity Evaluation of Heptamethinecyanine Near Infrared (NIR) Dyes. *Int. J. Mol. Sci.* **14**, 18557–71 (2013).
151. J.N., D. & Crosby, G. A. The measurement of Photoluminescence Quantum Yields. *J. Phys. Chem.* **75**, 991–1024 (1971).
152. Isak, S. J. & Eyring, E. M. Fluorescence Quantum Yield of Cresyl Violet in Methanol and Water as a Function of Concentration. *J. Phys. Chem.* **58**, 1738–1742 (1992).
153. Laufer, J., Zhang, E. & Beard, P. Evaluation of Absorbing Chromophores Used in Tissue Phantoms for Quantitative Photoacoustic Spectroscopy and Imaging. *IEEE J. Sel. Top. Quantum Electron.* **16**, 600–607 (2010).
154. Chen, Y.-S., Frey, W., Aglyamov, S. & Emelianov, S. Environment-dependent generation of photoacoustic waves from plasmonic nanoparticles. *Small* **8**, 47–52 (2012).
155. Tian, C. *et al.* Dual-pulse nonlinear photoacoustic technique: a practical investigation. *Biomed. Opt. Express* **6**, 2923–2933 (2015).
156. Oraevsky, A. A., Jacques, S. L. & Tittel, F. K. Measurement of tissue optical properties by time-resolved detection of laser-induced transient stress. *Appl. Opt.* **36**, 402–425 (1997).
157. Cooper, R. J., Chang, T. M. & Williams, E. R. Hydrated Alkali Metal Ions: Spectroscopic Evidence for Clathrates. *J. Phys. Chem. A* **117**, 6571–6579 (2013).
158. Mäemets, V. & Koppel, I. Effect of ions on the ^{17}O and ^1H NMR chemical shifts of water. *J. Chem. Soc. Faraday Trans.* **94**, 3261–3269 (1998).
159. Ahmed, M., Namboodiri, V., Singh, A. K. & Mondal, J. a. On the intermolecular vibrational coupling, hydrogen bonding, and librational freedom of water in the hydration shell of mono- and bivalent anions. *J. Chem. Phys.* **141**, (2014).
160. Dillon, S. R. & Dougherty, R. C. Raman studies of the solution structure of univalent electrolytes in water. *J. Phys. Chem. A* **106**, 7647–7650 (2002).

161. Han, L., Galier, S. & Roux-de Balman, H. Ion hydration number and electro-osmosis during electrodialysis of mixed salt solution. *Desalination* **373**, 38–46 (2015).
162. Kiriukhin, M. Y. & Collins, K. D. Dynamic hydration numbers for biologically important ions. *Biophys. Chem.* **99**, 155–168 (2002).
163. Bock, C. W., Markham, G. D., Katz, A. K. & Glusker, J. P. The arrangement of first- and second-shell water molecules around metal ions: Effects of charge and size. *Theor. Chem. Acc.* **115**, 100–112 (2006).
164. Sedlák, S. Mixtures of Liquids : I . Light Scattering Characterization. *J. Phys. Chem. B* **110**, 4329–4338 (2006).
165. Chen, Y. *et al.* Electrolytes induce long-range orientational order and free energy changes in the H-bond network of bulk water. *Sci. Adv.* **2**, e1501891–e1501891 (2016).
166. Krekeler, C. & Delle Site, L. Lone pair versus bonding pair electrons: The mechanism of electronic polarization of water in the presence of positive ions. *J. Chem. Phys.* **128**, 1–6 (2008).
167. Song, L., Hennink, E. J., Young, I. T. & Tanke, H. J. Photobleaching kinetics of fluorescein in quantitative fluorescence microscopy. *Biophys. J.* **68**, 2588–600 (1995).
168. Kolmakov, K. *et al.* Red-emitting rhodamine dyes for fluorescence microscopy and nanoscopy. *Chem. - A Eur. J.* **16**, 158–166 (2010).
169. Link, S., Burda, C., Nikoobakht, B. & El-Sayed, M. a. Laser-Induced Shape Changes of Colloidal Gold Nanorods Using Femtosecond and Nanosecond Laser Pulses. *J. Phys. Chem. B* **104**, 6152–6163 (2000).
170. Taylor, A. B., Siddiquee, A. M., Chon, J. W. M. & Al, T. E. T. Below Melting Point Photothermal Reshaping of Single Gold Nanorods Driven by Surface Diffusion. 12071–12079 (2014).
171. Link, S., Wang, Z. L. & El-Sayed, M. a. How does a gold nanorod melt? *J. Phys. Chem. B* **104**, 7867–7870 (2000).
172. Nunes, J. P. M. *et al.* Functional native disulfide bridging enables delivery of a potent, stable and targeted antibody–drug conjugate (ADC). *Chem. Commun.* **51**, 10624–10627 (2015).
173. Almeida, C. S., Herrmann, I. K., Howes, P. D. & Stevens, M. M. Tailoring Cellular Uptake of Conjugated Polymer Nanoparticles Using Modular Amphiphilic Peptide Capping Ligands. *Chem. Mater.* **27**, 6879–6889 (2015).
174. Treeby, B. E. & Cox, B. T. k-Wave: MATLAB toolbox for the simulation and reconstruction of photoacoustic wave fields. *J. Biomed. Opt.* **15**, 21314 (2010).
175. Treeby, B. E. Acoustic attenuation compensation in photoacoustic tomography using time-variant filtering. *J. Biomed. Opt.* **18**, 36008 (2013).
176. Zhang, E. Z. Ultrahigh-sensitivity wideband Fabry-Perot ultrasound sensors as an alternative to piezoelectric PVDF transducers for biomedical photoacoustic detection. *Proc. SPIE* **5320**, 222–229 (2004).
177. Bryden, F. *et al.* Regioselective and stoichiometrically controlled

- conjugation of photodynamic sensitizers to a HER2 targeting antibody fragment. *Bioconjug. Chem.* **25**, 611–617 (2014).
178. Tam, J. *et al.* Controlled Assembly of Biodegradable Plasmonic Nanoclusters for Near-Infrared Imaging and Therapeutic Applications. *ACS Nano* **4**, (2010).
 179. Liu, Z. *et al.* In vivo biodistribution and highly efficient tumour targeting of carbon nanotubes in mice. *Nat. Nanotechnol.* **2**, 47–52 (2007).
 180. Behnke, T., Würth, C., Laux, E. M., Hoffmann, K. & Resch-Genger, U. Simple strategies towards bright polymer particles via one-step staining procedures. *Dye. Pigment.* **94**, 247–257 (2012).
 181. McCarron, P. a., Marouf, W. M., Donnelly, R. F. & Scott, C. Enhanced surface attachment of protein-type targeting ligands to poly(lactide-co-glycolide) nanoparticles using variable expression of polymeric acid functionality. *J. Biomed. Mater. Res. - Part A* **87**, 873–884 (2008).
 182. Hong, J.-Y., Yoon, H. & Jang, J. Kinetic Study of the Formation of Polypyrrole Nanoparticles in Water-Soluble Polymer/Metal Cation Systems: A Light-Scattering Analysis. *Small* **6**, 679–686 (2010).
 183. Au, K. M., Lu, Z., Matchar, S. J. & Armes, S. P. Polypyrrole nanoparticles: A potential optical coherence tomography contrast agent for cancer imaging. *Adv. Mater.* **23**, 5792–5795 (2011).
 184. Song, S. *et al.* Novel peptide ligand directs liposomes toward EGF-R high-expressing cancer cells in vitro and in vivo. *FASEB J.* **23**, 1396–1404 (2009).
 185. Mitchell, N. *et al.* Incorporation of paramagnetic, fluorescent and PET/SPECT contrast agents into liposomes for multimodal imaging. *Biomaterials* **34**, 1179–1192 (2013).
 186. Sun, M. M. C. *et al.* Reduction–Alkylation Strategies for the Modification of Specific Monoclonal Antibody Disulfides. *Bioconjug. Chem.* **16**, 1282–1290 (2005).
 187. Bergin, J. Biologic Imaging Reagents: Technologies and Global Markets. *BccResearch* **BIO064B**, (2013).
 188. Highsmith, J. Nanoparticles in Biotechnology, Drug Development and Drug Delivery. *BccResearch* **BIO113B**, (2014).
 189. Molecular Diagnostics Market by Application (Infectious Disease (HIV, HPV, TB), Oncology, Genetics, Microbiology), Technology (PCR, Microarray, DNA Sequencing), End User (Hospital, Laboratories), Product (Instruments, Reagent, Software) - Forecast to 2020. *Mark. Mark.* **MD 2521**, (2015).
 190. Gold Nanoparticles Market Analysis By End-Use (Medical & Dentistry, Electronics, Catalysis) And Segment Forecasts To 2020. *Gd. View Res.* (2015). at <<http://www.grandviewresearch.com/industry-analysis/gold-nanoparticles-industry>>
 191. Clinical optical imaging market to reach \$2 bn in 2020. *Bus. Stand.* (2014). at <http://www.business-standard.com/content/b2b-pharma/clinical-optical-imaging-market-to-reach-2-bn-in-2020-114120800765_1.html>

192. Contrast Media/Contrast Agents Market by Product (Iodinated, Gadolinium, Barium, Microbubble), by Procedure (X-Ray/CT, MRI, Ultrasound), by Application (Radiology, Interventional Radiology, Interventional Cardiology) - Global Forecasts to 2020. *Mark. Mark. MD* **3577**, (2013).
193. Del Rey, M. The U.S. Market for Medical Imaging Contrast Media. *Bio-Tech* **260**, (2007).
194. Varotto, A. Nanomaterials in Personalized Medicine: Global Markets. *BccResearch HLC144A*, (2013).
195. Drug Delivery Technology Market by Route of Administration (Oral (Solid), Pulmonary (Nebulizer), Injectable (Device), Ocular (Liquid), Nasal (Drop), Topical (Solid), Implantable (Active), Transmucosal (Oral)), End User (Hospital, ASC, Home Care) -Forecast. *Mark. Mark. MD* **3871**, (2015).
196. Fron, R. Anti-Counterfeiting Packaging Technologies in the Global Pharmaceutical and Food Industries. *BccResearch FOD042C*, (2015).
197. Tatsuki, F., Yamauchi, F., Satoshi, Y. & Sachiko, I. Contrast agent for photoacoustic imaging and photoacoustic imaging method. (2014).
198. Kim, J.-H. *et al.* Contrast agent for combined photoacoustic and ultrasound imaging. (2015).
199. Jokerst, J. V. & Gambhir, S. S. Cellulose nanoparticle biodegradable photoacoustic contrast agents. (2014).
200. Rao, J., Pu, K. & Shuhendler, A. J. Semiconducting polymer nanoparticles as photoacoustic molecular imaging probes. (2015).